Study of exoplanetary atmospheres through the high-resolution spectroscopy technique

Ph.D. in Astronomy, Astrophysics and Space Science
(XXXVII Cycle)

Mario Basilicata
ID number 0307392

Thesis Advisor
Prof. Luigi Mancini

Co-advisor
Dr. Alessandro Sozzetti

Coordinators
Prof. Francesco Piacentini
Prof. Giuseppe Bono
Prof. Oscar Straniero

Academic Year 2023/2024

To Cristina
and my family

Acknowledgements

Prima di tutto, voglio ringraziare la persona più importante della mia vita, la donna che amo, il mio amore, Cristina. Senza di te, i tuoi abbracci, le tue parole dolci, le nostre chiacchierate, il tuo sorriso e il tuo amore, non ce l'avrei mai fatta. Quando ho avuto bisogno, ti ho sempre trovata al mio fianco, mi hai compreso, supportato e tirato su di morale, mi hai dato la forza per affrontare le difficoltà e mi hai aiutato a trovare la soluzione a qualsiasi problema, affrontandolo insieme me. Hai sempre creduto in me ed abbiamo esultato insieme per ogni traguardo che raggiungevo. Sono felice e mi sento fortunato di averti accanto a me nella mia vita. Se sono arrivato fino a qui è anche grazie a te e al nostro amore. Grazie di tutto, ti amo.

Ringrazio poi la mia famiglia. Vi ringrazio perché mi avete sempre supportato in tutti questi anni, avete sempre creduto in me e mi avete sempre fatto sentire al sicuro. Avete cercato di capire di cosa mi occupo con entusiasmo e mi siete sempre stati accanto nei momenti più difficili, strappandomi sempre qualche sorriso. Avete fatto tanti sacrifici e se sono arrivato fino a qui è anche grazie a voi. Vi voglio davvero tanto bene.

Ringrazio poi Luigi e Alessandro, i miei supervisori. Vi ringrazio poiché, in questi 3 anni di dottorato, mi avete aiutato grazie ai vostri preziosi consigli. Le vostre indicazioni mi hanno permesso di migliorare e di muovere i primi passi nel mondo della ricerca. Vi ringrazio anche per avermi dato l'opportunità di vivere esperienze davvero indimenticabili e formative.

Un ringraziamento davvero speciale lo voglio fare a Paolo. Ti ringrazio perché mi hai insegnato tanto, non solo da un punto di vista professionale, ma anche umano. La tua passione, la tua visione della ricerca, il tuo approccio sempre diretto e onesto nei confronti dei problemi, da sportivo, sono un esempio per me. Infine, ti ringrazio per la tua pazienza e per i tuoi tanti consigli, perché sono stati fondamentali per il mio percorso.

Ringrazio Enric che ha creduto in me e che, sempre con il sorriso e gran professionalità, ha saputo indirizzare e supervisionare una parte del mio lavoro. Anche se ho passato un breve periodo nel tuo gruppo di ricerca, ho imparato molto da te.

Ringrazio Matteo, Aldo e tutti i membri del gruppo GAPS per i loro preziosi consigli e suggerimenti, che hanno migliorato la qualità del mio lavoro e mi hanno fatto crescere come ricercatore.

Concludo con un grazie a me stesso, per non aver mollato mai e per aver affrontato qualsiasi sfida credendo che un passo alla volta sarei riuscito a farcela.

A tutti voi, grazie di nuovo.

Mario Basilicata

Abstract

In only three decades, mankind has gone from wondering if planets around stars different from the Sun could exist, to the confirmed discovery of more than 5 700 of them, with more than 7 200 other candidates yet to be confirmed. These extra-solar planets are called "exoplanets".
Different techniques have been developed to discover exoplanets and many instruments operate both from the ground and from the space to detect new exoplanets. In only 30 years, in addition to discovering new exoplanets, we also started investigating the atmosphere of hundreds of them.

Studying exoplanetary atmospheres ("exoatmospheres") is important, as it gives a fundamental contribution to the exoplanet characterisation process. For example, the study of the chemical properties of exoatmospheres can help to break possible degeneracies in the interior structure of exoplanets. In addition, atmospheric characterisation plays a crucial role in constraining planetary formation and evolution scenarios, since these processes leave imprints on the atmospheric composition of a planet. Finally, it can allow us to probe the habitability of exoplanets and the possible presence of biosignatures.

In the last 30 years, we discovered new classes of planets that are not present in the Solar System. This is the case of sub-Neptunes, whose variegated interior composition has still to be completely understood, and super-Earths, which are more massive versions of our planet. A new class of extreme planets that has discovered is that of hot giant planets (HGPs), which are massive gaseous planets, whose composition is dominated by H and He, with orbital periods $P_{\rm orb} \leq 10\,$days. This category includes hot Jupiters (HJs) and hot Neptunes (HNs), which are hot giant planets with a size similar to that of Jupiter and Neptune, respectively.
Since these planets orbit very close to their host star, they receive an enormous quantity of stellar radiation and their atmospheres reach temperatures $T \geq 1\,000\,$K (if their temperature is $T \geq 2\,000\,$K, we talk about ultra-hot giant planets, UHGPs). Due to their hot and inflated atmospheres, HGPs are ideal targets for atmospheric studies. Investigating their atmospheres is important because they constitute a natural laboratory to probe planetary atmospheres with extreme chemical and physical conditions, which cannot be found in the planets of the Solar System. In this way, they allow us to test and improve our current planetary atmospheric theories under a broader range of atmospheric conditions. Finally, the atmospheric study of HGPs is fundamental to improve our knowledge about the formation and evolution mechanisms behind these extreme planets.

Different techniques have been developed to study exoplanetary atmospheres. Among them, high-resolution spectroscopy demonstrated to be a very powerful technique to probe both the transmission and emission spectra of the atmosphere of close-in giant planets. High-resolution spectroscopy relies on the use of high-resolution spectrographs (spectral resolving power $R \geq 25\,000$) to measure single atmospheric spectral lines and their associated Doppler shift, which allow us to identify the chemical species that populate the atmosphere of an exoplanet in a very accurate way and to probe atmospheric dynamical effects, such as atmospheric circulation.

This Ph.D. thesis is focused on the search and characterisation of the atmospheric signal of exoplanets through the high-resolution spectroscopy technique. In particular, in this thesis, I present my contribution towards an improved comprehension of exoplanetary atmospheres, achieved through the analysis of the near-infrared (NIR) atmospheric transmission spectra of five HGPs, gathered with

the high-resolution spectrograph GIANO-B, mounted at the Telescopio Nazionale Galileo (TNG).

The first exoplanet analysed in this thesis is the warm Neptune HAT-P-11 b. The relatively small radius and low atmospheric temperature of warm Neptunes, make them more difficult targets for atmospheric studies than hot Jupiters. However, since HAT-P-11 b orbits a relatively bright host star ($V = 9.46$ mag; $H = 7.13$ mag), it is a valid target for atmospheric investigation. In Chapter 3, we reviewed the physical and architectural properties of the HAT-P-11 planetary system. Then, we report the results of the atmospheric analysis. The results show the presence of H_2O and NH_3, and a tentative detection of CH_4 and CO_2, in the atmosphere of the target. These results confirm the detection of H_2O obtained at low resolution by previous studies and constitute the first detection of NH_3 in the atmosphere of a warm Neptune. We also suggest two possible chemical scenarios that are more in accordance with the observations: the first model describes an atmosphere in chemical equilibrium with super-solar metallicity and enhanced C/O and N/O ratios relative to solar values. The second model describes an atmosphere with disequilibrium chemistry (i.e. NH_3 vertical quenching), lower metallicity, and C/O and N/O ratios close to solar values

In the second work reported in this thesis, we show the atmospheric study of the two hot Jupiters KELT-8 b and KELT-23 Ab. In this analysis, we report the first detection of the atmospheric signal of both targets, through the detection of H_2O in both atmospheres. In this work, we also report the first characterisation of the atmospheric chemical and physical properties of the two planets, by performing two different atmospheric retrieval analyses in a Bayesian framework, for each target. For both targets, we find an atmosphere rich in water vapour (from $\sim 0.1\%$ to $\sim 1\%$, in terms of volume mixing ratio) and put first constraints on the atmospheric metallicity and upper limits on the atmospheric C/O ratio. Thanks to the retrieved information about the atmospheric chemical composition, we suggest a possible formation scenario for each target. In particular, for both planets, we suggest that the accretion of gaseous material occurred within the H_2O snowline in a pebble-rich disk, where the gas was enriched in oxygen due to the sublimation of water ice from the inward-drifting pebbles.

Finally, the third analysis reported in this thesis is the atmospheric investigation of the two hot Jupiters WASP-13 b and HAT-P-1 b. In this work, we search for the first time the atmospheric signal of WASP-13 b and perform the first high-resolution investigation of the atmosphere at HAT-P-1 b. With our preliminary analysis, we do not detect the atmospheric signal of the two targets. However, in the case of WASP-13 b, we find a possible hint of the presence of CO.

Studying the atmosphere of HGPs helps us to refine our atmospheric investigation techniques, also in view of when we will be able to study the faint signal of the atmosphere of Earth-like planets, with future new-generation extremely large telescopes (e.g. the European Extremely Large Telescope, E-ELT), to search for biosignatures.

Contents

Chapter 1

Introduction

"The cosmos is also within us. We are made of star-stuff. We are a way for the cosmos to know itself."

Carl Sagan

This Ph.D. thesis is focused on the study of extra-solar planet atmospheres with high spectral resolution observations. In this first chapter, I will present an overview of the field of extra-solar planets ("exoplanets"), starting with a description of the two most successful methods for detecting them and the main properties of the known exoplanets. Then, I will describe the main chemical and physical characteristics of their atmospheres and the principal observing methods employed to study them, finishing with a dedicated section on the high-resolution spectroscopy technique.

1.1 The search for other worlds

One of the most ancient, deep, and fascinating questions human beings have always wanted to answer is whether there is life elsewhere in the Universe. It was only about thirty years ago that mankind started detecting the presence of extra-solar planets and studying their physical properties, moving the first steps towards the answer. Indeed, it was 1992, when the first two exoplanets were discovered around the pulsar PSR1257+12 (Wolszczan and Frail, 1992). Only three years later, 51 Pegasi b, the first exoplanet orbiting around a main-sequence star, was discovered (Mayor and Queloz, 1995), giving official birth to the exoplanets field of research. In only thirty years, significant progress has been made in terms of the number of detected exoplanets and the knowledge acquired about planetary physics. To date, according to data from the NASA Exoplanet Archive[1], the existence of more than 5 700 exoplanets has been confirmed, with more than 7 200 candidates still to be confirmed. As can be seen from Fig. 1.1, in the last decade the number of confirmed exoplanets has grown exponentially, particularly due to the transit discovery method. Indeed, thanks to two missions devoted to the exoplanets' discovery with the transit method, namely the *Kepler* mission (Borucki et al., 2010) launched in 2009 and the *TESS* mission (Transiting Exoplanet Survey Satellite; Ricker et al. 2015) launched in 2018, more than 3 800 transiting exoplanets have been discovered in the last 15 years. In Fig. 1.2, the confirmed exoplanets are reported in the mass-period diagram as a

[1] `https://exoplanetarchive.ipac.caltech.edu/`

function of the discovery method used. As it can be seen, even if different methods can be used to discover an exoplanet, two of them are clearly the most successful, they are the radial velocity and the transit method.

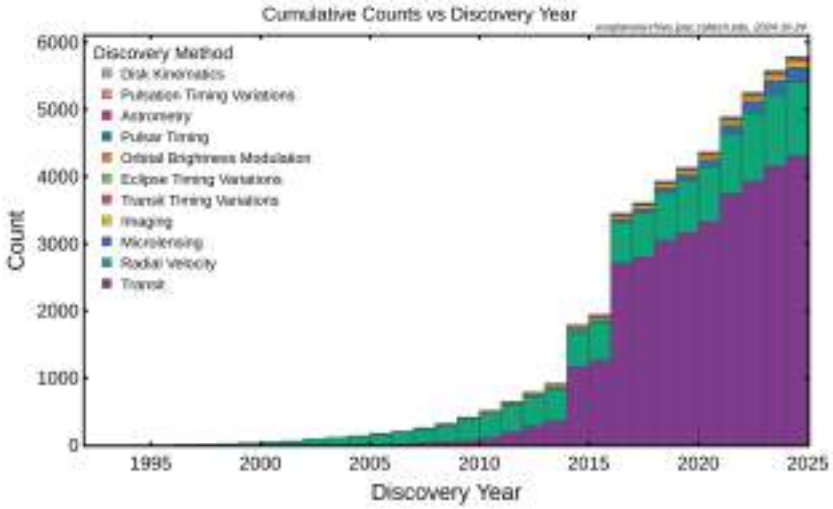

Figure 1.1: Cumulative number of exoplanets discovered per year from 1992 with different detection methods. Data from the NASA Exoplanet Archive.

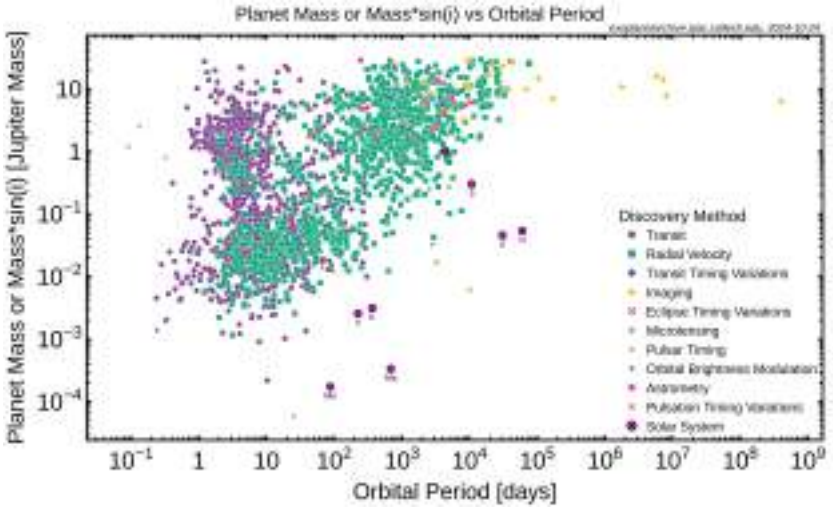

Figure 1.2: Mass-period distribution of the confirmed exoplanets (different colours represent different detection methods). Data from the NASA Exoplanet Archive.

1.1.1 Two powerful methods to discover exoplanets

The radial velocity (RV) method, the first method used for discovering exoplanets orbiting main-sequence stars (Mayor and Queloz, 1995), is based on measuring the reflex motion of the star induced by the gravitational pull of the planetary companion. The periodic motion of the star can be detected through the measurement of the Doppler shift of stellar lines: $\frac{\Delta\lambda}{\lambda} = \frac{v}{c}$, with λ = a generic stellar line wavelength, v = the velocity of the star projected along the line-of-sight (i.e. the radial velocity), and c = the speed of light. According to Kepler's equations, the periodic radial velocity (RV) of the star can be described through a combination of the orbital and physical parameters of the planetary

system in the following way:

$$RV = K_\star \cdot [\cos(\nu + \omega_\star) + e \cdot \cos(\omega_\star)] \,, \tag{1.1}$$

with ν = the orbital true anomaly, $\omega_\star$ = the stellar argument of periastron, e = the orbital eccentricity, and $K_\star$ = the stellar radial-velocity semi-amplitude. The latter can be expressed as a function of the orbital period $P_{\rm orb}$, the stellar mass $M_\star$, the planetary mass $M_{\rm p}$, and the orbital inclination i:

$$K_\star = \left(\frac{2\pi G}{P_{\rm orb}}\right)^{\frac{1}{3}} \cdot \frac{M_{\rm p} \cdot \sin(i)}{(M_\star + M_{\rm p})^{\frac{2}{3}}} \cdot \frac{1}{\sqrt{1-e^2}} \,, \tag{1.2}$$

with G = the gravitational constant. In the reasonable assumption of $M_\star \gg M_{\rm p}$, Eq. 1.2 can be expressed in solar system units as:

$$K_\star \,[{\rm m\,s^{-1}}] = 28.4 \cdot \left(\frac{P_{\rm orb}}{1\,{\rm yr}}\right)^{-\frac{1}{3}} \cdot \left(\frac{M_{\rm p} \cdot \sin(i)}{M_{\rm J}}\right) \cdot \left(\frac{M_\star}{M_\odot}\right)^{-\frac{2}{3}} \,, \tag{1.3}$$

with $M_{\rm J} = 1.898 \cdot 10^{27}\,{\rm kg}$ = Jupiter mass and $M_\odot = 1.988 \cdot 10^{30}\,{\rm kg}$ = solar mass. If we take the solar system as an example, an Earth-like planet ($M_\oplus = 5.972 \cdot 10^{24}\,{\rm kg}$ = Earth mass) at a distance of 1 au, produces on the Sun a reflex motion with a maximum RV amplitude of $\sim 10\,{\rm cm\,s^{-1}}$. On the other hand, a Jupiter-mass companion produces radial-velocity signals with an amplitude $\sim 10\,{\rm m\,s^{-1}}$, even at large orbital periods, because the larger the mass of the planet the larger the gravitational pull on the star. This is why, as can be seen from Fig. 1.2, the radial-velocity method is most sensitive to large-mass planets. Since with the RV technique, we are sensitive only to the motion of the star projected along the line-of-sight, the strength of the signal depends also on the orbital inclination of the planet. Indeed, there is a degeneracy between the planetary mass and the orbital inclination: the RV stellar signal due to a planet with a high mass but with a low orbital inclination is indistinguishable from the signal of a lower mass planet with a higher orbital inclination. Thus, RV allows us to measure only a lower limit on the mass of the planetary companion, i.e. the minimum mass $M_{\rm min}$, that is the term $M_{\rm min} = M_{\rm p} \cdot \sin(i)$ of Eq. 1.3. As it can be seen, with this method no information about the planetary radius can be extracted.

The transit method, the most successful one (the first planetary detection is by Charbonneau et al. 2000 and Henry et al. 2000), is based on measuring decreasing in radiation flux of a star due to the passage of a planet in front of its surface (i.e. a transit) that blocks part of the stellar light. In order to detect a transiting planet, an alignment between the star, the planet, and the line-of-sight must occur. Since planetary systems are randomly oriented through space, only a fraction of exoplanets appears to transit in front of their host star. Keeping into account the geometry of the problem, the probability p to observe the transit of a planet with a radius $R_{\rm p}$ in front of a star with a radius $R_\star$ is (Borucki and Summers, 1984):

$$p = \frac{R_\star + R_{\rm p}}{a \cdot (1-e^2)} \simeq 0.005 \cdot \left(\frac{R_\star}{R_\odot}\right) \cdot \left(\frac{1\,{\rm au}}{a}\right) \,, \tag{1.4}$$

where a = the semi-major axis of the orbit of the planet around the star, e = the orbital eccentricity, $R_\odot = 6.957 \cdot 10^8\,{\rm m}$ = solar radius. The right side of Eq. 1.4 is valid in the case of circular orbit and

$R_\star \gg R_\mathrm{p}$. This equation explains why it is more probable to observe transits from planets at small orbital separation (i.e. small period) from their host stars, as it can be seen in Fig. 1.2. The periodic drop of the stellar flux (i.e. the transit depth, δ) in the stellar light curve, due to the transiting planet, has a depth that depends on the relative projected area of the planet and the star:

$$\delta = \frac{R_\mathrm{p}^2}{R_\star^2}\,. \tag{1.5}$$

Therefore, large planets around small stars (i.e. large planet-to-star radii ratios) provide the largest transit signals. For example, an Earth-like planet ($R_\oplus = 6.378 \cdot 10^6\,\mathrm{m}$ = Earth radius) around a Sun-like star produces a transit depth $\delta \sim 0.008\%$, while a Jupiter-like planet ($R_\mathrm{J} = 6.991 \cdot 10^7\,\mathrm{m}$ = Jupiter radius) produces a $\delta \sim 1\%$ (in units of stellar flux). Since the transit phenomenon depends on the geometrical configuration of the planetary system, from the study of the stellar light curve during the transit it is possible to measure the planetary radius, knowing the stellar one, and to extract information about the orbital parameters (e.g. the eccentricity, the semi-major axis, and the inclination of the orbit), however, no information about the planetary mass can be extracted. As it can be seen, only by combining the radial-velocity method and the transit method is possible to break the mass-inclination degeneracy, and thus measure both the true mass and radius of an exoplanet, allowing to make first hypotheses about the interior composition from the measurement of the bulk density.

1.1.2 Population properties of exoplanets

The large number of discovered exoplanets and the comparative analysis of RV and transit surveys, allow to perform population studies. For example, Howard et al. (2010, 2012) showed that the planet-occurrence rate increases with decreasing mass and radius of the planet, indicating how smaller planets (from 2 to $4\,R_\oplus$) are more common than larger ones. It is worth noting that the number of terrestrial planets is small (around 9% of the total), but the discovery of these smaller planets remains biased by the fact that they are more difficult to detect. Johnson et al. (2010), Mortier et al. (2012), Petigura et al. (2018) also showed how that the occurrence rate of giant planets increases with the star metallicity and the orbital period. On the other hand, the occurrence of planets with small radius and mass is mostly independent of stellar metallicity in FGK dwarfs (Courcol et al., 2016, Sousa et al., 2019). One of the most interesting results in exoplanet-demographic studies is that planets with radii larger than Earth but smaller than Neptune ($1.0\,R_\oplus < R_\mathrm{p} < 3.9\,R_\oplus$) are the most common exoplanet type in the *Kepler* sample (Batalha et al. 2013) but are not present in the solar system. Indeed, in the solar system, we can identify three main classes of planets: the terrestrial planets, the gas giants, and the ice giants. Mercury, Venus, Earth, and Mars belong to the first group; they are made mostly of rock and metals with a thin or absent atmosphere very changed with respect to the formation stage. Jupiter and Saturn, belong to the second group; they are giant planets ($R_\mathrm{p} \sim 10\,R_\oplus$) made mainly of hydrogen and helium, with a very extended and primordial atmosphere and possibly a rocky core. Finally, the last group includes Uranus and Neptune, planets larger than the Earth but smaller than Jupiter ($R_\mathrm{p} \sim 4\,R_\oplus$) made of water, methane and ammonia ices, with a hydrogen and helium atmosphere less extended than those of gas giants. The most common type of exoplanets discovered falls between the terrestrial and neptunian planets, following a bimodal distribution in the case of short-period planets ($P_\mathrm{orb} < 100\,\mathrm{days}$) with peaks at $\sim 1.3\,R_\oplus$

and $\sim 2.4\,R_\oplus$ and a paucity of planets with radius $1.5 < R_\mathrm{p} < 2.0$ (i.e. the radius valley, Fulton et al. 2017), visible in Fig. 1.3.

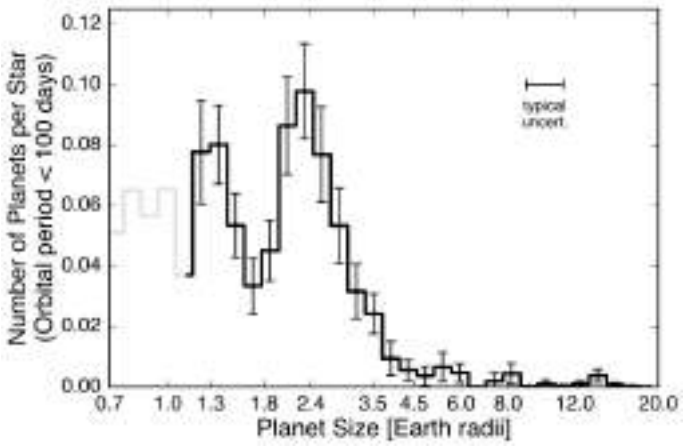

Figure 1.3: Histogram of planet radii for planets with orbital periods shorter than 100 days, from Fulton et al. (2017). The peak around $1.3\,R_\oplus$ defines the category of super-Earths, while the peak at $2.4\,R_\oplus$ defines the category of sub-Neptunes.

The bimodal distribution defines two new classes of planets, the super-Earths (with radius $1\,R_\oplus < R_\mathrm{p} < 1.5\,R_\oplus$), with a composition compatible with pure rock (silicates) and metals (Fe, Ni), and the sub-Neptunes (with radius $R_\mathrm{p} \sim 2 - 3\,R_\oplus$), with an interior composition that is not well understood yet. Sub-Neptune densities cannot be explained only by a rocky-metal interior and different compositions obtained combining different fractions of heavy and volatile elements are plausible (Zeng et al., 2019), e.g. a rocky core with a thick (few per cent by mass) H/He envelope (i.e. gas dwarfs), a 100% water (ices-fluids) composition (i.e. ocean worlds), or a large fraction of water by mass (up to 90%) surrounded by an H/He envelope (i.e. hycean worlds, Madhusudhan et al. 2021), as it can be seen from Fig. 1.4. The measurement of the atmospheric chemical properties, like the composition and metallicity, of sub-Neptunes plays a crucial role in breaking the degeneracies about their internal composition (e.g. Madhusudhan et al. 2023)

Another new class of exoplanet discovered, is that of hot-giant planets orbiting close to their parent star (orbital period $P_\mathrm{orb} < 10\,\mathrm{days}$). These planets, with a size similar to that of Jupiter, are very irradiated by their host stars and can be divided in groups depending on their equilibrium temperature: $T_\mathrm{eq} < 1\,000\,\mathrm{K}$ (warm Jupiters) and $1\,000 < T_\mathrm{eq} < 2\,000$ (hot Jupiters), to $T_\mathrm{eq} > 2\,000\,\mathrm{K}$ (ulta-hot Jupiters). Even if also smaller planets have been observed at short orbital periods (i.e. warm and hot Neptunes), Szabó and Kiss (2011) discovered a lack of hot-Neptunes/hot sub-Jupiters at very short orbital periods $P_\mathrm{orb} < 2.5\,\mathrm{days}$ (i.e. the sub-Jovian desert or evaporation desert, see Fig. 1.5).

Among the various hypotheses for the origin of this desert, the atmospheric evaporation was considered. Indeed, highly stellar-radiation exposed planets with no sufficient mass could lose their atmosphere through rapid evaporation (Lecavelier Des Etangs, 2007), while planets above the desert (i.e. hot Jupiters) have enough mass to gravitationally retain their atmosphere against the photoevaporation. Owen and Wu (2013) tried to give a theoretical explanation for the existence of the sub-Jovian desert exploring the effect of photoevaporation on the evolution of a population of planets (with varying core masses, envelope masses, orbital separations, and stellar spectral types). They concluded that evaporation is able to remove massive hydrogen envelopes for lower mass

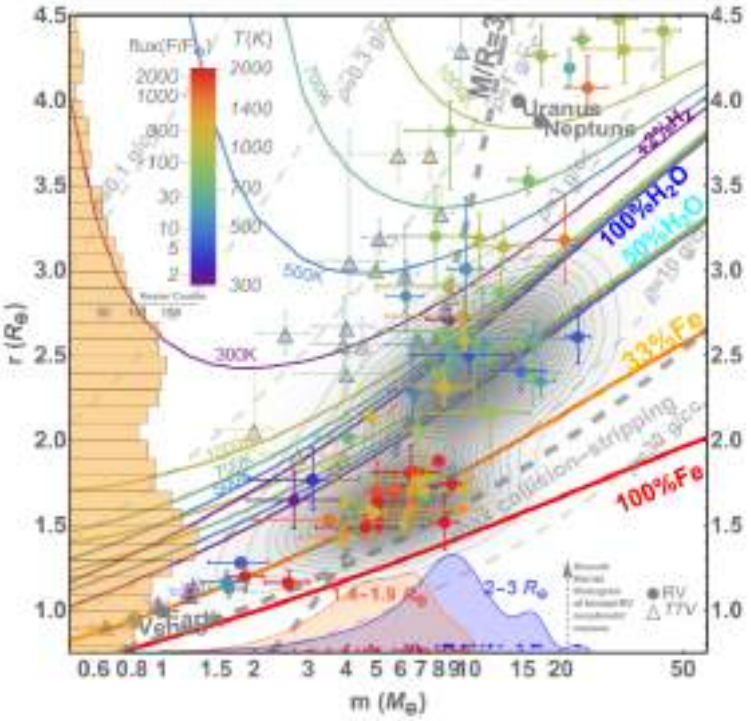

Figure 1.4: Radius-mass diagram for small-radii planets, from Zeng et al. (2019). The radius valley is visible and, as it can be seen, the masses and radii of the sub-Neptune population are compatible with multiple interior composition models (solid lines).

planets (i.e. hot Neptunes and sub-Jupiters), whilst this effect is negligible for hot Jupiters. In addition, they also predicted that photoevaporation would have produced a bimodal distribution in planetary radii with a paucity of planets around $2\,R_\oplus$, thus predicting the radius valley. In particular, depending on the planetary exposure to the X-ray and ultraviolet (XUV) stellar radiation, some sub-Neptune planets can lose their hydrogen envelope throguh photoevaporation exposing their naked cores and becoming super-Earths, and some other can retain their atmosphere (remaining in the right-part of the distribution). See Sect. 1.2.4 of this thesis work for a description of the main processes that drive atmospheric escape. The presence of hot Jupiters, whose occurrence is $\sim 1\%$ for Sun-like stars (Johnson et al., 2010), challenged the conventional giant planet formation theories (Pollack et al., 1996), based on the core-accretion mechanism. To date, their origin is still an open question, but three different formation scenarios have been proposed (Dawson and Johnson 2018 and the references therein): *in situ* formation, disk migration, and high-eccentricity tidal migration. In the first scenario, hot Jupiters form in the current position from the accretion of the local material (at ~ 0.1 au) with limited orbital migration. In the migration scenarios (that seem to be more plausible than the *in situ* formation), the planet forms in the outer part of the protoplanetary disk and then migrate to the current position. In particular, in the disk migration scenario, the Jupiter planet migrates in the inner part of the disk due to torques from the tidal friction with gaseous protoplanetary disk. In the high-eccentricity scenario, a third perturbing body extracts orbital angular momentum from the Jupiter by perturbing it onto a highly elliptical orbit and subsequently the Jupiter's orbit is circularised and shrunk to the current size by the dissipative tidal interaction with the host star. The study of the atmosphere of hot Jupiters, in particular the relative elemental abundances and the atmospheric metallicity, can help to constrain the formation

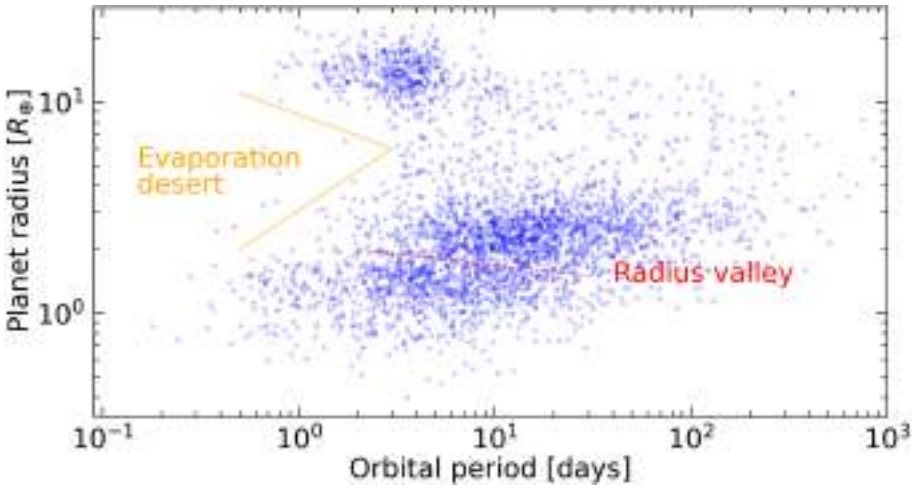

Figure 1.5: Radius-period distribution of the known exoplanets in which the evaporation desert and the radius valley are highlighted. Data from the NASA Exoplanet Archive.

scenario and evolution path followed by this kind of planets (see Sect. 1.2.5 of this thesis for further details).

The study of exoplanetary atmosphere can give a fundamental contribution to the exoplanet characterisation process, because not only it can help to break degeneracies on the interior structure of exoplanets and to constrain formation and evolution scenarios for intriguing targets such as hot Jupiters (e.g. Madhusudhan 2019), but atmospheres are natural laboratories to test theories about planetary atmospheric chemistry and dynamics (e.g. the origin of temperature-pressure profile, thermal inversions, cloud physics) in conditions that cannot be found in any planets of the solar system (e.g. Madhusudhan et al. 2016). Finally, it can allow to investigate the habitability of planets from the study of atmospheric and surface conditions, and to probe the possible presence of biosignatures (e.g. Seager et al. 2013), finding the so-desired answer to the question asked at the beginning of this section.

1.2 Exoplanet atmospheres

Exoplanet atmospheres (exoatmospheres) are very complex systems, in which chemistry, radiation and fluid dynamics interplay constantly. The aim of the exoplanetary scientist is to understand and characterise as most precisely as possible the chemical and physical properties of an exoplanet atmosphere, observing its spectrum. In this section, I will describe the main properties of exoatmospheres.

1.2.1 Chemical properties

What is the atmosphere of an exoplanet made of? This is the first question we ask ourselves when we start studying an exoatmosphere. Planetary atmospheres are composed of molecules, atoms, and ions. The relative abundances of the constituents depend on multiple factors, e.g. the planetary formation and evolution path, the temperature profile, the stellar radiation, possible disequilibrium processes, and atmospheric dynamics.

The atmosphere of gas giants is primordial, thus it reflects the constituents of the stellar formation

nebula. They are mainly constituted by hydrogen and helium (92% and 8%, respectively, in terms of number density), with traces (< 1%) of oxygen, carbon and nitrogen. Volatile molecules, such as H_2O, CO, CH_4, NH_3, CO_2, HCN, and C_2H_2 are expected to form in a H_2-He rich atmosphere, in different number densities depending on the atmospheric metallicity, the relative elemental abundances (e.g. the C/O and the N/O ratios), the temperature at the different atmospheric layers, and the stellar irradiation (e.g. Madhusudhan 2012, Moses 2014).
On the contrary, the atmosphere of terrestrial rocky planets are not primordial, since their low masses are not sufficient to retain the primordial thin and light hydrogen and helium atmosphere. Instead, their secondary atmospheres are made of molecules produced by processes such as volcanic activity and comet and asteroid impacts. In the case of Neptunian planets, their atmosphere resembles those of the giant gaseous planets, while in the case of mini-Neptunes, since a large variety of internal composition is possible, both H_2-He and volatile (H_2O, CO_2, CO, CH_4, or N_2) rich atmospheres are possible (e.g. Benneke and Seager 2013).
For what it concerns the chemical composition of an exoatmosphere at different layers:

- ions (e.g. CII, SiIII, and MgI) populate the upper layers ($P \leq 10^{-6}$ bar) of the atmosphere, where most of the star XUV (X-rays and extreme-UV) radiation is absorbed by atoms that loose electrons due to the high radiation energy;
- atomic species (e.g. Na and K) dominate the atmospheric composition at intermediate layers (10^{-6} bar $\leq P \leq 10^{-3}$ bar), since the formation of molecular species is prevented by photodissociation;
- molecules (e.g. H_2O, CO, CH_4, and CO_2) dominate the chemical composition of the deep layers (10^{-3} bar $\leq P \leq 1$ bar) where they are shielded from the high-energy stellar radiation by the upper layers.

An important quantity that is used to measure the abundance of a particular chemical species, is the volume mixing ratio $VMR_{\rm x}$, defined as:

$$VMR_{\rm x} = \frac{n_{\rm x}}{n_{\rm tot}}\,, \tag{1.6}$$

where $n_{\rm x}$ is the number density of the x species and $n_{\rm tot}$ is the total number density of the atmosphere.

Since gas-giant exoplanets are the most studied targets for atmospheric characterisation and are of particular interest for this thesis, it is important to describe more in detail the atmospheric chemistry of such planets. In H/He-dominated atmospheres, the chemical composition is controlled by chemical equilibrium in the deep atmospheric layers (pressure greater than $P \sim 1$ bar), by transport-induced quenching in the intermediate layers ($10^{-3} \leq P \leq 1$ bar), and by photochemistry in the higher layers (pressure smaller than $P \sim 10^{-3}$ bar, see Fig. 1.6 and Madhusudhan et al. 2016). In addition, cloud formation becomes increasingly important for cooler atmospheres while atmospheric escape for highly irradiated giant planets.
Chemical equilibrium occurs when there is no change in the number densities of atoms and molecules in a closed system even if the chemical reactions continue to occur. In order to reach chemical equilibrium, the atmosphere needs to be sufficiently hot and dense to ensure that chemical reactions occur faster than any other process at work (e.g. dynamics and interaction with energetic radiation).

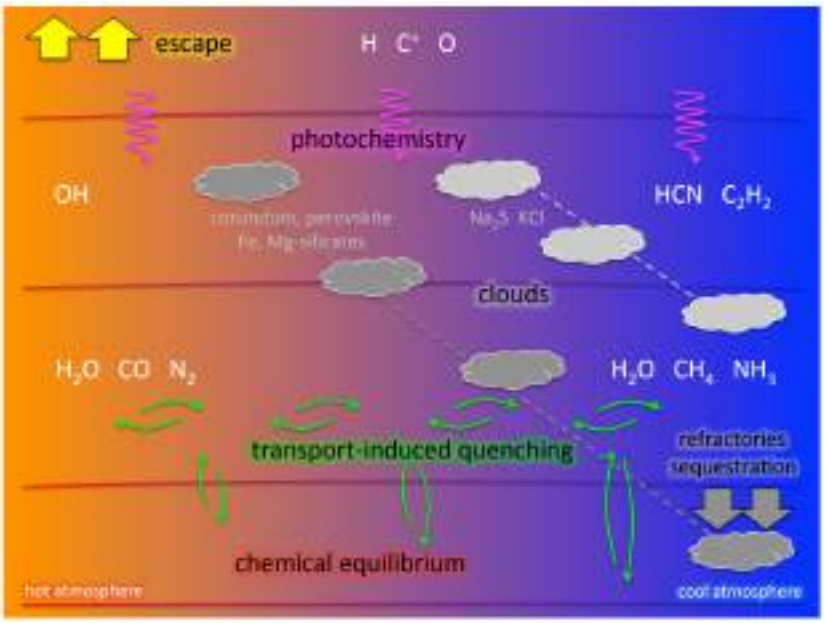

Figure 1.6: Scheme of the structure and processes at work in H/He-dominated atmospheres, from Madhusudhan et al. (2016). The chemical composition in deep layers is controlled by chemical equilibrium, by transport-induced quenching in upper layers, and by photochemistry in still upper layers.

Under chemical equilibrium condition, the chemical composition does only depend on temperature, pressure, and elemental abundances, and can be calculated by minimising the Gibbs free energy of the system. Since the higher the temperature, the faster the chemical reactions, chemical equilibrium is maintained in the atmosphere of very hot planets (with temperature exceeding $\sim 2\,000\,\mathrm{K}$), or in the hottest (deepest) layers of the atmosphere of cooler ones.

In a H/He-dominated atmosphere in chemical equilibrium, H_2O is the dominant secondary species over a broad range of temperature and elemental abundance ratios and the most common oxygen-bearing species (Madhusudhan, 2012). For what it concerns carbon-bearing species, CO and CH_4 are the most common species with relative abundance depending on the temperature (under the summary reaction $H_2O{+}CH_4 \leftrightarrow CO{+}3H_2$). In particular, at high temperatures ($T \geq 1\,300\,\mathrm{K}$) the former dominates, while at lower temperatures ($T \leq 1\,300\,\mathrm{K}$), the latter is more favoured to form. The most common reservoir of nitrogen is N_2 at high temperatures, while at low temperatures NH_3 is the most common nitrogen-bearing species (Moses et al., 2013). Also the relative elemental abundances (in particular the C/O ratio) play a crucial role in determining the chemical composition. Indeed, for example, a C/O ratio greater than unity favours the formation of carbon-bearing species over the oxygen-bearing ones, making possible to form hydrocarbons such as HCN and C_2H_2 in chemical equilibrium at temperatures higher than $\sim 2\,000\,\mathrm{K}$ (see Fig. 1.7 and Madhusudhan 2012). Also the metallicity of the atmosphere plays an important role in determining the abundance of chemical species, indeed for example CO_2 is one of the molecules most strongly enhanced with increasing atmospheric metallicity, becoming detectable for metallicities greater than ~ 10 times that of the Sun (e.g. Lodders and Fegley 2002, Moses et al. 2013). In cooler upper atmospheric regions, chemical disequilibrium can occur. There are different processes driving the chemistry out-of-equilibrium (e.g. vertical and horizontal quenching, cloud formation, and photochemistry).

In the regions of the atmosphere where transport processes like convection dominate over chemical reactions, materials can be transported from an atmospheric region to another, determining

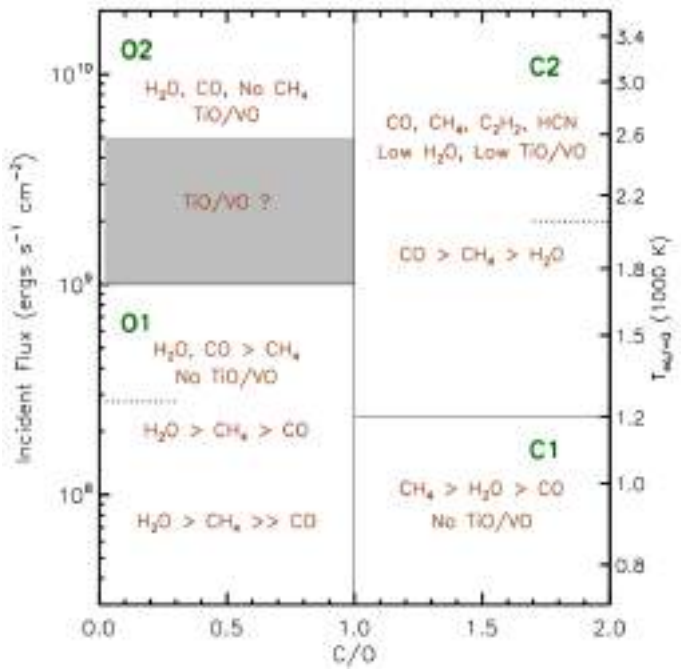

Figure 1.7: Two-dimensional classification scheme for hydrogen-dominated atmospheres, as a function of the atmosphere temperature and C/O ratio, from Madhusudhan (2012). Four classes are shown: O1, O2, C1, and C2. Atmospheres in O1 and O2 are O-rich (C/O < 1), and those in C1 and C2 are C-rich (C/O > 1). The distinction between O1 (C1) and O2 (C2) is based on irradiation or temperature. The major molecules in each class are shown, for a reference pressure of 1 bar.

a redistribution of heat and chemical composition with a net flow from hot to cooler regions. In this conditions, the bulk composition can be significantly driven out of equilibrium. The resulting mechanism that determines the vertical distribution of the atmospheric constituents is called transport-induced quenching. When the mixing-time scale induced by vertical transport drops below the chemical kinetics time scales required to maintain a constituent in equilibrium with other species (i.e. $\tau_{\rm mix} \ll \tau_{\rm chem}$), that constituent becomes quenched and its mole fraction remains fixed at the quenched abundance. Vertical quenching was first described by Prinn and Barshay (1977) to explain the presence of CO in the troposphere of Jupiter as a result of upward mixing from deeper and hotter levels, where is thermochemically stable. Indeed, in gas giant exoplanets, vertical quenching can induce CO to be overabundant compared to equilibrium chemistry predictions (e.g. Moses 2014), because the CO double bond has a high binding energy, making the CO to CH_4 conversion reaction very slow. So, since the vertical dredging of CO from the hot interior is faster than the CO to CH_4 conversion, chemical equilibrium is never reached. Similarly, the vertical dredging of N_2 from deep in the atmosphere where chemical equilibrium favors N_2, can drive the N_2 and NH_3 abundance out-of-equilibrium because the N_2 to NH_3 conversion reaction is slower than the vertical dredging rate. A quantitative evaluation of chemical quenching requires a good knowledge of both the chemical kinetics of the interconversion scheme of interest and the vertical eddy mixing coefficient. Transport-induced quenching can therefore affect species abundances even before their own quench points are reached, for example HCN and C_2H_2 abundances can depart from equilibrium when NH_3 and CH_4 quench, causing their column abundances to greatly exceed equilibrium predictions (Moses, 2014).

Quenching can also be due to horizontal transport of atmospheric material driven by winds

that move material from hot to cooler atmospheric regions. Hot Jupiters, that are usually tidally locked, can present high temperature contrasts, and thus possible variations in the composition, between the day and night sides. On the other hand, circulation dominated by a strong superrotating equatorial jet or day-to-nightside jet winds tends to homogenise both the temperature and chemical composition between the different planetary sides (e.g. Showman and Guillot 2002, Cooper and Showman 2006, Knutson et al. 2007). The main effect of horizontal chemical quenching is that molecular abundances are quenched horizontally to values typical of the hottest dayside regions, making the cooler nightside to be highly contaminated by the warmer dayside regions.

Hot Jupiters are strongly irradiated by their host stars and thus receive a high ultraviolet flux, which is absorbed in the upper atmosphere and induces photochemical reactions in the upper layers of the atmosphere (e.g. above $\sim 0.1\,\mathrm{mbar}$). The cooler the planet the larger the extent of atmospheric region where photochemistry is important in determining the composition, because high temperatures counterbalance photochemistry. The most common photochemical reaction is the production of atomic hydrogen through the photolysis of H_2, the main molecular component of hot-Jupiter atmospheres, or through the catalytic photolysis of H_2O (Liang et al., 2003). Another important photochemical species is HCN, which is efficiently formed in the photochemical atmospheric layers starting with the photodissociation of CH_4 and NH_3 (e.g. Moses et al. 2011, Zahnle et al. 2009). Photochemical reactions starting from the photodissociation of CH_4 also triggers the formation of larger hydrocarbons such as C_2H_2 (e.g. Bilger et al. 2013, Zahnle et al. 2009). Thus, since HCN and C_2H_2 can have abundances that significantly deviate from those expected from the chemical equilibrium due to different processes, these two species, whose spectral features can be detected in the near-infrared, are powerful chemical-disequilibrium indicators. Another common species produced by photochemistry is the radical OH, which results from the photodissociation of water and acts as a key intermediate in the synthesis of other O-bearing molecules such as O_2 and NO (Moses et al., 2011). As concerns sulfur compounds, the major photochemical products of the dominant equilibrium sulfur species, H_2S, are expected to be S, HS, S_2, SO, and SO_2 (Zahnle et al., 2009). Lavvas et al. (2014) showed that for very hot planets, atomic neutrals and ions such as Mg, Mg^+, Fe, Fe^+, Ca, Ca^+, K, K^+, Al^+ could be important photochemical and equilibrium species (this is the case of ultra-hot Jupiters).

1.2.2 The atmospheric vertical structure

Planetary atmospheres need to be in hydrostatic equilibrium to be stable, which means that there is a balance between the outward pressure gradient force and the inward gravitational force from the weight of the atmospheric material. The hydrostatic equilibrium equation is:

$$\frac{dP}{dz} = -g \cdot \rho\,, \tag{1.7}$$

where dP is the infinitesimal change in pressure, dz is the infinitesimal change in atmospheric height, g is the gravitational acceleration, and ρ is the atmospheric density. Assuming the ideal gas law as the atmospheric equation of state, for an isothermal atmosphere the solution to Eq. 1.7 is:

$$P\,(z) = P_0 \cdot e^{-\frac{z}{H_\mathrm{s}}}\,, \tag{1.8}$$

where $P(z)$ is the atmospheric pressure as a function of the atmospheric height, P_0 is a reference pressure, and H_s is the atmospheric scale height (or pressure scale height). H_s represents the characteristic length scale of the planetary atmosphere and can be expressed as:

$$H_s = \frac{k_B \cdot T}{\mu \cdot g}, \tag{1.9}$$

with k_B = the Boltzmann constant, T = the atmospheric temperature, μ = the atmospheric mean molecular weight, g = the gravitational acceleration. The mean molecular weight of the atmosphere depends on the chemical composition: for H/He composed atmospheres it is $\mu \sim 2.3\,\mathrm{g\,mol^{-1}}$. For typical hot-Jupiters atmosphere ($T \sim 1\,800\,\mathrm{K}$), $H_s \sim 250\,\mathrm{km}$, while, for comparison, an Earth-like atmosphere ($\mu \sim 29\,\mathrm{g\,mol^{-1}}$, $T \sim 250\,\mathrm{K}$), has an atmospheric scale height $H_s \sim 8\,\mathrm{km}$.

An important property of the atmosphere is the vertical temperature profile, that is the temperature-pressure profile ($T - P$ profile). Indeed, the temperature profile across the planetary atmosphere plays a crucial role in determining the atmospheric chemical composition as a function of the height and is strictly related to atmospheric dynamical effects, such as convection and global scale circulation. The temperature-pressure profile depends on the energy balance of the atmosphere (e.g. the internal heat flux due to cooling and the stellar irradiation) and on the opacity sources in the atmosphere, as a function of the wavelength. In order to compute the $T - P$ profile for an atmosphere in radiative-convective equilibrium, it is necessary to solve to solve a set of three equations (the radiative transfer equation, the radiative and convective equilibrium equation, and the hydrostatic equilibrium equation) for three unknown variables (the temperature, pressure, and radiation field). A typical useful simplification in this computation, is assuming local thermodynamic equilibrium (LTE), that is, in the local area of the atmosphere any temperature, pressure, or chemical gradients are small compared to the photon mean free path. The situation of LTE enables a decoupling of radiation from the local temperature, which greatly simplifies the radiative transfer problem since the atomic and molecular energy population levels are specified by the local temperature and do not have to be determined by a simultaneous solution with the radiative transfer equation.

Generally, when studying exoatmospheres, the simplest way to estimate the planetary temperature is assuming that the T/P profile is isothermal, that is, the temperature does not vary as a function of pressure. This is a simplification that is valid for the deepest part of the atmosphere (pressure greater than $P \approx 1\,\mathrm{bar}$), where the optical depth and density of the atmosphere is higher. Of course, in order to retrieve the atmospheric $T - P$ profile of an exoplanet from observations, also more complex parametric $T - P$ profile can be used. The most used profiles are the Guillot profile, derived by Guillot (2010) to approximate the structure of plane-parallel irradiated planetary atmospheres, and the Madhusudhan profile, derived by Madhusudhan and Seager (2009).
The Guillot profile can be expressed as follows:

$$T^4(\tau) = \frac{3T_{\mathrm{int}}^4}{4}\left[\frac{2}{3} + \tau\right] + \frac{3T_{\mathrm{irr}}^4}{4} f \left[\frac{2}{3} + \frac{1}{\gamma\sqrt{3}} + \left(\frac{\gamma}{\sqrt{3}} - \frac{1}{\gamma\sqrt{3}}\right) e^{-\gamma\tau\sqrt{3}}\right], \tag{1.10}$$

with f = a geometrical factor that is $f = 1/4$ if the incoming stellar flux is averaged over the entire planetary surface, T_{int} = the internal temperature that produces the internal heat flux from cooling, T_{irr} = the irradiation temperature, $\gamma = k_{\mathrm{VIS}}/k_{\mathrm{IR}}$, with k_{VIS} and k_{IR} = the atmospheric

visible and infrared opacity, respectively, and τ = the optical depth. The irradiation temperature can be expressed as a function of the stellar radius $R_\star$, the stellar effective temperature $T_\star$, and the star-planet distance D, as $T_{\rm irr} = T_\star \cdot \sqrt{\frac{R_\star}{D}}$, and the optical depth can be expressed as a function of the pressure P, the infrared opacity $k_{\rm IR}$, and the atmospheric surface gravity g, as $\tau = P \cdot k_{\rm IR}/g$. More complex versions of this profile have been developed including different visible and infrared channels opacity (e.g. Line et al. 2012, Parmentier and Guillot 2014).
The Madhusudhan profile assumes a generalised exponential profile for an atmosphere divided into three layers, for each layer:

$$P = P_0 e^{\alpha(T-T_0)^\beta}\,, \tag{1.11}$$

where P = the pressure, T = the temperature, and P_0, T_0, α, and β the free parameters.

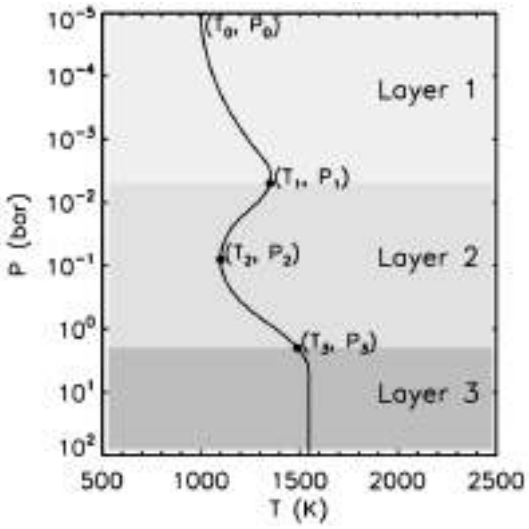

Figure 1.8: Schematic parametric $T - P$ profile adopted in Madhusudhan and Seager (2009).

Figure 1.8 shows a schematic parametric $T - P$ profile of this type:

- layer 1 is the upper-most layer that extends from P_0 (typically $P_0 \sim 10^{-5}$ bar) to P_1 and has no thermal inversions. In this layer, the atmosphere is being heated by lower layers and cools with increasing altitude;
- layer 2 is the middle layer, which extends from P_1 to P_3 is where most atmospheric spectral features are formed. In layer 2, the temperature structure is governed by radiative process and possibly by atmospheric dynamics, and it is the layer where thermal inversions may be formed (i.e. at some height the temperature increases with increasing altitude), depending on the level of irradiation from the parent star and the presence of strong absorbing gases (like O_3 in the Earth's stratosphere) or solid particles;
- layer 3 is the layer which extends at pressure higher than P_3. In this layer is the regime where a high optical depth leads to an isothermal temperature structure.

The layers, from number 1 to number 3, are defined as follows:

$$\begin{aligned} P_0 < P < P_1 &\rightarrow P = P_0 e^{\alpha_1 (T - T_0)^{\beta_1}} \\ P_1 < P < P_3 &\rightarrow P = P_2 e^{\alpha_2 (T - T_2)^{\beta_2}} \\ P > P_3 &\rightarrow T = T_3 \,, \end{aligned} \tag{1.12}$$

where the β parameter turns out to be a redundant parameter and can be set to $\beta_1 = \beta_2 = 0.5$ (Madhusudhan and Seager, 2009). Imposing continuity conditions at the two layer boundaries (that is, layers 1–2 and layers 2–3) and $P_0 = 10^{-5}$ bar, the parametric profile has six free parameters. The Madhusudhan profile, as it can produce inversion, provides a better match in the middle of the atmosphere. However, it does not match the deep atmospheric structures. A key aspect linked to the $T - P$ profile is understanding if whether or not a planet presents an atmospheric thermal inversion. Inversion layers can be detected studying the emission spectrum of an exoplanetary atmosphere (see Sect. 1.3.2 of this thesis), and has been suggested to be present in the upper atmosphere of different ultra-hot Jupiters, among which WASP-33 b (e.g. Haynes et al. 2015,Cont et al. 2022), WASP-121 b (e.g. Evans et al. 2016, 2018), WASP-103 b (Kreidberg et al., 2018), and KELT-9 b (Pino et al., 2019). While very high level of irradiation (and thus temperature) seems a necessary condition for temperature inversion to occur, some ultra-hot Jupiters do not show inversion (e.g. Beatty et al. 2017), and the conditions and molecular species responsible for the inversion (e.g. TiO and VO) are still under investigation (e.g. Parmentier et al. 2013, Lothringer et al. 2018).

1.2.3 Clouds and hazes

Exoatmospheres are not just made up of gases but also of aerosols, that are defined as particles suspended in the atmosphere. Aerosols that can be found in exoatmospheres are mainly clouds and hazes. Even if these two terms are often used interchangeably, clouds form by condensation processes, normally reversible processes, when the partial pressure of a constituent gas exceeds its saturation vapour pressure and thus the gas condensates into liquid or solid droplets. On the other hand, hazes are aerosols that form by the action of photochemistry or any other disequilibrium chemical process (e.g. the so-called "soots" discussed by Zahnle et al. 2009) or from photochemically produced gases flowing into cooler regions, where they can condense. For any gas species that might condense, clouds form when:

$$P_{\mathrm{g}}(T) = VMR_{\mathrm{g}} \cdot P(T) \geq P_{\mathrm{Vg}}(T) \,, \tag{1.13}$$

where $P(T)$ is the total gas pressure, P_{g} is the gas partial pressure, VMR_{g} is the volume mixing ratio of the gas, and P_{Vg} is the saturation vapor pressure for that particular gas. The subscript "g" refers to the gas under consideration. Knowing the atmospheric temperature-pressure profile it is possible to know the cloud base pressure for a particular species as the intersection of the saturation vapor pressure curve and the planet's temperature-pressure profile. Different compounds condense at different temperature and pressure conditions. As visible in Fig. 1.9, solar system cold giant planets (like Jupiter) can have methane clouds, ammonia clouds, and water clouds. Then, if we go towards higher temperature (e.g. 1 000-2 000 K), that are the conditions in hot Jupiters, exotic clouds made for example of magnesium silicates like bridgmanite ($MgSiO_3$) and forsterite

(Mg_2SiO_4) can be produced, and, for extremely high temperatures (i.e. ultra-hot Jupiter conditions), clouds made of perovskite ($CaTiO_3$), corundum (Al_2O_3), and liquid iron droplets can form in the atmosphere (for instance, iron is expected to condense in the nightside of WASP-76 b and thus to create clouds and droplets, Ehrenreich et al. 2020). The clouds are confined to layers and clouds of the same composition are present at lower altitudes in colder planets, indeed as temperature drops, the hotter clouds do not disappear, instead, they are pushed down into the atmosphere where the temperature is higher, according to Eq. 1.13, as visible Fig. 1.9.

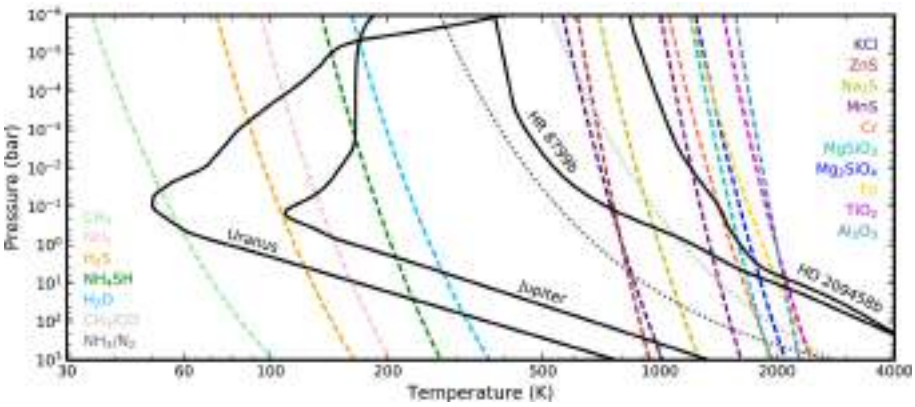

Figure 1.9: Condensation temperatures of various cloud species as a function of atmospheric pressure, compared to temperature-pressure ($T - P$) profiles of four planets (i.e. Uranus, Jupiter, the direct-imaged planet HR 8799 b and the famous hot-Jupiter HD 209458 b), from Gao et al. (2021). Where the $T - P$ profile intersects the condensation curve of a particular species, that species can condense forming clouds.

Aerosol particles interact with the stellar light and produces different effects on the atmospheric transmission spectra depending on their sizes. In particular, they can uniformly mute all the wavelengths or have a strong wavelength-dependent absorption in the visible, i.e. scattering. Wakeford and Sing (2015) found that small ($\leq 0.25\,\mu$m) particles show strong scattering (i.e. Rayleigh scattering) at visible wavelength and absorption features in the infrared. As the particle size increases, the scattering becomes less important. Medium-size particles ($0.25 - 1\,\mu$m) show indeed little scattering and muted infrared features. The scattering becomes negligible for particles with size $\geq 1\,\mu$m, where there is a uniform absorption and no infrared features. In particular, the scattering and thus the resulting transmission spectrum largely depend on the largest grain size in the particle distribution of the cloud. Infrared features can be used to constrain the aerosol composition, indeed major dust spectral features in the infrared are determined by vibrational modes between the main diatomic bond in the material. For instance, silicate dust has a major feature at $10\,\mu$m, while hydrocarbons have major features at $3\,\mu$m (Wakeford and Sing, 2015). Evidences of atmospheric aerosols have been detected in transmission spectra of multiple targets, both in Jupiter- and Neptune-sized planets, as reported by Sing et al. (2016) and Wakeford and Dalba (2020).
Dealing with cloudy atmosphere is difficult, because prediction of cloud properties such as cloud vertical height, fraction of gas condensed, and particle size distribution is complicated and the computation of the radiative transfer through clouds can be challenging. From an observing point of view, the larger the observing wavelength range the easier is possible to identify typical scattering slopes or clouds muting features. Thus, it is clear that more work is needed both in theory and in observations to better understand the role of aerosols in exoplanet atmospheres.

1.2.4 Atmospheric dynamics and escape

The energy received from the star is re-distributed across the atmosphere of a planet through the large-scale movement of gas, called atmospheric circulation. For example, on Jupiter, atmospheric circulation causes high wind speeds in jets and intricate weather patterns, with bands and vortices, including the great red spot. In order to describe the atmospheric circulation, fluid dynamics equations, that come from the conservation laws for momentum, mass, and energy, are used, however it is necessary to keep into account also the stellar irradiation and the equation of state of atmospheric gas (Holton, 1992). They are non-linear equations and the calculation of atmospheric circulation and dynamics is computationally time-consuming.
Even if a complete description of the equations and solving methods is beyond the scope of this work, an important aspect is worth noting, that is, atmospheric circulation acts to minimise temperature gradients. In other words, if the advective time-scale, that is the time for the absorbed stellar energy to be circulated around the planet, is smaller than the radiative time-scale ($\tau_{\rm adv} \ll \tau_{\rm rad}$), that is the time for absorbed stellar energy to be re-emitted as radiation, than the heat is efficiently re-distributed across the planet through atmospheric circulation.

An interesting case is that of hot-giant exoplanets because they orbit very close to their host stars (orbital period $P_{\rm orb} < 10$ days) and so they are expected to be tidally locked. Hot Jupiters receive a hundred times more radiation than Earth and tens of thousand times more than Jupiter. These high levels of stellar irradiation dominate any internal flux for hot Jupiters and, together with the permanent day and night sides, produce very high temperature gradients between the two sides of the planet, that are expected to induce strong atmospheric circulation phenomena, like superrotating equatorial jet-winds and day-to-night side winds (with speeds of few km s^{-1}), and shift of the day side hot-spot from the substellar point (e.g. Lewis et al. 2010, Showman and Polvani 2011, Heng and Showman 2015). In the literature, these effects have been observed multiple times on different targets, such as the two famous hot-Jupiters HD 189733 b (e.g. Louden and Wheatley 2015, Wyttenbach et al. 2015, Brogi et al. 2016, Boucher et al. 2021, Keles et al. 2024) and HD 209458 b (e.g. Snellen et al. 2010, Sánchez-López et al. 2019), and the warm-Neptune HAT-P-11 b (e.g. Allart et al. 2018). In order to extract atmospheric dynamics information from observations, it is important to build atmospheric models that include such effects. The most effective models available to date are the complex three-dimensional (3D) global circulation models (GCMs) that keep into account the three-dimensionality of the fluid dynamics equations and the radiative transfer equation, in order to predict the temperature and wind fields across the planetary surface (Fig. 1.10) and at different atmospheric layers as a function of the atmospheric chemical properties and irradiation (e.g. Madhusudhan 2019 and references therein). Different studies (e.g. Koll and Komacek 2018) also highlighted the importance of considering the role of the magnetic field in atmospheric dynamics (e.g. magnetic drag). Even if employing 3D atmospheric models is computationally time-consuming, in some circumstances not considering 3D effects (like possible differences in the atmospheric properties of morning and evening limbs of tidally locked planets), can lead to retrieving less accurate atmospheric properties (e.g. temperature) from observations (e.g. MacDonald et al. 2020).

Another important phenomenon that characterises the dynamics of planetary atmospheres is atmospheric escape. Atmospheric loss usually refers to the loss of gases (mainly H and He) that escape from the gravitational field of a planet and disperse into space. Escape is a fundamental process affecting planetary atmospheric structure, composition, and evolution. In nature, several

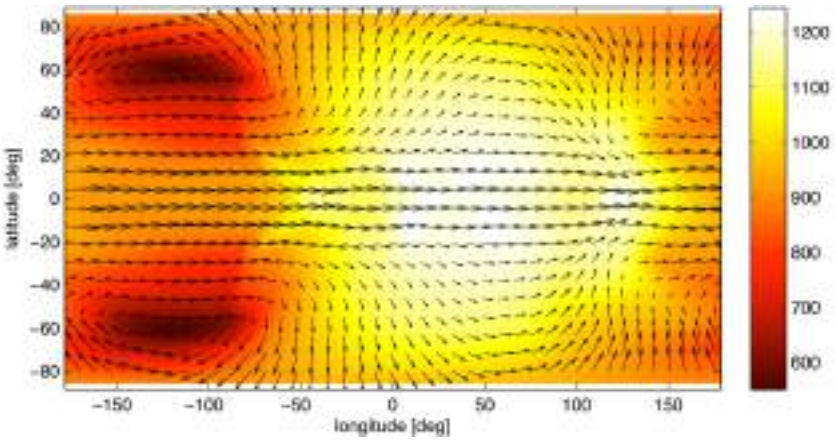

Figure 1.10: Theoretical predictions from a GCM of HD 189733 b show an eastward jet and shifting of the day side hot-spot away from the substellar point. The colour scale represents the temperature in Kelvin. Image from Showman and Polvani (2011).

ways allow the gas molecules to acquire a velocity beyond the planet's escape velocity leading to atmospheric escape. These mechanisms can be divided into two categories: thermal escape processes and non-thermal processes.

Thermal escape occurs if the thermal energy of a gas particle exceeds its gravitational binding energy:

$$\sqrt{\frac{2k_{\mathrm{B}}T}{m}} > \frac{1}{6}\sqrt{\frac{2GM_{\mathrm{p}}}{R_{\mathrm{p}}}}\,, \tag{1.14}$$

where k_{B} = the Boltzmann's constant, T = the temperature of the exosphere, m = the molecular or atomic mass, G = the gravitational constant, M_{p} = the planet mass, and R_{p} = the planet radius. Loss of atmospheric particles by thermal escape occurs in the planetary exosphere. The exosphere is the uppermost region of the planetary atmosphere (pressure lower than $\sim 10^{-12}$ bar). The bottom of the exosphere is the exobase, defined to be the altitude above which the atmosphere becomes collisionless. Thus, the exobase is the altitude where a particle's mean free path is greater than the particle-specific atmospheric scale height. Below the exobase, there is the thermosphere, at the bottom it defines the thermobase ($P \sim 10^{-6}$ bar). Thus, the thermosphere is between the exobase and the thermobase. In the thermosphere, the actual heating of the upper atmosphere happens (Fig. 1.11).

There are two main thermal escape processes: the hydrostatic escape (or Jeans escape) and the hydrodynamic escape.
In the first process, the escape is driven by the thermal motion of atoms and molecules, indeed it consists of thermal evaporation from the exobase. The kinetic energy of the gas particles at temperature T is described by the Maxwell-Boltzmann distribution, which gives the number of molecules with speeds between v and $v + dv$:

$$f(v)dv = \frac{4n}{\sqrt{\pi}}\left(\frac{m}{2k_{\mathrm{B}}T}\right)^{\frac{3}{2}} v^2 e^{-\frac{mv^2}{2k_{\mathrm{B}}T}} dv\,, \tag{1.15}$$

with n = the numerical density of particles, m = the particle mass. Molecules that are within the higher-velocity tail of the Maxwell-Boltzmann distribution, may exceed the escape velocity of the

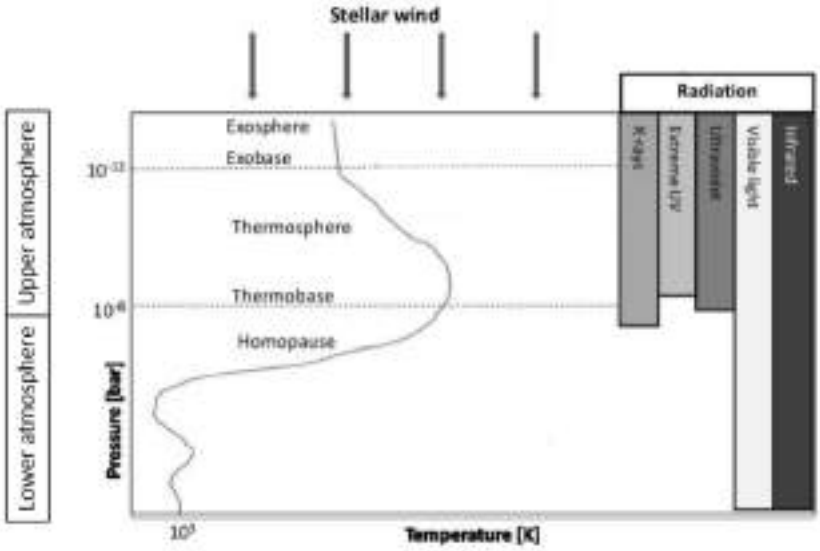

Figure 1.11: Atmospheric structure. At the top we have the collisionless part of the atmosphere, i.e. the exosphere. The exobase separates it from the underlying atmospheric level that is the thermosphere, where the actual heating of the upper atmosphere happens. At the bottom of the thermosphere there is the thermobase, that is located near the maximum of the temperature and lines the division between the upper and the lower atmosphere. Credits: Dr. Luca Fossati.

planet, and leave the planet's atmosphere. Once they have escaped, slower atoms and molecules move to fill the high-velocity tail. The flux of particles escaping through Jeans escape is the Jeans escape flux:

$$\Phi_{\rm Jeans} = \frac{n_{\rm c}}{2\sqrt{\pi}} B \sqrt{\frac{2k_{\rm B}T_{\rm c}}{m}} (1+\lambda_{\rm c}) e^{-\lambda_{\rm c}} \,, \tag{1.16}$$

where the subscript c refers to exobase properties and the escape parameter $\lambda_{\rm c}$ is the escape parameter, defined as the ratio between the escape energy $E_{\rm esc} = \frac{1}{2}mv_{\rm esc}^2$ and $k_{\rm B}T_{\rm c}$. The factor B ($B \sim 0.5-0.8$) accounts for the slow re-population time of the energetic tail of the Maxwellian distribution.
The second important escape process is the hydrodynamic escape. Focusing on close-in hot-giant planets, the upper atmosphere is heated by the stellar XUV (X-rays and extreme-UV) radiation, and at some orbital distance, the flux should be high enough to cause a transition from kinetic escape to XUV-driven hydrodynamical escape. At wavelengths shorter than 91.2 nm (which corresponds to the hydrogen ionisation energy) we are into the XUV range that is responsible for metal photoionisation, molecular photodissociation, and hydrogen photoionisation which is extremely important to drive the escape. Indeed, when the energy of a photon with a shorter wavelength (i.e. higher energy) is transferred to the electron of an hydrogen atom, a fraction of it is used to ionise the atom, while the remaining fraction is transferred to the lost electron and goes to heat the atmosphere mostly through collisions. The hydrodynamic escape state is reached when the atmosphere is heated by the star to the point where the particles are so energetic that gravity cannot stop the outward flow and the atmospheric escape is so fast that the atmosphere behaves like a dense fluid expanding radially outward. During hydrodynamic escape, heavier elements such as C, N, and O can be carried away with the hydrodynamic flow of the lighter species.
In the energy-limited approximation (Watson et al., 1981), that is, all incoming energy is balanced by total gravitational potential energy gain of the evaporated atmospheric material, it is possible to

compute the mass loss rate $\dot{m}$ as (Erkaev et al., 2007):

$$\dot{m} = \eta \frac{F_{\rm XUV} R_{\rm p} R_{\rm eff}^2}{G M_{\rm p} K}\,, \tag{1.17}$$

with η = the heating efficiency of the conversion of the radiative energy input that is available for atmospheric heating, G = the gravitational constant, $R_{\rm p}$ = the radius of the planet, $M_{\rm p}$ = the planetary mass, K = a factor to account for the Roche-lobe effects, $F_{\rm XUV}$ = the high-energy flux received by the planet from its host star, and $R_{\rm eff}$ = the effective radius, i.e. the location where most of the XUV radiation is absorbed. To date, escape calculations couple hydrodynamic calculations with radiative transfer and require the knowledge of stellar radiation and constituents of the planetary upper atmosphere in order to model the hydrodynamic escape more precisely (e.g. Stone and Proga 2009, Owen and Jackson 2012, Bourrier and Lecavelier des Etangs 2013, Tian 2015).

Young stars have very high X-ray and extreme-UV (EUV) flux, where levels can reach thousands of times present-day solar levels. The situation is most critical for M stars, where these high levels of EUV emission can last up to 8 billion years for late-tipe M stars. If the initial planetary atmosphere has not survived during the stellar EUV high-emission phase, a new atmosphere could develop only if the outgassing rate of the core is higher than the escape rate. For hot-giant planets, atmospheric escape can be present but different works (e.g. Lecavelier des Etangs et al. 2004, Yelle 2004) led to the conclusion that the total mass loss over the lifetime of the system should be negligible. Unfortunately, for smaller planets it is not the same; indeed the entire atmosphere can be stripped away due to evaporation, which plays a crucial role in driving the atmospheric evolution, creating gaps in the exoplanet population, as already described in Sect. 1.1.2.

Finally, different types of non-thermal processes can drive the atmospheric escape, among which the most important are:

- charge exchange, which involves a collision between an ion (e.g. a stellar wind proton) and an atom that receives the energy from the ion escaping into the space;
- conversion of photochemical energy into kinetic energy, in which electrons created from photoionisation or atoms created from molecular photodissociation can carry excess kinetic energy that makes them leave the atmosphere;
- ion escape, that refers to ions that escape along magnetic field lines that are open to a planetary magnetotail, or ion-pickup, that refers to ions picked-up by the stellar magnetic field that accelerates them away from the planet.

1.2.5 From atmospheric composition to planetary formation

The study of the present-day chemical composition of the atmosphere of exoplanets can give important clues about the mechanisms driving their formation and evolution (e.g. Madhusudhan et al. 2016, Mordasini et al. 2016, Madhusudhan 2019, Pacetti et al. 2022). The planetary formation and migration processes involve a large number of highly complex and stochastic processes that can leave different observable imprints on planetary atmospheres.
The primary assumption is that the initial elemental composition of the protoplanetary disk is the same as the host star, since both form from the collapse of the same protostellar nebula. After the

collapse, as the disk cools, the snow lines (that are defined as the distance into the disk from the star over which a particular species condensates) of the various volatile species move inward toward the star. As a result, the chemical compositions of both the gas and solids in the disk evolve as a function of time and location in the disk. For example, H_2O remains in solids outside the H_2O snow line, whereas it contributes to the gas composition inside the snow line. For this reason, the chemical composition of a planet (and its atmosphere) depends on the location and time of its formation in the disk (e.g. Eistrup and Henning 2022, Eistrup et al. 2016, 2022).

The most important property influencing the disk's composition is the temperature, which governs the phase at a given location in the disk. Indeed, snow lines of different species occur at different orbital distances due to their different condensation temperatures. For example, the H_2O snow line is the closest to the host star, followed by snow lines of CO_2, CO, CH_4, and N_2. This means, that oxygen abundance in the gas phase clearly decreases outward in the disk, with a decrement at each snow line, whereas that in the solids increases. This implies that the relative abundance of C and O (i.e. the C/O ratio) in the gas increases, whereas that in the solids decreases as a function of distance in the disk (e.g. Öberg et al. 2011). As a consequence, as it is visible in Fig. 1.12, the

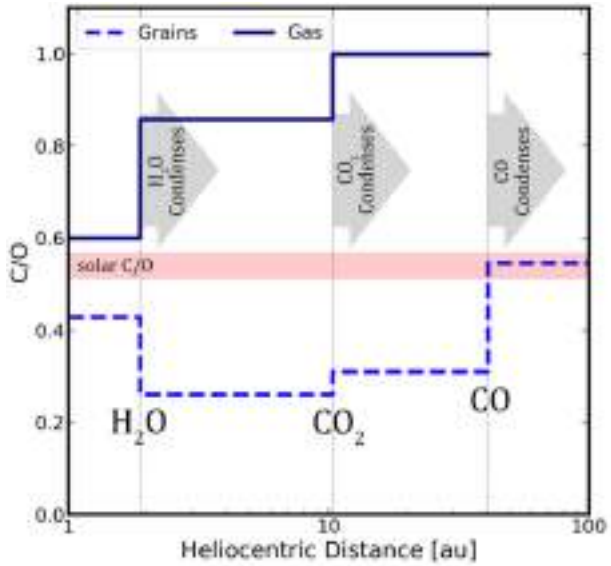

Figure 1.12: The C/O ratio of grains and gas as a function of the distance from the star (in this case the Sun). The ratio is impacted by condensation of oxygen-and carbon-bearing molecules at and beyond their respective snowlines (i.e. H_2O snow line at ~ 2 au, CO_2 snow line at ~ 10 au, and CO snow line at ~ 40 au). Image from Seligman et al. (2022).

C/O ratio of the gas component approaches 1 in the outer part of the protoplanetary disk. Thus, depending on how much gas versus solids a planet accretes at a given formation location, it can accrete a gas with a wide range of C/O ratios spanning from subsolar to supersolar C/O ratios (the solar C/O ratio is 0.59, Asplund et al. 2021).
In general, the higher the atmospheric C/O ratio, the more is probable that the planet formed in the outer parts of the protoplanetary disk. However, because the planet may migrate through the disk during formation, crossing different snow lines, it can be enriched by the elements encountered during migration and the net composition is governed by the cumulative accretion history (as well as the relative amounts of accreted gas and solids) of the planet over its migration pathway. For example, if a planet formed through core accretion (Pollack et al., 1996) beyond the CO_2 snow line

(i.e. at distances greater than$\sim 5-8\,$au) and then underwent disk-free migration after the disk dissipation, it is expected to have a C/O ratio in the gas phase that approaches 1 and atmospheric sub-solar metallicity (Madhusudhan et al., 2014), while a giant planet formed via core accretion beyond the H_2O snow line (at $2-3\,$au) that then migrated towards the inner disk with significant accretion of water-ice and/or oxygen-rich gas would yield an atmospheric super solar metallicity and subsolar C/O ratio.

Also, the inward drifting of pebbles can influence the chemical composition of exoplanetary atmospheres, since during their drift they sublimate at each snow line crossed, enriching the metallicity of the gas inward of the snow lines and producing different elemental abundance ratios (e.g. C/O and N/O ratios) depending on the pebbles composition and sublimation position in the protoplanetary disk (e.g. Turrini et al. 2021). For example, Bitsch et al. (2022) showed that the formation of close-in Neptunian planets in the inner part of the protoplanetary disk and their atmospheric composition (e.g. the H_2O abundance) depend on the flux of water ice-rich pebbles drifting inward from the outer regions of the protoplanetary disc. In particular, a Neptunian planet can form in a wet environment if the inwards migrating pebbles evaporate inside the water snow line (enriching the inner disk in water vapour), or in a dry environment if pebbles migration is blocked before crossing the water snow line (for example by the presence of an outer companion). Thus, measuring the atmospheric chemical properties (i.e. chemical abundances, metallicity and elemental abundance ratios of different species such as C, O, and N) is crucial to probe the formation history of a planet.

Finally, also the presence of an external companion can play a crucial role in the formation of a planet, by either creating gaps in the protoplanetary disk that block the pebbles migration (e.g. Banzatti et al. 2020) or inducing a violent planet migration through planet-planet scattering. Thus, in order to reconstruct the formation and evolution history of an exoplanet in a more precise way, it is necessary to combine the study of the chemical composition of the exoplanet atmosphere with the information about the planetary interior (e.g. the bulk density) and the planetary system architecture.

1.3 How to study exoplanetary atmospheres

Atmospheric signals are weak and with current instrumental capabilities, we can mainly study the atmosphere of the largest close-in hot planets (i.e. hot and warm Jupiters and Neptunes), because they have atmospheres that are larger and brighter than the atmosphere of cooler and smaller terrestrial planets. It is impressive how only thirty years ago mankind wondered if planets around other stars could exist, while today it is possible to effectively study the atmospheric properties of many of them, such as the chemical composition and the presence of winds. Absolutely fascinating will be, in the next decade, the possibility to study the atmosphere of terrestrial-sized planets with the new-generation extremely large telescopes (ELTs, see Sect. 1.4.4).

The large amount of information about the physical and chemical properties of the atmosphere of an exoplanet can be effectively extracted by using spectroscopy. Currently, there are two observing setups for studying spectra of exoplanetary atmospheres: low-resolution spectroscopy (LRS) and high-resolution spectroscopy (HRS) from ground-based observatories. A key property of any spectrograph is the spectral resolving power ($R = \frac{\lambda}{\Delta\lambda}$), which represents the minimum wavelength difference that can be resolved at a specific wavelength, this can also be expressed in terms of the Doppler effect,

as the speed of light c over the smallest Doppler velocity Δv that can be resolved ($R = \frac{\lambda}{\Delta\lambda} = \frac{c}{\Delta v}$). Typically, the term "high-resolution spectrograph" refers to those spectrographs that have $R \geq 25\,000$, whilst the term low-resolution spectrographs typically refers to those instruments that work with $R = 100 - 2\,000$ (more in general $R \leq 25\,000$).

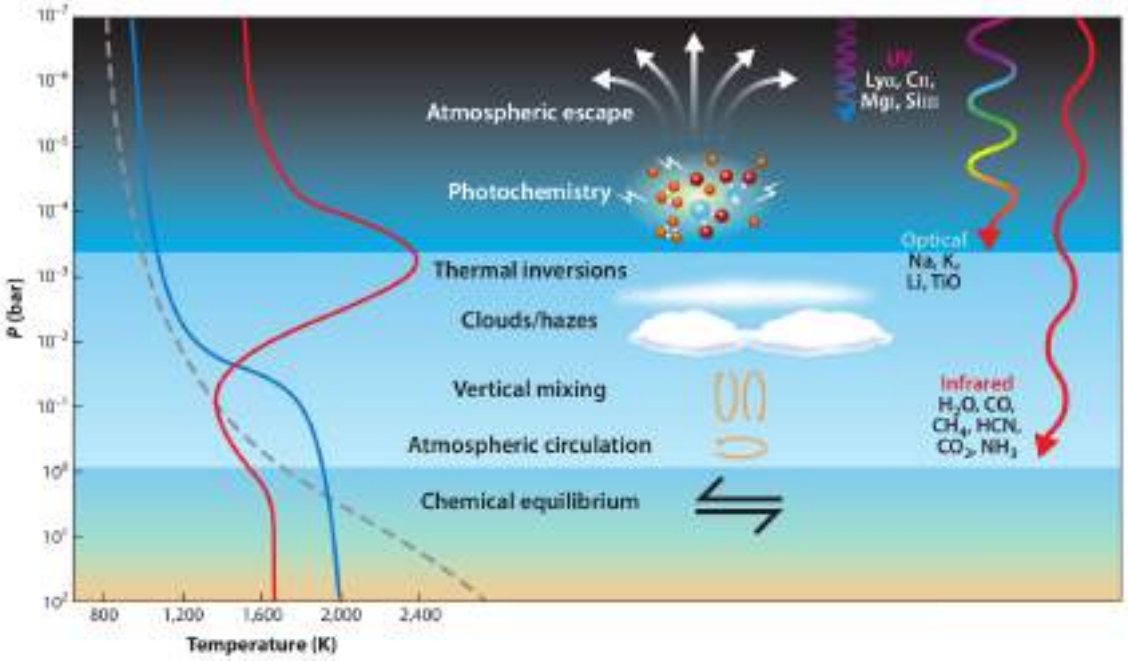

Figure 1.13: Processes active in exoplanetary atmospheres and how they are probed by different parts of the electromagnetic spectrum. On the right, the typical penetration depths of UV, VIS, and IR radiation are shown together with the main chemical species whose signatures can be detected in each wavelength range. On the left, three types of temperature profiles are shown, which can arise as a result of different atmospheric processes: a highly irradiated planet with a thermal inversion (red line), an irradiated planet without a thermal inversion (cyan line), and a poorly irradiated planet (gray dashed line). Image from Madhusudhan (2019).

By studying exoplanetary atmospheres in different wavelength ranges it is possible to probe different regions and, hence, different processes in the atmosphere (see Fig. 1.13). For example, by studying exoatmospheres in the ultraviolet (UV) band, it is possible to probe the upper layers of the atmospheres where atmospheric escape can be present, because UV radiation is involved in the ionisation and recombination of neutral species that populate the upper atmospheric layers, and in photochemical processes. Optical light (VIS) probes intermediate layers where thermal inversion can occur and clouds and hazes can be present, since visible photons interact with neutral atomic species through electronic transitions and with aerosols through scattering processes. Finally, by studying exoatmospheres in the infrared (IR), it is possible to probe deeper layers where molecules are shielded from the high energy radiation by the upper atmospheric layers and interact with IR light through thousands of rotational and vibrational transitions. As it can be seen, in order to extract the largest number of information about an exoplanetary atmosphere a multi-wavelength approach is preferable.

Except for the extremely rare young giant planets on wide orbits that can be directly imaged using space telescopes or very large ground-based telescopes equipped with extremely precise adaptive optics to correct for the effects introduced by our atmosphere, the light from an exoplanet cannot be spatially resolved from that coming from its host star, the latter being completely dominant

by several orders of magnitude. For this reason, for close-in exoplanets, indirect measurements of time-varying signals are performed, and by monitoring the changes of the star plus planet flux as a function of time it is possible to isolate the planetary signal to study its atmosphere. Indeed, in addition to direct imaging, in the case of transiting exoplanets, three main observational methods are possible to study exoatmospheres: transit, secondary eclipse (or occultation) and phase curve observations (Crossfield, 2015, Madhusudhan, 2019). The three different observing configurations are schematised in Fig. 1.14.

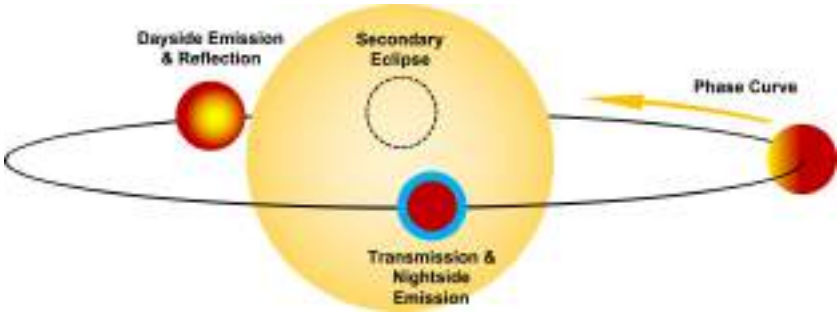

Figure 1.14: Schematic illustration of the possible observing configurations for atmospheric studies along the orbit of a transiting planet.

This thesis is focused on transit observations (in particular, transmission spectroscopy with HRS in the near-infrared). Still, some insights on eclipse and phase curve observations are given in this section as well.

1.3.1 Transmission spectroscopy

When a planet transits in front of its host star, it is not only possible to measure its radius but also to extract important information about its atmosphere. Indeed, during a planetary transit, the light of the host star is filtered through the planet's atmosphere, if present, which leaves spectral imprints on the starlight, creating the so-called transmission spectrum.

With transmission spectroscopy, it is possible to probe only a small portion, an annulus (Fig. 1.14), of an exoatmosphere, corresponding to the terminator, that is the border region between the dayside and the nightside of a planet. As short-period planets are usually tidally locked, with extreme day-night temperature gradients, probing the planetary terminator can provide information on the presence of atmospheric circulation (e.g. winds) that re-distribute the heat between the two planetary faces.

Atoms and molecules that are present in the atmosphere of an exoplanet, absorb and scatter the stellar light at specific wavelengths, that depend on the chemical species responsible for the absorption/scattering. A transmission spectrum is thus an absorption spectrum. At these precise frequencies, the atmosphere is opaque, so the amount of stellar light blocked by the planet is bigger, and thus the planet will have a slightly larger apparent radius at these wavelengths, which can be directly measured from the transit depth.
Therefore, the measurement of the transit depth at different wavelengths, $\delta(\lambda)$, provides the transmission spectrum $T(\lambda)$ of the exoplanet (see Fig. 1.15):

$$T(\lambda) = 1 - \delta(\lambda) = 1 - \frac{R_{\rm p}^2(\lambda)}{R_\star^2}\,. \tag{1.18}$$

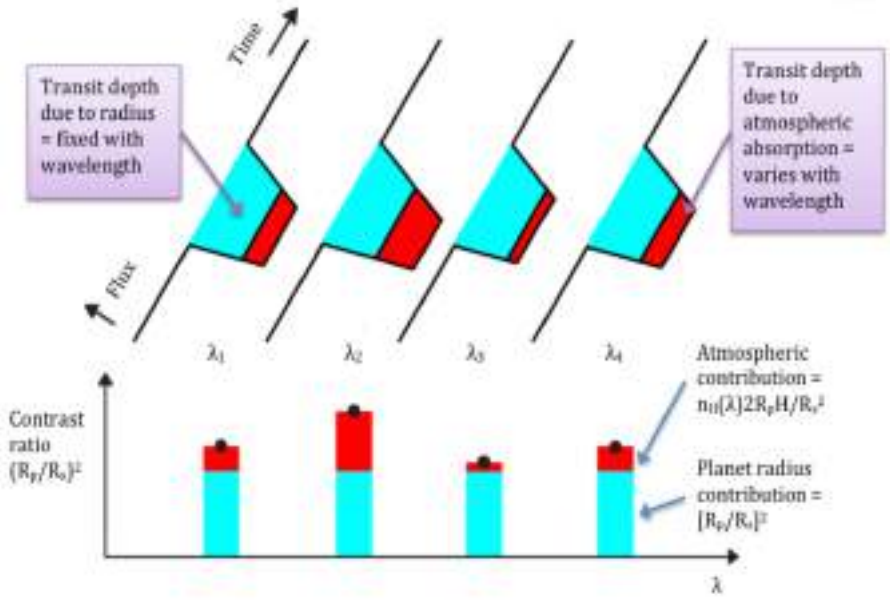

Figure 1.15: Schematic transit light curves as a function of the wavelength. It is visible how the transit depth is made of two contributions: the radius of the planet, which blocks the stellar light at all the wavelengths in the same way, and the atmospheric contribution, whose absorption depends on the wavelength (i.e. transmission spectrum) according to the chemical composition.

The planet effective radius $R_\mathrm{p}(\lambda)$ measured during a transit event is made of two contributions: the radius of the planet R_p, defined as the radius at which the planet is opaque at all the wavelengths, and the atmosphere contribution, whose absorption depends on the wavelength (i.e. transmission spectrum) according to the chemical composition, that can be expressed as an effective atmospheric scale height $H_\mathrm{s}(\lambda)$: $R_\mathrm{p}(\lambda) = R_\mathrm{p} + H_\mathrm{s}(\lambda) = R_\mathrm{p} + n(\lambda) \cdot H_\mathrm{s}$, with H_s = the atmospheric scale height (defined in Eq. 1.9), and $n(\lambda)$ = a parameter that contains the wavelength-dependence of the measured scale height.
Thus, it is possible to estimate the expected strength of the atmospheric transmission signal S of a planet, to distinguish the known planets that could be potential candidates for atmospheric studies, by computing the contrast in the area between the annular region of the planetary atmosphere observed during transit and the stellar area, assuming $n(\lambda) = 1$:

$$S = \frac{R_\mathrm{p}^2(\lambda)}{R_\star^2} - \frac{R_\mathrm{p}^2}{R_\star^2} \approx \frac{2R_\mathrm{p}H_\mathrm{s}}{R_\star^2}\,, \tag{1.19}$$

with the last relation valid under the assumption of $H_\mathrm{s} \ll R_\mathrm{p}$. As it can be seen, the larger the atmosphere and the planetary radius are, the larger the expected transmission signal is (since the planet blocks more light), thus the inflated atmospheres of hot-giant planets are the most suitable for atmospheric studies. Since atmospheric features are typically on the order of $n(\lambda) \sim 1 - 5$ times the atmospheric scale height in size, if the transit depth can be measured to about $1\,H_\mathrm{s}$ in precision, detectable spectral features will start to appear (Sing, 2018).
For instance, the expected signal for the two best-studied hot Jupiters, namely HD 189733 b and HD 209458 b, is $S \sim 107$ ppm and $S \sim 164$ ppm, respectively. For Earth-like planets, S is orders of magnitude smaller, depending on the host-star size.

Another key ingredient, that must be kept into account when performing a transmission spectroscopy study, is the expected noise N. The noise is proportional to $N \propto 1/(\sqrt{F_\star}\sqrt{T_{14}})$, with $F_\star \propto 10^{-mag/2.5}$ = the observed stellar flux (with mag = the apparent stellar magnitude) and T_{14} = the transit duration. Thus, the signal-to-noise ratio (S/N) expected from a transmission atmospheric measurement can be estimated as:

$$S/N \cong \frac{2R_{\rm p}H_{\rm s}}{R_\star^2}\sqrt{F_\star}\sqrt{T_{14}}\,. \tag{1.20}$$

In Fig. 1.16, the expected transmission spectral signal for a large sample of known exoplanets from the TEPCat[2] database is reported as a function of the host-star magnitude.

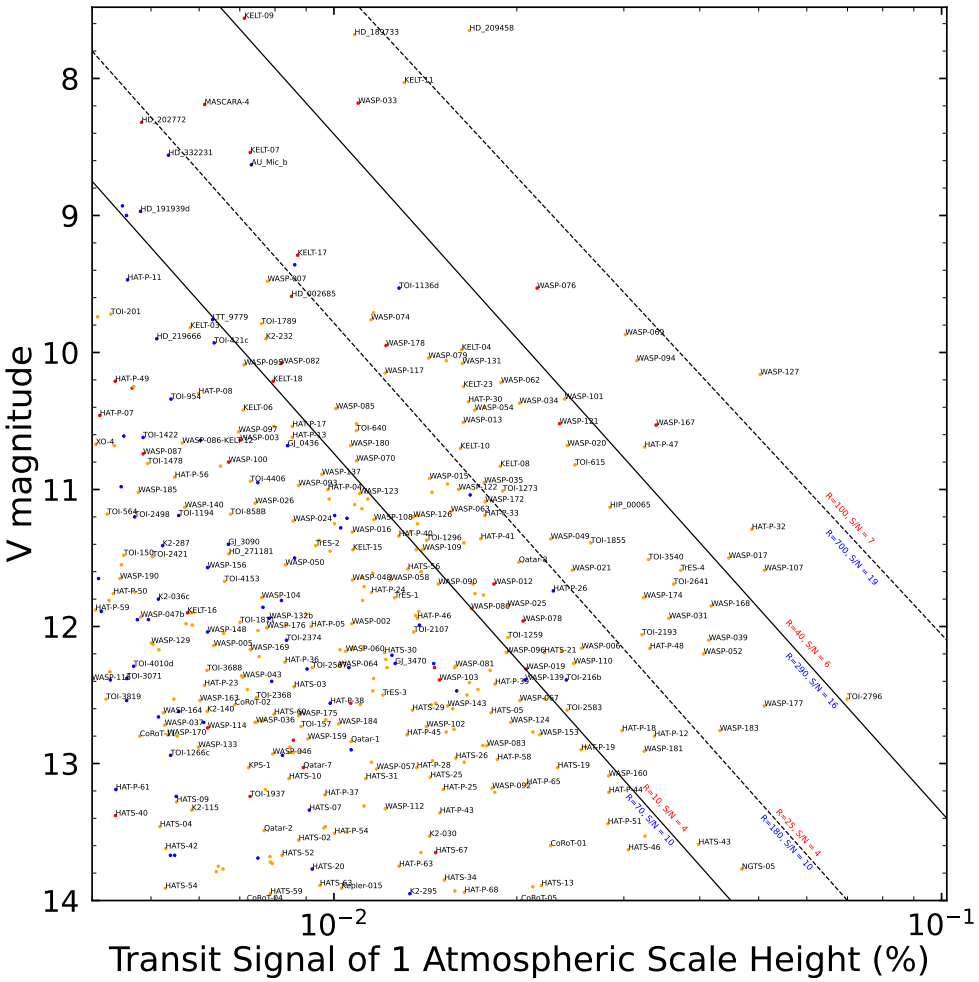

Figure 1.16: Transmission spectral signal of 1 atmospheric scale height as a function of the host-star magnitude for a large sample of known exoplanets. Data are taken from TEPCat. Planets to the upper-right of the figure are easier to observe according to Eq. 1.20. Blue dots represent Neptune-mass planets; orange dots represent Jupiter-mass planets; red dots represent ultra-hot Jupiters. The curves are adopted from (Sing, 2018) and give an indication of constant values for S/N and spectral resolution (see also Heng and Showman 2015). The numbers in red and blue refer to HST and JWST, respectively.

The first detection of an exoplanetary atmosphere was performed by Charbonneau et al. (2002), who obtained an optical transmission spectrum of HD 209458 b with a sodium absorption signal at a level of $0.0232 \pm 0.0057\%$, following the technique proposed in Seager and Sasselov (2000) namely to

[2] `https://www.astro.keele.ac.uk/jkt/tepcat/`

divide the observations gathered during planetary transit (i.e. the stellar + planetary spectrum) by the ones collected outside the transit (i.e. the stellar spectrum alone). Vidal-Madjar et al. (2003), then detected hydrogen in the atmosphere of HD 209458 b and Tinetti et al. (2007) obtained the first molecular detection (i.e. water vapour) in the atmosphere of the hot-Jupiter HD 189733 b. These first detections were then followed by many others, in particular through low-resolution observations performed with the Wide Field Camera 3 (WFC3) mounted at the Hubble Space Telescope (HST, Turner-Valle et al. 2004). In Fig. 1.17, a sequence of transmission spectra of some hot Jupiters, obtained with HST and the infrared Spitzer Space Telescope (Werner et al., 2004) is shown. The HST sensitivity to the water vapour absorption feature at $\lambda \sim 1.4\,\mu$m, is evident, allowing us to measure the presence of H_2O on many targets.

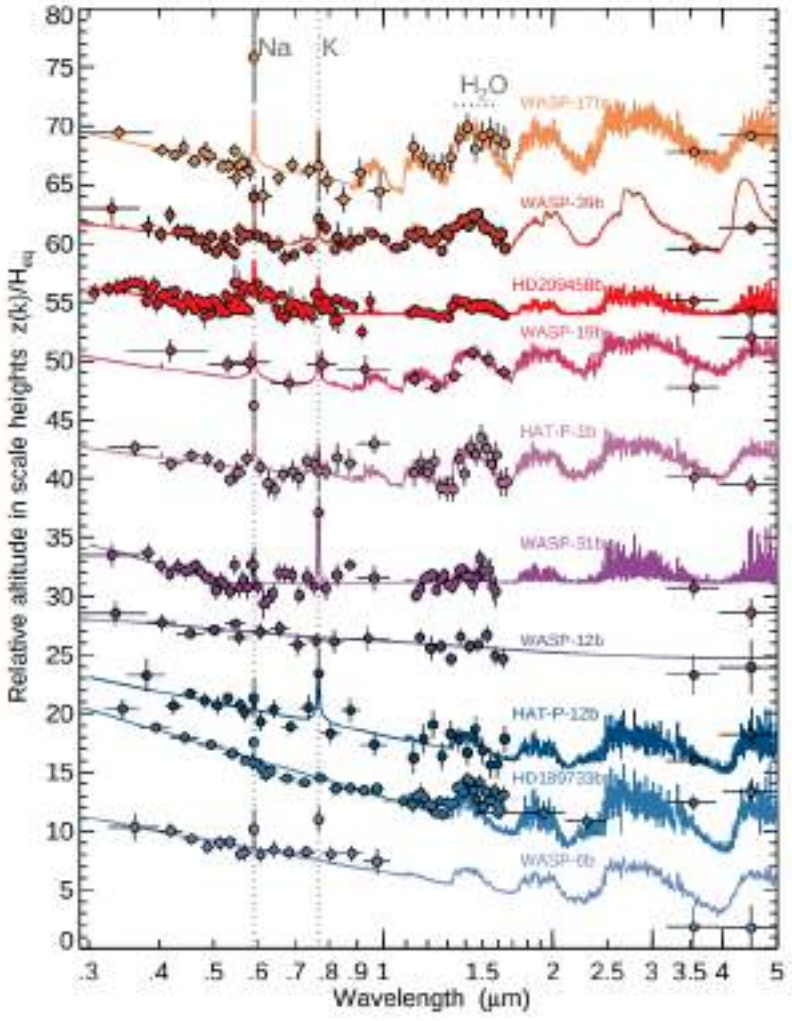

Figure 1.17: HST/Spitzer transmission spectral sequence of some hot-Jupiter targets. Solid coloured lines show fitted atmospheric models, while dotted lines indicate the prominent spectral features including Na, K, and H_2O. It is also visible how heavily hazy and cloudy planets (towards the bottom) have strong optical scattering slopes and H_2O absorption that is partially or completely obscured. Image from Sing (2018).

1.3.2 Secondary eclipse and phase-curve study

Secondary eclipse atmospheric observations are based on comparing the data gathered before and/or after the secondary eclipse (i.e. the stellar + planetary spectrum) with the ones collected during the

eclipse (i.e. the stellar spectrum alone) to isolate the planetary contribution (Fig. 1.14). With this configuration is possible to measure both the emission spectrum of the atmosphere of a planet and the reflection spectrum, depending on the observing wavelength range. Indeed, planetary emission (approximately the emission of a black body at $T \sim 1\,000\,\mathrm{K}$, for a close-in planet) has a peak in the infrared, while the visible light coming from a planet is essentially the stellar light reflected by the atmosphere (or surface) of the planet.

When attempting to characterise an exoplanet by means of secondary-eclipse observations, it is important to quantify its expected dayside flux. In general, the exoplanet dayside flux is the combination of two components: the thermal (emission) component and the reflected one. The thermal component can be estimated assuming that the planet and the star are black bodies, with their respective radiation temperatures (i.e. T_{eff} = stellar effective temperature and T_{day} = planetary dayside temperature), while the light reflected by a planet depends on the radiation received from its parent star and the geometric albedo $A_{\mathrm{g}}(\lambda)$ at a particular wavelength. $A_{\mathrm{g}}(\lambda)$ is defined as the ratio of the planet's luminosity at full phase to the luminosity from a Lambert disk (a Lambertian surface is an ideal, isotropic reflector at all wavelengths) with the same cross-sectional area as the planet (Rowe et al., 2006). Since, the radiation that a planet receives can be defined as $P_{\mathrm{rec}} = F_{\star,\mathrm{p}} \cdot \pi R_{\mathrm{p}}^2$, where R_{p} = the planetary radius and $F_{\star,\mathrm{p}} = L/(4\pi a^2)$ = the stellar flux received by the planet, being L = the luminosity of the star and a = the planet-star distance (semi-major axis), the relative variation of the observed flux f during the eclipse (i.e. the eclipse depth) at wavelength λ can be defined as a sum of two terms, a reflection term and an emission term:

$$\left(\frac{\Delta f}{f}\right)_{\lambda} = A_{\mathrm{g}}(\lambda) \cdot \left(\frac{R_{\mathrm{p}}}{a}\right)^2 + \frac{BB_{\lambda}(T_{\mathrm{day}})}{BB_{\lambda}(T_{\mathrm{eff}})} \cdot \left(\frac{R_{\mathrm{p}}}{R_{\star}}\right)^2, \tag{1.21}$$

with $R_{\star}$ = the stellar radius, $BB_{\lambda}(T_{\mathrm{day}})$ and $BB_{\lambda}(T_{\mathrm{eff}})$ = the black-body brightness, given by Plank's equation, at the temperature of the planetary dayside and the stellar effective temperature, respectively. The planetary dayside temperature depends on the amount of absorbed stellar radiation $(1 - A_{\mathrm{g}})$, the planet-star distance a, and the heat re-distribution efficiency ϵ.
At visible wavelengths the first term is the dominant one, while in the infrared since the BB_{IR} contrast is higher, the emission term is the dominant one. Assuming that the thermal emission is the main component, it is possible to estimate the secondary eclipse observability (i.e. the expected S/N) considering the magnitude of the host star:

$$S/N \cong \frac{BB_{\lambda}(T_{\mathrm{day}})}{BB_{\lambda}(T_{\mathrm{eff}})} \cdot \left(\frac{R_{\mathrm{p}}}{R_{\star}}\right)^2 \cdot \sqrt{F_{\star}}, \tag{1.22}$$

with $F_{\star} \propto 10^{-mag/2.5}$ = the observed stellar flux (with mag = the apparent stellar magnitude).

With emission observations, if the planetary atmosphere is almost transparent, we can observe the radiation coming from deep layers, where the planetary continuum forms. Instead, if there is an opacity source, the atmosphere will become optically thick at higher altitudes at certain wavelengths. In the case of non-inverted atmospheres, i.e. the temperature decreases with pressure, the planetary flux emitted at wavelengths with increased opacity will be lower than the continuum flux, and thus absorption lines will form and be visible in the emission spectrum. On the other hand, in the case of atmospheric layers with temperature inversion, i.e. the temperature increases with pressure, the

planetary flux emitted at wavelengths with increased opacity will be higher than the continuum flux, and the planet emission spectrum will show emission lines.
The first secondary eclipse measurements were achieved by Deming et al. (2005) and Charbonneau et al. (2005) who observed HD 209458 b and TrES-1 b, respectively, using the Spitzer Space Telescope. Shortly after, Knutson et al. (2008) found evidence of a thermal inversion in the atmosphere of HD 209458 b.

When the observations are continuously performed along the orbit of the exoplanet, one can measure the phase curve, that is the temporal changes in the planet-star flux combination. These differences occur because our geometric view of the exoplanet surface changes during the observations (Fig. 1.14). Using phase curve observations, the temperature difference between the day and night side can be inferred, but it is also possible to map the atmospheric temperature around the planet. Thus, studying phase curves is the best technique for monitoring the three-dimensional structure of the atmosphere of an exoplanet. Although phase curve studies do not necessary require a transiting planet, these have been the most studied planets due to their ephemeris precision and the higher flux modulation (Bozza et al., 2018). Phase curves are one of the most demanding and challenging observations, as they require a photometric precision of the order of 100 ppm, and long, continuous observations ($\sim$ days). Therefore, they arise mostly from satellite mission data.

Two different techniques can be employed to measure a planet's phase curve. On the one hand, phase curves are created by studying photometry. These photometric phase curves are mainly observed to measure the planetary albedo and thermal brightness maps of several atmospheric portions (e.g. Demory et al. 2016). On the other hand, spectroscopic phase curves can help to study the differences in the temperature structure and composition of different atmospheric regions (e.g. Stevenson et al. 2014).
One of the first phase curves measurements was made with Spitzer observations of the exoplanet HD 189733 b (Knutson et al., 2007), and the first secondary eclipse map of an exoplanet was performed by Majeau et al. (2012), using observations of the same planet.

1.4 High-resolution spectroscopy technique

During the last 15 years, high-resolution spectroscopy has become one of the most successful techniques to investigate exoplanetary atmospheres. It can be used to study exoatmospheres of both transiting and non-transiting planets, because it searches for the direct contribution of the exoplanet atmosphere to the observed host star spectrum taking advantage of the differential velocities of the star, the Earth, and the exoplanet (see Birkby 2018, for a review). Since this technique needs high-resolution spectrographs (spectral resolving power $R \geq 25\,000$), that are too weighty (i.e. too expensive and cumbersome) to be launched in space, HRS observations are only conducted from the ground.

1.4.1 State-of-the-art of HRS technique

The first HRS detection of molecules in an exoplanet atmosphere has been obtained by Snellen et al. (2010), who detected absorption features of CO during a transit of the hot-Jupiter HD 209458 b using the CRyogenic high-resolution InfraRed Echelle Spectrograph (CRIRES, Kaeufl et al. 2004) mounted at the 8 m-class ESO-Very Large Telescope (VLT), at a resolving power of $R \sim 100\,000$. Since then,

the number of atmospheric studies using high-resolution spectroscopy observations has increased exponentially. Among the first works that detected molecules in the atmosphere of non-transiting planets with HRS, Rodler et al. (2012) detected the presence of this molecule in the atmosphere of the hot-Jupiter τ Boo b and used it to infer the orbital inclination and the absolute mass of the target.

HRS demonstrated to be a valid technique to detect different chemical species both in the visible and near-infrared, in the atmosphere of different kinds of targets, from warm Neptunes to hot and ultra-hot Jupiters. With HRS observations in the near-infrared, it has been possible to identify the spectral features of different molecules, such as CO (Snellen et al., 2010), H_2O (Birkby et al., 2013), HCN (Hawker et al., 2018), CH_4 (Guilluy et al., 2019), NH_3 and C_2H_2 (Giacobbe et al., 2021), and OH (Nugroho et al., 2021).

Several leading near-infrared instruments in the field allow both to detect molecular species and atmospheric escape (through the observation of the metastable HeI triplet at 1038 nm). Among them, there is GIANO-B ($R \sim 50\,000$), mounted at the Telescopio Nazionale Galileo, which allows to identify multiple molecular species in the atmosphere of different targets (e.g. Giacobbe et al. 2021, Guilluy et al. 2022, Carleo et al. 2022) and detected for the first time NH_3 in the atmosphere of a warm Neptune (Basilicata et al., 2024a). GIANO-B also plays an important role in the detection of metastable HeI triplet in the atmosphere of many targets (e.g. Guilluy et al. 2023).
CRIRES$^+$ ($R \sim 100\,000$, Follert et al. 2014), the updated version of CRIRES, mounted at ESO-VLT, allows to perform very high S/N atmospheric detection for different targets (e.g. Maimone et al. 2022, Ramkumar et al. 2023, Blain et al. 2024, Nortmann et al. 2024) together with the Immersion GRating INfrared Spectrometer (IGRINS, $R \sim 45\,000$, Park et al. 2014), mounted at the Gemini South Telescope (e.g. Line et al. 2021, Brogi et al. 2023, Line et al. 2024, Wardenier et al. 2024, Weiner Mansfield et al. 2024), and the near-infrared channel of the Calar Alto high-Resolution search for M dwarfs with Exoearths with Near-infrared and optical Echelle Spectrographs instrument (CARMENES, $R \sim 80\,000$, Quirrenbach et al. 2014, 2018), mounted at the 3.5 m Calar-Alto Telescope (e.g. Allart et al. 2018, Nortmann et al. 2018, Salz et al. 2018, Alonso-Floriano et al. 2019).

For what it concerns the detection of atomic and ionic species, HRS observations in the visible allow to identify many species in different targets. The first ground-based high-resolution detection of sodium absorption in the transmission spectrum of an extrasolar planet is from Redfield et al. (2008), who measured NaI absorption in the atmosphere of HD 189733 b using the High Resolution Spectrograph mounted on the 9.1 m Hobby-Eberly Telescope (HET, Ramsey 1998). Wyttenbach et al. (2015) also measured NaI absorption in the atmosphere of HD 189733 b through observations from the High Accuracy Radial velocity Planet Searcher (HARPS, $R \sim 120\,000$, Mayor et al. 2003), mounted at the ESO-3.6 m Telescope, and subsequent studies using HARPS and HARPS-N (HARPS-north, $R \sim 120\,000$, Cosentino et al. 2012, mounted at the Telescopio Nazionale Galileo) transit observations of other hot Jupiters would result in similar detections (e.g. Casasayas-Barris et al. 2017, Wyttenbach et al. 2017, Chen et al. 2020a). NaI, together with KI, have also been detected using the Echelle SPectrograph for Rocky Exoplanets and Stable Spectroscopic Observations instrument (ESPRESSO, $R \sim 140\,000$, Pepe et al. 2010, 2014, mounted at the ESO-VLT) in atmosphere of WASP-52 b Chen et al. (2020b). Neutral and ionised iron (FeI, FeII) have been two of the most detected species in the atmosphere of ultra-hot Jupiters (e.g. Hoeijmakers et al. 2018). Hoeijmakers et al. (2019), ended up with detections of rare neutral and ionised metals such as ScII, TiII, CrII, and YII, by probing the

atmosphere of the well-studied ultra-hot Jupiter KELT-9 b.

Due to their inflated atmosphere and high temperature, hot and ultra-hot Jupiters are the most suitable targets for atmospheric characterisation. For this reason, in the last years, they were the most studied targets for testing 2D- and 3D-atmospheric models to retrieve their atmospheric properties (e.g. Gandhi et al. 2022, Wardenier et al. 2023, Nortmann et al. 2024).

Two ways of working with HRS are possible: the high-resolution single-line transmission spectroscopy and the high-resolution cross-correlation spectroscopy (HRCCS). The first one (e.g. Wyttenbach et al. 2015) is based on differential spectroscopy, namely the comparison between stellar spectra taken when the planet is crossing the stellar disc (transiting) and those taken when it is not. The aim is to combine the Doppler-corrected in-transit spectra to build the high-resolution transmission spectrum of single strong atmospheric absorption lines (e.g. the metastable HeI triplet and the hydrogen Lyman α line), however, a detailed description of this technique is beyond the scope of this work. On the other hand, since HRCCS is of great interest for this thesis, the following paragraph describes the main methods on which this technique is based.

1.4.2 Methodology

Working with high-resolution spectrographs has two big advantages with respect to the low-resolution counterparts.

The first advantage is that by using high-resolution instruments, it is possible to solve the spectral features of atmospheric components (e.g. molecular absorption bands) into a dense forest of single spectral lines. Since these lines are unique for each chemical species, they constitute a sort of fingerprint that allows us to unambiguously detect the presence of a certain chemical species in the observed exoatmosphere. In addition, even if the S/N on the single spectral lines is low ($\mathrm{S/N_{line}} < 1$) because of the large dispersion of the light on the detector, combining the signal of thousands of lines observed simultaneously results in a boost of the S/N of the detection that is proportional to the square root of the number of strong lines observed (N_{lines}): $\mathrm{S/N_{tot}} \propto \sqrt{N_{\mathrm{lines}}}$. Thus, spectrographs with both a high spectral resolving power and instantaneous wavelength coverage (i.e. the number of wavelengths observed in a single exposure) are the ideal instruments for studying exoatmospheres with HRS observations.

The second advantage is that high-resolution observations of atmospheric spectra are sensitive to the Doppler shift of the spectral lines. In this way, in order to be sure that a particular spectral feature is produced by the atmosphere of an exoplanet, it is necessary to measure a Doppler shift of the signal that "follows" the planetary movement. The measured Doppler shift of the planetary spectral lines ($V_{\mathrm{RV}} = c \cdot \frac{\Delta\lambda}{\lambda}$, with λ = a generic wavelength and c = the speed of light), as a function of time t, is produced by three velocity components:

$$V_{\mathrm{RV}}(t) = V_{\mathrm{p}}(t) + V_{\mathrm{sys}} - V_{\mathrm{bary}}(t)\,, \tag{1.23}$$

where $V_{\mathrm{bary}}(t)$ = the velocity induced by Earth's motion around the barycentre of the solar system (barycentric velocity), V_{sys} = the centre of mass velocity of the star-planet system with respect to the Earth (systemic velocity), and $V_{\mathrm{p}}(t)$ = the planet RV. The time-dependent contribution $V_{\mathrm{p}}(t)$ can be expressed as a function of two of the planetary orbital parameters (i.e. the eccentricity e and the planetary argument of periastron ω_{p}), the planetary RV semi-amplitude K_{p} and the true orbital

anomaly $\nu(t)$:

$$V_{\rm p}(t) = K_{\rm p} \cdot [\cos(\nu(t) + \omega_{\rm p}) + e \cdot \cos(\omega_{\rm p})]\,, \tag{1.24}$$

that, in the case of a circular orbit, reduces to:

$$V_{\rm p}(t) = K_{\rm p} \cdot \sin(2\pi\phi(t))\,, \tag{1.25}$$

with $\phi(t)$ = the planetary orbital phase at time t, defined as the fractional part of $(t - T_{\rm c})/P_{\rm orb}$, where $P_{\rm orb}$ = the orbital period and $T_{\rm c}$ = the mid-transit time (for transiting planets) or the inferior conjunction time (for non-transiting targets).
The planetary radial-velocity semi-amplitude $K_{\rm p}$ can be expressed as a function of the orbital eccentricity e, orbital inclination i, orbital period $P_{\rm orb}$, the mass of the planet $M_{\rm p}$, and mass of the star $M_\star$:

$$K_{\rm p} = \left(\frac{2\pi G}{P_{\rm orb}}\right)^{\frac{1}{3}} \cdot \frac{M_\star \cdot \sin(i)}{(M_\star + M_{\rm p})^{\frac{2}{3}}} \cdot \frac{1}{\sqrt{1-e^2}}\,. \tag{1.26}$$

Since the observations are performed from the ground, also the Earth's atmospheric absorption spectrum (telluric lines) is imprinted on the astrophysical signal. However, the planet spectrum experiences a detectable change in Doppler shift during the observations (Fig. 1.18). This change allows to disentangle the planetary signal, whose orbital velocity has a non-zero radial component ($\sim 10\,{\rm km\,s^{-1}}$), from the stationary telluric spectrum (telluric lines have a null Doppler shift in the observer rest-frame) and quasi-stationary stellar lines (the stellar radial velocity changes by few ${\rm m\,s^{-1}}$ during transit events).

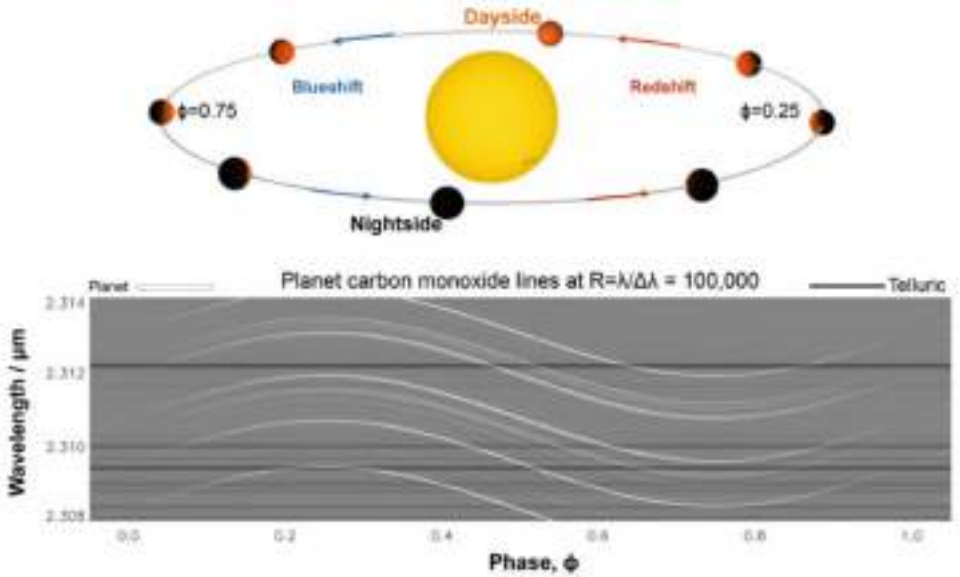

Figure 1.18: Scheme of HRS atmospheric signal. Top panel: illumination of a planet throughout its orbit and the Doppler shift of its spectrum. Bottom panel: example of planetary atmospheric emission spectral lines (white lines) as a function of the orbital phase, in which is visible how they trace out the radial velocity curve of the planet during the orbit (visible in the top panel) with respect to the stationary stellar and telluric lines (horizontal dark lines). Image from Birkby (2018).

In this way, it is also possible to derive the true mass of non-transiting planets, despite not knowing the orbital inclination, via the velocity and mass ratios. In particular, the true mass of the planet $M_{\rm p}$ can be derived by knowing the $K_\star$, the $M_\star$, and measuring the $K_{\rm p}$ from the Doppler shift of

their atmospheric emission (or reflection) spectral lines, according to:

$$\frac{K_\star}{K_\mathrm{p}} = \frac{M_\mathrm{p}}{M_\star}\,. \tag{1.27}$$

If the planet is also a transiting system, HRS allows model-independent measurements of the mass and radius of the host star and its planet.

The planetary atmospheric signal can be extracted from the noise combining the signal of thousands of spectral lines observed simultaneously thanks to the cross-correlation function (CCF). This technique exploits the fact that we know precisely at what wavelengths certain lines are formed, and by having a sufficient number of spectral lines we can average out the noise to obtain the measurement of an average spectral line. In particular, it is based on computing the cross-correlation between data (i.e. the spectrum $S(\lambda)$) and template atmospheric spectra (i.e. the model $M(\lambda)$), shifting the model in wavelength on a fixed grid of RV lags ($\Delta RV = \frac{\Delta\lambda}{\lambda}\cdot c$). The analytical expression for the CCF is:

$$CCF(\Delta\lambda) = \int_{-\infty}^{+\infty} S(\lambda)\cdot M(\lambda+\Delta\lambda)\,d\lambda\,. \tag{1.28}$$

If a chemical species is present in the atmosphere of the target (i.e. if the atmospheric model matches the data), a peak in the CCF is observed. The CCF is computed for each spectrum obtained during the time series, so the data-model matching (i.e. the CCF peak) should move in the Doppler-space according to the planetary RV. In other words, the atmospheric signal as a function of time (or orbital phase) must shift in wavelength according to the Doppler shift induced by the planetary motion, as it is visible in the left panel of Fig. 1.19.

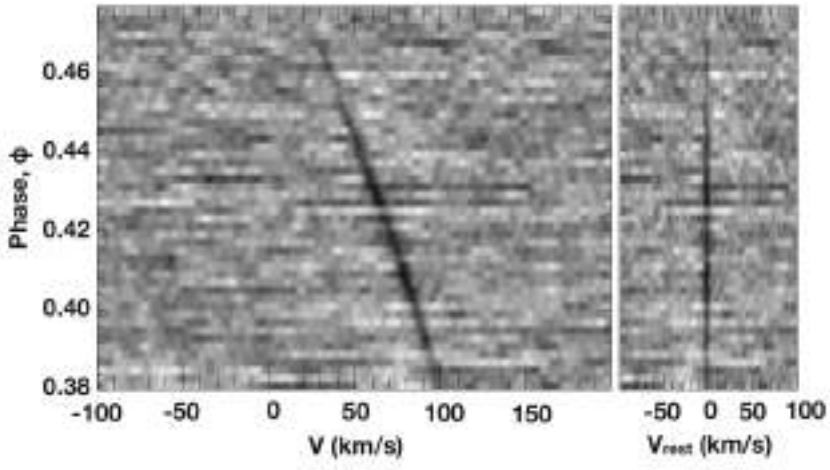

Figure 1.19: Example of CCF values as a function of the orbital phase. Left panel: CCF values as a function of the orbital phase for a model containing water lines and injected into real observations of HD 189733 from Birkby et al., 2013. The CCF peak trail as a function of time is visible and moves in the Doppler-space according to the planetary RV. Right panel: the CCF values are shifted into the planet rest-frame according to the expected K_p. Image from Birkby (2018).

The atmospheric signal has a null Doppler shift measured in the exoplanet rest frame ($V_\mathrm{rest} = 0\,\mathrm{km\,s^{-1}}$, with V_rest = the RV measured in the planetary rest-frame), in the absence of a Doppler shift induced by atmospheric dynamics. It follows that, after having subtracted the barycentric, systemic and planetary RV from the CCF trails (that is, after having moved to the exoplanet rest-frame), all the CCF peaks should align at $V_\mathrm{rest} = 0\,\mathrm{km\,s^{-1}}$, as visible in the right panel of Fig. 1.19. By subtracting

different orbital solutions to the CCF peak trail, typically by changing the K_p, a different CCF trail alignment is obtained. Finally, by co-adding the CCF values in phase into a single CCF, for each trial K_p, it is possible to obtain the so-called $K_p - V_{rest}$ maps (or $K_p - \Delta V_{sys}$ maps), in which the planetary signal as a function of the rest-frame velocity and K_p is maximised.

When an atmospheric signal is detected, a strong cross-correlation peak in the $K_p - V_{rest}$ map at the expected K_p and $V_{rest} = 0\,km\,s^{-1}$ is visible. However, exploring a large parameter space offers a strong diagnostic of the sources of noise and allows us to check the presence of spurious signals that could produce a significant detection near the planet's rest frame position. Eventual shifts of the CCF peak in the $K_p - V_{rest}$ map can be due to atmospheric dynamics effects (Fig. 1.20). For example, a net blueshift ($V_{rest} < 0\,km\,s^{-1}$) of the CCF peak during transit can be due to the presence of a wind that, blowing from the day side to the night side of the planet, moves atmospheric materials towards the observer (e.g. Brogi et al. 2016), while a K_p shift can be related to planetary rotation (e.g. Wardenier et al. 2023). The origin of these residual Doppler shifts depends on the atmospheric dynamics of the target, the accuracy of the orbital parameters and the geometry of the observations (i.e. emission or transmission spectroscopy) and can be different for different targets.

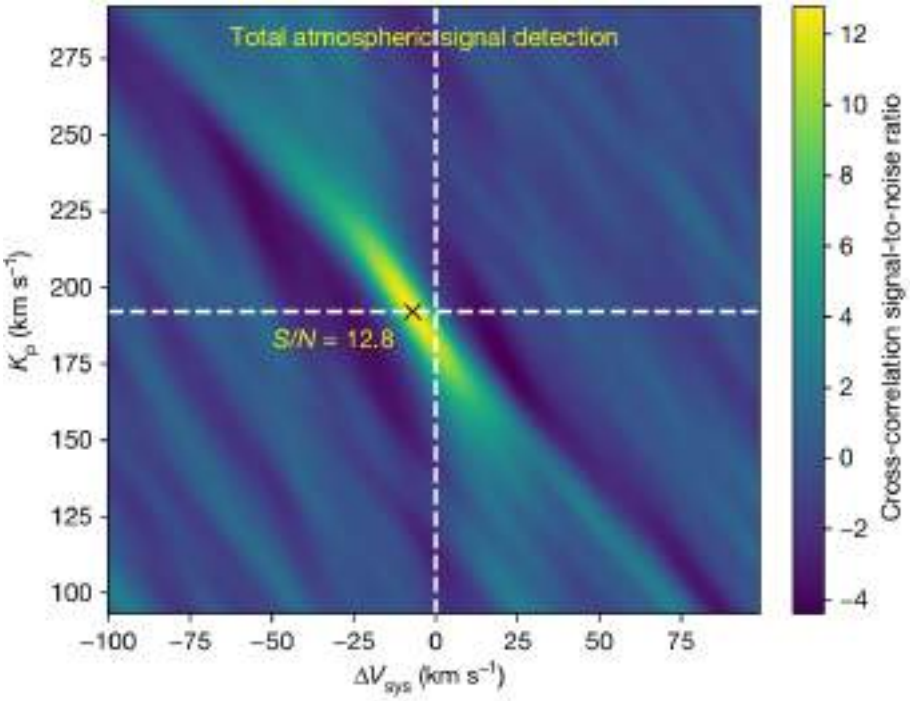

Figure 1.20: Example of $K_p - V_{rest}$ map, from Line et al. (2021). This map is obtained by cross-correlating a retrieved atmospheric emission model template for the hot-Jupiter WASP-77 Ab with data taken with the IGRINS spectrograph. White dashed lines indicate the known velocities (i.e. the expected $K_p = 192.06\,km\,s^{-1}$, $\Delta V_{sys} = V_{rest} = 0\,km\,s^{-1}$) and the "x" denotes the location of the peak signal (S/N = 12.8). The visible blueshift of the CCF peak can be due to a combination of rotation ($\sim 4.5\,km\,s^{-1}$), which might preferentially blue shift a dayside hot spot and/or longitudinal temperature advection (west-to-east winds, $\sim 2\,km\,s^{-1}$).

1.4.3 Observing from the ground: the telluric contamination

Since HRS observations are performed using ground-based instruments, the strongest contamination in high-resolution spectra is the telluric contamination, especially in the near-infrared, where H_2O (but also O_3, CO, CH_4, and CO_2) has numerous and strong absorption bands.

In order to remove telluric lines, we can take advantage of the fact that they are at fixed known wavelength and do not experience any Doppler shift during the observations. The only variation that affects them is the intensity (i.e. line depth) variation, which depends on the air mass variation at first order, and on many other second-order effects, such as variations in the precipitable water vapour (PWV), telescope temperature, and seeing.
A possible method to remove telluric contamination is to fit the logarithm of the flux in each spectral channel as a function of the air mass using a linear fit (since the intensity of telluric lines scales as the exponential of the air mass). In order to include higher-order variations, a quadratic fit can be employed. This method has been successfully used in different works (e.g. Snellen et al. 2010, Brogi et al. 2018, 2012, Brogi et al. 2013, Brogi et al. 2014, 2017).
An alternative approach is based on modelling telluric lines using theoretical calculations based on the observing atmospheric conditions, using codes such as ESO's Molecfit (Smette et al., 2015), however, this approach does not automatically account for instrumental systematic effects occurring during the observation, leaving residuals.

To date there is no consensus on which is the best way of removing telluric contamination, however a third approach that seems to be very effective in removing both the telluric and stellar spectra contamination, that also takes into account instrumental systematic effects that may occur during the observations, is the principal component analysis (PCA, Murtagh and Heck 1987), and the use of algorithms that employ it, such as SYSREM (Tamuz et al., 2005). PCA has been successfully employed in many works to study the atmosphere of exoplanets (e.g. de Kok et al. 2013, Birkby et al. 2013, 2017, Piskorz et al. 2017) and applied to GIANO-B data multiple times to detect molecular species in exoatmospheres (e.g. Giacobbe et al. 2021, Carleo et al. 2022, Guilluy et al. 2022, Basilicata et al. 2024a).

The basic idea of PCA is to identify common trends in the spectra as a function of time (in this case represented by telluric and stellar lines, that are stationary in wavelength) in different spectral channels, and remove them. In order to do this, the eigenvectors of the data covariance matrix (i.e. the principal components) are computed and ordered by decreasing contribution to the global variance (identified by the associated eigenvalue). Once the principal components are calculated, it is possible to re-construct the matrix that should mainly describe the telluric and stellar contaminations via the linear combination of a set of principal components, and removed it from the original data matrix, obtaining a residual matrix that can be used for the cross-correlation analysis.

It is worth noting, that in some conditions stellar contamination is not effectively removed from the data. In particular, the star may contain sufficiently similar spectral lines to the planet at certain wavelengths (e.g. this is the case of CO lines in cooler host stars such as K-dwarfs), or may have non-negligible velocity changes that interfere with the telluric removal process. This kind of effects, can leave residual contamination in the spectra and introduce some distortions of the line profile during the transit, due for example to the Rossiter-McLaughlin effect (RM) or to center-to-limb variations (CLV), that can produce spurious artifacts when cross-correlating data with planetary model spectra. In these cases, stellar contamination can be modelled and removed before applying the telluric removal procedure, as described in e.g. Brogi et al. (2016) and Schwarz et al. (2016).

1.4.4 Combining high- and low-resolution spectroscopy

High-resolution spectroscopy and low-resolution spectroscopy (LRS) give complementary information about planetary atmospheres. Indeed, they probe different altitudes of the atmosphere, for example in the NIR, the LRS targets pressures around $1.0 - 0.1$ bar, while HRS probes higher layers, with a pressure range of $\sim 10^{-2} - 10^{-5}$ bar.
In the case of HRS, with the different approaches used to remove telluric contamination, like PCA, the spectra are typically normalised. This removes information about the true continuum level of the planetary spectrum and has two effects. First, LRS is more sensitive to broad features and the continuum from the optical to the NIR, that make LRS extensively used to study the presence of aerosols (through the measurements of typical scattering slopes) in the atmosphere of exoplanets (e.g. Nascimbeni et al. 2013, 2015, Sing et al. 2016). The second effect is that with respect to LRS, HRS is more sensitive to line position rather than depth.
This make the retrieval of atmospheric absolute abundances (related to line depth) from high-resolution spectra more challenging, but allows to investigate atmospheric dynamics effects such as atmospheric rotation and winds in a very effective way.
On the other hand, the HRS methodology allows a self-calibration of data and has the advantage of combining the signal of thousands of spectrally resolved absorption or emission lines rather than bands from a chemical species, resulting in a more accurate spectral identification of chemical species.
Furthermore, LRS can take advantage of the two very sensitive space telescopes currently in operation, that are the Hubble Space Telescope and the James Webb Space Telescope (JWST, Gardner et al. 2006), which allow observers to avoid telluric contamination, while HRS observations can be performed by ground-based large-aperture instruments, such as the VLT and the future 40 m-class extremely large telescopes (ELTs) like the European Extremely Large Telescope (E-ELT, Padovani and Cirasuolo 2023). On one hand, from the space, with JWST is possible to study hot Jupiter atmospheres at high S/N and the atmospheric composition of warm Neptunes and super Earths (e.g. Rustamkulov et al. 2023, Esparza-Borges et al. 2023, Carter et al. 2024, Espinoza et al. 2024, Schlawin et al. 2024). On the other hand, from the ground, when the ELTs will be available for HRS observations, they will allow to detect and explore the atmosphere of smaller planets and fainter targets. Indeed, according to some simulations (e.g. Snellen et al. 2013, Palle et al. 2023), using tens of transits, transmission spectroscopy with ELTs will probably make possible the detection of molecular oxygen in the atmosphere of habitable exoplanets, allowing us to search for biosignatures in planetary environments similar to the Earth.

Previous analyses of multi-resolution transmission spectroscopy treated low- and high-resolution data sets separately, each with its statistical framework (e.g. Pino et al. 2018), and explored only a limited parameter space. The most effective way of extracting physical information from atmospheric spectral observations is performing atmospheric retrieval in a Bayesian framework. The basic idea is to iteratively compare many thousands of atmospheric parametric models with data in order to find the one that best fits the data on a statistical base. Typically, the parameters space is explored through algorithms like Markov chain Monte Carlo methods (e.g. Blecic et al. 2017) and nested sampling algorithm (e.g. Benneke and Seager 2013), that retrieve the posterior distribution of the model parameters computing the likelihood between the data and the model for each trial parameters set. The biggest obstacle is converting the cross-correlation values into a goodness-of-fit estimator, but Brogi and Line (2019a) introduced a new approach to solve this restriction. They

built a new robust and unbiased framework to perform Bayesian retrieval analyses on HRS data, by converting the cross-correlation values into log-likelihood mapping. This approach also makes possible to perform HRS-LRS joint retrievals by combining the likelihoods (e.g. Smith 2023).

The combination of these two complementary techniques and the use of very powerful present and future instruments will improve the amount of information that can be inferred about the physics and chemistry of exoplanetary atmospheres and will refine our ability of studying them, enlarging our comprehension about these complex systems and making us have well-robust and even more reliable methods to search for biosignatures on potentially habitable planets in the future.

1.5 Overview of the work presented in this thesis

The focus of my Ph.D. work was the atmospheric characterisation of extrasolar planets through the high-resolution spectroscopy technique. My work has been mainly based on the atmospheric study of short-period gas giant planets (one warm Neptune and four hot Jupiters) that, as explained in the previous sections of this thesis, represent the ideal targets for atmospheric characterisation because of their inflated atmospheres. In the following chapters of this thesis, I review the results of the research work I conducted during my three years of Ph.D. showing already published results as well as the results of publications submitted or in preparation.

For the main part of my research, I have used the HRS technique to analyse the spectra acquired with the high-resolution near-infrared spectrograph GIANO-B, mounted at the Telescopio Nazionale Galileo (TNG), La Palma, Spain, as part of the Global Architecture of Planetary Systems (GAPS) Project[3]. In Chapter 2 of this thesis, I present the GIANO-B spectrograph, describing the main technical aspects of this instrument and I describe some details of the data reduction procedure performed on high-resolution GIANO-B spectra, from the calibration to the telluric removal procedure.

In Chapter 3, I present the work published in Basilicata et al. (2024a), where I report the observation of multiple molecular species in the atmosphere of the warm Neptune HAT-P-11 b. In the first part of this work, we reviewed the physical and architectural properties of the HAT-P-11 planetary system by analysing transits and occultations of HAT-P-11 b from the *Kepler* data set as well as HIRES at Keck archival radial-velocity data. In the second part, we combined data gathered with GIANO-B during the observation of four planetary transits, in order to study the high-resolution NIR transmission spectrum of the atmosphere of HAT-P-11 b. In this work, we report for the first time the detection of NH_3 in the atmosphere of a warm Neptune and confirm the presence of H_2O. We also tentatively detect the presence of CH_4 and CO_2. These results, whose robustness was assessed with different statistical tests, are particularly interesting since warm Neptunes are difficult targets for atmospheric characterisation due to their relatively small radii and temperature, which both reduce the atmospheric transmission signal. After this first work, I tried to develop an approach as much standard as possible to reduce GIANO-B data, in terms of spectral orders to employ in the analyses and the number of principal components to remove from data with PCA. I applied this reproducible reduction procedure to analyse GIANO-B transmission spectra of four hot Jupiters, namely KELT-8 b, KELT-23 Ab, WASP-13 b, and HAT-P-1 b. In Chapter 4, I present the work reported in a paper submitted to the Astronomy & Astrophysics journal as Basilicata et al. (2024b) (article reference: AA52733-24), where I report the first investigation of the atmospheres of

[3] `https://theglobalarchitectureofplanetarysystems.wordpress.com/`

the two hot Jupiters KELT-8 b and KELT-23 Ab. By analysing data of one transit for each target, for the first time, we detect the atmospheric signature of both planets, measuring the signal of H_2O, with an S/N= 6.6 and S/N= 4.2, for KELT-8 b and KELT-23 Ab, respectively. We also performed a preliminary characterisation of the chemical and physical properties of the two atmospheres by running two atmospheric retrievals for each target: a retrieval assuming chemical equilibrium and a "free-chemistry" retrieval, in which the abundance of each molecule could vary freely. We put first constraints on the abundance of H_2O and the chemical parameters, such as the metallicity and the C/O ratio, of the two atmospheres, and suggested a possible formation scenario for both targets. In Chapter 5, I present the preliminary results of the investigation of the atmospheres of the two hot Jupiters WASP-13 b and HAT-P-1 b, reported in a paper currently in preparation (Basilicata et al., in prep.). In this work, we searched for the atmospheric signal of WASP-13 b for the first time and performed the first study of the atmosphere of HAT-P-1 b at high spectral resolution. We analysed one transit observation of WASP-13 b and two transit observations of HAT-P-1 b, collected with GIANO-B. We do not detect the atmospheric signal of the two hot Jupiters, with our preliminary cross-correlation analysis. We only find a possible hint of the presence of CO in the atmosphere of WASP-13 b that needs to be confirmed with further studies. Since the analysis is still ongoing, we conclude the chapter with a list of future steps that we will perform in order to refine our analysis. Finally, in Chapter 6, I summarise the studies performed in this thesis and point out the main conclusions. An overview of possible future work is also included at the end of this last chapter.

Chapter 2

High-resolution spectroscopy with GIANO-B

The bulk of the research work presented in this thesis is focused on the characterisation of exoplanetary atmospheres at high-spectral resolution using data collected by the GIANO-B near-infrared spectrograph. In this chapter, I report an overview of the GIANO-B spectrograph and the data extraction and reduction procedure adopted in the works reported in this thesis.

2.1 The GIANO-B spectrograph

GIANO is an high-resolution echelle spectrograph mounted at the Telescopio Nazionale Galileo (TNG), a telescope with a diameter of 3.58 m located at the Roque de los Muchachos Observatory (La Palma, Canary Islands, Spain). It has a mean spectral resolving power of $R = 50\,000$ and works in the near-infrared (wavelength range: $0.95 - 2.45\,\mu$m) with a nearly contiguous coverage of the entire Y, J, H, and K bands, split into fifty orders (from order number 32 to 81, Origlia et al. 2014). The instrument was provisionally commissioned in 2012 and was used in the GIANO-A configuration. In this configuration it was mounted in the TNG Nasmyth-A focus and was fed through a pair of fibers. The spectrometer was eventually moved to the originally foreseen configuration in September 2016. In this final configuration, named GIANO-B, the instrument is placed in the TNG Nasmyth-B focus (hence the name GIANO-B) and the light collected by the telescope reaches directly the instrument through a slit.

The spectrograph HgCdTe detector is a HAWAII-2 2048x2048 array, with a pixel size of $18\,\mu$m, cooled at cryogenic temperature by a bath of liquid nitrogen. The minimum integration time is 10 s, the possible integration times on target are 10, 30, 60, 100, 200, 300, and 600 s.

GIANO-B is equipped with two calibration lamps: an halogen lamp for flat-field and a U-Ne lamp for wavelength calibration. Most of the observations are performed with the nodding acquisition mode ABAB, where target and sky spectra are taken simultaneously while alternating between two nodding positions along the slit (A and B) separated by 5", allowing an optimal subtraction of the detector noise and thermal background. In Fig. 2.1, an example of two GIANO-B echellograms forming a nodding pair is shown. It is visible how, for each spectral order, the target trace switches position along the slit (and the detector) from position A to B, while the sky trace switches from position B to A.

GIANO-B has been the first spectrograph mounted on a $\sim$ 4-m class telescope to combine such broad spectral coverage with such high resolving power. In addition, the observing mode called GIARPS (Claudi et al., 2017) is possible. In this observing mode, GIANO-B can operate simultaneously with HARPS-N (an high-resolution optical spectrograph mounted at the TNG, with $R = 115\,000$) to achieve high-resolution spectroscopy over the full visual and near-infrared range ($0.383 - 2.45\,\mu$m, with a small gap between $0.70 - 0.92\,\mu$m) in a single exposure. The two spectrographs are still able to work separately, so it is possible to have three different configurations: GIANO–B only, HARPS-N only, and GIARPS by splitting the light between the two instruments with a dichroic.

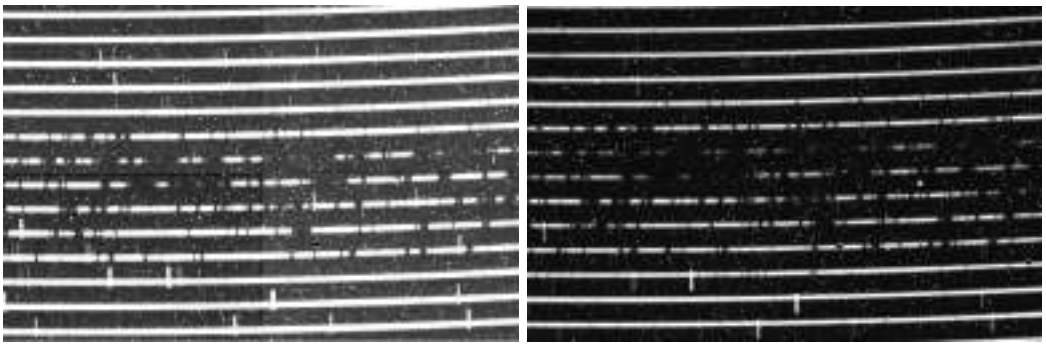

Figure 2.1: Example of two GIANO-B echellograms (zoomed view) forming a nodding pair. Left panel: the target is in nodding position A and the sky in the nodding position B. Right panel: the target is in nodding position B and the sky in the nodding position A. For each spectral order the two sources spectra (i.e. white for the target and dark for the sky) are visible. Dark regions of the spectra correspond to telluric absorption lines, while bright vertical lines correspond to sky emission lines. By looking at the sky emission (that fills the whole slit), it is clearly visible how the spectra of the two sources switch position on the slit and, thus, on the detector, between the two frames.

2.2 GIANO-B data reduction procedure

For my Ph.D. work, GIANO-B raw spectra were extracted and calibrated using the GOFIO pipeline Python 3 version (Rainer et al., 2018), a pipeline expressly developed to reduce GIANO-B spectra. In particular, GOFIO allows the application of dark subtraction and flat-field correction to the spectra. For the analyses reported in this thesis, the flat-field correction has not been performed. This strategy has been chosen because the flat-field calibration corrected both the detector inhomogeneities and the spectral blaze function. Since we noted that the blaze function correction for low-S/N spectra usually increased the noise of the spectra, we decided not to apply this procedure. GOFIO also performs a preliminary wavelength calibration using U-Ne lamp spectra as a template. In this way, for each spectral order, GOFIO produces a 2D matrix made of the wavelength-calibrated spectra as a function of time.

In order to study exoplanet atmospheres through high-resolution spectroscopy technique, after these initial steps, a correction for the mechanical instability of the GIANO-B instrument was necessary. Indeed, U-Ne lamp spectra are only acquired at the end of the observing night to avoid the persistence effect on the detector, but the mechanical instability of the instrument causes the wavelength solution to change during the observations. This means that the wavelength solution of the spectra determined by GOFIO is not sufficiently accurate for our analysis and is expected to

shift and jitter between consecutive exposures.
In order to correct this shift, a custom-made Interactive Data Language[1] (IDL) pipeline was used. In particular, after the data extraction with GOFIO, the spectra were aligned to a common reference frame via cross-correlation with a time-averaged observed spectrum of the target used as a template. After this procedure, it was possible to reach a residual spectral shift of $\leq 0.3\,\mathrm{km\,s^{-1}}$ for most of the spectral orders.

As a subsequent step of the reduction process, a refined wavelength calibration of the spectra was performed. In order to refine the wavelength solution provided by GOFIO, the wavelength position of telluric lines was used. Indeed, the telluric spectrum provides a good wavelength-calibration source, since the lines' position does not change with time and the lines' wavelength is well known. Refined wavelength calibration was made by matching a set of telluric lines in the time-averaged observed spectrum with a high-resolution model of the Earth transmission spectrum generated via the ESO Sky Model Calculator (Noll et al., 2012), and solving for the pixel-wavelength relation with a fourth-order polynomial fit. In Fig. 2.2, an example of this wavelength calibration is shown.

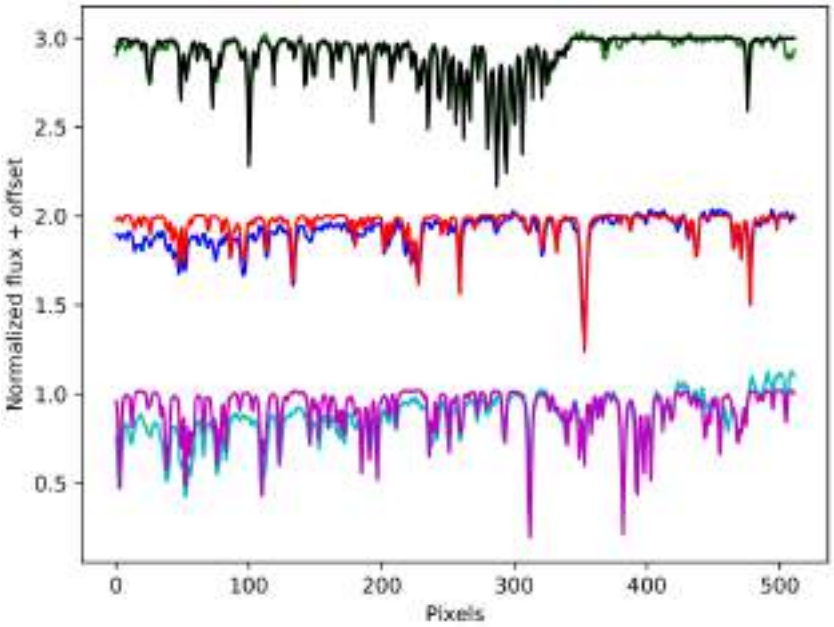

Figure 2.2: Example of wavelength calibration for 3 portions of the order 1. It is visible how the ESO model (black, red and purple lines) has been matched with the observed telluric spectrum (green, blue and cyan lines, respectively), in order to find the refined pixel-wavelength relation.

An important step of the data reduction procedure, is the telluric removal. In the works reported in this thesis, a principal component analysis (PCA) was performed to this aim (see Sect. 1.4.3). The PCA aim is to identify common trends between different wavelength channels in the spectra as a function of time (represented by the stationary telluric lines or quasi-stationary stellar lines) to correct them.
The PCA was applied to each spectral order, considered as an MxN data matrix (with M = number of spectra and $N = 2048$ pixels). Before computing the principal components, for each order, the standardisation described in the following was applied.
First, each spectrum was normalised to its median value to correct baseline flux variations. Then,

[1] `https://www.nv5geospatialsoftware.com/Products/IDL`

the spectral channels with stronger or saturated telluric lines were masked in the following way: the time-averaged spectrum was subtracted to all the spectra, the standard deviation of data in each spectral channel and its median value ($\sigma_{\rm m}$) were computed, and then the spectral channels that had a standard deviation $\sigma > 1.5 \cdot \sigma_{\rm m}$ were masked. After having subtracted the time-averaged spectrum from all the spectra and masking highly contaminated spectral channels, data were reduced to a null-mean variable by subtracting to each spectrum its mean value computed on the different spectral channels.
Then, the principal components were computed using the PYDL.PCOMP[2] routine. The matrix that should mainly describe the telluric and stellar contaminations was built via a linear combination of a set of principal components and removed from the original data matrix, obtaining a residual matrix. Finally, a high-pass filter was applied to each row of the residual matrix to remove any possible residual correlation between different spectral channels.
In this way, for each spectral order, a telluric-corrected residual matrix ready for the cross-correlation analysis was obtained. An illustration of the telluric removal process applied to real GIANO-B spectra is reported in the next chapter (Fig. 3.7).

[2] `https://pydl.readthedocs.io/en/latest/api/pydl.pcomp.html`

Chapter 3

Multiple molecular species in the atmosphere of HAT-P-11 b and review of the HAT-P-11 planetary system

In this chapter, I present the work published in Basilicata et al. (2024a), where we review the physical and architectural properties of the HAT-P-11 planetary system and investigate the atmospheric composition of the warm Neptune HAT-P-11 b with GIANO-B.

The atmospheric characterisation of hot and warm Neptune-size exoplanets is challenging mainly due to their relatively small radius and atmospheric scale height, which reduce the amplitude of atmospheric spectral features. The warm-Neptune HAT-P-11 b is a remarkable target for atmospheric characterisation because of the large brightness of its host star ($V = 9.46\,\mathrm{mag}$; $H = 7.13\,\mathrm{mag}$). The aims of this work are to review the main physical and architectural properties of the HAT-P-11 planetary system, and to probe the presence of eight molecular species in the atmosphere of HAT-P-11 b through near-infrared (NIR) high-resolution transmission spectroscopy. We reviewed the physical and architectural properties of the HAT-P-11 planetary system by analysing transits and occultations of HAT-P-11 b from the *Kepler* data set as well as HIRES at Keck archival radial-velocity data. We modelled the latter with Gaussian-process regression and a combined quasi-periodic and squared-exponential kernel to account for stellar variations on both (short-term) rotation and (long-term) activity-cycle timescales. In order to probe the atmospheric composition of HAT-P-11 b, we observed four transits of this target with the NIR GIANO-B at TNG spectrograph and cross-correlated the data with template atmospheric transmission spectra. For HAT-P-11 b, we measure a radius of $R_\mathrm{p} = 0.4466 \pm 0.0059\,R_\mathrm{J}$, a mass of $M_\mathrm{p} = 0.0787 \pm 0.0048\,M_\mathrm{J}$, a bulk density of $\rho_\mathrm{p} = 1.172 \pm 0.085\,\mathrm{g\,cm^{-3}}$, and an orbital eccentricity of $e = 0.2577^{+0.0033}_{-0.0025}$. These values are compatible with those from the literature. Probing its atmosphere, we detect the presence of H_2O (with an S/N of 5.1 and a significance of $3.4\,\sigma$), confirming the low-resolution detection, and we detect NH_3 (with an S/N of 5.3 and a significance of $5.0\,\sigma$), for the first time in the atmosphere of a warm Neptune. We also tentatively detect the presence of CO_2 and CH_4, with an S/N of 3.0 and 4.8, and a significance of 3.2 σ and 2.6 σ, respectively.

3.1 Introduction

The majority of known exoplanets have orbital and physical characteristics that are different from those of the Solar System planets. This is the case, for example, for hot and warm Neptunes, which are planets with a mass similar to that of Neptune and with equilibrium temperatures of $T_{\rm eq} \gtrsim 1000\,{\rm K}$ and $T_{\rm eq} \lesssim 1000\,{\rm K}$, respectively. The existence of such planets so close to their host stars (orbital periods $P_{\rm orb} \lesssim 10\,{\rm days}$) provides a unique opportunity to study atmospheric physical and chemical conditions that cannot be studied in the Solar System.

The study of exoplanetary atmospheres makes a crucial contribution to the exoplanet characterisation process. For example, by knowing the chemical composition of the primary atmosphere of an exoplanet, it is possible to constrain its formation and evolution path based on the study of relative elemental abundances (e.g. Öberg et al. 2011, Madhusudhan et al. 2017, Madhusudhan 2019, Banzatti et al. 2020, Bitsch et al. 2022, Pacetti et al. 2022).

By studying exoplanetary atmospheres in the near-infrared (NIR), it is possible to probe deep layers (down to pressures $P \approx 0.1\,{\rm bar}$) where molecular species dominate the atmospheric composition and absorb the IR light through thousands of rotational-vibrational transitions. Over the past few years, the large number of transiting exoplanet discoveries and the possibility to use space instruments have made low-resolution spectroscopy (LRS) the most used technique for exoplanetary atmospheric characterisation (Madhusudhan, 2019); in particular, for probing the terminator region of planetary atmospheres via the transmission-spectroscopy technique. This method is based on measuring how the planetary effective radius varies with wavelengths during transit because of the absorption of the stellar light by the chemical species present in the atmosphere of the target.

An alternative technique for probing exoplanetary atmospheres using high spectral-resolution instruments is high-resolution spectroscopy (HRS) from ground-based observatories (see Birkby 2018 for a review). For what concerns the NIR studies, different molecular species have been identified in the atmosphere of hot Jupiters with the HRS technique, such as CO (Snellen et al., 2010), H_2O (Birkby et al., 2013), TiO (Nugroho et al., 2017), HCN (Hawker et al., 2018), CH_4 (Guilluy et al., 2019), NH_3 and C_2H_2 (Giacobbe et al., 2021), and OH (Nugroho et al., 2021). Having improved the data analysis approach (e.g. employing the principal component analysis to remove the telluric and stellar contaminations and performing an optimal selection of the spectral orders), it is now possible to simultaneously detect multiple molecular species in the atmospheres of both hot and warm giant planets (e.g. Carleo et al. 2022, Giacobbe et al. 2021, Guilluy et al. 2022).

With respect to LRS, HRS is more sensitive to line position than depth, allowing a self-calibration of data, and has the advantage of combining the signal of thousands of spectrally resolved absorption or emission lines rather than bands from a chemical species. On the other hand, LRS can take advantage of the two space telescopes currently in operation (HST and JWST), which allow observers to avoid telluric contamination. A future combination of these two complementary techniques will improve the amount of information that can be inferred about the physics and chemistry of exoplanetary atmospheres (Brogi and Line, 2019a).

The ideal targets for atmospheric studies are close-in giant exoplanets given the higher planet–star radius and flux contrast. In the case of Neptune-size planets, the relatively small radius and the smaller atmospheric scale height combined with the possible presence of clouds or hazes reduce the expected amplitude of the atmospheric absorption, making the atmospheric characterisation

of these targets more difficult. Indeed, there are only a few works in the literature reporting the detection of molecular species in the atmosphere of warm and hot-Neptunes (i.e. A-thano et al. 2023, Benneke et al. 2019, Bézard et al. 2022, Brande et al. 2022, Fraine et al. 2014, Kreidberg et al. 2020, Mikal-Evans et al. 2023), and most of them report the detection of water vapour obtained with LRS using data from *HST/WFC3* (A-thano et al. 2023 also report the presence of titanium oxide on HAT-P-26 b, while Bézard et al. 2022 only report the presence of methane on K2-18 b).

A remarkable target for atmospheric studies is HAT-P-11 b, a warm Neptune-size exoplanet (the first of this class of planets discovered with transit searches) orbiting a K4 V-class star (Bakos et al., 2010). Fraine et al. (2014), Tsiaras et al. (2018), Chachan et al. (2019), and Cubillos et al. (2022) detected the presence of water vapour in its atmosphere at low resolution by analysing transmission spectra from HST. With the same data, Welbanks et al. (2019) estimated an abundance of $\log(X_{\mathrm{H_2O}}) = -3.66^{+0.83}_{-0.57}$. The analyses presented by Chachan et al. (2019) (*HST/WFC3+STIS*) and by Cubillos et al. (2022) (*HST/WFC3*) also suggest the presence of methane; however, when also considering the *Spitzer* observations, both these analyses found no evidence for the presence of this molecule due to an offset between the *Spitzer* and HST transit depths. The detection of atmospheric absorption in the He metastable 1083 nm triplet during transit (Allart et al., 2018, Mansfield et al., 2018) also provided complementary constraints on the size of the planet's upper atmosphere (extending beyond two planetary radii) and the corresponding mass-loss rate (the planet has only lost up to a few percent of its mass over its history, leaving its bulk composition largely unaffected). Due to the large brightness of its host star ($H = 7.131 \pm 0.021$ mag, Cutri et al. 2003) and the presence of already detected chemical species (i.e. He and H_2O) in its atmosphere, this target provides a great opportunity to characterise the atmosphere of warm Neptunes. In addition, the orbit of HAT-P-11 b is eccentric and Sanchis-Ojeda and Winn (2011) estimated a high obliquity angle ($\psi = 106^{+15}_{-12}$ deg) between the orbital plane of the planet and the equatorial plane of its host star, indicating a quasi-polar orbit. This planet therefore offers a rare occasion to explore complex planetary evolution paths, such as the one that led to its current orbital configuration.

To study the atmosphere of the planet HAT-P-11 b at high spectral resolution, precise and accurate knowledge of its orbit (in particular the eccentricity e and the planetary argument of periastron ω_{p}) is mandatory. Multiple analyses of the orbital parameters of HAT-P-11 b can be found in the literature (i.e. Allart et al. 2018, Bakos et al. 2010, Huber et al. 2017, Knutson et al. 2014a, Southworth 2011, Yee et al. 2018). The most recent is that of Yee et al. (2018), which is based on the analysis of the radial-velocity (RV) data of HAT-P-11. In particular, these authors obtained the following values for the eccentricity and the planetary argument of periastron: $e = 0.218^{+0.034}_{-0.031}$; $\omega_{\mathrm{p}} = 199^{+14}_{-16}$ deg. The most precise estimation of the orbital parameters was reported by Huber et al. (2017). These latter authors simultaneously modelled the planetary transits and secondary eclipses in the *Kepler* data, obtaining the following values: $e = 0.26459^{+0.00069}_{-0.00048}$; $\omega_{\mathrm{p}} = 197.774^{+0.203}_{-0.094}$ deg. Although these two sets of estimations are compatible with each other at the $2\,\sigma$ level, mainly due to the large uncertainty on the values by Yee et al. (2018), it is important to note that the two values of e differ by about 0.05, with the analysis of Huber et al. (2017) pointing towards a higher value of the eccentricity. Even such a small inaccuracy on the value of e still produces an RV shift of roughly $\approx 10\,\mathrm{km\,s^{-1}}$ (larger than the GIANO-B spectral resolution of $6\,\mathrm{km\,s^{-1}}$) during the transit, with severe impacts on the atmospheric characterisation using the HRS method. To improve the accuracy of the orbital solution, we decided to determine the HAT-P-11 b orbital parameters

through independent analysis of both the *Kepler* photometric data and the RV measurements. Moreover, by doing so, we reviewed the physical parameters of HAT-P-11 b and the architecture of the HAT-P-11 planetary system. All the details of this preliminary analysis are described in the following subsections. The main parameters of the HAT-P-11 planetary system are summarised in Table 3.1[1].

In this work, we report a review of the physical and architectural properties of the HAT-P-11 planetary system and the results of the study of four transit events of HAT-P-11 b recorded with GIANO-B, the high-resolution NIR échelle spectrograph mounted at the 3.58 m Telescopio Nazionale Galileo (TNG), in order to probe the presence of eight molecular species in its atmosphere with the transmission HRS as part of the Global Architecture of Planetary Systems (GAPS) Project[2] and in particular as part of the exoplanetary atmospheres characterisation subprogramme, described in Guilluy et al. (2022).

In Sect. 3.2 we review the HAT-P-11 planetary system; in Sect. 3.3 we describe the high-resolution transit observations and data analysis process in detail, and discuss the results of the atmospheric characterisation. Finally, our conclusions and future perspectives are reported in Sect. 3.4.

3.2 Revisitation of the HAT-P-11 planetary system

3.2.1 *Kepler* light-curve data analysis

We downloaded the *Kepler* (wavelength range: $420 - 900$ nm) light curves of HAT-P-11 b from the Mikulski Archive for Space Telescopes (MAST[3]). These consist of short-cadence (60 s) light curves from 14 quarters out of the total 17 observed from 2 May 2009 to 11 May 2013. The short-cadence light curves of each quarter are subdivided into tranches of three except for quarters 0 and 1 with a single and quarter 17 with two light curves. This results in a total of 37 separate light curves to be analysed independently.

Transits and occultations

We trimmed the *Kepler* light curves around the transits and occultations, whose central times are predicted using the ephemeris of Huber et al. (2017). The width of each time interval is equal to three times the transit duration T_{14} and is large enough to include the time of the eclipses for both the orbital solutions discussed above. We discard all the transits and occultations that, due to gaps in the *Kepler* light curve, do not cover the whole time interval of $3\,T_{14}$.

Many transits of HAT-P-11 b show clear signs of starspot crossings (see, e.g. Béky et al. 2014, Morris et al. 2017b, Sanchis-Ojeda and Winn 2011, Scandariato et al. 2017, for a detailed analysis of the transit anomalies of HAT-P-11 b), which may bias the fit of the light curve. For this reason, we

[1]The symbols of the parameters listed in the table have the following meanings: $M_\star$ - stellar mass; $R_\star$ - stellar radius; $T_{\rm eff}$ - stellar effective temperature; [Fe/H] - stellar metallicity; $\log g$ - logarithm of stellar surface gravity; $V_{\rm sys}$ - systemic radial velocity; H - apparent magnitude in the photometric H band; $M_{\rm p}$ - planetary mass; $R_{\rm p}$ - planetary radius; $\rho_{\rm p}$ - planetary mean density; $T_{\rm eq}$ - planetary equilibrium temperature computed at the planet-to-star distance during the secondary eclipse, assuming an inefficient (full) heat re-distribution for the derived geometrical albedo ($A_{\rm g} = 0.440^{+0.044}_{-0.049}$); $P_{\rm orb}$ - orbital period; T_0 - transit epoch; T_{14} - transit duration; i - orbital inclination; e - orbital eccentricity; $\omega_{\rm p}$ - planetary argument of periastron; a - orbital semi-major axis; $K_{\rm p}$ - planetary radial-velocity semi-amplitude.

[2]`https://theglobalarchitectureofplanetarysystems.wordpress.com/`

[3]`https://archive.stsci.edu/missions-and-data/kepler`

Table 3.1: Main physical and orbital parameters of the HAT-P-11 system.

Parameter	Value	Reference
Stellar Parameters		
Spectral Class	K4 V	Bakos et al. (2010)
$M_\star$ [$M_\odot$]	0.86 ± 0.06	Lundkvist et al. (2016)
$R_\star$ [$R_\odot$]	0.76 ± 0.01	Lundkvist et al. (2016)
$T_{\rm eff}$ [K]	4780 ± 50	Bakos et al. (2010)
[Fe/H] [dex]	0.31 ± 0.05	Bakos et al. (2010)
$\log g$ [$\log_{10}$, cgs]	$4.563^{+0.092}_{-0.080}$	Stassun et al. (2019)
$V_{\rm sys}$ [km s^{-1}]	-63.24 ± 0.26	Gaia Collaboration et al. (2018)
Distance [ly]	123.17 ± 0.11	Gaia Collaboration et al. (2018)
Age [Gyr]	$6.5^{+5.9}_{-4.1}$	Lundkvist et al. (2016)
H	7.131 ± 0.021	Cutri et al. (2003)
Planetary Parameters		
$M_{\rm p}$ [$M_{\rm J}$]	0.0787 ± 0.0048	This work
$R_{\rm p}$ [$R_{\rm J}$]	0.4466 ± 0.0059	This work
$M_{\rm p}$ [$M_\oplus$]	25.0 ± 1.5	This work
$R_{\rm p}$ [$R_\oplus$]	4.901 ± 0.065	This work
$\rho_{\rm p}$ [g cm^{-3}]	1.172 ± 0.085	This work
$T_{\rm eq}$ [K]	847^{+46}_{-54} (663^{+36}_{-42})	This work
$P_{\rm orb}$ [days]	$4.887802443 \pm 0.000000034$	Huber et al. (2017)
T_0 [BJD$_{\rm TDB}$]	$2\,454\,957.8132067 \pm 0.0000053$	Huber et al. (2017)
T_{14} [hr]	$2.35562^{+0.00093}_{-0.00094}$	This work
i [deg]	89.027 ± 0.068	This work
e	$0.2577^{+0.0033}_{-0.0025}$	This work
$\omega_{\rm p}$ [deg]	$192.0^{+2.9}_{-3.0}$	This work
a [au]	0.0532 ± 0.0010	This work
$K_{\rm p}$ [km s^{-1}]	123.4 ± 9.9	This work

adopted an iterative approach aimed at selecting the transits with minimum evidence of anomalies. Using the orbital period derived by Huber et al. (2017), we phase-folded the planetary transits and we processed the phase-folded data using a running median average. The width of the running

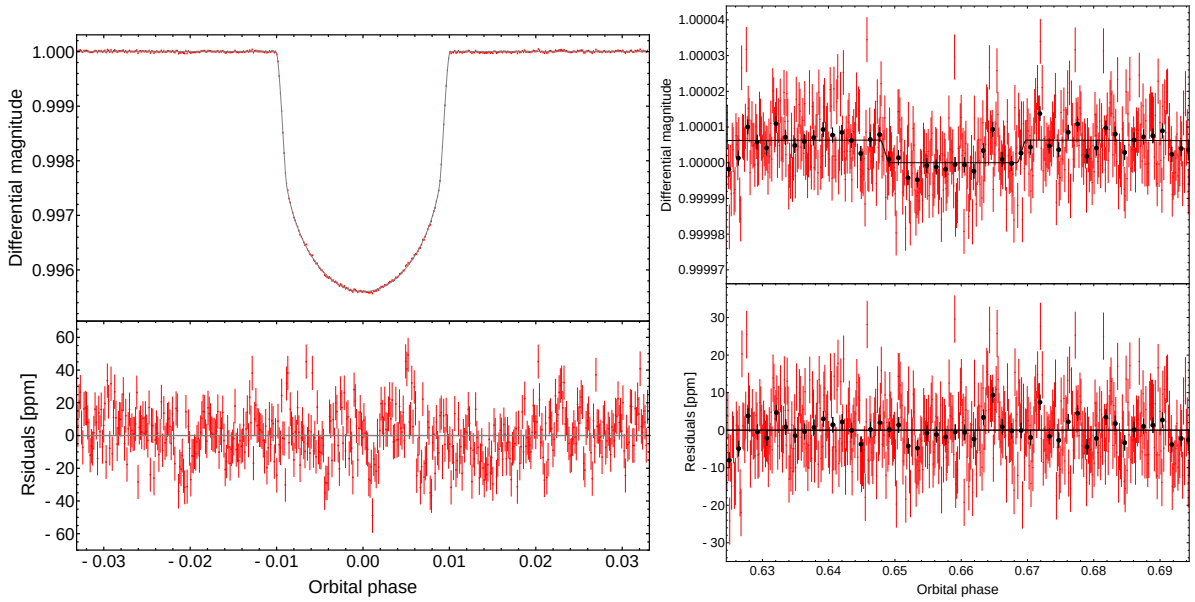

Figure 3.1: Transit and occultation light curve analyses. Top-left panel: Phase-folded *Kepler* transit light curve of HAT-P-11 b binned by 1 minute, based on 64 bona fide transits (see text). Our best-fitting model of the transit in the Kepler bandpass is overplotted in grey. Bottom-left panel: Residuals of the fit of the transit. Top-right panel: Phase-folded *Kepler* occultation light curve of HAT-P-11 b binned by 1 minute, based on 196 occultations (see text). Our best-fitting model of the occultation in the Kepler bandpass is overplotted with a black solid line. The data have been binned for clarity (black dots with error bars). Bottom-right panel: Residuals of the fit of the occultation.

window was 15 s, which is less than the cadence of the light curves. This guarantees that the averaged transit profile is negligibly time-smoothed by our approach.

Once the average transit profile was obtained, we computed the Median Absolute Deviation (MAD) of the data with respect to it. We then rejected all the transits with at least one data point located more than 6 MAD above the averaged transit profile. We iteratively repeated this process until no additional transit was rejected. At the end of this process, we noticed that a few transits passed our selection despite showing correlated noise due to either bad data detrending or stellar activity. We therefore refined the selection of the transits in the following way. For each transit, we first computed the residuals with respect to the averaged profile. Then, we associated each transit with the standard deviation of the corresponding residuals. Finally, we rejected the 10% transits with the largest standard deviations. This produced a final list of 64 bona fide transits free from anomalies above the noise level. Of course, the possible presence of non-crossed starspots can influence the stellar flux level and therefore the measured transit depth; however, this effect mainly affects the value of the planetary radius (with an over-estimation of $\approx 1\,\%$[4]) rather than the orbital parameters and is therefore negligible for the main scope of this work.

For the occultations, we adopted a similar approach. The only difference is that we do not expect anomalies during the eclipses, and therefore the first iterative selection of "unspotted" light curves is skipped. The final selection is made up of 196 occultations.

In summary, the dataset that we used to fit the orbit of the planet is composed of two subsets of data, centred on the transits and occultations respectively. To save computation time, we fit the phase-folded and rebinned data (1 min). The timestamps of the rebinned light curve were defined so

[4]This value is computed using Eq. (12) in Ballerini et al. (2012) with a maximum out-of-transit HAT-P-11 flux modulation of 2% (see the top panel of Fig. 1 in Béky et al. 2014).

that the time of transit provided by Huber et al. (2017) corresponds to the origin of the time axis.

The transit profile was modelled with the quadratic limb darkening (LD) law provided by Mandel and Agol (2002), with the reparametrisation of the coefficients proposed by Kipping (2013). Similarly, the occultation profile was modelled following Mandel and Agol (2002), but assuming that the planetary dayside is uniformly bright (Scandariato et al., 2022, Singh et al., 2022). Since we have operated a different data rejection with respect to Huber et al. (2017), we re-derived all the orbital parameters except for the orbital period, which we fixed to the best estimate of Huber et al. (2017) to phase-fold the data. The free parameters of the model are the stellar density $\rho_\star$, the time of transit T_0, the planet-to-star radius ratio $R_\mathrm{p}/R_\star$, the impact parameter b, the LD coefficients q_1 and q_2, the $e_\mathrm{c} = e\cos\omega_\star$ and $e_\mathrm{s} = e\sin\omega_\star$ parameters (where e and $\omega_\star$ are the orbital eccentricity and the stellar argument of periastron, respectively) and the occultation depth δ_ecl.

In the model, we also included a jitter term and a renormalisation coefficient independently for the transit and eclipse subcurves. The two jitter terms take into account the fact that the two subcurves have different noise properties, being the combination of a different number of transits/eclipses. The renormalisation coefficients fix the preliminary normalisation of the transit and eclipse subcurves computed by the extraction pipeline.

We adopted a maximum-likelihood Bayesian approach where the data were fitted by running a Monte Carlo sampling of the parameter space. The parameter space was defined by the priors listed in Table 3.2. We remark that we have used uniform priors for all the parameters. The priors on e_c and e_s have been conveniently set to span a large range around the expected values and include both the orbital solutions of Huber et al. (2017) and Yee et al. (2018), while saving computation time.

For the log-likelihood maximisation, we first searched the parameter space for the global maximum position using the python package `PyDE`[5]. Afterwards, we sampled the posterior probability distribution of the model parameters using the `emcee` package version 3.1.3 (Foreman-Mackey et al., 2013). Given the demand for resources for the model fitting, we ran the code in the HOTCAT computing infrastructure (Bertocco et al., 2020, Taffoni et al., 2020). We let the chains run for 250 000 steps, long enough to ensure formal convergence. The best-fitting model of the light curve, together with the corresponding residuals, is shown separately in the left and right panels of Fig. 3.1, for the transit and the occultation, respectively. The list of the free parameters and their corresponding priors and best-fitting $1\,\sigma$ confidence interval is given in Table 3.2. Our estimates are consistent with previous analyses within 2σ.

Albedo and equilibrium temperature

The day-side flux of an exoplanet is a combination of reflected starlight off the planet's illuminated hemisphere and its thermal irradiation. The former is parameterised by the geometric albedo A_g while the latter is parameterised by the brightness temperature $T_\mathrm{d}(\Delta\lambda)$, which is a measure of the day-side temperature in a given wavelength interval $\Delta\lambda$ (Santerne et al., 2011, Singh et al., 2022). Consequently, the occultation depth can be expressed as the following:

$$\delta_\mathrm{ecl} = A_\mathrm{g}\left(\frac{R_\mathrm{p}}{d_\mathrm{sec}}\right)^2 + \pi\left(\frac{R_\mathrm{p}}{R_\star}\right)^2 \frac{\int_{\Delta\lambda} \frac{2hc^2}{\lambda^5}\left[\exp\left(\frac{hc}{k_\mathrm{B}\lambda T_\mathrm{d}}\right)-1\right]^{-1}\Omega_\lambda d\lambda}{\int_{\Delta\lambda} S_\lambda^\mathrm{CK}\Omega_\lambda d\lambda}\,, \tag{3.1}$$

[5] `https://github.com/hpparvi/PyDE`

Table 3.2: Model parameters for the fit of the *Kepler* data. *U* stands for a uniform prior.

Parameters	Symbol	Units	C.I.	Prior
Stellar density	$\rho_\star$	$\rho_\odot$	1.915±0.081	U(1.5,2.5)
Time of transit	T_0	days	$0.0000967^{+0.0000084}_{-0.0000082}$	U(-0.05,0.05)
Planet-to-star radius ratio	$R_\mathrm{p}/R_\star$	-	$0.058993^{+0.000065}_{-0.000070}$	U(0.05,0.07)
Impact parameter	b	-	$0.227^{+0.013}_{-0.015}$	U(0,0.6)
First LD coefficient	q_1	-	$0.4644^{+0.0062}_{-0.0063}$	U(0,1)
Second LD coefficient	q_2	-	$0.4813^{+0.0064}_{-0.0062}$	U(0,1)
	$\sqrt{2e}\cos\omega_\star$	-	$0.7021^{+0.0035}_{-0.0041}$	U(0.5,0.9)
	$\sqrt{2e}\sin\omega_\star$	-	0.150±0.037	U(0,0.5)
Secondary eclipse depth	δ_ecl	ppm	$6.95^{+0.66}_{-0.64}$	U(0,20)
Derived parameters	**Symbol**	**Units**	**C.I.**	
Planetary radius[a]	R_p	$\mathrm{R_J}$	0.4466 ± 0.0059	
Scaled semi-major axis	$a/R_\star$	-	$15.05^{+0.21}_{-0.22}$	
Orbital inclination	i	deg	89.027±0.068	
Transit duration	T_{14}	hr	$2.35562^{+0.00093}_{-0.00094}$	
Orbital eccentricity	e	-	$0.2577^{+0.0033}_{-0.0025}$	
Stellar argument of periastron	$\omega_\star$	degree	$12.0^{+2.9}_{-3.0}$	

Notes. [(a)] The uncertainty includes the uncertainty on the stellar radius.

where h is the Planck constant, k_B the Boltzmann constant, c the speed of light, d_sec the distance of the planet from the star during the secondary eclipse and S_λ^CK is the stellar Kurucz flux (Castelli and Kurucz, 2003) (computed for $T_\mathrm{eff} = 4750\,\mathrm{K}$, $\log g = 4.5$, and [Fe/H]= 0.2). Both the planetary and the stellar fluxes are integrated over the *Kepler* passband $\Delta\lambda$ with the corresponding response function Ω_λ.

For the derived occultation depth, the relationship between the geometric albedo and the brightness temperature is shown in Fig. 3.2. For HAT-P-11 b, the thermal contribution to the observed depth in optical passbands is practically negligible given the low temperature of its atmosphere. Therefore, the occultation depth is the result of a highly reflective atmosphere. We derive a geometric albedo of $A_\mathrm{g} = 0.440^{+0.044}_{-0.049}$ corresponding to the occultation depth of $\delta_\mathrm{ecl} = 6.95^{+0.66}_{-0.64}$ ppm reported in Table 3.2. We therefore confirm and improve the results obtained by Huber et al. (2017). Following Han et al. (2014), we assume that the geometric albedo and Bond albedo are related via $A_\mathrm{b} = \frac{3}{2}A_\mathrm{g}$. We use this A_b to estimate the planet's day-side equilibrium temperature[6] as a function of time

[6]We equate the optical brightness temperature with the planet's equilibrium temperature, which is reasonable if the planetary emission spectrum closely resembles a Planck distribution at temperature T_d.

following (Cowan and Agol, 2011):

$$T_{\rm d}(t) = T_{\rm eff}\sqrt{\frac{R_\star}{d(t)}}\,(1-A_{\rm b})^{\frac{1}{4}}\left(\frac{2}{3}-\frac{5}{12}\epsilon\right)^{\frac{1}{4}}, \tag{3.2}$$

where ϵ is the heat re-circulation efficiency and $d(t)$ the distance of the planet from the star as a function of the time (to take into account the eccentricity of the orbit).

We considered two extreme scenarios: one with inefficient ($\epsilon = 0$) and another with complete ($\epsilon = 1$) heat re-circulation. We report in the plot the equilibrium temperature estimates at the occultation position. As a result of the varying stellar irradiation, the temperature estimates at the periastron are: 970^{+52}_{-62} K and 759^{+41}_{-49} K for $\epsilon = 0$ and $\epsilon = 1$, respectively, and at the apoastron are 750^{+41}_{-47} K and 587^{+32}_{-37} K for $\epsilon = 0$ and $\epsilon = 1$, respectively. During the transit, the planet-to-star separation distance is $d_{\rm tr} = 13.33 \pm 0.26\,R_\star$ and therefore, the corresponding day-side temperatures are 894^{+48}_{-57} K and 699^{+38}_{-44} K assuming no changes in planetary albedo throughout the eccentric orbit. The pairs of $T_{\rm d}$ values we report represent the extremes of the range in which the planet's equilibrium temperature is expected to be at different planet positions along its orbit. At the transit position, we consider the scenario $\epsilon = 1$, that is, a uniform temperature distribution throughout the planet, so that we can use $T_{\rm eq} = 699^{+38}_{-44}$ K as the equilibrium temperature around the day-night terminator to build our atmospheric transmission spectrum models described in Sect. 3.3.3.

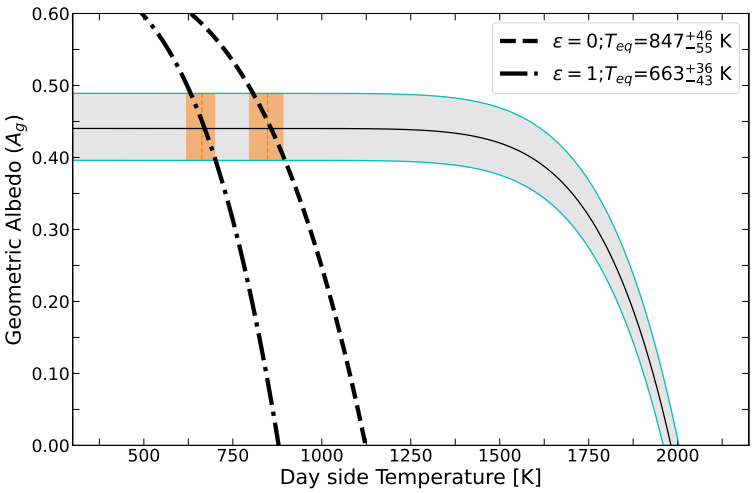

Figure 3.2: Geometric albedo ($A_{\rm g}$) estimated as a function of the day-side temperature for the measured occultation depth ($\delta_{\rm ecl} = 6.95^{+0.66}_{-0.64}$ ppm). The cyan lines represent the $1\,\sigma$ uncertainty curves. The dash-dotted and dashed lines represent the variation of $A_{\rm g}$ with varying $T_{\rm d}$ for the 2 heat re-circulation cases (ϵ) considered, computed at $d = d_{\rm sec} = 14.83 \pm 0.30\,R_\star$ (that is, during the occultation). The 2 orange shaded regions correspond to the intersection of the curves, identifying the average HAT-P-11 b day-side temperatures for the 2 extreme scenarios of ϵ, computed at $d = d_{\rm sec}$. These two values of the equilibrium temperature with the associated uncertainties are reported in the legend.

3.2.2 Radial-velocity data analysis

We also analysed 180 publicly available radial velocities of HAT-P-11 (median error on RV measurements: $1.33\,{\rm m\,s^{-1}}$), which were obtained with the HIRES at Keck spectrograph (possible RV instrumental drift of the order of a couple of ${\rm m\,s^{-1}}$ on years timescale) by Bakos et al. (2010) and Yee et al. (2018), after discarding the in-transit measurements to avoid the Rossiter-McLaughlin

effect (McLaughlin, 1924, Rossiter, 1924) and three outliers at the observing epochs 4334.9662, 4957.0433 and 7933.0122 $\mathrm{BJD_{TDB}} - 2450000$, which were identified in the residuals of our RV model (Sect. 3.2.2) through the Chauvenet's criterion (e.g. Bonomo et al. 2023).

Planet c or magnetic activity cycle?

The HIRES RVs show a clear long-term trend (Fig. 3.3, top panel), which was attributed by Yee et al. (2018) to a second planet companion, HAT-P-11 c, with $P_{\rm orb} \sim 3410$ d (9.3 yr), $M_{\rm p} \sin i \approx 1.6\,M_{\rm J}$, and $e \approx 0.6$, and, to a lesser extent, to the stellar magnetic activity cycle. Despite the very similar behaviour of the trend in both the S-index and the RVs (see Fig. 3.3), the stellar activity cycle was not deemed sufficient by Yee et al. (2018) to account for the RV variations in the long term for three main reasons (see their Sect. 3 for more details): (*i*) the large RV semi-amplitude (~ 30 $\mathrm{m\,s^{-1}}$) of the long-term signal compared to semi-amplitudes of $\lesssim 10\,\mathrm{m\,s^{-1}}$ observed by Lovis et al. (2011) for magnetic activity cycles in ~ 300 solar-type stars; (*ii*) the presence of a shift of ~ 500 days between the minimum of the S-index and that of the RVs (Fig. 3.3); and (*iii*) the relatively weak correlation between the S-index and RV measurements with a Pearson's coefficient of ~ 0.34.

In our view, these three motivations do not provide strong evidence that the long-term signal is planetary in origin. Indeed, concerning (*i*), HAT-P-11 is considerably more active than the stars in the sample studied by Lovis et al. (2011), with a $\log R^{'}_{\rm HK}$ of -4.35 (Morris et al., 2017a) higher than the typical $\log R^{'}_{\rm HK}$ of -4.8 – -5.0 of that stellar sample. Since one of those stars, namely HD 21693, shows a semi-amplitude of ~ 10 $\mathrm{m\,s^{-1}}$ for $\log R^{'}_{\rm HK} = -4.89$ (see Fig. 16 in Lovis et al. 2011), a semi-amplitude of ~ 30 $\mathrm{m\,s^{-1}}$ for the RV variation associated with the activity cycle is certainly possible for an unusually active star such as HAT-P-11 (Morris et al., 2017a).

Regarding (*ii*), detailed studies of the correlation between RV and S-index measurements by Meunier et al. (2019) (therefore subsequent to Yee et al. 2018) showed that a combination of geometrical effects (stellar inclinations and butterfly diagrams) and variations of magnetic activity level over time may easily produce hysteresis patterns, and hence temporal shifts of a few hundreds of days in the minima of the RV and S-index variations (see Fig. 8 in Meunier et al. 2019). For example, the minimum of the long-term RV variations of the above-mentioned star HD 21693, which are caused by the magnetic activity cycle, also leads the minimum of the $\log R^{'}_{\rm HK}$ variations by ~ 500 d, similarly to HAT-P-11 (Lovis et al., 2011, Meunier et al., 2019). Given the high inclination $i_\star = 100 \pm 2$ deg of the host star HAT-P-11 and a starspot latitudinal distribution similar to the solar butterfly diagrams, as unveiled from the occultations of starspots by HAT-P-11 b during transits (Morris et al., 2017b), the temporal difference in the minima of the RV and S-index variations could be due to the hysteresis patterns described by Meunier et al. (2019). After all, the fact that the magnetic activity cycle from the S-index was found to have the same periodicity as the hypothetical planet c (Morris et al., 2017a) remains suspicious.

Last but not least, even the absence of a strong correlation between the S-index and RV measurements does not necessarily lean towards the planetary origin of the RV long-term signal; this is because a relatively low correlation, at least partly, ensues from the temporal shift between the S-index and RV variations, while it is much higher in the first ~ 1000 d of observations (Knutson et al., 2014b). Since we observed HAT-P-11 in GIARPS mode, we extracted the HAT-P-11 RVs (median error on RV measurements: $1.24\,\mathrm{m\,s^{-1}}$) and activity indicators from the HARPS-N spectra (possible RV instrumental drift $< 1\,\mathrm{m\,s^{-1}}$ on years timescale) of the four transits of HAT-P-11 b to

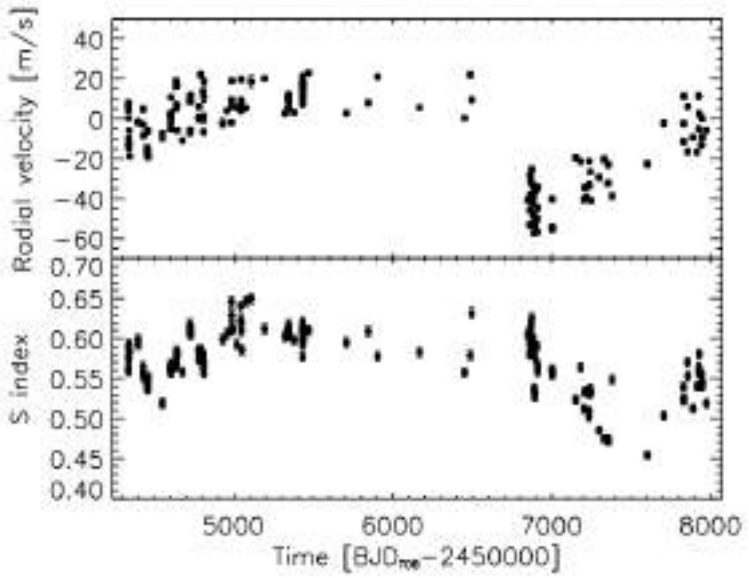

Figure 3.3: HIRES RV (top panel) and CaII S-index (bottom panel) measurements of HAT-P-11. The two-time series show almost identical long-term variations with a shift of ~ 500 days in the minimum.

look at their behaviour. For that purpose, we used the online v3.7 Data Reduction Software (DRS) and cross-correlated the HARPS-N spectra with a K5 V synthetic stellar template (Pepe et al., 2002). The S-index activity indicator is defined as the ratio between the sum of the fluxes of the CaII H & K line cores, at 3968.470 Å (H) and 3933.664 Å (K), and the sum of the fluxes of the continuum in two pass-bands centred at 3901.070 Å (V) and at 4001.070 Å (R): $S = \alpha \cdot \frac{H+K}{R+V}$, with $\alpha =$ a calibration constant (Lovis et al., 2011). It was computed with the v3.7 DRS as well, using the YABI interface with custom parameters (e.g. Borsa et al. 2015). The variations of the HARPS-N RVs, S-index and full width at half maximum (FWHM) of the cross-correlation function show an almost identical behaviour (Fig. 3.4): the Pearson's correlation coefficient is 0.94 between RVs and S-index, and 0.98 between RVs and FWHM. This suggests that the $\sim 9 - 10$ yr long-term RV signal is more likely due to the stellar activity cycle than to the long-period eccentric companion HAT-P-11 c. Moreover, if the RV measurements of the last transit night actually caught the minimum of the activity cycle, given that the HARPS-N RV peak-to-peak variation of ~ 60 m s^{-1} is the same as that observed by Yee et al. (2018), temporal shifts between the RV and S-index minima as caused by hysteresis phenomena may not have occurred in the current activity cycle.

Even though our data suggest that the magnetic activity cycle is the most plausible origin of the long-term RV signal, Hipparcos-Gaia absolute astrometry still provides hints that a long-period companion may actually exist. The catalogues of astrometric accelerations produced by Brandt (2018, 2021) and Kervella et al. (2019, 2022) indicate the presence of a proper motion anomaly (PMA) at the mean Gaia epoch, whose signal-to-noise ratio (S/N) grows from S/N$\simeq$ 2.1 to S/N$\simeq$ 4.7 and from S/N$\simeq$ 2.8 to S/N$\simeq$ 4.3 between the Gaia DR2 and Gaia EDR3 editions of the former and latter catalogue, respectively. Indeed, Xuan and Wyatt (2020) used the Hipparcos-Gaia DR2 PMA values in combination with the Bakos et al. (2010) RVs of HAT-P-11 to constrain the true mass and inclination of the putative companion HAT-P-11 c. Fig. 3.5 shows the Hipparcos-Gaia DR2 and DR3 PMA sensitivity curves based on Eq. (15) of Kervella et al. (2019), along with the minimum-mass value of HAT-P-11 c derived by Yee et al. (2018) and the best-fit true mass obtained

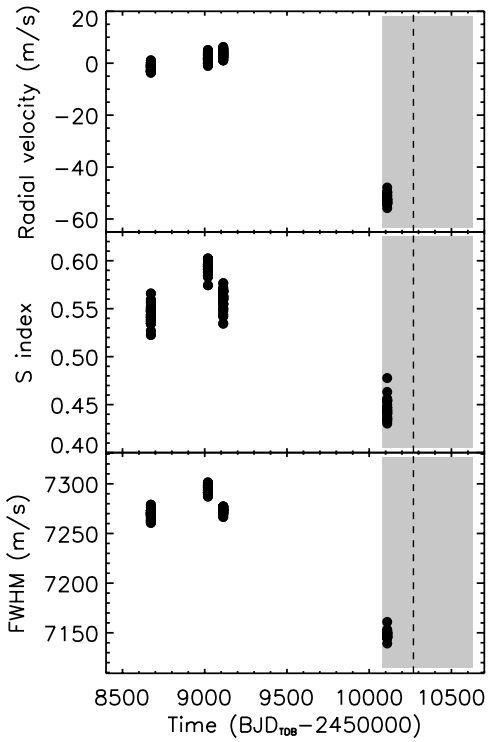

Figure 3.4: HARPS-N RV (top panel), CaII S-index (middle panel), and FWHM (bottom panel) measurements of HAT-P-11 during the four HAT-P-11 b transit nights for atmospheric characterisation. The three time series are highly correlated showing the same long-term trend, with no apparent shifts in the minima of variations. The vertical dashed line indicates the predicted periastron time of the hypothetical planet c, and the grey area shows its 1σ error bar accounting for the uncertainty on the orbital period from Yee et al. (2018). Note: the HARPS-N radial velocities were divided by their median of -63420.4 $\mathrm{m\,s^{-1}}$, to make a straightforward comparison with the HIRES radial velocities in Fig. 3.3.

by Xuan and Wyatt (2020). The Hipparcos-Gaia DR3 PMA sensitivity curve indicates that, at the orbital separation of HAT-P-11 c, a companion inducing a statistically significant PMA should have a mass of $\sim 3.5\ M_{\mathrm{Jup}}$. In the Xuan and Wyatt (2020) analysis, the true mass value of HAT-P-11 c falls below the PMA sensitivity curve, with a companion having true mass equal to the minimum mass from Yee et al. (2018) compatible at $\sim 1.4\,\sigma$. This is somewhat surprising as such a companion is not expected to produce a PMA with S/N$\gtrsim 3$. As the PMA technique heavily relies on the constraints from the RVs in order to successfully provide inferences on the mass and inclination of a companion, it is therefore possible that, if the long-term modulation in the RVs is actually dominated by the activity cycle, then HAT-P-11 c exists at larger separation and with a different mass than those inferred by Xuan and Wyatt (2020).

Radial-velocity modelling and improved mass determination for HAT-P-11 b

In the lack of strong evidence that the RV long-term trend is caused by the planet c with the orbital parameters given in Yee et al. (2018) for the reasons explained above, we modelled the HIRES RVs with a Keplerian orbit for the transiting planet HAT-P-11 b only, which has six free parameters: T_0, P_{orb}, e_c, e_s, the RV semi-amplitude, $K_\star$, and the RV zero point, γ.

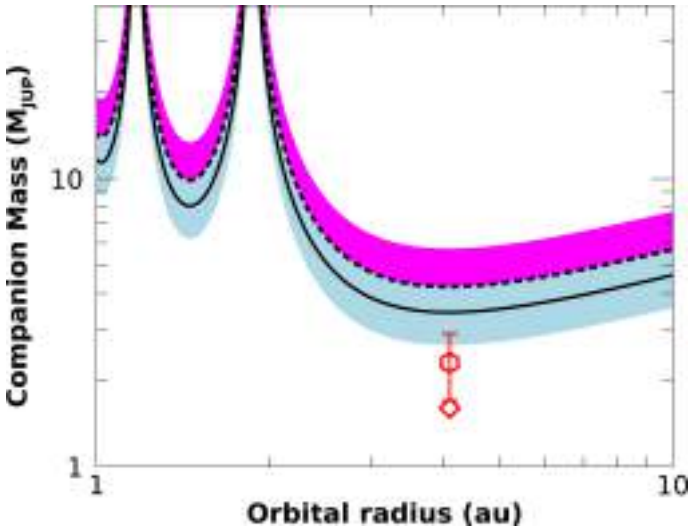

Figure 3.5: Sensitivity of the PMA technique to companions of given mass and orbital separation orbiting HAT-P-11. The black long-dashed and solid curves correspond to the combinations of mass and orbital radius explaining the PMA values at the mean Gaia DR2 and DR3 epochs, respectively. The shaded light blue region corresponds to the 1σ uncertainty domain of the DR3 PMA, while the shaded magenta region encompasses the 1 σ uncertainty of the DR2 PMA. The red diamond indicates the separation and minimum mass of the HAT-P-11 c companion proposed by Yee et al. (2018), while the red hexagon corresponds to the true mass value determined by the Xuan and Wyatt (2020) analysis.

To account for non-stationary stellar variations produced by magnetic activity phenomena, we used Gaussian-process (GP) regression (e.g. Grunblatt et al. 2015, Haywood 2015, Haywood et al. 2014) with three different kernels, namely the squared-exponential (SE) kernel:

$$k(t,t') = h^2 \cdot \exp\left[-\frac{(t-t')^2}{2\lambda^2}\right] + \left[\sigma_{\rm RV}^2(t) + \sigma_{\rm jit}^2\right] \cdot \delta_{t,t'}, \tag{3.3}$$

the quasi-periodic (QP) kernel

$$k(t,t') = h^2 \cdot \exp\left[-\frac{(t-t')^2}{2\lambda^2} - \frac{2\sin^2\left(\frac{\pi(t-t')}{P_{\rm rot}}\right)}{w^2}\right] + \left[\sigma_{\rm RV}^2(t) + \sigma_{\rm jit}^2\right] \cdot \delta_{\rm t,t'}, \tag{3.4}$$

and a third (QP-SE) kernel that is the sum of the QP and SE kernels in such a way as to simultaneously model the stellar activity variations on both short-term rotation timescales (Eq. 3.4) and long-term activity cycle timescales (Eq. 3.3), namely

$$\begin{aligned} k(t,t') = h_{\rm rot}^2 \cdot \exp\left[-\frac{(t-t')^2}{2\lambda_{\rm rot}^2} - \frac{2\sin^2\left(\frac{\pi(t-t')}{P_{\rm rot}}\right)}{w_{\rm rot}^2}\right] \\ + h_{\rm cycle}^2 \cdot \exp\left[-\frac{(t-t')^2}{2\lambda_{\rm cycle}^2}\right] + \left[\sigma_{\rm RV}^2(t) + \sigma_{\rm jit}^2\right] \cdot \delta_{\rm t,t'}, \end{aligned} \tag{3.5}$$

where t and t' are the epochs at two different RV observations, h is the semi-amplitude of the correlated noise, λ is the correlation decay timescale, $P_{\rm rot}$ is the period of the quasi-periodic variations, w is the inverse complexity harmonic parameter, $\sigma_{\rm RV}(t)$ is the formal uncertainty of the RV point

at time t, and $\sigma_{\rm jit}$ is the uncorrelated jitter term, which would absorb any extra white noise not modelled by either the Keplerian or the GP.

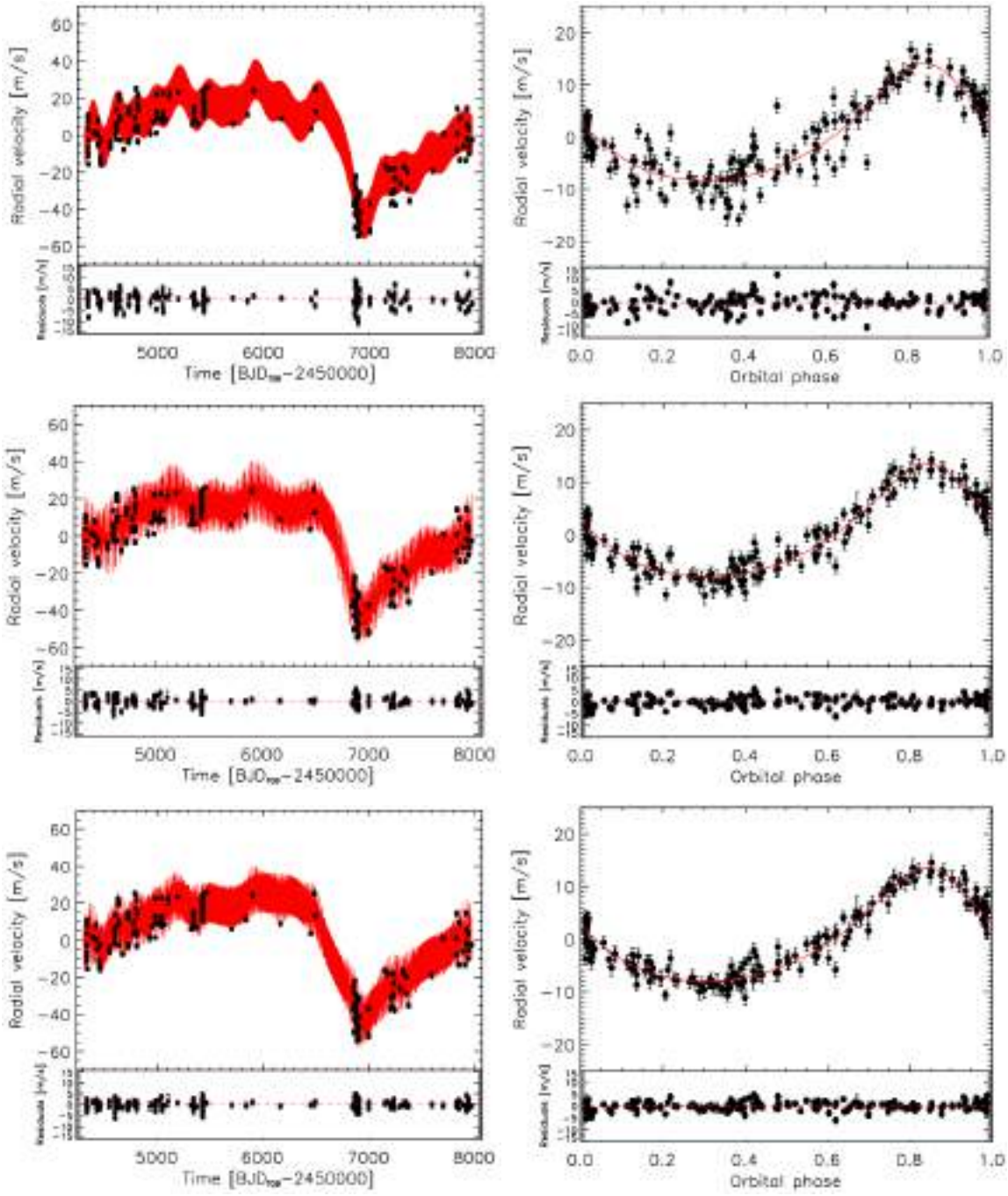

Figure 3.6: Radial-velocity data analysis. Left panels: HIRES radial velocities of HAT-P-11 (black circles) showing a clear long-term trend likely due to the stellar magnetic activity cycle. The best-fit models including both the Keplerian signal of HAT-P-11 b and Gaussian-process regression with squared-exponential (top; Eq. 3.3), quasi-periodic (middle; Eq. 3.4), and quasi-periodic+squared-exponential (bottom; Eq. 3.5) kernels are indicated with red solid lines. Right panels: HAT-P-11 RVs (black circles) phase-folded with the transit ephemeris of HAT-P-11 b, after removing the long-term trends modelled with Gaussian processes and the same kernels as in the corresponding left panels. The Keplerian eccentric model is displayed with a red solid line. We note the smaller and smaller scatter in the residuals as we move from top (SE kernel) to bottom (QP+SE kernel).

We employed Bayesian differential evolution Markov chain Monte Carlo (DE-MCMC; Bonomo

et al. 2015, Eastman et al. 2013, Ter Braak 2006) techniques to derive the posterior distributions of the model parameters, by using the same prescriptions for the number and convergence of the DE-MCMC chains given in Eastman et al. (2013) and Ford (2006). We imposed Gaussian priors on T_0 and $P_{\rm orb}$ from the *Kepler* transit ephemeris and uniform priors on $K_\star$ and γ as well as on the GP hyper-parameters h, λ, $P_{\rm rot}$, and w, with the boundaries specified in Table 3.3 for each GP kernel. As for the eccentricity and stellar argument of periastron, we ran two analyses per kernel: in the first one, we used uninformative priors on e and $\omega_\star$, while in the second one we adopted Gaussian priors from the results of the modelling of the optical secondary eclipse (Sect. 3.2.1). We took the medians and the 15.87%-84.14% quantiles of the posterior distributions as the values and $1\,\sigma$ uncertainties of the fitted and derived parameters.

In the first analysis with uniform priors on e and ω, we determined $e = 0.277 \pm 0.025$ and $\omega_\star = 26.8 \pm 8.6$ with the SE kernel, $e = 0.288 \pm 0.022$ and $\omega_\star = 27.9 \pm 7.0$ with the QP kernel, and $e = 0.290 \pm 0.021$ and $\omega_\star = 29.2 \pm 6.7$ with the QP-SE kernel. These are consistent with the e and ω values derived in Sect. 3.2.1 at $\lesssim 1.5\,\sigma$ and $\lesssim 2.3\,\sigma$, respectively. In the second analysis, we found $e = 0.2608 \pm 0.0086$ and $\omega_\star = 13.5 \pm 2.7$ deg with the SE kernel, $e = 0.2638 \pm 0.0090$ and $\omega_\star = 14.2 \pm 2.6$ deg with the QP kernel, and $e = 0.2654 \pm 0.0091$ and $\omega_\star = 14.7 \pm 2.6$ deg with the QP-SE kernel. These e and ω determinations are closer to the values from the secondary eclipse ($\sim 0.6\,\sigma$ and $\sim 0.8\,\sigma$, respectively) as expected from the use of the Gaussian priors on them. The radial-velocity semi-amplitude, $K_\star$, does not vary from the first to the second analysis for a given kernel, but was found to be slightly higher for the SE kernel, that is, $K_\star = 11.20 \pm 0.50\,{\rm m\,s^{-1}}$, to be compared to $K_\star = 10.75 \pm 0.41\,{\rm m\,s^{-1}}$ and $K_\star = 10.78 \pm 0.42\,{\rm m\,s^{-1}}$ for the QP and QP-SE kernels, respectively (see Table 3.3).

By using the Bayesian information criterion (BIC) as a proxy for the Bayesian evidence, we found that the model with the QP-SE kernel is the most favoured, while that with the SE kernel is highly disfavoured. We therefore adopted the orbital parameters of the former (QP-SE) model (Table 3.3), which has also a more physical rationale because the rotation and activity cycle signals were modelled with two different (QP and SE) kernels. On the other hand, the QP kernel had to adapt to fit the activity cycle long-term variation in addition to the rotational signal, with its hyper-parameters h and λ taking intermediate values between $h_{\rm rot}$ and $h_{\rm cycle}$, and $\lambda_{\rm rot}$ and $\lambda_{\rm cycle}$ in the third kernel (Eq. 3.5). We note that the GP models with both the QP and QP-SE kernels properly retrieved a stellar rotation period of $P_{\rm rot} \sim 32 - 33$ d, close to $P_{\rm rot} \sim 29 - 30$ d as estimated from the *Kepler* photometry, despite the large uniform prior adopted (see Table 3.3). We show the best-fit GP+Keplerian models as a function of time in the left panel of Fig. 3.6, and the Keplerian orbit due to HAT-P-11 b as a function of the orbital phase, after the removal of the GP activity model, in the right panel of the same figure.

For the rest of our analysis, we decided to use the orbital solution that we obtained from the analysis of transits and occultations due to the higher precision/accuracy in the determination of e and ω. We combined the stellar parameters, the transit parameters from the *Kepler* light curve (Sect. 3.2.1), and the RV parameters to derive a mass of $M_{\rm p} = 0.0787 \pm 0.0048\ M_{\rm J}$ ($M_{\rm p} = 25.0 \pm 1.5\,M_\oplus$) and a mean density of $\rho_{\rm p} = 1.172 \pm 0.085\,{\rm g\,cm^{-3}}$, for HAT-P-11 b. Finally, by knowing both the mass of the star and the planet, we computed the value of the planetary RV semi-amplitude $K_{\rm p}$, which we used for the atmospheric characterisation in Sect. 3.3. All the derived parameters of the HAT-P-11 planetary system are reported in Table 3.1.

Table 3.3: Parameters and adopted priors of the RV models with Gaussian processes and three different kernels (U and N stand for uniform and Gaussian priors, respectively).

Parameter	Symbol	Units	C.I.	Prior
Squared-exponential Gaussian process model [ΔBIC = 56.8]				
RV zero point	γ	$\mathrm{m\,s^{-1}}$	-3.2 ± 4.6	$U]-\infty,+\infty[$
RV jitter	$\sigma_{\rm jit}$	$\mathrm{m\,s^{-1}}$	3.29 ± 0.24	$U[0,+\infty[$
GP-SE amplitude	h	$\mathrm{m\,s^{-1}}$	$17.8^{+3.0}_{-2.4}$	$U[0,+\infty[$
GP-SE decay timescale	λ	days	$93.0^{+10.9}_{-9.9}$	$U[0,500]$
Eccentricity	e	-	0.2608 ± 0.0086	$N(0.258,0.004)$
Stellar argument of periastron	$\omega_\star$	deg	13.5 ± 2.7	$N(12,3)$
Radial-velocity semi-amplitude	$K_\star$	$\mathrm{m\,s^{-1}}$	11.20 ± 0.50	$U[0,+\infty[$
Quasi-periodic Gaussian process model [ΔBIC = 18.6]				
RV zero point	γ	$\mathrm{m\,s^{-1}}$	$-3.11^{+4.38}_{-4.51}$	$U]-\infty,+\infty[$
RV jitter	$\sigma_{\rm jit}$	$\mathrm{m\,s^{-1}}$	2.16 ± 0.24	$U[0,+\infty[$
GP amplitude	h	$\mathrm{m\,s^{-1}}$	$16.4^{+2.5}_{-2.0}$	$U[0,+\infty[$
GP decay timescale	λ	days	146^{+34}_{-45}	$U[0,500]$
GP rotational period	$P_{\rm rot}$	days	$32.73^{+0.27}_{-0.45}$	$U[25,40]$
GP harmonic inverse complexity	w		$1.87^{+0.40}_{-0.29}$	$U[0.1,5]$
Eccentricity	e	-	0.2638 ± 0.0090	$N(0.258,0.004)$
Stellar argument of periastron	$\omega_\star$	deg	14.2 ± 2.5	$N(12,3)$
Radial-velocity semi-amplitude	$K_\star$	$\mathrm{m\,s^{-1}}$	10.72 ± 0.43	$U[0,+\infty[$
Quasi-periodic+squared-exponential Gaussian process model [ΔBIC = 0]				
RV zero point	γ	$\mathrm{m\,s^{-1}}$	$-3.3^{+11.7}_{-12.1}$	$U]-\infty,+\infty[$
RV jitter	$\sigma_{\rm jit}$	$\mathrm{m\,s^{-1}}$	$1.94^{+0.21}_{-0.19}$	$U[0,+\infty[$
GP rotational amplitude	$h_{\rm rot}$	$\mathrm{m\,s^{-1}}$	$6.84^{+1.34}_{-1.12}$	$U[0,+\infty[$
GP rotational decay timescale	$\lambda_{\rm rot}$	days	$58.1^{+13.4}_{-11.9}$	$U[0,500]$
GP rotational period	$P_{\rm rot}$	days	$31.81^{+0.76}_{-0.82}$	$U[25,40]$
GP rotational harmonic inverse complexity	$w_{\rm rot}$		$1.09^{+0.26}_{-0.21}$	$U[0.1,5]$
GP cycle amplitude	$h_{\rm cycle}$	$\mathrm{m\,s^{-1}}$	$23.4^{+12.9}_{-6.6}$	$U[0,+\infty[$
GP cycle decay timescale	$\lambda_{\rm cycle}$	days	435^{+156}_{-119}	$U[0,1000]$
Eccentricity	e	-	0.2654 ± 0.0091	$N(0.258,0.004)$
Stellar argument of periastron	$\omega_\star$	deg	14.7 ± 2.6	$N(12,3)$
Radial-velocity semi-amplitude	$K_\star$	$\mathrm{m\,s^{-1}}$	10.78 ± 0.42	$U[0,+\infty[$

3.3 Atmospheric characterisation of HAT-P-11 b at high spectral resolution

3.3.1 Observations and data reduction

Four transits of HAT-P-11 b were simultaneously observed with the GIANO-B (wavelength range: $950 - 2450$ nm, spectral resolving power $R \approx 50\,000$) and the HARPS-N (wavelength range: $383 - 693$ nm, spectral resolving power $R \approx 115\,000$) high-resolution spectrographs in the GIARPS at TNG configuration (Claudi et al., 2017) during the following nights: 7 July 2019; 18 June 2020; 19 September 2020; 13 June 2023. We only used the NIR (GIANO-B) observations for the present work. A total of 240 spectra were collected during the four observing nights (60 during the first one, 60 during the second one, 58 during the third one, and 62 during the fourth one), each with an exposure time of 200 s. The observations were performed with the nodding acquisition mode ABAB, where target and sky spectra were taken in pairs while alternating between two nodding positions along the slit (A and B) separated by $5''$, allowing an optimal subtraction of the detector noise and background. All the observations were scheduled in order to obtain spectra before, during, and after the transit with airmass between 1 and 2. The measured mean signal-to-noise ratio (S/N) per spectrum, averaged across the entire spectral range and dataset, is between 48 and 59. In Table 3.4 a schematic log of the observations is reported.

GIANO-B spectra cover the Y, J, H, K spectral bands in 50 spectral orders. The raw spectra were dark-subtracted and extracted using the GOFIO pipeline Python 3 version (Rainer et al., 2018). Although GOFIO also performs a preliminary wavelength calibration using U-Ne lamp spectra as a template, the mechanical instability of the instrument causes the wavelength solution to change during the observations.

Table 3.4: Log of the GIANO-B observations of the four transits of HAT-P-11 b.[a]

Night	Airmass	$N_{\rm obs}$	$t_{\rm exp}$ [s]	$(\mathrm{S/N})_{\rm avg}$	$(\mathrm{S/N})_{\rm min}$ to $(\mathrm{S/N})_{\rm max}$
7 July 2019	$1.17 \rightarrow 1.06$	60	200	58	$12 - 115$
18 June 2020	$1.23 \rightarrow 1.06$	60	200	59	$9 - 110$
19 September 2020	$1.06 \rightarrow 1.23$	58	200	52	$2 - 100$
13 June 2023	$1.37 \rightarrow 1.09$	62	200	48	$2 - 101$

Notes. [(a)] From left to right we report: the date at the start of the observing night; the airmass during the planetary transit; the number of observed spectra $N_{\rm obs}$; the exposure time per spectrum $t_{\rm exp}$; the signal-to-noise ratio averaged across the whole spectral range $(\mathrm{S/N})_{\rm avg}$; the range of signal-to-noise ratios $(\mathrm{S/N})_{\rm min}$ to $(\mathrm{S/N})_{\rm max}$ in the individual spectral orders.

Since the U-Ne lamp spectrum is only acquired at the end of the observations to avoid persistence on the camera, the wavelength solution of the spectra determined by GOFIO is not sufficiently accurate and is expected to shift and jitter between consecutive exposures.
In order to correct this shift, the spectra have been aligned to a common reference frame via cross-correlation with a time-averaged observed spectrum of the target used as a template. Thanks to this correction, we achieved a residual scatter in the measured peak position of the cross-correlation function (i.e. a residual shift of the spectra) well below $0.3\,\mathrm{km\,s^{-1}}$ (approximately $1/10^{\rm th}$ of a pixel) for most of the spectral orders.

As these observations were performed from the ground, the spectra are contaminated by the

presence of telluric lines (i.e. absorption lines due to the chemical species present in the Earth's atmosphere). However, the telluric spectrum provides a good wavelength-calibration source, since the lines' position does not change with time and the lines' wavelength is well known. Refined wavelength calibration is made by matching a set of telluric lines in the time-averaged observed spectrum with a high-resolution model of the Earth transmission spectrum generated via the ESO Sky Model Calculator (Noll et al., 2012), and solving for the pixel-wavelength relation with a fourth-order polynomial fit. The spectral orders that showed either heavily saturated telluric lines or a high residual drift (> 0.4 pixels) have been excluded from the rest of the analysis. In particular, the excluded orders are: 8-10, 23, 24, 40-49 (in the GIANO-B spectra, order 0 is the reddest and order 49 is the bluest).

3.3.2 Orders' selection and telluric removal procedure

At this stage of the analysis, the planet spectrum is overshadowed by the stellar and telluric spectra. However, the planet's orbital velocity has a non-zero radial component during transit ($v_{\mathrm{p},\perp} \approx 10\,\mathrm{km\,s^{-1}}$); consequently, while telluric and stellar lines are stationary or quasi-stationary (the stellar barycentric radial velocity changes by few $\mathrm{m\,s^{-1}}$ during transit events) in wavelength, the planet spectrum experiences a detectable change in Doppler shift during the ~ 140 min of transit. This property can be used to disentangle the planetary signal from the stationary components that we have to remove.

Before removing these contaminating components, we performed an optimal selection of the spectral orders, for each molecular species we wanted to search for and for each night, to discard the orders that did not contain enough signal (i.e. molecular lines) and/or were strongly contaminated by telluric and stellar lines, following the method explained by Giacobbe et al. (2021). In particular, we injected single-species model planetary spectra at planetary radial velocity into the observations just before the telluric removal procedure. We then searched for these artificial signals and measured their significance order by order, by using the same procedure as for the detection of molecules (including the telluric removal procedure). The injected models were computed as those used for cross-correlation (see Sect. 3.3.3), except that they were amplified to be detectable at $> 3\,\sigma$ potentially in each order. Therefore, an order was selected if we were able to recover the injected signal in that order. In particular, an order was selected when the most significant signal was recovered within $\pm 3\,\mathrm{km\,s^{-1}}$ from the planetary rest-frame velocity and $\pm 30\,\mathrm{km\,s^{-1}}$ from the expected planetary radial-velocity semi-amplitude K_{p} (see Sect. 3.3.3) with a significance greater than $3\,\sigma$. The spectral orders selected for each molecular species, for each night, are reported in Table 3.5.

We underline that, for the orders' selection procedure, the injected signal was not used to optimise the telluric removal procedure via the signal-recovery maximisation, but it was used only with the aim of selecting the orders where molecular absorption for a single species was likely to occur and/or the contamination by telluric residuals and other systematic effects (e.g. the wavelength-dependent efficiency of GIANO-B, night-by-night variations of the observing conditions) was minimised.

In this work, in order to remove telluric and stellar spectra, a principal component analysis (PCA) was conducted, after having masked the deepest absorption lines. PCA is often used in HRS analyses (e.g. de Kok et al. 2013) and successfully applied to GIANO-B data in previous works (e.g. Carleo et al. 2022, Giacobbe et al. 2021, Guilluy et al. 2022). As briefly described in Sect. 1.4.3, the idea behind this technique is to identify common trends in the spectra as a function of time (in this case

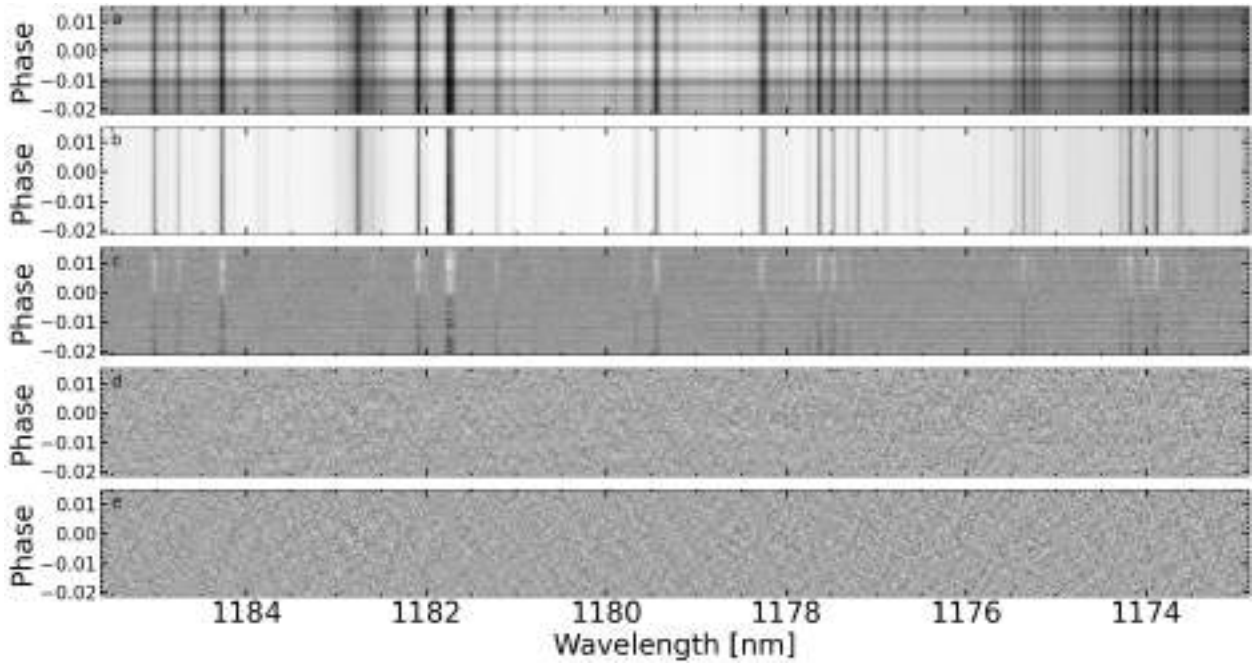

Figure 3.7: Example of the stages of the GIANO-B data reduction process applied to real GIANO-B spectra over a short wavelength interval (x-axis). The planetary orbital phase is reported on the y-axis . From top to bottom panel: (a) the extracted spectra; (b) residual spectra after having normalised each spectrum (each row) by its median value to correct baseline flux differences between the spectra that are due, for example, to variable transparency of the atmosphere, imperfect telescope pointing, or instability of the stellar point spread function; (c) residuals after each spectral channel (each column) had its mean subtracted; (d) residuals after having masked the strongest or saturated telluric lines and having removed the telluric and stellar spectra with the PCA; as it can be seen also other spurious effects such as the alternating pattern visible at certain wavelengths likely related to the instrument A-B nodding are effectively removed with PCA; (e) residuals after having applied a high-pass filter to each row of the residual matrix (this step mitigates any residual correlation between different spectral channels).

represented by telluric and stellar lines in different spectral channels) and remove them. PCA was applied to data of each spectral order selected for a particular molecular species, for each night. It consists of computing the principal components of the M×N data matrix ($M = 58 - 62$ spectra, $N = 2048$ pixels) representing the single spectral order. The principal components correspond to the eigenvectors of the associated covariance matrix and, for each eigenvector, the associated eigenvalue denotes the contribution of that component to the data variance.

The complete telluric removal procedure was conducted as follows. First, we normalised each spectrum to its median value, to correct baseline flux variations. Then, we masked the spectral channels with stronger or saturated telluric lines. To do this, we subtracted the time-averaged spectrum to all the spectra (i.e. we subtracted to each spectral channel its mean value), computed the standard deviation of data in each spectral channel and its median value ($\sigma_{\rm m}$), and then we masked the spectral channels that had a standard deviation $\sigma_\lambda > 1.5 \cdot \sigma_{\rm m}$. After subtracting the time-averaged spectrum from all the spectra and masking highly contaminated spectral channels, we reduced data to a null-mean variable by subtracting to each spectrum its mean value computed on the different spectral channels. Then, the principal components were computed using the PCOMP IDL routine[7]. The output eigenvectors were ordered in decreasing contribution to the variance and we selected the minimum number of components that together contributed up to 70% to the

[7] `https://www.nv5geospatialsoftware.com/docs/PCOMP.html`

data-variance. In the literature there is no consensus on how to choose the appropriate number of components to remove; we adopted the 70% threshold on the variance as it was an empirical value that seemed to be representative of the telluric contribution to the data variance, according to different tests performed during last years. It is worth noting that, as shown in Sect. 3.3.4, the results of this work are not significantly affected by small changes in the number of principal components removed. Once the number of principal components was selected (between 9 and 23, depending on the quality of the night and the spectral order), the matrix that should mainly describe the telluric and stellar contaminations was built via a linear combination of the principal components and removed from the original data matrix, obtaining an ideal residual telluric- and stellar-free matrix. Finally, we applied a high-pass filter to each row of the residual matrix to remove any possible residual correlation between different spectral channels. In Fig. 3.7, we report the stages of the GIANO-B data reduction process are described with an example. The goodness of the telluric (or stellar) lines removal was evaluated by a visual inspection of the residual matrix of each spectral order and of the cross-correlation values as a function of planetary orbital phase computed between data and the H_2O (or CO) model (see, e.g. Fig. 3.9).

In Table 3.5 we report the number of principal components removed by PCA for each selected spectral order, for the different molecular species and nights.

3.3.3 Planet signal extraction via cross-correlation

As the faint planetary signal is very dispersed by the high-resolution spectrograph, it can only be extracted by cross-correlating the residual data with template transmission spectra of the planet's atmosphere, as described in Sect. 1.4.2. In order to do this, we built different models of the atmospheric transmission spectrum of HAT-P-11 b with PetitRADTRANS (Mollière et al., 2019). All the simulated models assumed an isothermal atmosphere at the equilibrium temperature of the exoplanet at the transit epoch, assuming a heating re-distribution efficiency of $\epsilon = 1$ ($T_{\rm eq} = 699\,{\rm K}$), as described in Sect. 3.2.1, and are computed between 10 bar and 10^{-8} bar in pressure. The models assume constant-with-altitude abundance (volume mixing ratio) profiles. The different models, one for each molecule that we wanted to test the presence of, assumed fixed values of the volume mixing ratios (VMR) of molecular hydrogen $\mathrm{VMR_{H_2}} = 0.855$ and helium $\mathrm{VMR_{He}} = 0.145$ and assumed a $\mathrm{VMR_{molecule}} = 10^{-3}$ for the molecule to test (single-species models). Although these values do not match any specific chemical scenarios, this was the simpler framework we could adopt to probe the presence of a particular molecule. We investigated the presence of eight molecular species, very common in the atmosphere of hot giant planets: water vapour (H_2O), methane (CH_4), ammonia (NH_3), acetylene (C_2H_2), hydrogen cyanide (HCN), carbon monoxide (CO), carbon dioxide (CO_2), and hydrogen sulfide (H_2S). In Fig. 3.8, we show the model atmospheric spectra used as templates for the different molecular species that we probed.

In order to probe the presence of a particular molecule, after having performed the PCA, we computed the cross-correlation function (CCF) between the template spectrum associated with the molecule and the data. The CCF was evaluated shifting the model in wavelength on a fixed grid of RV lags ($\Delta RV = c \cdot \frac{\Delta\lambda}{\lambda}$) from $-270\,{\rm km\,s^{-1}}$ to $+270\,{\rm km\,s^{-1}}$, in steps of $0.1\,{\rm km\,s^{-1}}$. The numeric computation was performed using the C_CORRELATE Pxy(L) IDL function[8], with null lag

[8] https://www.nv5geospatialsoftware.com/docs/C_CORRELATE.html

Table 3.5: Selected orders (Sel. Ord.) and number of principal components removed by PCA (PCA Comp.) for each selected order, for the different molecular species and nights.

	7 July 2019	18 June 2020	19 September 2020	13 June 2023
H_2O				
Sel. Ord.	[3, 5, 6, 7, 11, 12, 16, 21, 26, 27, 32, 36, 37]	[21, 22, 26, 32, 33, 34, 35, 36]	[6, 12, 15, 17, 26, 34]	[2, 6, 13, 16, 17, 18, 19, 20, 21, 26, 28, 34, 36, 37]
PCA Comp.	[20, 17, 9, 12, 17, 19, 20, 14, 14, 15, 14, 9, 10]	[9, 9, 16, 17, 17, 16, 10, 9]	[9, 21, 23, 22, 14, 14]	[22, 9, 21, 21, 20, 20, 16, 9, 9, 9, 9, 9, 9, 9]
CH_4				
Sel. Ord.	[4, 13, 18, 20]	[1, 3, 7, 12, 15]	[3]	[15, 38]
PCA Comp.	[19, 20, 20, 15]	[20, 20, 9, 22, 23]	[21]	[21, 9]
NH_3				
Sel. Ord.	[3, 5, 6, 11, 14, 15, 17, 18, 26, 35]	[2, 3, 19, 21]	[6, 7]	[2, 5, 7, 11, 12, 13, 19, 20, 31]
PCA Comp.	[20, 17, 9, 17, 21, 20, 19, 20, 14, 11]	[21, 20, 20, 9]	[9, 9]	[22, 12, 9, 9, 20, 21, 16, 9, 9]
C_2H_2				
Sel. Ord.	[13, 25]	[0, 2, 3, 18, 28]	[36]	[3, 4, 17, 19]
PCA Comp.	[20, 9]	[23, 21, 20, 23, 21]	[9]	[20, 21, 20, 16]
HCN				
Sel. Ord.	[15]	[2, 17]	[4, 16, 20]	[13, 15, 16, 17, 19, 20, 22]
PCA Comp.	[20]	[21, 22]	[21, 22, 12]	[21, 21, 21, 20, 16, 9, 9]
CO				
Sel. Ord.	[1]	[14, 15]	[16, 17]	[1]
PCA Comp.	[21]	[23, 23]	[22, 22]	[21]
CO_2				
Sel. Ord.	[16, 17, 21]	[14, 20]	[6, 30]	[6, 7, 17]
PCA Comp.	[9, 19, 14]	[23, 13]	[9, 20]	[9, 9, 20]
H_2S				
Sel. Ord.	[14, 15, 16, 17, 18, 19]	[0, 4, 6, 7, 14, 15, 16, 26, 27]	[14, 15, 16, 17, 18, 19]	[14, 15, 16, 17, 18, 19]
PCA Comp.	[21, 20, 20, 19, 20, 18,]	[23, 21, 9, 9, 23, 23, 22, 16, 20]	[22, 23, 22, 22, 23, 21]	[22, 21, 21, 20, 20, 16]

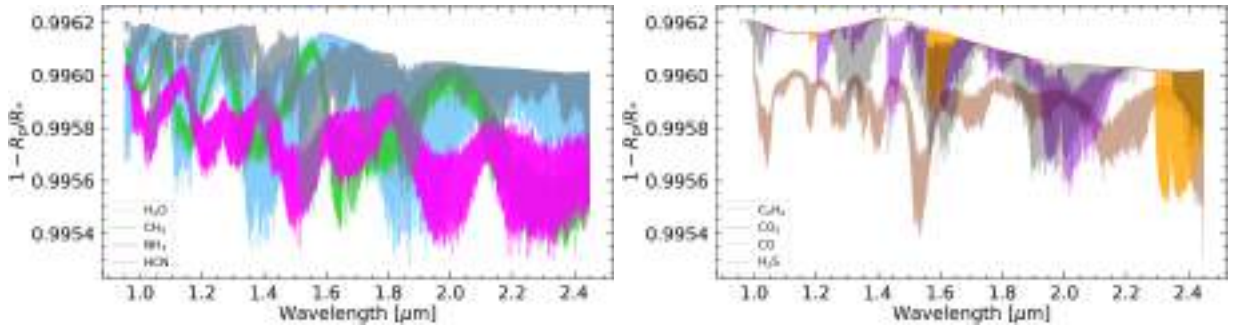

Figure 3.8: Model atmospheric transmission spectra used as templates, in the GIANO-B spectral range. In order to search for the presence of a molecular species, we computed the CCF between the template spectrum associated with the molecule and the data, as described in the text. The spectra of the eight molecular species that we probed are split into two panels for clarity (left panel: H_2O, CH_4, NH_3, HCN; right panel: C_2H_2, CO_2, CO, H_2S).

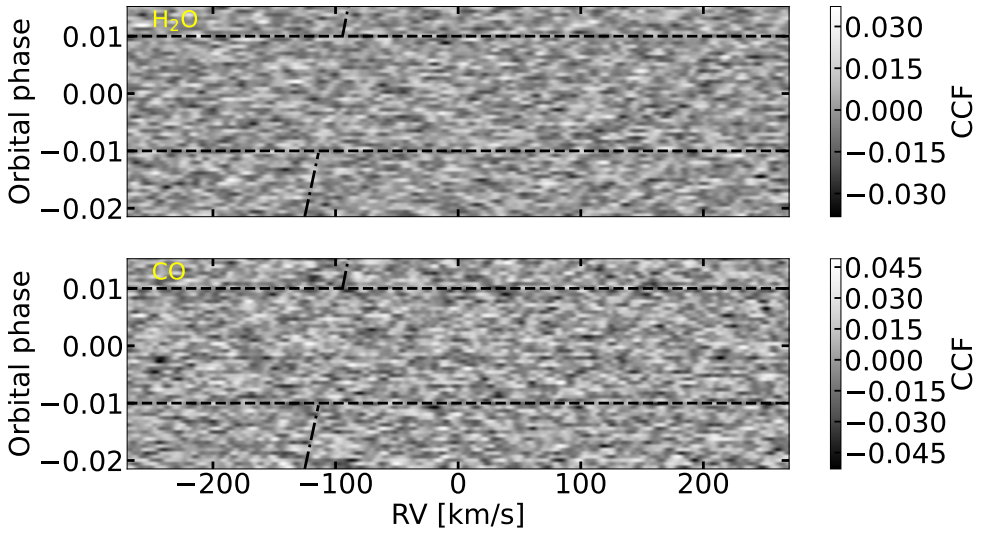

Figure 3.9: Examples of CCF values as a function of planetary orbital phase computed with data from the second observing night (18 June 2020) and model containing only H_2O (top panel) or CO (bottom panel) lines. The horizontal dashed lines represent the transit ingress and egress while the dash-dotted line represents the expected CCF peak trail due to the planetary motion as measured in the observer rest frame. The expected CCF peak trail in transit is not represented for clarity. As it can be seen, due to the faintness of the signal, the CCF peak trail is not visible by eye. This kind of plots serves as a visual check of any remaining telluric and stellar residuals, in this case showing no residuals and signifying that these are adequately corrected by the PCA.

(L = 0), since the RV lags were applied to the wavelength array associated to the model and then the model was interpolated (via spline interpolation) on the same wavelength array of data before computing the CCF (i.e. with lag = 0). For every night and exposure, the CCFs calculated for each selected spectral order are co-added to obtain a single CCF for each exposure of each night.

Thanks to the high-resolution spectroscopy technique, it is possible to measure the Doppler shift of the spectral lines due to the planet's orbital motion. In this way, in order to be sure that a particular spectral feature is produced by a molecule in the atmosphere of an exoplanet, the signal should have a Doppler shift that 'follows' the planetary movement and therefore we should observe that the peak of the CCF moves in wavelength as time passes according to the planetary motion-induced Doppler shift. We assumed that the measured Doppler shift of the planetary spectral lines ($V_{\rm RV} = c \cdot \frac{\Delta\lambda}{\lambda}$) is made of three-velocity components (see Eq. 1.23). For what it concerns

the planetary radial velocity time-dependent contribution ($V_{\rm p}$, see Eq. 1.24), for our analysis, it is convenient to re-express $K_{\rm p}$ isolating the term containing the eccentricity (see Eq. 1.26) and grouping all the others in the constant $\tilde{K}_{\rm p}$:

$$K_{\rm p} = \tilde{K}_{\rm p} \cdot \frac{1}{\sqrt{1-e^2}} \,. \tag{3.6}$$

In Fig. 3.9 we report, as an example, a plot of the CCF values as a function of the planetary orbital phase computed between the models of H_2O and CO and the data of the second observing night (18 June 2020). As it can be seen, the CCF peak trail is not visible by eye, since also at this stage of the analysis the planetary signal is too faint. This kind of plot helps in checking the telluric (stellar) spectrum-removal procedure since any strong residual signal due to a non-optimal telluric (stellar) subtraction would produce a spurious vertical trail of CCF peaks at a radial-velocity $RV = 0\,{\rm km\,s^{-1}}$ ($RV = V_{\rm sys}$, neglecting the few $\rm m\,s^{-1}$ motion induced by the planet onto the star) when data are cross-correlated with the H_2O (CO) templates. A benefit of the eccentric orbit of HAT-P-11 b is that the planetary radial velocity during the transit always remains strictly negative ($\sim -30\,{\rm km\,s^{-1}}$ at the transit midpoint). This, combined with the high $V_{\rm sys}$, shifts the planetary signal at $\sim 100\,{\rm km\,s^{-1}}$ far from the signal of the telluric lines (that is at $RV = 0\,{\rm km\,s^{-1}}$), further reducing spurious contaminations due to the Earth's atmosphere.

If in the atmosphere of an exoplanet a molecule is present, its spectral signal has a null Doppler shift measured in the exoplanet rest frame (i.e. planetary rest-frame velocity $V_{\rm rest} = 0\,{\rm km\,s^{-1}}$), in the absence of a Doppler shift induced by atmospheric dynamics, as described in Sect. 1.4.2. It follows that, after having subtracted the barycentric, systemic and planetary RV from the CCF trails, all the CCF peaks should align at $V_{\rm rest} = 0\,{\rm km\,s^{-1}}$.

We took advantage of the high sampling of the CCF (larger than the GIANO-B pixel scale of $\sim 3\,{\rm km\,s^{-1}}$) for a precise shift of the CCF trails into the planetary rest frame. However in order to avoid the use of correlated data points in our analysis, we binned the CCF values in radial velocity using a bin width of $2.7\,{\rm km\,s^{-1}}$. We took the median of the CCF values in each radial velocity bin as the value of the CCF associated with each bin, before co-adding the CCF values in phase for each trial $K_{\rm p}$.

In this work, we explored a range of $K_{\rm p}$ values by varying the value of $\tilde{K_{\rm p}}$ between $0\,{\rm km\,s^{-1}}$ and $200\,{\rm km\,s^{-1}}$ in steps of $2.7\,{\rm km\,s^{-1}}$, having fixed the eccentricity and the other orbital parameters to the values reported in Table 3.1. This means that the corresponding explored range of $K_{\rm p}$ is $[0; 207]\,{\rm km\,s^{-1}}$ (this is the $K_{\rm p}$ range reported in the $K_{\rm p} - V_{\rm rest}$ maps in the next section and it is computed from $\tilde{K}_{\rm p}$ using Eq. 3.6 with the value of e from Table 3.1). The expected value of $K_{\rm p}$ was computed according to Eq. 1.26, by using the orbital and physical parameters (i.e. $P_{\rm orb}$, e, i, $M_\star$, $M_{\rm p}$) reported in Table 3.1. As reported in Table 3.1, the expected value of $K_{\rm p}$ is $\hat{K}_{\rm p} = 123.4 \pm 9.9\,{\rm km\,s^{-1}}$ and, consequently, the expected value of $\tilde{K}_{\rm p}$ is $\hat{\tilde{K}}_{\rm p} = 119.3 \pm 9.5\,{\rm km\,s^{-1}}$.

3.3.4 Results

We first co-added the data of all the 4 observing nights and built the signal-to-noise ratio (S/N) $K_{\rm p} - V_{\rm rest}$ maps for the different probed molecules, obtained by cross-correlating data with models and dividing the result by the standard deviation of the noise far from the peak ($|V_{\rm rest}| > 25\,{\rm km\,s^{-1}}$), to search for significant (S/N > 3) signals following the expected planetary RV ("potential detections").

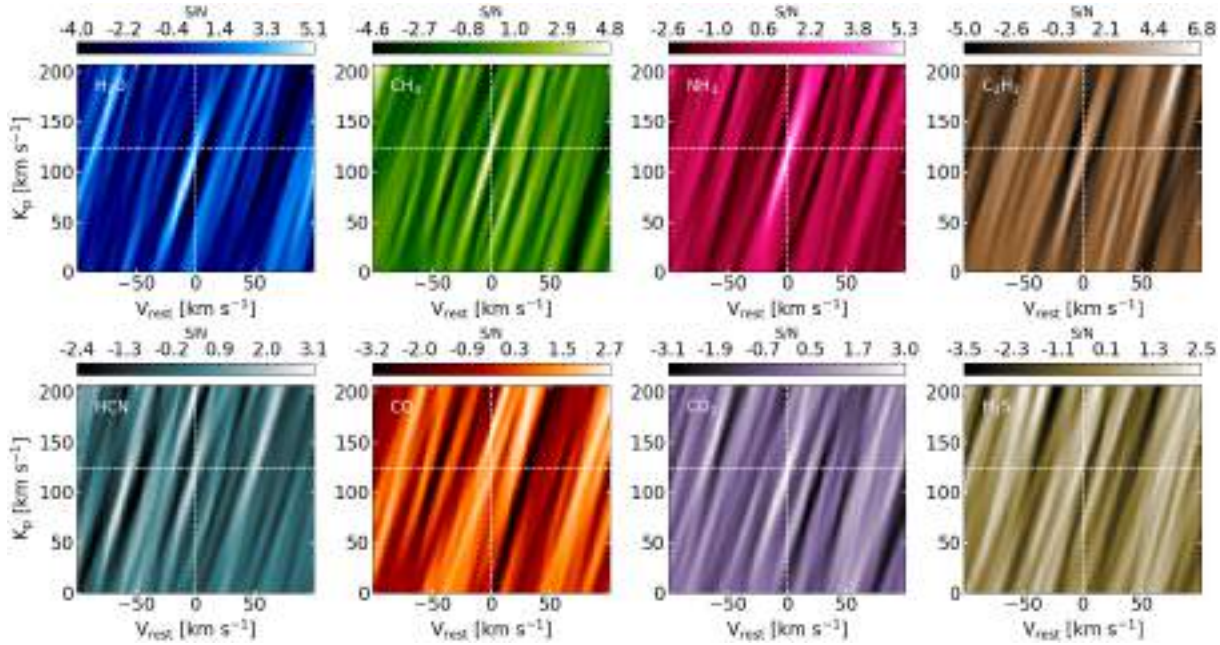

Figure 3.10: Signal-to-noise ratio $K_\mathrm{p} - V_\mathrm{rest}$ maps for the probed chemical species: H_2O, CH_4, NH_3, C_2H_2, HCN, CO, CO_2, and H_2S. Each $K_\mathrm{p} - V_\mathrm{rest}$ map shows the S/N of the cross-correlation of the GIANO-B spectra (4 transits combined) with isothermal atmospheric models, as a function of the planet's RV semi-amplitude (K_p) and the planet's rest-frame velocity (V_rest). The S/N is computed by dividing the peak value of the cross-correlation function at each K_p by the standard deviation of the noise far from the peak, as described in the text. Negative S/N values correspond to anti-correlation. The vertical and horizontal white dashed lines correspond to $V_\mathrm{rest} = 0\,\mathrm{km\,s^{-1}}$ and the expected K_p value ($\hat{K}_\mathrm{p}$), respectively.

In Fig. 3.10, we report the S/N $K_\mathrm{p} - V_\mathrm{rest}$ maps for the different tested molecules, obtained by cross-correlating data with the different models and following the procedure explained in Sect. 3.3.3. As it can be seen, we obtain a signal around the expected planetary position in the $K_\mathrm{p} - V_\mathrm{rest}$ maps with S/N > 3 for 4 molecular species: H_2O (S/N $= 5.1$), CH_4 (S/N $= 4.8$), NH_3 (S/N $= 5.3$), and CO_2 (S/N $= 3.0$).

Then we computed the significance of the planetary signals by performing a Welch *t-test* (Welch, 1947) on two samples of CCF values: the former far ($|V_\mathrm{rest}| > 25\,\mathrm{km\,s^{-1}}$) from the planet's rest-frame velocity ("out-of-trail") and the latter near to it ($|V_\mathrm{rest}| < 3\,\mathrm{km\,s^{-1}}$, "in-trail"). The test rejects the null hypothesis (H_0) that the two samples have the same mean (and therefore that the CCF signal produced by the planet is only a statistical fluctuation of the background signal value) at a certain significance level that we adopted as the significance (σ) of our detections. In particular, the Welch *t-test* rejected the null-hypothesis with a certain probability value ($p - value$). We then computed the Gaussian distribution inverse survival function of this probability value (halved), in order to compute the σ value associated to that probability. This σ value was adopted as the significance of the detection. Our significance calculations are based on the hypothesis of uncorrelated noise, which has been shown to be a valid approximation in previous works (e.g. Brogi et al. 2018, Guilluy et al. 2019). The distributions of CCF values "in-trail" and "out-of-trail" used for computing the significance of the detections via the Welch *t-test* are shown in Fig. 3.11, for all the probed species. In case of a non-detection for a particular molecular species, the mean values of the "in-trail" and "out-of-trail" CCF histograms are expected to be the same (and equal to 0).

In order to build the significance $K_p - V_{rest}$ maps, for each molecular species, the Welch *t-test* was performed on CCF "in-trail" and "out-of-trail" distributions centred at the different V_{rest} explored, for each trial K_p. In Fig. 3.12, we report the significance $K_p - V_{rest}$ maps for the different tested molecules, obtained by performing the Welch *t-test* on "in-trail" and "out-of-trail" CCF distributions. As it can be seen from the maps, the peak of the signal for the four potentially detected species has a significance of 3.4 σ (H_2O), 2.6 σ (CH_4), 5.0 σ (NH_3), and 3.2 σ (CO_2). For the other four probed species, we measure no significant chemical signature at the planetary RV, and therefore we consider them as non-detections and focus our attention and following analyses on the signals of H_2O, CH_4, NH_3, and CO_2 only.

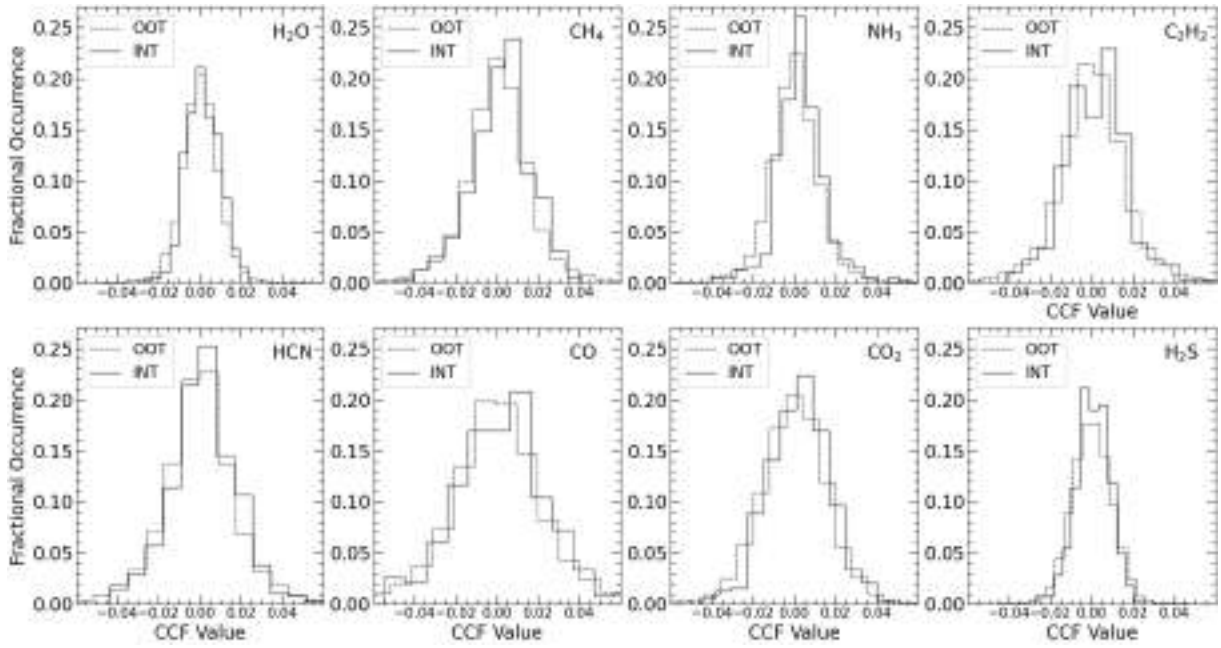

Figure 3.11: Distribution of CCF values far ($|V_{rest}| > 25\,km\,s^{-1}$) from the planet's rest-frame velocity ("out-of-trail", OOT, dashed lines) and near to it ($|V_{rest}| < 3\,km\,s^{-1}$, "in-trail", INT, solid lines) for the probed chemical species. The Welch *t-test* used to estimate the significance of the detections was performed on these distributions.

It is interesting to notice the orientation of the signals in the $K_p - V_{rest}$ maps, which is typically vertical for atmospheric transmission studies (e.g. Giacobbe et al. 2021) and sloped for atmospheric emission studies (e.g. Line et al. 2021). This is due to the eccentric orbit of HAT-P-11 b that makes the planetary RV to be not symmetrical around $0\,km\,s^{-1}$ during the transit (it is always strictly negative), as it happens for planets on circular orbit observed in emission (i.e. at orbital phases different from 0 or 0.5).

Finally, for the four selected species, we computed how much the Doppler signature of the signals is in accordance with the expected planetary RV. In order to do this, we built contour plots of the detection significance, defining the $1\,\sigma$ and $2\,\sigma$ significance intervals as the regions of the $K_p - V_{rest}$ maps where the significance drops by $1\,\sigma$ and $2\,\sigma$, respectively, with respect to the significance peak, and looked at where the expected position of the atmospheric signal in the $K_p - V_{rest}$ maps was with respect to those intervals. In Fig. 3.13, we report the contour plots of the detection significance for the four chemical species. As it can be seen, the signals we measure have a Doppler signature compatible with the planetary one at $< 1\,\sigma$, for all four molecules.

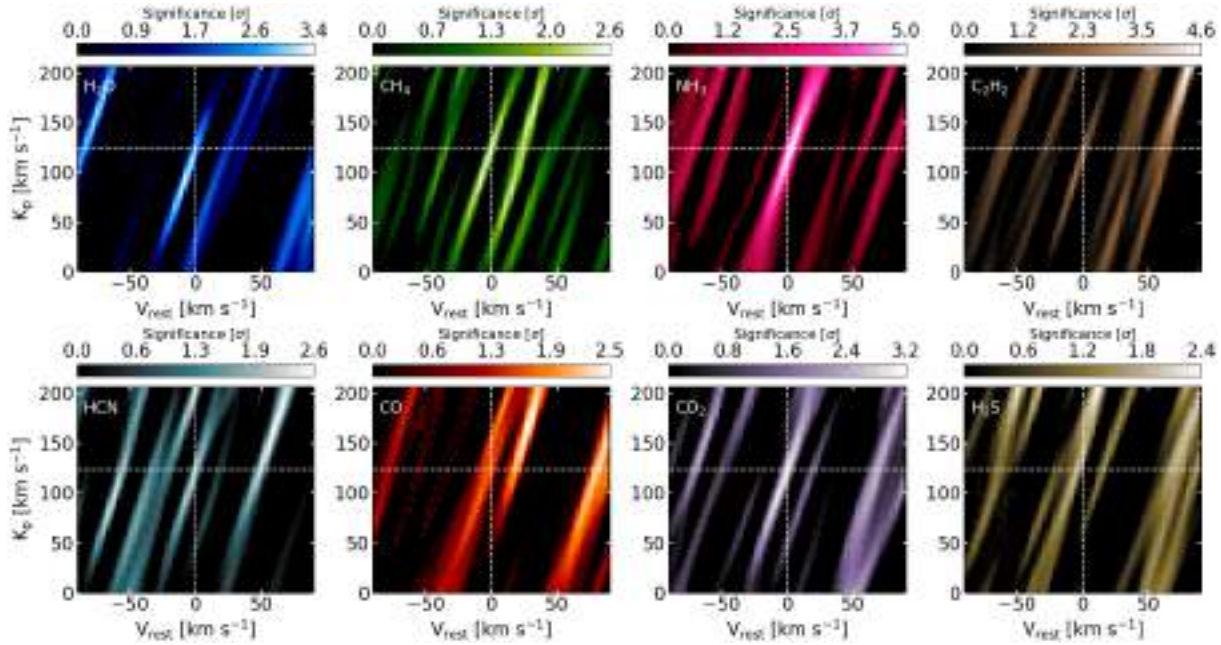

Figure 3.12: Significance $K_\mathrm{p} - V_\mathrm{rest}$ maps for the tested chemical species: H_2O, CH_4, NH_3, C_2H_2, HCN, CO, CO_2, and H_2S. Each $K_\mathrm{p} - V_\mathrm{rest}$ map shows the significance of the cross-correlation signal of the GIANO-B spectra (4 transits combined) with isothermal atmospheric models, as a function of the planet's RV semi-amplitude (K_p) and the planet's rest-frame velocity (V_rest). The significance is computed with a Welch *t-test*: for each molecular species, the Welch *t-test* was performed on CCF "in-trail" and "out-of-trail" distributions centred at the different V_rest explored, for each trial K_p. The vertical and horizontal white dashed lines correspond to $V_\mathrm{rest} = 0\,\mathrm{km\,s^{-1}}$ and the expected K_p value ($\hat{K}_\mathrm{p}$), respectively.

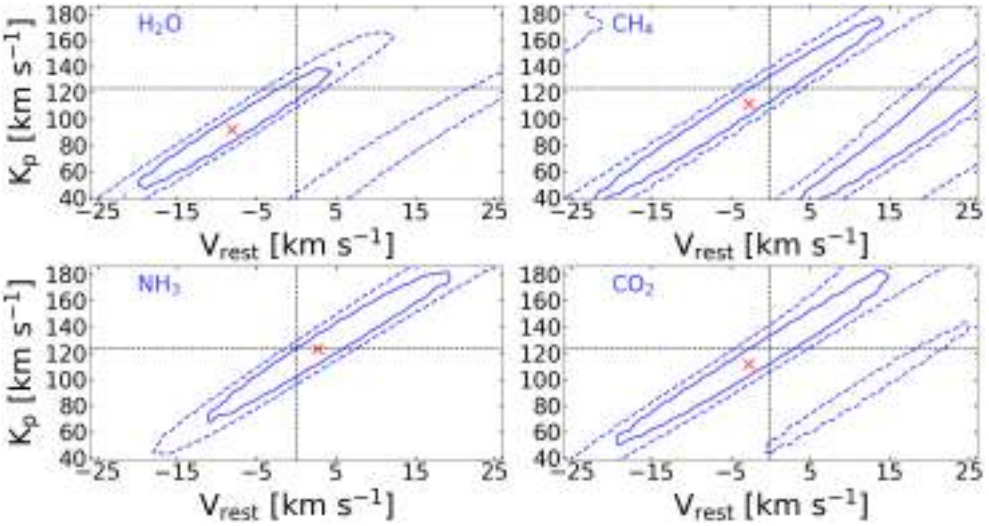

Figure 3.13: Contour plots of the detection significance of the four selected chemical species. The solid (dashed) lines represent the $1\,\sigma$ ($2\,\sigma$) interval around the peak value of the significance (marked with a red cross). These intervals are computed as described in the text. The point of the $K_\mathrm{p} - V_\mathrm{rest}$ map in which the 2 black dashed lines (the horizontal one corresponds to the expected K_p value, while the vertical one corresponds to $V_\mathrm{rest} = 0\,\mathrm{km\,s^{-1}}$) cross each other represents the expected detection significance peak position in the case in which the detected signal has a planetary origin. As it can be the significance peak position is compatible with the planetary origin hypothesis at better than 1 σ for all the 4 species.

Before claiming any detection, we checked the reliability of our results by performing a further test, described in the following. For each of the four chemical species, we combined the matrices of the CCF as a function of the orbital phase (see, e.g. Fig. 3.9) of the four observing nights in a single

CCF matrix with the rows sorted in crescent orbital phase. Then, we randomly shuffled the CCF order in phase (this corresponds to shuffling the sequence of observed spectra in time, including the out-of-transit ones) 250 times. For each shuffle, we built both the S/N and the significance $K_p - V_{rest}$ maps in a restricted interval of $K_p = [89.4; 156.5]\,km\,s^{-1}$ (corresponding to $\hat{K}_p \pm 34\,km\,s^{-1}$) and $V_{rest} = [-10; 10]\,km\,s^{-1}$, in order to test the presence of spurious signals that have not a planetary origin but can produce significant features around the expected signal position in the maps due to some peculiar time-correlated noise. We only analysed a restricted interval around the expected K_p and V_{rest} since we were interested to look for possible spurious signals that could be interpreted as a detection by having an RV similar to the planetary one. The chosen interval seemed a good trade-off between being sufficiently large to include possible shifts of the signal in K_p and V_{rest} and being sufficiently small to exclude RV values not compatible with the planetary one. We repeated this test for the four selected chemical species and for each species we studied the distributions of the S/N and significance values obtained in the chosen $K_p - V_{rest}$ interval, combining the 250 permutations. In this way, we obtained a distribution of 43 750 values of S/N (corresponding to the 25 values of K_p of the interval $\times$ the 7 values of V_{rest} of the interval $\times$ 250 permutations) and 43 750 values of significance. In Fig. 3.14 and Fig. 3.15, we report the distributions of S/N and significance values obtained, respectively. The results of this test are reported in Table 3.6. As it can be seen, for all the 4 molecular species, 95% of the test yields signals with S/N < 3 and significance $\leq 2.5\ \sigma$ in the selected $K_p - V_{rest}$ interval, while 99.73% of the test yields S/N ≤ 4.6 and significance $\leq 4.2\ \sigma$, in the same interval.

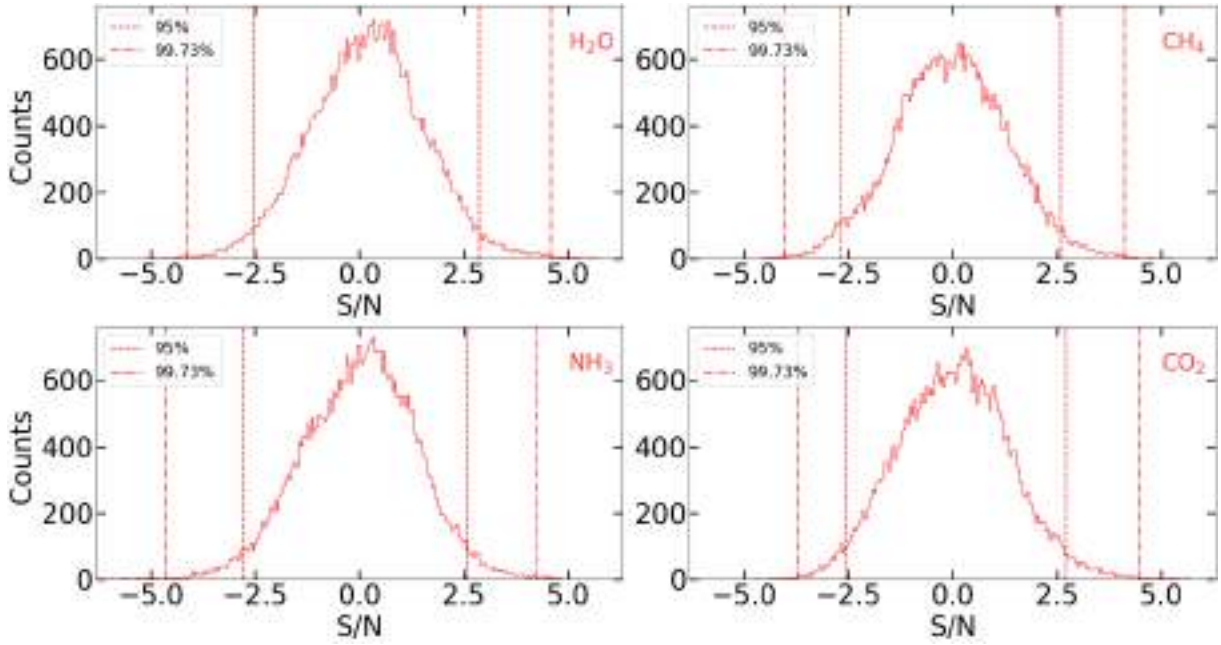

Figure 3.14: Distribution of S/N obtained in the selected $K_p - V_{rest}$ interval by shuffling 250 times the time order of the observed spectra, for each of the four selected chemical species. The vertical dashed (dash-dotted) lines represent the borders of the intervals enclosing the 95% (99.73%) of the S/N values, corresponding to the $2.5\% - 97.5\%$ ($0.135\% - 99.865\%$) quantiles of the distributions. These intervals are reported in Table 3.6.

After having performed this test, for each of the four molecular species we computed the probability (*p-values*) of randomly drawing from the distributions reported in Fig. 3.14 and Fig. 3.15, the S/N and significance values that we measure. To compute the *p-values* for the S/N (significance)

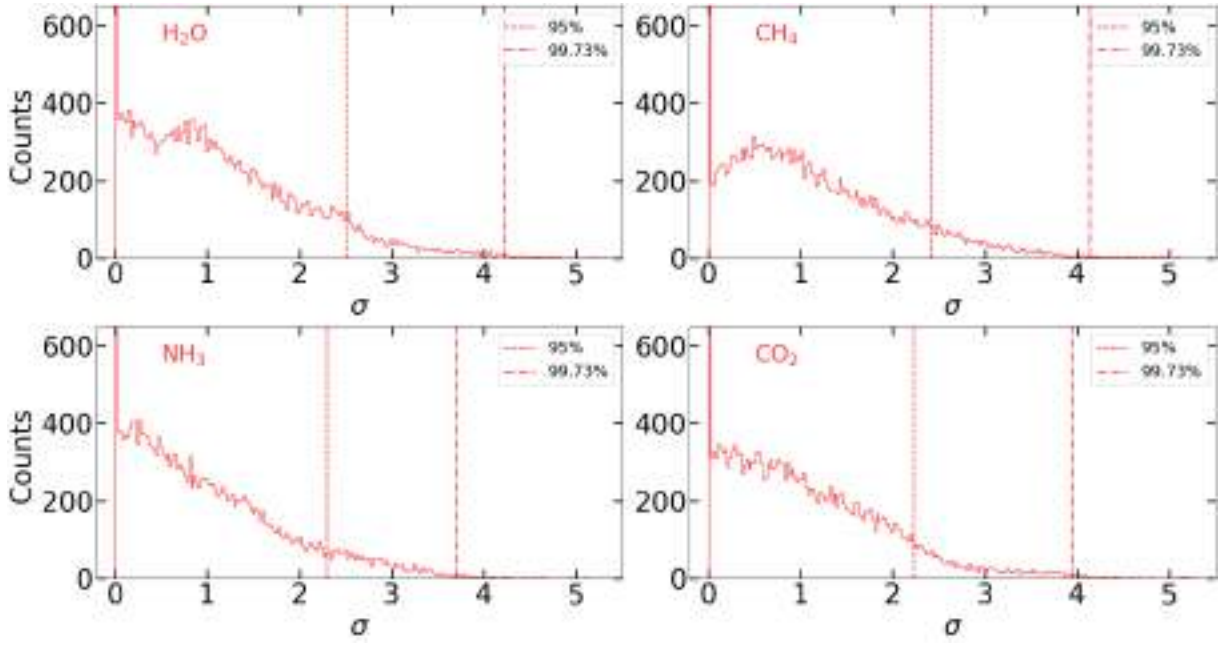

Figure 3.15: Distribution of significance (from the *t-test*) obtained in the selected $K_p - V_{rest}$ interval by shuffling 250 times the time order of the observed spectra, for each of the four selected chemical species. The vertical dashed (dash-dotted) lines represent the borders of the intervals enclosing the 95% (99.73%) of the significance values, corresponding to the 95% (99.73%) quantile of the distributions. These intervals are reported in Table 3.6. Since the 50% of the significance values ($\sim 20\,000$ values) are $< 0.2\ \sigma$ for all the 4 chemical species, the plots of the distributions are limited on the y-axis in the interval [0; 650] for clarity.

Table 3.6: Signal-to-noise ratio and significance from the *t-test* (σ *t-test*) values delimiting the 95% and 99.73% intervals of the distributions obtained by performing the reliability test described in the text for the four selected molecular species.

Molecule	S/N (95%)	S/N (99.73%)	σ *t-test* (95%)	σ *t-test* (99.73%)
H_2O	$[-2.5; 2.9]$	$[-4.1; 4.6]$	≤ 2.5	≤ 4.2
CH_4	$[-2.8; 2.6]$	$[-4.0; 4.1]$	≤ 2.4	≤ 4.1
NH_3	$[-2.8; 2.6]$	$[-4.6; 4.2]$	≤ 2.3	≤ 3.7
CO_2	$[-2.5; 2.7]$	$[-3.7; 4.5]$	≤ 2.2	≤ 3.9

value, we summed the occurrences of S/N (significance) greater than the S/N (significance) measured and divided them by 43 750. We report the *p-values* in Table 3.7. As it can be seen, for all the four molecular species we obtain a *p-value* $\leq 2.5\%$ for the S/N and $\leq 3.8\%$ for the significance, so there is less than 5% of probability that these signals are due time-correlated noise.

In Table 3.7, we summarise the significance level of the signal of the four molecular species of interest obtained with different statistical methods. From these results, we conclude that we have a statistically robust detection of NH_3, which is the most significant signal ($5\ \sigma$) and the one with the lowest $p - values$ ($< 0.04\%$). We consider the H_2O as a detection, even though it is less statistically robust than the NH_3 one, since it has already been detected at low-resolution multiple times in the atmosphere of HAT-P-11 b (see the literature cited in Sec. 3.1) and therefore we can be more confident about the reliability of the signal we measure. Since the *t-test* significance for the signal of CH_4 is $< 3\ \sigma$, the significance $K_p - V_{rest}$ map presents a second comparable peak at $V_{rest} \approx 20\,km\,s^{-1}$, and the associated *p-value* is the highest among the four chemical species, even

if the signal has an S/N= 4.8 and a Doppler signature that is compatible with the planetary one at $< 1\ \sigma$, the detection of this molecular species remains tentative as it is not sufficiently robust from a statistical point of view. Even though the signal from CO_2 has both the S/N and significance $\geq 3\ \sigma$ and the RV trail is compatible with the planetary one at $< 1\ \sigma$, it has the lowest S/N and the highest S/N *p-value* among the four selected species. For these reasons, we consider the detection of CO_2 as tentative too. As it can be seen, for what concerns these two tentative detections, even though we obtain signals at the expected planetary RV, they are not sufficiently statistically robust and we suggest conducting further studies to unambiguously assess the presence of CH_4 and CO_2 in the atmosphere of HAT-P-11 b.

Table 3.7: Significance of the detections calculated with different statistical methods.

Molecule	S/N	Welch *t-test* Significance	Planetary RV Compatibility	*p-value* S/N	*p-value* σ *t-test*	Status[a]
H_2O	5.1	3.4 σ	$< 1\ \sigma$	0.046%	1.3%	*D*
CH_4	4.8	2.6 σ	$< 1\ \sigma$	0.023%	3.8%	*TD*
NH_3	5.3	5.0 σ	$< 1\ \sigma$	0.039%	0.011%	*D*
CO_2	3.0	3.2 σ	$< 1\ \sigma$	2.5%	1.3%	*TD*

Notes. [(a)] *D* stands for 'detected' and *TD* stands for 'tentatively detected'.

In order to further assess the robustness of our analysis, for what it concerns the impact of the number of principal components removed by the PCA (changing with the spectral order and night) on the final results, we also repeated the whole analysis removing a fixed number of principal components with the PCA for all the selected spectral orders per-molecule, an for all the observing nights. We performed this test twice, the first time we removed 9 principal components (the minimum number of principal components removed in our work among the different spectral orders and nights), the second time we removed 23 components (the maximum number of principal components removed in our work among the different spectral orders and nights). We obtain that none of these 2 extreme conditions changes our interpretation of which chemical species we detect (i.e. H_2O and NH_3), and which chemical species we tentatively detect and need further investigations (i.e. CH_4 and CO_2), even if their S/N and significance slightly change (at less than 1 σ level), as expected.

Finally, to assess the robustness of the final results (in particular the detection of H_2O and NH_3) in relation to the impact of the spectral orders' selection procedure on the CCF analysis, we performed an additional test. In this test, we repeated the analysis refining the orders' selection procedure to assess the presence of possible spurious signals near the expected planetary radial velocity that could lead to possible false positive detections.

In particular, for each of the two detected molecules (i.e. H_2O and NH_3) and for each night, we started from the spectral orders' lists selected with the procedure described in Sect. 3.3.2 (and reported in Table 3.5) and refined the selection in the following way:

- step 1) for each of the selected spectral order, we applied the PCA and computed the signal-to-noise ratio (S/N) $K_\mathrm{p} - V_\mathrm{rest}$ maps by cross-correlating the spectra of that order with the single-species model for the tested molecule;
- step 2) for each of the selected spectral order, we injected the single-species model for the tested molecule into the data at the planetary radial velocity and then applied the PCA and computed the

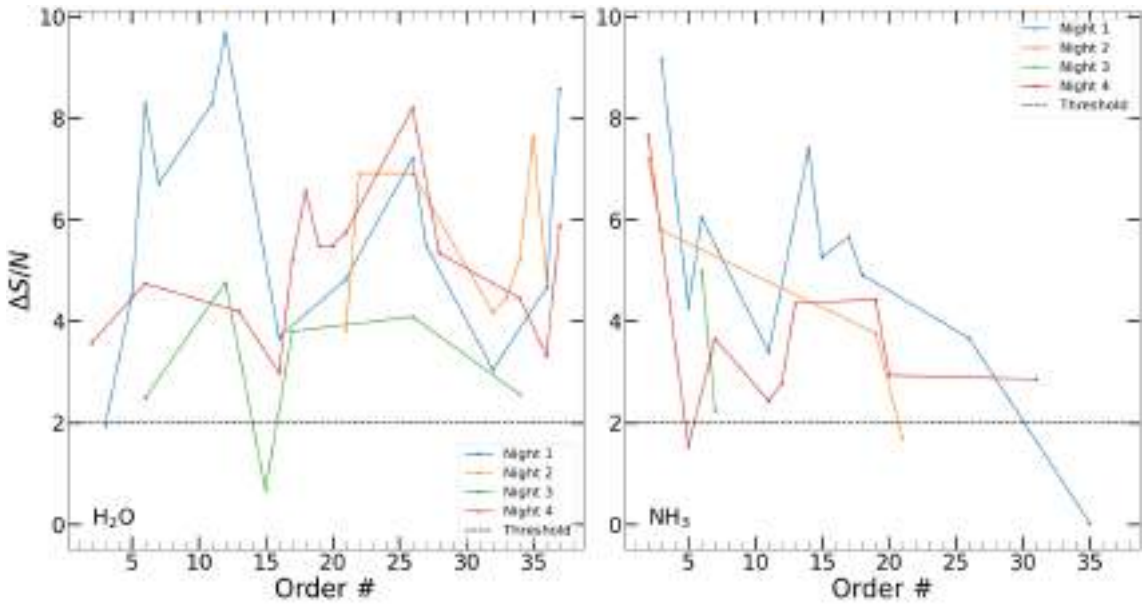

Figure 3.16: Change in S/N ($\Delta S/N$) due to the injection of the model of H_2O (left) and NH_3 (right) into the data, as a function of the selected spectral orders in the different nights. The black horizontal dashed line represents the 2 σ threshold.

signal-to-noise ratio (S/N) $K_p - V_{rest}$ maps by cross-correlating them with the model itself;
- step 3) finally, for each spectral order, we computed the change ($\Delta S/N$) in the S/N of the CCF peak at the planetary radial velocity obtained in the two previous steps (i.e. data alone and data+injected model) and selected the orders that showed a $\Delta S/N \geq 2\ \sigma$.

With this kind of selection, we selected the orders that not only allowed to retrieve the injected signal but also showed a significant increase of the S/N of the CCF peak when the model itself was injected into the data, further minimising the possible presence of spurious systematics in the final dataset that could lead, for example, to false positive signals. In Fig. 3.16 we report the $\Delta S/N$ for the different selected orders and nights. As it can be for most of the selected spectral orders the increase of S/N is $> 2\ \sigma$.

Given the 2 σ threshold we discarded the following orders from the original lists:
- for H_2O: order 3 (night 1), order 15 (night 3);
- for NH_3: order 35 (night 1), order 21 (night 2), order 5 (night 4).

We then repeated the telluric removal procedure and the CCF analysis using the updated selected orders' lists and built the $K_p - V_{rest}$ maps (Fig. 3.17), obtained by combining the signal of the four nights. As it can be seen, we confirm the detection of both the molecules obtained in the main analysis: for H_2O we obtain a CCF peak at the expected planetary radial velocity with an S/N= 5.1 and a *t-test* significance of 3.5 σ; for NH_3 we obtain a CCF peak at the expected planetary radial velocity with an S/N= 4.8 and a *t-test* significance of 4.0 σ. As it can be seen, removing the orders that showed a $\Delta S/N < 2\ \sigma$, the result of this test does not lead to significative differences ($\leq 1\ \sigma$) with the conclusion reached in our work, giving more robustness to our analysis.

In summary, in this work, we report the detection of two molecular species (i.e. H_2O and NH_3) in the atmosphere of HAT-P-11 b and the tentative detection of two others (i.e. CH_4 and CO_2), whose presence has to be assessed by further studies.

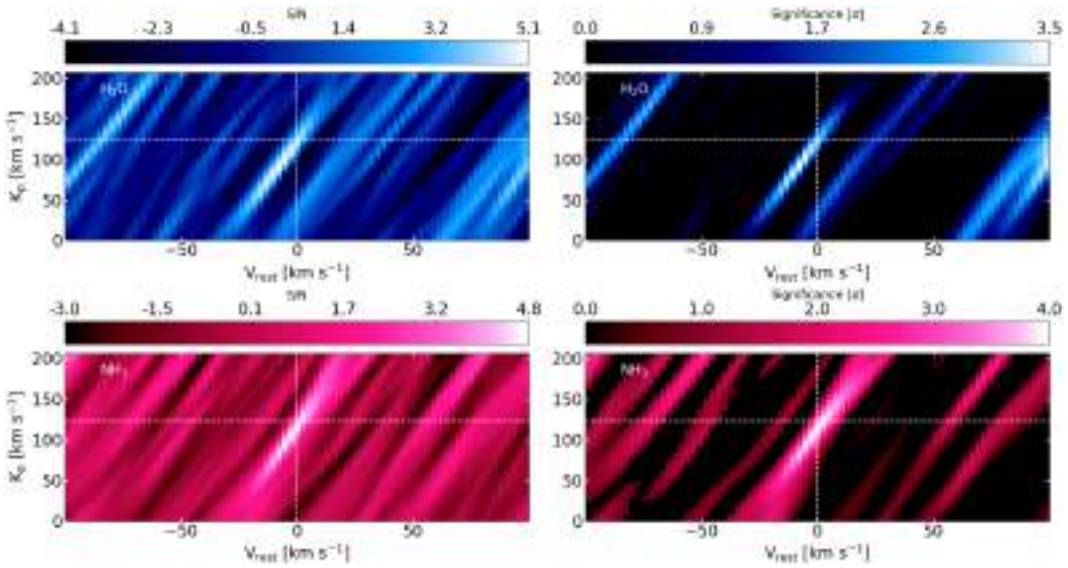

Figure 3.17: Signal-to-noise ratio (left panels) and Welch *t-test* significance (right panels) $K_\mathrm{p} - V_\mathrm{rest}$ maps for the 2 tested chemical species (top for H_2O, bottom for NH_3) obtained by combining data from the four observing nights excluding spectral orders with $\Delta S/N < 2\ \sigma$. The point where the 2 white dashed lines cross each other is the expected position of a signal with planetary origin.

3.3.5 Discussion

The significance of the detections reported in this work is lower than that of the species detected in other hot and warm Jupiters' atmospheres, which even reached the $10\,\sigma$ level (e.g. Giacobbe et al. 2021). This is mainly due to the lower atmospheric signal level of warm Neptune-size exoplanets (the atmospheric signal level is $\approx 2H_\mathrm{s}R_\mathrm{p}/R_\star^2$, where H_s is the atmospheric scale height, and therefore it is $\sim 55\,\mathrm{ppm}$[9], assuming an atmospheric mean molecular weight of $\mu = 2.3\,\mathrm{g\,mol^{-1}}$, for HAT-P-11 b) and underlines the difficulty in probing the atmospheric features of this class of exoplanets.

Detected species in the HAT-P-11 b planetary context

Our detection of water vapour in the atmosphere of HAT-P-11 b is in accordance with the results of Fraine et al. (2014), Tsiaras et al. (2018), Chachan et al. (2019), and Cubillos et al. (2022). The signal from the methane, which we measure at the expected planetary radial velocity, supports the results obtained by Chachan et al. (2019) and Cubillos et al. (2022), who suggested the presence of CH_4 from the analysis of HST data however, as told in the previous section, the significance of the signal is very low and therefore we cannot confirm the presence of this molecular species in the atmosphere of HAT-P-11 b and further studies are required.

The hot and warm Neptunes' atmospheric chemistry and dynamics are different from the ones that act in the hot and warm Jupiters' atmospheres, mainly because of the smaller radius and mass and the possible higher metallicity of the former (Moses et al., 2013). The atmospheric composition of individual exoplanets also depends on their effective temperature, formation history, atmospheric evolution, orbital parameters, and irradiation environment, so it is difficult to predict their exact atmospheric properties. However, for what concerns the chemical composition, some general trends with temperature, metallicity and C/O ratio can be found, as shown in the works of Moses et al.

[9]For comparison, HD 209458 b investigated by Giacobbe et al. (2021) has a $2H_\mathrm{s}R_\mathrm{p}/R_\star^2 \sim 164\,\mathrm{ppm}$, assuming $\mu = 2.3\,\mathrm{g\,mol^{-1}}$.

(2013), who particularly focused on hot Neptunes, Madhusudhan (2012) and Fonte et al. (2023).

Even though with this work we are not able to constrain HAT-P-11 b atmospheric physical and chemical properties (such as the elemental abundances), we can still make some general considerations about our detections. In particular, under thermochemical equilibrium, the presence of hydrocarbons, like HCN and C_2H_2, is particularly favoured in carbon-rich environments (C/O $\gtrsim$ 1) at high temperatures ($T \gtrsim 1000$ K). This is in line with our non-detections of these two chemical species, given the relatively low-temperature atmosphere ($T_{\rm eq} \sim 700$ K) of the target we analysed. Chachan et al. (2019) measured an atmospheric C/O ratio close to unity (C/O$= 0.97^{+0.59}_{-0.46}$). A C/O value close to unity together with a low-temperature environment favours the formation of ammonia, which is the molecule that we detected with the highest significance and the second nitrogen-bearing species we probed. In addition, at temperatures lower than $T \lesssim 1300$ K, the formation of H_2O and CH_4 is favoured, in accordance with our detection of H_2O and tentative detection of CH_4, considering the HAT-P-11 b equilibrium temperature.

Another interesting result of our work is the tentative detection of CO_2 in the atmosphere of HAT-P-11 b. Carbon dioxide is an important indicator of the metal enrichment of the atmosphere of exoplanets and therefore it can give important information about the formation processes of the primary atmospheres of gas giants. Indeed several models for warm gas giant atmospheres predict that CO_2 is one of the molecules most strongly enhanced with increasing atmospheric metallicity, becoming detectable for metallicities greater than ≈ 10 times that of the Sun (Lodders and Fegley, 2002, Moses et al., 2013). Until now, only JWST Transiting Exoplanet Community Early Release Science Team et al. (2023) have firmly detected the presence of CO_2 in the atmosphere of an exoplanet (the warm Saturn WASP-39 b) at low spectral resolution, while at high spectral resolution Carleo et al. (2022) tentatively detected it in the atmosphere of the warm Jupiter WASP-80 b. Therefore, our tentative detection of CO_2 represents the first hint of the presence of this molecule in the atmosphere of a warm Neptune and, if confirmed, could point towards a super-solar metallicity for the atmosphere of HAT-P-11 b. However, as underlined before, further studies are needed and only a statistical comparison between different atmospheric chemical-physical models (for example through atmospheric retrievals), could robustly determine the atmospheric chemical-physical characteristics of this target.

For the case of HAT-P-11 b, the estimated metallicity is $Z < 4.6\ Z_\odot$ at $2\,\sigma$ level (Chachan et al., 2019) with $Z_\odot$ the solar metallicity, that is, $Z < 2.3\ Z_\star$ referred to the host-star metallicity $Z_\star = 2.0 \pm 0.2\, Z_\odot$ (Bakos et al., 2010), while Welbanks et al. (2019) estimated a substellar H_2O/H metallicity. At this level of metallicity, CO_2 should be scarce (see Moses et al. 2013, Fig. 5), but if we consider the $3\,\sigma$ confidence level upper limit on metallicity ($Z < 86\ Z_\odot = 43\ Z_\star$) by Chachan et al. (2019), the CO_2 abundance could increase up to the point of being detectable with our kind of analysis.

It is worth noting that the cross-correlation analysis is more sensitive to molecular lines' position in wavelength rather than their depths with respect to the continuum. This means that a more significant detection for a particular chemical species does not necessarily imply that species is more abundant with respect to the other ones because it could arise for example from a denser forest of lines and consequently from a stronger correlation peak. In addition, our non-detections do not necessarily imply the absence of such chemical species, for which further investigations are needed. Finally, for what concerns the non-detections, the $K_{\rm p} - V_{\rm rest}$ significance maps show spurious

signals that are not related to the planetary signal. They are typically aliases generated by the autocorrelation function of the template that can also be seen in the maps of the detected species far from the planetary RV.

Atmospheric chemical modelling

In order to better characterise the atmospheric properties of HAT-P-11 b, we tried to find the chemical scenarios that are most compatible with the detection of H_2O and NH_3, and possibly CH_4 and CO_2 (while also considering a non-detection of the other species) in the atmosphere of HAT-P-11 b, by exploring with a grid of theoretical models the possible radiative state and elemental compositions. To this end, we employed the Pyrat Bay (Cubillos and Blecic, 2021) modelling framework to compute transmission spectra from an atmosphere in radiative and thermochemical equilibrium. The code iterates over a two-stream radiative-transfer calculation until the atmosphere converges towards a stable radiative equilibrium solution at each layer (Heng et al., 2014, Malik et al., 2017). The end products of this approach are the temperature and composition profiles of an atmosphere in radiative equilibrium, from which we can produce transmission-spectrum models to determine which species have observable spectral features.

The inputs of the models are the known system parameters, a stellar spectrum (Castelli and Kurucz, 2003), and the atmospheric elemental composition. We explored a range of plausible scenarios by varying the elemental composition over a range of metallicities (from [M/H] = -1.0 dex to 2.0 dex), C/O ratios (from 0.1 to 1.5), N/O ratios from (0.14 to 0.85), and over a range of heat radiation regimes by varying the $\beta_{\rm irr} = (1 - A_{\rm b})/f$ parameter (from $\beta_{\rm irr} = 0.5$ to 1.0), where $A_{\rm b}$ is the Bond albedo and f is the day-night heat redistribution efficiency.

The atmospheric model spans a pressure range from 100 to 10^{-9} bar, and a wavelength grid ranging from 0.3 to 30 μm sampled at a resolving power of $R = 15\,000$, sufficient to contain the bulk of the stellar and planetary fluxes. The chemical network includes 45 neutral and ionic species that are the main carriers of H, He, C, N, O, Na, Si, S, K, Ti, V, and Fe. The opacity sources include line-list data for CO, CO_2, and CH_4 from HITEMP (Rothman et al. 2010, Li et al. 2015, Hargreaves et al. 2020), and H_2O, C_2H_2, NH_3, and HCN from ExoMol (Polyansky et al. 2018, Chubb et al. 2020, Yurchenko et al. 2011, Harris et al. 2006, 2008, Coles et al. 2019). We preprocessed these large data sets with the repack package (Cubillos, 2017) to extract the dominant line transitions. Additionally, we included Na and K opacities (Burrows et al., 2000); H, H_2, and He Rayleigh opacities (Kurucz, 1970); H_2-H_2 and H_2-He collision-induced absorption (Borysow et al. 1988, Borysow et al. 1989, 2001, Borysow and Frommhold 1989, Borysow 2002, Jørgensen et al. 2000), and H^- free-free and bound-free opacity (John, 1988). Once we obtained a grid of radiative-equilibrium atmospheric models, we post-produced transmission spectra at the GIANO-B spectral resolution.

In general, our grid of HAT-P-11 b models indicates that the strong H_2O absorption bands dominate the transmission spectra at most wavelengths. The scenarios that are more consistent with the detected species required super-solar metallicity, since this enhances the CO_2/H_2O abundance ratio, which in turn makes CO_2 detectable. Similarly, the lower-heat models improve the detection of both NH_3 and CH_4, since both of these species are more abundant than at higher temperatures. However, NH_3 is never the dominant nitrogen bearer at these pressure and temperature conditions. Consequently, only for the highest N/O ratios tested (N/O=0.85) the NH_3 absorption lines impact the transmission spectra (Fig. 3.18), this is well above the solar N/O ratio of 0.14 (Asplund et al.,

2021). Alternatively, one can invoke disequilibrium-chemistry processes to enhance the abundance of NH_3 with respect to the other species (Moses, 2014). Specifically, vertical quenching can transport NH_3 from deeper layers where it is significantly more abundant (Fig. 3.18, bottom-left panel). Combining these constraints with future observations of HAT-P-11 b (e.g. JWST GO proposals 2950 and 4150) has the potential to place stronger constraints on the planet's atmospheric composition and further infer which physical processes shape its atmospheric properties.

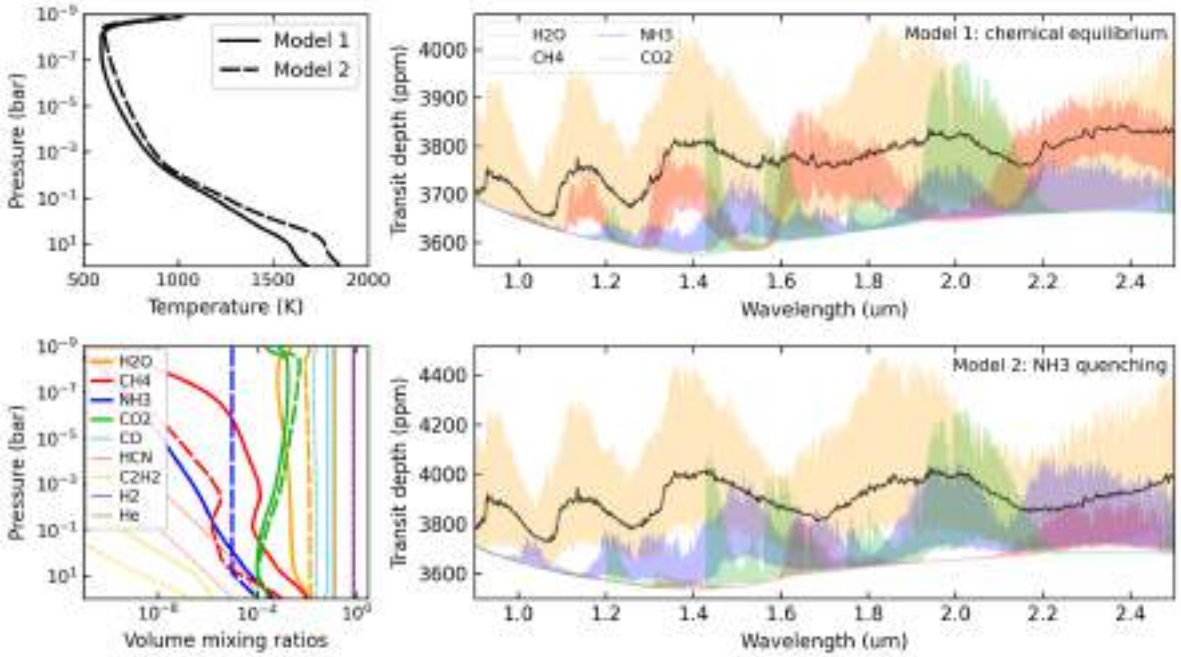

Figure 3.18: Most favourable atmospheric chemical models. Top-left panel: HAT-P-11 b atmospheric temperature-pressure profile corresponding to the most favourable chemical-equilibrium model that shows spectral features from all the detected species, including the tentatively detected ones (Model 1: [M/H]=2.0 dex, C/O=0.9, N/O=0.85, $\beta_{\rm irr}$=0.5; solid line) and to a grid model modified including NH_3 vertical quenching at the 10 bar level (Model 2: [M/H]=1.7 dex, C/O=0.59, N/O=0.14, $\beta_{\rm irr}$=0.5; dashed lines). Bottom-left panel: volume mixing ratios of the dominant chemical species (see legend) as a function of the atmospheric pressure corresponding to Model 1 (solid lines) and to Model 2 (dashed line). Right panels: theoretical transmission spectra of HAT-P-11 b for atmospheres in thermochemical equilibrium (top-right panel) and with NH_3 quenching (bottom-right panel). The coloured curves show the contribution to the synthetic spectra of the four species detected by GIANO-B, including the tentatively detected ones (see legend). The black curve shows a lower-resolution ($R = 500$) spectrum combining the absorption from all atmospheric species in the model.

The right-hand panels in Fig. 3.18 also highlight the complementary potential of combining low- and high-resolution observations for atmospheric characterisation. For a molecule to be detectable, its absorption lines must be at least at the same level as the dominant species in the atmosphere; in this case, they overlap with the H_2O lines, as shown by the coloured curves on the right panels of Fig. 3.18. While this can be the case for several species at high resolution, instead, at low resolution (black curves) many of these individual line features are washed out and blend into the absorption of the dominant species. Therefore, with sufficient S/N, high-resolution observations can pick up molecular features that may go undetected at low resolution.

How the possible presence of planet c could have influenced the formation and the atmospheric composition of planet b

The study of the atmospheric chemical composition of close-in sub-Neptunes and Neptunes, such as HAT-P-11 b, can give important constraints about giant-planet formation in the pebble-accretion scenario. In particular, in this scenario, the formation of these kinds of planets in the inner part of the protoplanetary disc depends on the flux of water ice-rich pebbles drifting inward from the outer regions of the protoplanetary disc (Bitsch et al., 2022). At the water ice line, the ice on the pebbles evaporates enriching the inner part of the disc with water vapour. Substructures and cavities in the protoplanetary disc, for example, due to the formation of a Jupiter-size exoplanet, create pressure bumps that might block the inward migration of pebbles (Banzatti et al., 2020). In this way the presence of a rapidly growing external Jupiter-size companion and its position with respect to the water ice line could influence the chemical composition of the inner protoplanetary disc and therefore of the close-in Neptune: if the giant outer companion forms outside the water ice line it could block the water-rich pebbles before they cross the water ice line and therefore it prevents them from enriching the inner disc with water; if the giant outer companion forms inside the water ice line, the inward migrating pebbles might be blocked after they cross the water ice line and their ice evaporates enriching the inner disc with water. In the first case the close-in Neptune would form in a "dry" environment, in the second case it would form in a "wet" environment accreting a water-rich (up to a few per cent) atmosphere (Bitsch et al., 2022). A third scenario is also possible: the close-in Neptune forms beyond the water ice line by the accretion of a large amount of water ice before migrating inwards. In this case, the Neptunian planet would contain up to 50% of its total mass in water ice ("very wet" Neptune) and the formation time and location of the giant companion would not matter. Also carbon-bearing species can be blocked by growing giant planets, reducing the metal enrichment of the inner disc and therefore the atmosphere of the close-in Neptune. Of course, it is important to underline that protoplanetary discs evolve over time by cooling down, shifting the ice lines inwards over time and therefore both the time and the position of the forming planets inside the protoplanetary disc play an important role in this scenario (e.g. Eistrup and Henning 2022, Eistrup et al. 2016, 2022).

In addition, a late accretion of planetesimals or planet-planet scattering could further influence the atmospheric composition of the Neptunian planet. For example, the high eccentricity of the orbit of HAT-P-11 b could be explained by the interaction with a possible external companion (if any) through planet-planet scattering migration. During the migration, HAT-P-11 b might have been enriched in heavy elements mainly through the accretion of planetesimals present in the protoplanetary disc instead of pebbles (blocked by the external companion). In the orbital region populated by HAT-P-11 b, planetesimals are more effective in delivering O than N to the accreting planet (Turrini et al., 2021). As their accretion acts to lower the high N/O ratio of giant planets formed by pebble accretion, this scenario favours the second atmospheric model we considered in Sect. 3.3.5. As it can be seen, the presence of an external companion could have played a crucial role in the HAT-P-11 b formation, influencing its atmospheric composition, as also highlighted by Chatziastros et al. (2023). Of course, the investigation of the presence of an outer giant companion and its characterisation, as well as the retrieval of the elemental abundance and the elemental ratios (e.g. C/O, N/O) of the chemical species present in the atmosphere of HAT-P-11 b, are crucial to probe the formation history of the planetary system and to enlarge our knowledge about the

planetary formation process.

Planetary radial-velocity semi-amplitude shift investigation

As can be seen from the $K_p - V_{rest}$ maps and from the contour plots, even though the signals of all the molecules for which we obtain a detection (including the tentative ones) cross the expected K_p and V_{rest} values, they span a large range of K_p and V_{rest} values, of the order of $\approx 100\,km\,s^{-1}$ and $\approx 30\,km\,s^{-1}$, respectively. The possible presence of winds and the planetary rotation, combined with other complex atmospheric dynamics effects involving global circulation[10], introduces distortions of molecular line profiles during the transit event that produce shifts of the detection signal peak in K_p and V_{rest} (e.g. Kesseli et al. 2022, Pelletier et al. 2023, Wardenier et al. 2021). In particular, for the case of HAT-P-11 b, Allart et al. (2018) found evidence for a high-altitude wind flowing from the day-side to the night-side of the planet at a velocity of $v_{wind} \approx 3\,km\,s^{-1}$. For what concerns the planetary rotation speed, due to its eccentric orbit, the most probable rotation configuration for HAT-P-11 b is the pseudo-synchronous one (Hut, 1981), in which the planet rotation is synchronous at periastron, implying a rotation period P_{rot} that is shorter than the orbital one by about 29% (for an eccentricity of $e = 0.2577$). In the case of HAT-P-11 b, this rotation period would correspond to an equatorial rotation velocity of $v_{eq} \approx 1\,km\,s^{-1}$. As it can be seen, these kinds of effects have typical velocity scales of a few $km\,s^{-1}$, which is about one order of magnitude smaller than our precision. This implies that we are not sensitive to them. With future more precise measurements, it will be possible to investigate the complex atmospheric dynamics of this warm Neptune.

Even though our results do not allow us to probe the presence of atmospheric dynamics effects, we observe (see Fig. 3.13) a systematic shift of the signal peak at K_p values smaller than the expected one (with the exception of the signal of NH_3 that is at the expected K_p). In order to quantify this shift, we made a weighted average of the K_p values corresponding to the peak of significance for each of the detected molecules (including the tentatively detected one), assuming as the extremes of the $1\,\sigma$ uncertainty intervals the K_p values where the significance drops by $1\,\sigma$ from the peak (after having marginalised over the V_{rest} values). The averaged value of the measured K_p is: $K_{p_{meas}} = 107 \pm 29\,km\,s^{-1}$, which is compatible at $0.54\,\sigma$ with the expected value reported in Table 3.1.

We note that the large uncertainty in K_p, due to the relatively small change in planet RV during transit (a few tens of $km\,s^{-1}$), makes the systematically observed downward shift in K_p of the order of $\approx 10\,km\,s^{-1}$ not significant on a statistical basis. However, we decided to investigate the possible presence of a systematic effect by studying how the uncertainties on e and ω_p affect the retrieved value of K_p and therefore the position of the peak of significance in the $K_p - V_{rest}$ maps. These two parameters are the two main sources of uncertainties in determining the planetary orbital configuration and the atmospheric Doppler signature (Montalto et al., 2011).

We generated $N = 500\,000$ couples of values of eccentricity and planetary argument of periastron $(e; \omega_p)$, extracted randomly from two Gaussian distributions (one for e and one for ω_p) with mean equal to the values of the two parameters that we used in this work ($e = 0.2577$; $\omega_p = 192.0\,deg$) and standard deviation equal to the $1\,\sigma$ uncertainties on these values. For each $(e; \omega_p)$ couple, we

[10]See, for example, the results of the global circulation models that Lewis et al. (2010) obtained for the eccentric warm Neptune GJ 436 b, whose physical and orbital characteristics are similar to those of HAT-P-11 b.

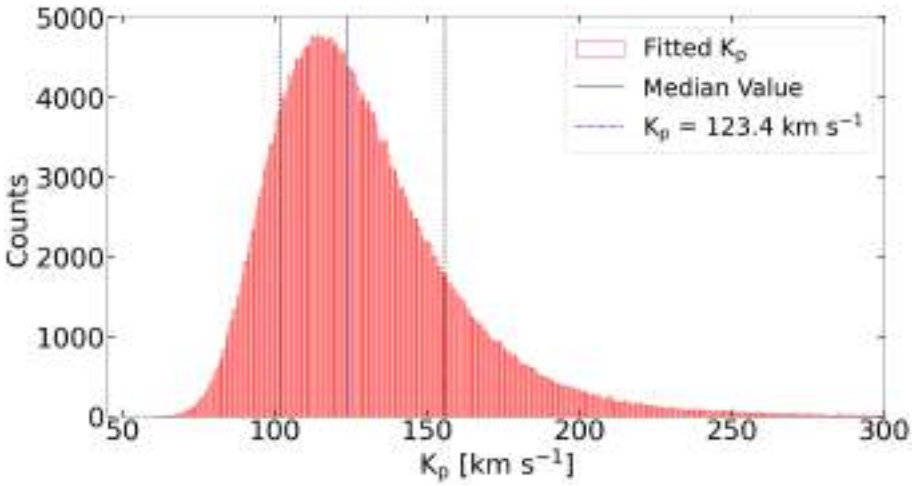

Figure 3.19: Distribution of K_p values fitted on randomly generated planetary RV curves with properties described in the text. The vertical black solid line represents the median value of the distribution, while the 2 vertical black dashed lines represent the 2 quantile values delimiting the 68% ($1\,\sigma$) interval of K_p around the median. The vertical dash-dotted blue line represents the expected K_p value: $\hat{K}_\mathrm{p} = 123.4\,\mathrm{km\,s^{-1}}$. The median and the expected values are coincident and therefore they are not visibly distinguishable.

computed the planetary RV curve during the transit combining equations 1.24 and 3.6:

$$RV = \tilde{K}_\mathrm{p} \cdot [\cos(\nu(t) + \omega_\mathrm{p}) + e \cdot \cos(\omega_\mathrm{p})] \cdot \frac{1}{\sqrt{1-e^2}} \tag{3.7}$$

fixing the $\tilde{K}_\mathrm{p}$ value to the expected one ($\hat{\tilde{K}}_\mathrm{p} = 119.3\,\mathrm{km\,s^{-1}}$). In this way, we simulate different possible orbital configurations according to our limited knowledge of the (e; ω_p) parameters. Subsequently, we fitted the $\tilde{K}_\mathrm{p}$ value for each of the N RV curves keeping fixed the (e; ω_p) values to the ones we used in this work.

Following this procedure, we obtained a distribution of retrieved $\tilde{K}_\mathrm{p}$ values that we transformed into a distribution of K_p values (using the e value reported in Table 3.1) in order to compare them with the K_p value obtained from the significance maps. In Fig. 3.19, we show this distribution. With this procedure we simulated the effect of the choice of (e; ω_p) used in this work on the K_p value estimation from the peak of the CCF signal, taking into account our limited knowledge of the orbital solution. The RV semi-amplitude value is strictly related to the slope of the planetary RV curve. In our data analysis, the slope of the planetary RV curve is not directly fitted but, since it influences the alignment of the CCF trails, it changes the position of the peak of significance in the $K_\mathrm{p} - V_\mathrm{rest}$ maps and therefore the value of K_p we can estimate from the maps.

The first result worth noting is that the K_p distribution is asymmetric with a long tail extending towards $K_\mathrm{p} > 150\,\mathrm{km\,s^{-1}}$ values. In terms of the properties of the distribution, its median value coincides with the expected value and by computing the $1\,\sigma$ interval of this distribution, the estimated value of K_p can be obtained: $\overline{K}_\mathrm{p} = 123^{+32}_{-22}\,\mathrm{km\,s^{-1}}$. This is consistent with the expected value but, as it can be seen, the distribution has not a peak at the expected K_p value, instead, the modal value is: $K_{\mathrm{p_{mode}}} = 114\,\mathrm{km\,s^{-1}}$. This means that the most probable measured K_p value is $\approx 10\,\mathrm{km\,s^{-1}}$ smaller than the expected one, which is consistent with our measured $K_{\mathrm{p_{meas}}}$ value. From this investigation, two important considerations can be made: 1) even if the values of eccentricity and argument of periastron are very precise ($\approx 1\%$), the K_p value that can be extracted from our kind of

data analysis cannot be known at better than $\approx 25\%$, due to the relatively small change in planet RV during transit; 2) this investigation suggests the presence of a systematic effect that we do not fully understand that makes more probable to observe a shift of the signal of the order of $\approx 10\,\mathrm{km\,s^{-1}}$ towards K_p values lower than the expected one, at least in the case of the analysed target, related to the uncertainties about the orbital solution adopted. This has to be taken into consideration for future atmospheric dynamics studies, since in that case precise but also accurate measurements are needed.

3.4 Conclusion

In this work, we revisited the HAT-P-11 planetary system. Using *Kepler* and HIRES at Keck archival data, we refined the orbital and physical parameters of HAT-P-11 b. We further showed that the long-term RV signal with a semi-amplitude of $30\,\mathrm{m\,s^{-1}}$ and periodicity of $\sim 9-10$ yr is more likely due to the stellar activity cycle than to the presence of the planet HAT-P-11 c (Yee et al., 2018). Nonetheless, the Hipparcos–Gaia difference in proper-motion anomaly suggests that an outer-bound companion might still exist, though with S/N $\lesssim 5$. The continuation of RV monitoring and, even more importantly, a combined analysis of RV and future DR4 Gaia astrometric data, will help to characterise this possible companion.

This review of the HAT-P-11 planetary system allowed us to perform a consistent analysis of the atmosphere of planet b at high spectral resolution. Moreover, HAT-P-11 b represents a remarkable target as it can provide a better understanding of the atmospheres of warm Neptunes, which remain to be explored in detail.

In particular, we probed the presence of eight chemical species in the atmosphere of HAT-P-11 b by cross-correlating template atmospheric models with data taken with the NIR GIANO-B high-resolution spectrograph at the 3.58 m TNG telescope during four planetary transits. We detect the presence of two molecular species, H_2O and NH_3, with an S/N of 5.1 and 5.3, and a significance of $3.4\,\sigma$ and $5.0\,\sigma$, respectively. The signals from these molecules have a Doppler signature compatible with the planetary one at $< 1\,\sigma$. We also tentatively detect the presence of CH_4, whose signal has an S/N of 4.8 but a significance level of $2.6\,\sigma$, and of CO_2, with an S/N of 3.0 and a significance level of $3.2\,\sigma$. Further studies are necessary to confirm the presence of CH_4 and CO_2 in the atmosphere of HAT-P-11 b. These results constitute the first simultaneous observation of multiple molecular species in the atmosphere of a warm Neptune-type planet.

Our results are in accordance with the previous water vapour detections made by Fraine et al. (2014), Tsiaras et al. (2018), Chachan et al. (2019), and Cubillos et al. (2022) and with the suggestion of the presence of methane by Chachan et al. (2019) and Cubillos et al. (2022). We hereby enlarge the number of chemical species known to be present in the atmosphere of this exoplanet, which allows us to start exploring plausible physical conditions for the atmosphere of HAT-P-11 b. Our models suggest two scenarios that are more in accordance with the observations: the first model describes an atmosphere in chemical equilibrium with supersolar metallicity and enhanced C/O and N/O ratios relative to solar values; the second model describes an atmosphere with disequilibrium chemistry (i.e. NH_3 vertical quenching), lower metallicity, and C/O and N/O ratios close to solar values.

We note that the significance peak of the detected species (including the tentatively detected

ones) is shifted by $\approx 10\,\mathrm{km\,s^{-1}}$ towards K_p values smaller than the expected one ($\hat{K}_\mathrm{p} = 123.4\,\mathrm{km\,s^{-1}}$). Indeed the average value of the planetary RV semi-amplitude estimated from our significance maps is $K_{\mathrm{p_{meas}}} = 107 \pm 29\,\mathrm{km\,s^{-1}}$, which is compatible at 0.54 σ with the expected one due to the large uncertainty. We show how a small error ($\approx 1\%$) on the eccentricity and argument of periastron parameters translates into a large uncertainty ($\approx 25\%$) on the retrieved K_p parameter due to the small change in RV during the transit, and can introduce the observed systematic K_p shift.

The next step in our analysis will be to statistically retrieve the chemical physical properties of the atmosphere of HAT-P-11 b (e.g. the elemental abundances and the temperature-pressure profile) in order to better characterise its atmosphere and to constrain its formation path. Finally, a future combination of high- and low-resolution observations will improve the characterisation of the atmosphere of this target and our knowledge about warm Neptunes.

Role of the Ph.D. candidate in the work

As the leading author of this work, published in A&A as Basilicata et al. (2024a), I have coordinated the whole work. In particular, I performed the entire atmospheric analysis, reducing the GIANO-B raw data and extracting the planetary signal with the cross-correlation analysis. I also performed the different statistical tests to assess the robustness of the detections. I performed the atmospheric analysis by using the pipeline developed by Dr. Paolo Giacobbe, who supervised this work and, together with Prof. Matteo Brogi, gave important advices about the data analysis approach. For what concerns the atmospheric chemical modelling, it was performed by Dr. Patricio E. Cubillos. The analysis of *Kepler* light curves was conducted by Dr. Gaetano Scandariato and Dr. Vikash Singh, while the RV analysis was conducted by Dr. Aldo S. Bonomo. Finally, Dr. Alessandro Sozzetti performed the PMA sensitivity analysis.

Chapter 4

Detection of water and preliminary characterisation of the atmospheres of the two hot Jupiters KELT-8 b and KELT-23 Ab

In this chapter, I describe the work reported in a paper submitted to the Astronomy & Astrophysics journal as Basilicata et al. (2024b) (article reference: AA52733-24). In this work, we measure the atmospheric signal of the two hot Jupiters KELT-8 b and KELT-23 Ab, and present the first investigation of the chemical-physical properties of their atmospheres.

Hot Jupiters are among the most suitable targets for atmospheric studies. Expanding the number of hot gaseous giant planets with atmospheric characterisation can improve our understanding of the chemical-physical properties of their atmospheres as well as the formation and evolution of these extreme planets. In this work, we use high-resolution spectroscopy in the near-infrared (NIR) to search for chemical signatures in the atmosphere of the two hot Jupiters KELT-8 b and KELT-23 Ab, and perform a first characterisation of their atmospheric properties. For each target, we analysed their transmission spectra with GIANO-B at the TNG. We searched for atmospheric signals by cross-correlating the data with synthetic transmission spectra. In order to characterise the chemical-physical properties of the atmosphere of both planets, we ran two different atmospheric retrievals for each dataset: a retrieval assuming chemical equilibrium and a "free-chemistry" retrieval, in which the abundance of each molecule could vary freely. We detect for the first time the atmospheric signal of the two planets. In particular, we detect water vapour (H_2O) in both the atmospheres of KELT-8 b and KELT-23 Ab with an S/N = 6.6 and S/N = 4.2, respectively. The two retrievals indicate a water-rich atmosphere for both targets. In the case of KELT-8 b, we determine a water volume mixing ratio of $\log_{10}(\mathrm{VMR}_{\mathrm{H_2O}}) = -2.07^{+0.53}_{-0.72}$, a metallicity $[\mathrm{M/H}] = 0.77^{+0.61}_{-0.89}$ dex, and a sub-solar C/O ratio ($\mathrm{C/O} \leq 0.30$, at $2\,\sigma$). For KELT-23 Ab, we find $\log_{10}(\mathrm{VMR}_{\mathrm{H_2O}}) = -2.26^{+0.75}_{-1.24}$, a metallicity $[\mathrm{M/H}] = -0.42^{+1.56}_{-1.35}$ dex, and a C/O ratio ≤ 0.78 (at $2\,\sigma$). Finally, by comparing the atmospheric chemical characteristics of the targets with those of the host stars, we suggest that, for both planets, the accretion of gaseous material occurred within the H_2O snowline in a pebble-rich disk enriched in oxygen due to sublimation of water ice from the inward-drifting pebbles.

4.1 Introduction

The study of exoplanetary atmospheres plays a crucial role in the exoplanets' characterisation process. For example, the study of relative abundances of atmospheric species can help to constrain the formation and evolution paths experienced by an exoplanet (e.g. Öberg et al. 2011, Madhusudhan et al. 2014, Mordasini et al. 2016, Madhusudhan 2019, Banzatti et al. 2020, Bitsch et al. 2022, Pacetti et al. 2022). Moreover, by studying the chemical properties of exo-atmospheres, we can place stronger constraints on the internal composition of planets, breaking possible degeneracies from the measurement of the bulk density alone (e.g. Madhusudhan et al. 2020). The exo-atmosphere investigation also offers the opportunity to study environments without analogues in the Solar System. This is the case, for example, of hot Jupiters, which are Jupiter-size planets with orbital periods $P_{\rm orb} < 10$ days and equilibrium temperatures $T_{\rm eq} \gtrsim 1\,000$ K. Inflated hot Jupiters are ideal targets for atmospheric studies, in particular in transmission, because of their large radii and thus atmospheric scale heights, which produce relatively high atmospheric transmission-signal amplitudes Δ:

$$\Delta = 2 \cdot \frac{R_{\rm p} \cdot H_{\rm s}}{R_\star^2}\,, \tag{4.1}$$

where $R_{\rm p}$ is the planetary radius, $H_{\rm s}$ is atmospheric scale height, and $R_\star$ is the stellar radius. As a reference, for HD 209458 b, a typical hot-Jupiter, $\Delta \sim 160$ ppm (assuming an atmospheric mean molecular weight of $\mu = 2.3\,{\rm g\,mol^{-1}}$, representative of H/He-dominated atmospheres; Lecavelier Des Etangs et al. 2008).

High-resolution spectroscopy (HRS) from ground-based facilities (see, e.g. Birkby 2018 for a review), proved to be a valid technique to probe atmospheric features of warm- and hot-giant planets, because a large spectral resolving power ($R \gtrsim 25\,000$) allows to identify the characteristic spectral features of the different chemical components of an exo-atmosphere and to detect their Doppler shift due, for instance, to atmospheric dynamical effects.

Hot (and ultra-hot) Jupiters are the most studied targets with high-resolution spectroscopy. In the last years, the sample of hot-giant planets, whose atmospheres have been investigated, has increased and we are entering an era of comparative atmospheric studies of exoplanets (e.g. Gandhi et al. 2023). In this frame, increasing the statistical sample of hot Jupiters with atmospheric characterisation is important for improving our understanding of the main physical and chemical mechanisms driving their atmospheres and their formation (e.g. Dawson and Johnson 2018, Madhusudhan 2019).

In this work, we searched for the atmospheric signature of the two hot-Jupiter planets KELT-8 b (Fulton et al., 2015) and KELT-23 Ab (Johns et al., 2019), which both orbit Sun-like stars. Both targets were discovered using data from the Kilodegree Extremely Little Telescope survey (KELT, Pepper et al. 2007) and confirmed with photometric and spectroscopic follow-up observations. As the name suggests, KELT-23 Ab orbits around a star that is a member of a wide binary system, composed of KELT-23 A (aka BD+66 911 A; aka 2MASS J15283520+6621314) and KELT-23 B (aka BD+66 911 B; aka 2MASS J15283577+6621288), with a minimum mutual distance between the components of 570 au (Johns et al., 2019). In Table 4.1[1] we report a summary of the physical and

[1]The symbols of the parameters listed in the table have the following meanings: $B_{\rm T}$, $V_{\rm T}$ - apparent magnitudes in the Tycho photometric bands; J, H, K - apparent magnitudes in the 2MASS photometric bands; $W1$, $W2$, $W3$, $W4$ - apparent magnitudes in the WISE photometric bands; $M_\star$ - stellar mass; $R_\star$ - stellar radius; $T_{\rm eff}$ - stellar effective temperature; [Fe/H] - stellar iron abundance; $\log_{10}$(g) - logarithm of surface stellar gravity; $V_{\rm sys}$ - systemic radial velocity; $M_{\rm p}$ - planetary mass; $R_{\rm p}$ - planetary radius; $\rho_{\rm p}$ - planetary mean density; $T_{\rm eq}$ - planetary equilibrium

orbital parameters of the two planetary systems.

Both the targets are inflated versions of Jupiter; indeed, their low density (less than half Jupiter's) reflects the fact that they have a radius larger than Jupiter ($\sim 1.6\,R_{\rm J}$ and $\sim 1.3\,R_{\rm J}$, for KELT-8 b and KELT-23 Ab, respectively) and a slightly smaller mass ($\sim 0.83\,M_{\rm J}$ and $\sim 0.94\,M_{\rm J}$, for KELT-8 b and KELT-23 Ab, respectively). The two hot atmospheres have a large atmospheric scale height ($H_{\rm s} = 708\,$km for KELT-8 b and $H_{\rm s} = 406\,$km for KELT-23 Ab, assuming $\mu = 2.3\,{\rm g\,mol^{-1}}$), which makes the two hot Jupiters ideal targets for atmospheric investigation. Even if KELT-23 Ab has an $H_{\rm s}$ that is smaller than that of KELT-8 b, the host-star has a smaller radius too, resulting in a similar atmospheric transmission signal amplitude ($\Delta = 167\,$ppm for KELT-8 b and $\Delta = 156\,$ppm for KELT-23 Ab). Although these targets are promising candidates for atmospheric investigations, there are no atmospheric studies in the literature for any of them.

The aim of this work is to search for the atmospheric signal of KELT-8 b and KELT-23 Ab in transmission and perform a first investigation of the chemical-physical properties of their atmospheres under simple assumptions. In Sect. 4.2 we describe the observations, the data reduction process, and the analyses we performed for the atmospheric characterisation of the targets. In Sect. 4.3, we report the results of our atmospheric studies, while in Sect. 4.4, we discuss the results. Finally, in Sect. 4.5, we report our conclusions and future perspectives.

4.2 Methods

4.2.1 Observations and data reduction

We simultaneously collected the data with both GIANO-B (wavelength range: $950 - 2\,450\,$nm, $R \approx 50\,000$) and HARPS-N (wavelength range: $383 - 693\,$nm, $R \approx 115\,000$) high-resolution spectrographs, in the GIARPS configuration (Claudi et al., 2017), at the Telescopio Nazionale Galileo (TNG), as part of the Global Architecture of Planetary Systems (GAPS) Project[2]. We used the HARPS-N spectra extracted with the DRSv3.7 online pipeline to redetermine the stellar atmospheric and physical parameters of KELT-8 (Sect. 4.2.3). For the characterisation of the atmospheres of KELT-8 b and KELT-23 Ab, we only used the near-infrared (NIR) GIANO-B data, as we were primarily concerned with estimating the volatile content of the atmospheres via molecular signatures.

The observations were taken with the nodding ABAB acquisition mode in which the target and sky spectra were taken in pairs while alternating between two nodding positions along the slit (A and B) separated by $5''$, allowing an optimal subtraction of the detector noise and background.

For KELT-8 b, two transit observations were available (i.e. 23 June 2020 and 19 July 2020). However, during the second transit, the weather conditions were not optimal due to the presence of calima (i.e. a meteorological phenomenon that occurs when fine sand and dust particles from the Sahara desert are lifted into the atmosphere and transported by winds), which lowered the

temperature; $P_{\rm orb}$ - orbital period; T_0 - transit epoch; T_{14} - transit duration; i - orbital inclination; e - orbital eccentricity; a - orbital semi-major axis; $K_{\rm p}$ - planetary radial-velocity semi-amplitude. The left reference numbers are for the parameters of the KELT-8 system, and the right ones for those of the KELT-23 A system. The references of the values in the table are: 1. Fulton et al. (2015); 2. Johns et al. (2019); 3. Høg et al. (2000); 4. Cutri et al. (2003); 5. Cutri et al. (2013); 6. This work and Baratella et al. (in prep.); 7. Gaia Collaboration et al. (2023); 8. Kokori et al. (2023); 9. Bonomo et al. (2017).

[2] `https://theglobalarchitectureofplanetarysystems.wordpress.com/`

Table 4.1: Main physical and orbital parameters of the KELT-8 and KELT-23 A systems.

Parameter	KELT-8	KELT-23 A	References
Stellar Parameters			
Spectral Class	G2 V	G2 V	1, 2
B_T	11.713 ± 0.057	11.029 ± 0.049	3, 3
V_T	10.925 ± 0.048	10.376 ± 0.039	3, 3
J	9.586 ± 0.026	9.208 ± 0.032	4, 4
H	9.269 ± 0.032	≥ 8.951	4, 4
K	9.177 ± 0.021	≥ 8.904	4, 4
$W1$	8.981 ± 0.021	8.754 ± 0.022	5, 5
$W2$	8.983 ± 0.019	8.789 ± 0.020	5, 5
$W3$	8.928 ± 0.028	8.766 ± 0.022	5, 5
$W4$	8.533 ± 0.339	8.564 ± 0.202	5, 5
$M_\star$ [$M_\odot$]	$1.131^{+0.084}_{-0.079}$	$0.944^{+0.060}_{-0.054}$	6, 2
$R_\star$ [$R_\odot$]	1.391 ± 0.025	0.996 ± 0.015	6, 2
$T_{\rm eff}$ [K]	$5\,742 \pm 44$	$5\,899 \pm 49$	6, 2
[Fe/H] [dex]	0.26 ± 0.10	$-0.105^{+0.078}_{-0.077}$	6, 2
$\log_{10}$(g) [$\log_{10}$, cgs]	4.19 ± 0.08	$4.417^{+0.026}_{-0.025}$	6, 2
$V_{\rm sys}$ [km s^{-1}]	-34.51 ± 0.20	-14.99 ± 0.30	7, 7
Parallax [mas]	5.074 ± 0.011	7.871 ± 0.013	7, 7
Distance [pc]	$197.10^{+0.42}_{-0.44}$	127.04 ± 0.21	7, 7
Age [Gyr]	$6.4^{+2.9}_{-2.0}$	$6.3^{+3.5}_{-3.2}$	6, 2
Planetary Parameters			
$M_{\rm p}$ [$M_{\rm J}$]	0.83 ± 0.12	$0.938^{+0.048}_{-0.044}$	6, 2
$R_{\rm p}$ [$R_{\rm J}$]	1.586 ± 0.046	1.323 ± 0.025	6, 2
$M_{\rm p}$ [$M_\oplus$]	264 ± 38	298^{+15}_{-14}	6, 2
$R_{\rm p}$ [$R_\oplus$]	17.40 ± 0.50	14.83 ± 0.28	6, 2
$\rho_{\rm p}$ [g cm^{-3}]	0.276 ± 0.047	$0.503^{+0.039}_{-0.036}$	6, 2
$T_{\rm eq}$ [K]	$1\,675^{+61}_{-55}$	$1\,561 \pm 20$	1, 2
$P_{\rm orb}$ [days]	3.24408156 ± 0.0000010	$2.25528745 \pm 0.00000018$	8, 8
T_0 [BJD$_{\rm TDB}$]	$2\,457\,986.46737 \pm 0.00026$	$2\,458\,918.461247 \pm 0.000021$	8, 8
T_{14} [hr]	$3.466^{+0.082}_{-0.079}$	2.381 ± 0.022	1, 2
i [deg]	$82.65^{+0.81}_{-1.00}$	$85.37^{+0.31}_{-0.30}$	1, 2
e	≤ 0.047	≤ 0.05	9, 2
a [au]	0.0382 ± 0.0025	$0.03302^{+0.00068}_{-0.00064}$	6, 2
$K_{\rm p}$ [km s^{-1}]	149 ± 25	159 ± 11	6, 2

signal-to-noise ratio (S/N). Moreover, GIANO-B showed greater instability than during the first night. For these reasons, we chose to include only the first data set in this analysis. On 23 June 2020, 70 spectra were recorded (with an exposure time $t_{\rm exp} = 200\,{\rm s}$) and the target was observed at a mean airmass of 1.03.

For KELT-23 Ab, only one complete transit observation was available (i.e. 15 April 2023). A second transit was observed on 24 April 2023, but it was only partial due to an instrumental problem. Therefore, we did not include it in our analysis. On 15 April 2023, 60 spectra (with $t_{\rm exp} = 200\,{\rm s}$) were recorded, and the target was observed at a mean airmass of 1.27. See Table 4.2 for a schematic log of the observations used for our analysis.

The raw spectra were dark-subtracted, extracted, and calibrated in wavelength, using the GOFIO pipeline Python-3 version (Rainer et al., 2018). The wavelength calibration performed by GOFIO is based on observing the spectrum of a U-Ne lamp as a template. Since the lamp is only observed at the end of the night to avoid persistence on the camera, the GOFIO wavelength solution is not sufficiently accurate and is expected to shift and jitter during the observations due to the mechanical instability of the instrument. In order to correct the spectral drift of the instrument, we aligned all the spectra of a single night to a common reference frame via cross-correlation with a time-averaged observed spectrum of the target used as a template. Thanks to this correction, we achieved a residual shift of the spectra well below $0.3\,{\rm km\,s^{-1}}$ (approximately 1/10th of a pixel) for most of the spectral orders. Finally, we refined the wavelength calibration by matching a set of telluric lines in the time-averaged observed spectrum with a high-resolution atmospheric transmission model of the Earth generated via the ESO Sky Model Calculator (Noll et al., 2012) and solving for the pixel-wavelength relation with a fourth-order polynomial fit.

The GIANO-B spectral range covers the Y, J, H, K bands in 50 spectral orders (order 0 is the reddest and order 49 is the bluest). For our analysis, we excluded a fixed set of spectral orders dominated by tellurics (8-11, 23-26, 34-37) and the Y band (orders 38-49) in which GIANO-B has a characteristic drop of throughput. Finally, in each observing night, we excluded a few orders with high residual drift, or for which the refined wavelength calibration procedure failed (i.e. orders number 3, 4, 30 for KELT-8 b spectra and 4, 13, 15, 18, 30-32 for KELT-23 Ab spectra). In this way, we used a spectral range that is as more uniform as possible among the nights and in which the small differences are mainly due to the stability of the pixel-wavelength solution, which for a few orders depends on the S/N of the observations.

Table 4.2: Log of the GIANO-B observations of KELT-8 b and KELT-23 Ab.[a]

Target	Night	Airmass	$N_{\rm obs}$	$t_{\rm exp}$ [s]	$({\rm S/N})_{\rm avg}$	$({\rm S/N})_{\rm min}$ to $({\rm S/N})_{\rm max}$
KELT-8 b	23 June 2020	$1.12 \rightarrow 1.00 \rightarrow 1.06$	70	200	30	$4 - 51$
KELT-23 Ab	15 April 2023	$1.31 \rightarrow 1.26 \rightarrow 1.27$	60	200	22	$5 - 36$

Notes. [(a)]From left to right we report: the date at the start of the observing night; the airmass during the planetary transit; the number of observed spectra $N_{\rm obs}$; the exposure time per spectrum $t_{\rm exp}$; the signal-to-noise ratio averaged across the whole spectral range $({\rm S/N})_{\rm avg}$; the range of signal-to-noise ratios $({\rm S/N})_{\rm min}$ to $({\rm S/N})_{\rm max}$ in the individual spectral orders.

4.2.2 Telluric and stellar spectra removal procedure

In order to remove telluric and stellar contamination we employed a principal component analysis (PCA), which is often used in HRS analyses (e.g. de Kok et al. 2013) and successfully applied to

GIANO-B data in previous works (e.g. Basilicata et al. 2024a, Carleo et al. 2022, Giacobbe et al. 2021).

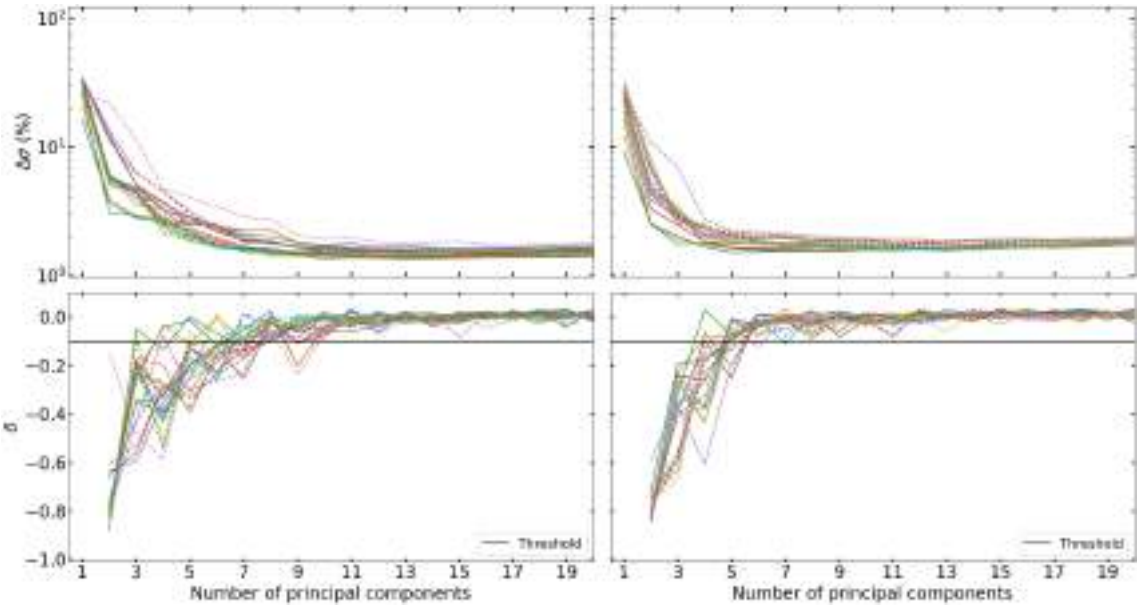

Figure 4.1: Variation of the standard deviation (σ) of the residuals as a function of the number of principal components removed via PCA for the KELT-8 b (left panels) and the KELT-23 Ab (right panels) dataset. Top panels: relative variation $\Delta\sigma$ of the standard deviation of the residuals (expressed in percentage value and reported in logarithmic scale for a better visualisation) in the different spectral orders (coloured solid and dashed lines). Bottom panels: relative variation of $\Delta\sigma$ (δ) in the different spectral orders (coloured solid and dashed lines). The solid black horizontal line represents the -0.1 threshold on δ used to identify the minimum number of principal components to select in order to remove the telluric and stellar contamination.

The PCA was applied to each spectral order, considered as an $M \times N$ data matrix (with $M = 60 - 70$ spectra and $N = 2048$ pixels). We performed the telluric removal procedure following the method described in Sect. 3.3.2, with the exception that we adopted a different criterion to select the appropriate number of principal component to remove. Since in the literature, there is no agreement on how to choose the appropriate number of principal components to employ in the telluric removal procedure, we explored a different method with respect to the one used for the analysis of HAT-P-11 b, with the aim to apply a telluric correction as more uniform as possible among the different orders. In order to choose the appropriate number of principal components to remove, we followed the method suggested by Spring & Birkby (private communication). In particular, for each spectral order, we computed the relative variation of the standard deviation (σ) of the residuals by gradually increasing the number of components removed from the data: $\Delta\sigma = \frac{\sigma_{i-1} - \sigma_i}{\sigma_{i-1}}$, with i = the i-th number of principal components removed. As can be seen from Fig. 4.1, the $\Delta\sigma$ of the residuals gradually decreases when the number of principal components removed increases, down to a plateau, as expected. In order to find the minimum number of components at which the standard deviation of the residuals does not change in a significative way (i.e. the plateau is reached), we studied the relative variation of $\Delta\sigma$ (indicated with the symbol δ) to see where this variation approaches zero. We placed a threshold at -0.1 and selected the minimum number of principal components for which $-0.1 < \delta < 0$ for all the spectral orders (see Fig. 4.1). Following this procedure, the number of principal components we decided to remove for the two datasets is: 10 for the 23 June 2020 dataset and 9 for the 15 April 2023 dataset.

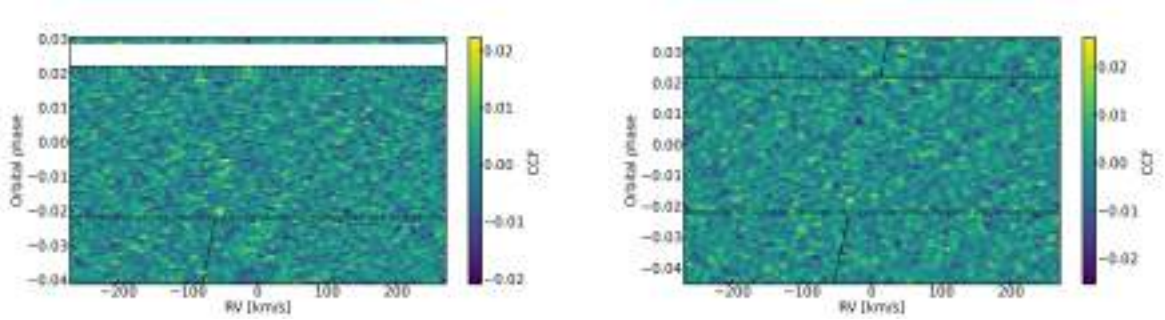

Figure 4.2: Example of CCF values as a function of the orbital phase computed by cross-correlating the model containing only H_2O with the data of 23 June 2020 (left panel) and 15 April 2023 (right panel). The horizontal dashed lines represent the transit ingress and egress while the dash-dotted line represents the expected CCF peak trail due to the planetary motion, as measured in the observer rest frame. The expected CCF peak trail in transit is not represented for clarity. As it is visible, no telluric residuals are visible by eye at RV $= 0\,\mathrm{km\,s^{-1}}$ in both datasets. The white horizontal band in the left panel corresponds to a lack of out-of-transit spectra.

Once we applied the telluric correction, we visually inspected the map of cross-correlation function (CCF) values as a function of the orbital phase obtained with the model of water that we used for the CCF analysis (see Sect. 4.2.4), as a further check. As it is visible by the maps in Fig. 4.2, there are no visible telluric residuals at a radial-velocity RV $= 0\,\mathrm{km\,s^{-1}}$. It is worth noting that due to the combined effect of Earth's velocity around the barycenter of the Solar System (barycentric velocity) and velocity of the centre of mass of the star-planet systems with respect to the Earth (systemic velocity), the planetary signals are shifted from the telluric rest-frame in terms of RV (at $\sim -36\,\mathrm{km\,s^{-1}}$ for KELT-8 b and $\sim -11\,\mathrm{km\,s^{-1}}$ for KELT-23 Ab, at the mid-transit point), during most of the transit and thus are less affected by the telluric contamination.

4.2.3 Update of the KELT-8 system parameters

Since the search for and interpretation of atmospheric signals (Sect. 4.2.4 and Sect. 4.2.5) depends on the system (stellar and planetary) parameters, we first compared the parameters of both host stars KELT-8 and KELT-23 A given in the discovery papers (Fulton et al., 2015, Johns et al., 2019) with those reported by Gaia DR3 (Gaia Collaboration et al., 2023). After noticing a discrepancy between the KELT-8 mass and radius in Fulton et al. (2015) ($M_\star = 1.211^{+0.078}_{-0.066}$ $\mathrm{M_\odot}$ and $R_\star = 1.67^{+0.14}_{-0.12}$ $\mathrm{R_\odot}$) and those provided by Gaia ($M_\star = 0.93 \pm 0.04$ $\mathrm{M_\odot}$ and $R_\star = 1.37 \pm 0.03$ $\mathrm{R_\odot}$), we decided to recompute them.

We first redetermined the stellar atmospheric parameters (effective temperature $T_{\rm eff}$, surface gravity $\log g$, and iron abundance [Fe/H]) of KELT-8 through the same procedure as other works of the GAPS Program (see Biazzo et al. 2022 and references therein). Specifically, we considered the co-added spectrum of the target built from the collected individual HARPS-N spectra and used the *qoyllur-quipu* (q2[3]) tool developed by Ramírez et al. (2014). This code allows the iterative use of the 2019 MOOG version (Sneden et al., 2012) to derive the stellar parameters and to measure the elemental abundances through the standard equivalent width (EW) method (i.e., $T_{\rm eff}$ and $\log g$ obtained by imposing the excitation/ionisation equilibria of FeI and FeII lines). The EWs of the iron transitions taken from the line list published in Biazzo et al. (2022) were measured using the

[3] `https://github.com/astroChasqui/q2`

software ARES v2 (Sousa et al., 2015), which automatically fits a Gaussian profile to the observed line profile. However, lines stronger than ∼120 mÅ were manually checked with the task *splot* of IRAF[4] since these are better reproduced with a Voigt profile. We then excluded from the analysis those lines with uncertainties larger than 10%. Regarding the model atmospheres, we used the plane-parallel models linearly interpolated from the ATLAS9 grids of Castelli and Kurucz (2003), computed with solar-scale chemical composition and new opacities (ODFNEW). The final stellar atmospheric parameters ($T_{\rm eff}$, $\log g$, and [Fe/H][5]) are reported in Table 4.1.

We determined the mass, radius, and age of the host star by modelling the stellar Spectral Energy Distribution (sampled with the magnitudes given in Table 4.1) and using the MESA Isochrones and Stellar Tracks (Paxton et al., 2015). Specifically, we computed their best values and 1σ uncertainties from the medians and 68.3% confidence intervals of the posterior distributions as obtained with the `EXOFASTv2` tool in a Bayesian differential evolution Markov chain Monte Carlo (DE-MCMC) framework (Eastman, 2017, Eastman et al., 2019). For this purpose, we adopted Gaussian priors on the spectroscopically determined $T_{\rm eff}$ and [Fe/H] as well as on the Gaia DR3 parallax (Gaia Collaboration et al., 2023). The derived stellar radius is compatible with that provided by Gaia within 1σ, while the stellar mass is more in agreement with that found by Fulton et al. (2015). We then redetermined the parameters of the hot Jupiter KELT-8 b by using the updated stellar parameters and the transit and radial velocity parameters given in Fulton et al. (2015) (see Table 4.1).

4.2.4 Search for atmospheric signals through cross-correlation analysis

In order to probe the presence of an atmosphere around the two hot Jupiters, we first searched for the presence of water vapour (H_2O), the most common primary molecular species in hot-giant planets' atmosphere in a large range of atmospheric temperatures (Madhusudhan, 2012). We built a model for each planet using the petitRADTRANS code (Mollière et al., 2019), assuming an isothermal atmosphere at the equilibrium temperature reported in Table 4.1, computed between 10 and 10^{-8} bar in pressure. The model assumes constant-with-altitude abundance (volume mixing ratio, VMR) profiles for molecular hydrogen ($\mathrm{VMR_{H_2}} = 0.855$), helium ($\mathrm{VMR_{He}} = 0.145$) and water ($\mathrm{VMR_{H_2O}} = 10^{-3}$). Although single-species models do not match any specific chemical scenarios, this was the simplest framework we could adopt to probe the presence of H_2O and, thus, of trace species in addition to H_2 and He. After having detected the atmospheric H_2O signal, we also tried to search for the signal of other secondary chemical species, including CO, CH_4, HCN, C_2H_2, CO_2, and NH_3, building single-species models following the method described before. We note that while H_2O is expected to provide most of the opacity and therefore searching for water alone should still result in a single-species model with meaningful continuum, a single-species model with minor species alone will *not* have the right continuum, and thus they are uninformative to infer the bulk composition of the planet. They can only be used in this context to search for the presence of a species.

To search for the atmospheric signature, for each planet, we computed the CCF between the models and the data. The CCF was evaluated by shifting the model in wavelength on a fixed grid of

[4]IRAF is distributed by the National Optical Astronomy Observatories, which are operated by the Association of Universities for Research in Astronomy, Inc., under the cooperative agreement with the National Science Foundation. NOAO stopped supporting IRAF, see `https://iraf-community.github.io`.

[5][Fe/H]=logA(Fe)$_\star$-logA(Fe)$_\odot$, where logA(Fe)$_\odot$ is the solar value taken from Table 2 in Biazzo et al. (2022).

RV lags:

$$\Delta\mathrm{RV} = \mathrm{c} \cdot \frac{\Delta\lambda}{\lambda}\,, \tag{4.2}$$

where c is the speed of light and λ is the wavelength of any spectral line. We explored a range of RV lags from $-270\,\mathrm{km\,s^{-1}}$ to $+270\,\mathrm{km\,s^{-1}}$, in steps of $0.1\,\mathrm{km\,s^{-1}}$. The numeric computation was performed using the C_CORRELATE PXY(L) IDL function[6], with null lag ($L = 0$), since the RV lags were applied to the wavelength array associated with the model. For each lag, the model was interpolated (via spline interpolation) on the same wavelength array of data before computing the CCF. The CCFs calculated for each spectral order were co-added to obtain a single CCF for each exposure of each night.

High-resolution measurements of exoplanet atmospheres are sensitive to the Doppler motion of the atmospheric spectral lines. In absence of atmospheric dynamical effects, this time-dependent Doppler shift is made up of three RV components, according to Eq. (1.23). Since the orbital eccentricity of the two planets is negligible (i.e. compatible with 0 at $< 3\,\sigma$, Bonomo et al. 2017, Fulton et al. 2015, Johns et al. 2019), we assumed a circular orbit for both targets. Therefore, the planetary radial velocity term $V_\mathrm{p}(t)$ reduces to Eq. (1.25).

By subtracting different orbital solutions from the CCF trail (in our analysis we explored different values of the planetary radial-velocity semi-amplitude K_p, defined in Eq. 1.26), a different alignment of the CCF peaks as a function of the orbital phase is obtained. Summing in phase all the CCF values for each trial K_p, we built the $K_\mathrm{p} - V_\mathrm{rest}$ maps, to search for a detection of the atmospheric signal. From Table 4.1, the predicted values of K_p are $K_\mathrm{p} = 149 \pm 25\,\mathrm{km\,s^{-1}}$ for KELT-8 b and $K_\mathrm{p} = 159 \pm 11\,\mathrm{km\,s^{-1}}$ for KELT-23 Ab. In this work, we explored a range of K_p that spans from 0 to $270\,\mathrm{km\,s^{-1}}$ in steps of $1.0\,\mathrm{km\,s^{-1}}$.

We took advantage of the high sampling of the CCF (larger than the GIANO-B pixel scale of $\sim 3\,\mathrm{km\,s^{-1}}$) for a precise shift of the CCF trails into the planetary rest frame. However, in order to avoid the use of correlated data points in our analysis, we binned the CCF values in RV using a bin width of $3.1\,\mathrm{km\,s^{-1}}$. We took the median of the CCF values in each RV bin as the value of the CCF associated with each bin, before co-adding the CCF values in phase for each trial K_p. The bin width is slightly wider than the one used in Sect. 3.3.3 because different independent measurements of the GIANO-B spectral resolving power seemed to point towards a pixel scale with small differences across the large spectral range and, in particular, slightly larger than $2.7\,\mathrm{km\,s^{-1}}$. For this reason, we conservatively chose to use a slightly larger bin width, which could be more representative of the true spectral resolving power of GIANO-B. It is worth noting that such a small difference in the bin width (i.e. $0.4\,\mathrm{km\,s^{-1}}$) does not affect in a significative way the results of our analysis (i.e. the differences in the significance of the detections are $\sim 0.1\,\sigma$).

4.2.5 Temperature and abundance retrieval analysis

The CCF analysis provides us with a catalogue of the molecular species present in the atmosphere. However, it cannot determine the abundance of the species found nor the physical characteristics, such as temperature, of the atmospheric layers that most contribute to the observed transmission spectrum. To investigate the chemical and physical properties of the atmosphere of KELT-8 b and KELT-23 Ab, we need an atmospheric retrieval in a Bayesian framework.

[6] `https://www.nv5geospatialsoftware.com/docs/C_CORRELATE.html`

As common in the literature (e.g. Boucher et al. 2023, Kasper et al. 2021, 2022, Line et al. 2021), our framework is based on the cross-correlation-to-log-likelihood remapping (Brogi and Line, 2019b, Gibson et al., 2020). In particular, we employed the likelihood equation described in Section 3.3 of Gibson et al. (2020), but we decided not to fit the two parameters α (the scaling factor of the model) and β (a scaling term for the white noise). We did not fit α because the scale height of the atmosphere is included in our parametrisation of the atmospheric model; therefore, there are no physical reasons to rescale the model. We did not fit β because we directly estimated the error of each spectral channel from the data by computing the standard deviation of the time sequence of each spectral channel. In this way, the error already includes the possible presence of uncorrelated (e.g. astrophysical) jitter. Both our approach and the one by Gibson et al. (2020) rely on the same assumption, namely the absence of correlated noise in the residual spectra.

To model the exoplanet atmospheres we assumed a one-dimensional (1D) isothermal atmosphere (with temperature T_0) in hydrostatic equilibrium. The planetary radius corresponding to the atmospheric pressure of 0.1 bar was set equal to the value shown in Table 4.1 and not retrieved. This is a common approximation for high-resolution retrievals (e.g. Boucher et al. 2023) that can be avoided when low-resolution measurements are available. We also considered a grey cloud layer by parameterising the pressure (P_c) above which the atmosphere becomes completely opaque.

We modelled the chemical composition following two distinct approaches: an equilibrium chemistry approach and a "free-chemistry" approach. In the first one, chemical equilibrium is assumed and the VMR of each element is derived by the chemical network *Chemcat*[7] (Cubillos et al. in prep.) and varies accordingly with two parameters: the metallicity ([M/H]) referred to the solar value and the carbon-to-oxygen (C/O) ratio. For each trial [M/H], the C/O ratio is varied by changing only the carbon abundance, which is scaled relatively to the oxygen abundance. In the "free-chemistry" approach, the VMR of each molecule corresponds to one parameter and can vary freely.

We stress that while in "free-chemistry" the VMR profiles are assumed constant-with-altitude, in chemical equilibrium they depend on the temperature and pressure profile and even an isothermal profile can lead to non-constant VMRs, as shown in Fig. 4.3.

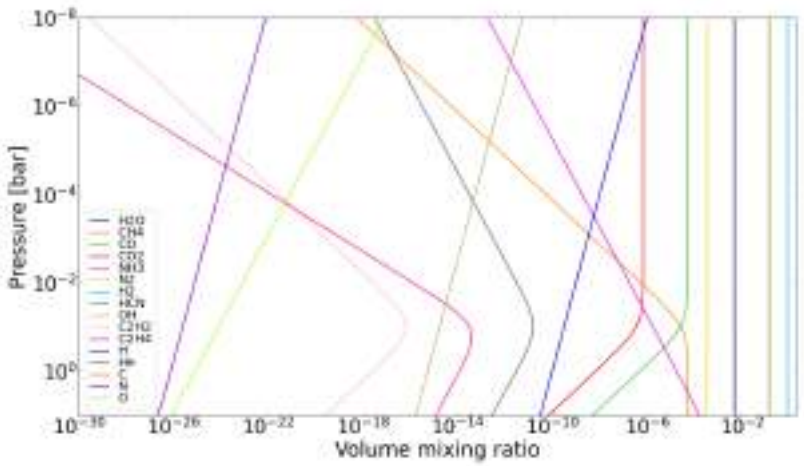

Figure 4.3: VMRs of different chemical species as a function of atmospheric pressure. The VMRs are computed assuming an isothermal atmosphere in chemical equilibrium with the best-fit parameters retrieved for KELT-8 b and reported in Sect. 4.3.2.

[7] `https://chemcat.readthedocs.io/en/main/chemistry_tutorial.html`

As common practice, although only H_2O is detected in cross-correlation for both planets, for our "free-chemistry" retrieval, we considered also the presence of other molecular species, in particular CO, CH_4, CO_2, C_2H_2, HCN and NH_3, since these are common molecular species in the atmospheres of hot Jupiters (e.g. Madhusudhan 2012) and, even in the case of non-detections in CCF, we can put upper limits on their abundances with our retrieval. In "free-chemistry", the VMR of H_2 and He is derived assuming a constant H_2/He equal to 5.897 (Asplund et al., 2009). This means that an atmosphere of only hydrogen and helium will contain 85% H_2 and 15% He. The mean molecular weight is computed accordingly.

For the radiative transfer computation, we employed the petitRADTRANS code on a pressure grid of 50 layers equidistant in log-space ($1 \leq \log_{10}[P\,(\mathrm{bar})] \leq -8$). The cross-sections employed in this work are summarised in Table 4.3. We also included the collision-induced absorption (CIA) cross-sections for the H_2-H_2 and H_2-He pairs.

Table 4.3: Cross section employed by petitRADTRANS.

Molecule	Cross section	Reference
H_2O	POKAZATEL	Polyansky et al. (2018)
CH_4	HITEMP	Hargreaves et al. (2020)
NH_3	CoYuTe	Coles et al. (2019)
HCN	ExoMol	Barber et al. (2013)
C_2H_2	aCeTY	Chubb et al. (2020)
CO_2	Ames	Huang et al. (2017)
CO	HITEMP	Rothman et al. (2010)

The transmission spectrum thus obtained had then to be convolved with the instrumental profile of GIANO-B (assumed as a Gaussian with an FWHM of $3.1\,\mathrm{km\,s^{-1}}$) and shifted accordingly to Eq. (1.23).

When using the likelihood approach, it is essential to replicate the effects of telluric removal analysis on each model generated by the parameter sampling algorithm. This helps to prevent or mitigate potential biases caused by signal distortion induced by the filtering procedures. In the field, this analysis step is called "model reprocessing". Apart from the name, there is no agreement in the literature on the optimal approach to model reprocessing. In this work, we followed the same recipe described in Giacobbe et al. (2021) where the fitted telluric spectrum, stored after processing the observations, is multiplied by each transmission model generated by the sampler and passed through the same procedures as described above, including the PCA.

The framework described above is implemented within a custom parallelised version of the DE-MCMC (Bonomo et al., 2015, Eastman et al., 2013, Ter Braak, 2006). We employed a number of walkers $n_\mathrm{w} = n_\mathrm{f} \cdot 2$, with n_f being the number of free parameters. The number of burn-in iterations discarded is variable and is computed as the minimum number of iterations for which all the chains have a likelihood value greater than the median value. The maximum number of steps is fixed to 100 000 but the DE-MCMC is interrupted when the distributions of all the parameters converge according to the Gelman-Rubin statistics (Gelman and Rubin, 1992), following the prescription of Ford (2006). The retrieved parameters and their uniform priors are summarised in Table 4.4 and Table 4.5.

4.3 Results

4.3.1 Detection of atmospheric signals

We built the S/N $K_\mathrm{p} - V_\mathrm{rest}$ maps by converting the CCF values into detection S/N. To do so, we divided the CCF values by the standard deviation of the noise far ($|V_\mathrm{rest}| \geq 25\,\mathrm{km\,s^{-1}}$) from the peak.

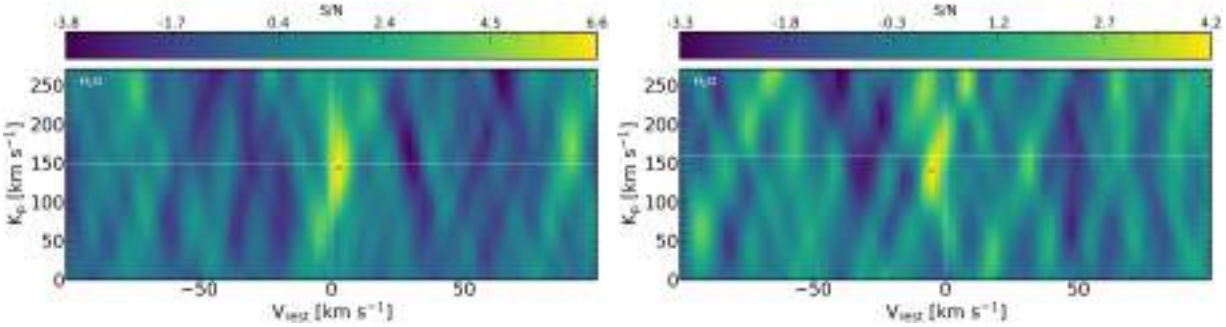

Figure 4.4: (S/N) $K_\mathrm{p} - V_\mathrm{rest}$ maps. These maps are built by cross-correlating a single-species model of H_2O with data of KELT-8 b (left panel) and KELT-23 Ab (right panel), as described in the text. The maps are computed dividing the CCF values by the standard deviation of the noise far ($|V_\mathrm{rest}| \geq 25\,\mathrm{km\,s^{-1}}$) from the peak. The horizontal (vertical) white dashed lines represent the expected K_p (V_rest) of the atmospheric signal. The black "×" marks denote the cross-correlation maximum in each plot.

In Fig. 4.4 we report the (S/N) $K_\mathrm{p} - V_\mathrm{rest}$ maps for the H_2O signal, in which it can be seen that we detected the atmospheric signal of the two targets. In particular, we detect the presence of H_2O with an S/N of 6.6 and 4.2 in the atmosphere of KELT-8 b and KELT-23 Ab, respectively. In the case of KELT-8 b, the peak of the signal is at a radial-velocity semi-amplitude $K_\mathrm{p} = 144^{+33}_{-32}\,\mathrm{km\,s^{-1}}$, compatible with the expected one at $< 1\,\sigma$ and at a $V_\mathrm{rest} = 2.7^{+2.7}_{-2.7}\,\mathrm{km\,s^{-1}}$. In the case of KELT-23 Ab, the peak is shifted at $K_\mathrm{p} = 140^{+26}_{-29}\,\mathrm{km\,s^{-1}}$ ($\sim 20\,\mathrm{km\,s^{-1}}$ smaller than the expected value but compatible at $1\,\sigma$) and at a $V_\mathrm{rest} = -5.4^{+2.7}_{-2.7}\,\mathrm{km\,s^{-1}}$. The origins of these RV shifts are discussed in Sect. 4.4.1. Thus, our detection of the H_2O signal constitutes the first measurement of the atmospheric signal of the two targets. For what concerns the other chemical species, we did not find any significant CCF signal (S/N$\geq$ 3) for either planet. Even though we do not detect the other secondary chemical species, we cannot exclude their presence in the atmosphere of the two targets, as discussed in Sect. 4.4.

4.3.2 Atmospheric-retrieval analyses

In this section, we report the first investigation of the atmospheric properties of the two targets. As described in Sect. 4.2.5, we performed an atmospheric retrieval with the simplest assumption of an isothermal atmosphere in chemical equilibrium and a second retrieval in "free-chemistry". We report the retrieved value of the fitted parameters and the associated uncertainties in Table 4.4 and Table 4.5 for the chemical-equilibrium and "free-chemistry" retrieval, respectively. We took the medians and the 15.87% and 84.14% quantiles of the posterior distributions as the values and $1\,\sigma$ uncertainties of the fitted parameters.

Table 4.4: Parameters, best-fitting values, and adopted uniform (U) priors for the chemical-equilibrium retrieval.[a]

Parameter	KELT-8 b	KELT-23 Ab	Prior
K_p [km s^{-1}]	154 ± 10	163^{+25}_{-26}	U[0; 250]
V_rest [km s^{-1}]	$3.30^{+0.89}_{-0.76}$	$-3.14^{+2.50}_{-1.93}$	U[-10; 10]
$\log_{10}(P_\mathrm{c})$ [$\log_{10}$, bar]	≥ -2.29	≥ -4.58	U[-8; 2]
[M/H] [dex]	$0.77^{+0.61}_{-0.89}$	$-0.42^{+1.56}_{-1.35}$	U[-3; 3]
$\log_{10}$(C/O)	≤ -0.52	≤ -0.11	U[-3; 2]
T_0 [K]	897^{+162}_{-113}	1833^{+612}_{-667}	U[300; 3000]

Notes. [(a)]For each target we report the best-fitted value and the $1\,\sigma$ confidence interval of the retrieved parameters with the exception of $\log_{10}(P_\mathrm{c})$ and $\log_{10}$(C/O) for which we report the $2\,\sigma$-level lower and upper limit, respectively.

Table 4.5: Parameters, best-fitting values, and adopted uniform (U) priors for the "free-chemistry" retrieval.[a]

Parameter	KELT-8 b	KELT-23 Ab	Prior
K_p [km s^{-1}]	152^{+11}_{-12}	152^{+21}_{-22}	U[0; 250]
V_rest [km s^{-1}]	$3.21^{+0.96}_{-1.02}$	$-3.88^{+1.86}_{-1.40}$	U[-10; 10]
$\log_{10}(P_\mathrm{c})$ [$\log_{10}$, bar]	≥ -2.50	≥ -4.88	U[-8; 2]
T_0 [K]	880^{+198}_{-148}	2306^{+490}_{-765}	U[300; 3000]
$\log_{10}(\mathrm{VMR}_{\mathrm{H_2O}})$	$-2.07^{+0.53}_{-0.72}$	$-2.26^{+0.75}_{-1.24}$	U[-10; -1]
$\log_{10}(\mathrm{VMR}_{\mathrm{CO}})$	≤ -2.55	≤ -2.14	U[-10; -1]
$\log_{10}(\mathrm{VMR}_{\mathrm{CH_4}})$	≤ -3.52	≤ -2.17	U[-10; -1]
$\log_{10}(\mathrm{VMR}_{\mathrm{CO_2}})$	≤ -2.49	≤ -2.16	U[-10; -1]
$\log_{10}(\mathrm{VMR}_{\mathrm{C_2H_2}})$	≤ -2.14	≤ -1.87	U[-10; -1]
$\log_{10}(\mathrm{VMR}_{\mathrm{HCN}})$	≤ -4.40	≤ -2.25	U[-10; -1]
$\log_{10}(\mathrm{VMR}_{\mathrm{NH_3}})$	≤ -4.47	≤ -3.38	U[-10; -1]

Notes. [(a)]For each target we report the best-fitted value and the $1\,\sigma$ confidence interval of the retrieved parameters. The values of the $\log_{10}(P_\mathrm{c})$ and the VMRs reported for all the chemical species but H_2O, which is the only detected species, are the $2\,\sigma$-level lower and upper limits, respectively.

KELT-8 b

In Fig. 4.5 we report the corner plots with retrieved posterior distributions of the fitted atmospheric parameters for the chemical-equilibrium retrieval for KELT-8 b.

For this target, the atmospheric retrieval in chemical equilibrium converges at the expected planetary orbital solution (K_p) at a confidence level $< 1\,\sigma$. The retrieval converges to a $V_\mathrm{rest} = 3.30^{+0.89}_{-0.76}$ km s^{-1}, confirming the residual redshift of the CCF peak visible in the left panel of Fig. 4.4. We find a lower limit on the cloud-top pressure of $P_\mathrm{c} \geq 5.13$ mbar (at $2\,\sigma$ level). For KELT-8 b we are able to constrain a metallicity of [M/H] $= 0.77^{+0.61}_{-0.89}$ dex, that corresponds to 3.2 times the stellar metallicity (i.e. [Fe/H] $= 0.26 \pm 0.10$ dex). For what concerns the C/O ratio, we are only able to place an upper limit; in particular, we retrieve a sub-solar C/O ratio (i.e. C/O ≤ 0.30, at $2\,\sigma$ level). The non-constrained $\log_{10}$(C/O) distribution, which has a median at C/O$= 0.01$, is due to the lack

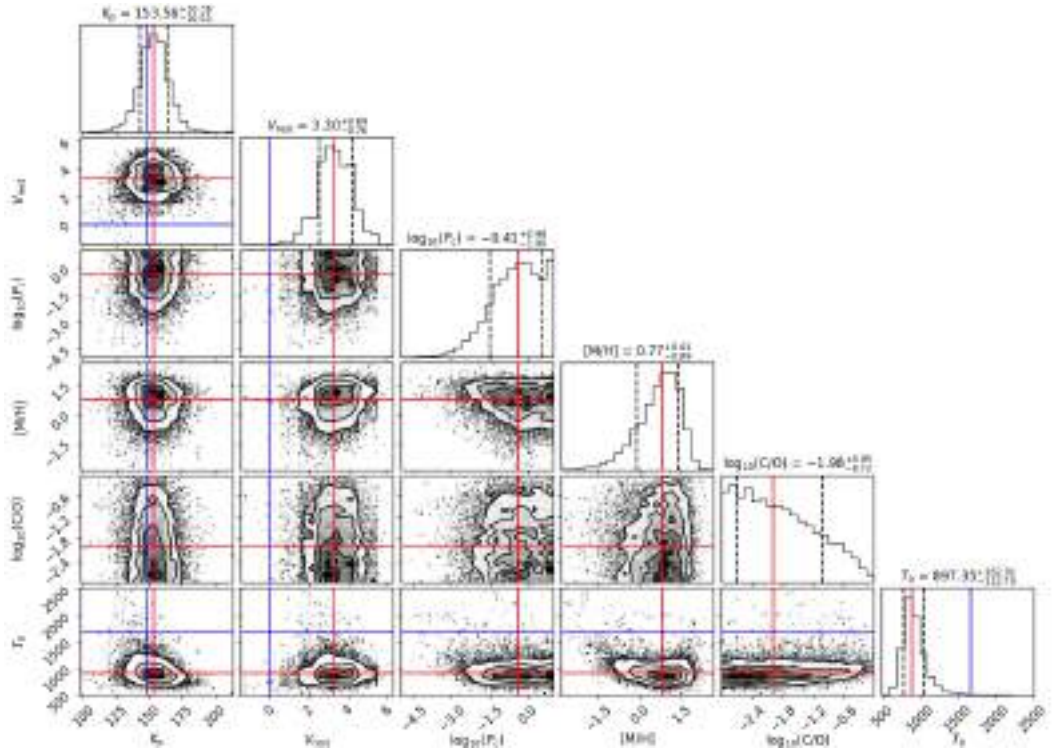

Figure 4.5: Posterior distributions for all the parameters of the chemical-equilibrium retrieval, for KELT-8 b. Off-diagonal plots report the 2D posterior distribution for pairs of parameters with the $1\,\sigma$-, $2\,\sigma$-, and $3\,\sigma$-confidence intervals. On-diagonal plots report the posterior distributions of each parameter marginalised over the remaining parameters. The blue lines represent the predicted values for some parameters and the red lines represent the median of the posterior distributions.

of detection of any carbon-bearing species with our dataset. A sub-unity C/O ratio was expected given these non-detections and the simultaneous detection of H_2O, the most common oxygen-bearing species. Even if we put an upper limit on the C/O ratio, the posterior probability distribution seems to increase when the C/O ratio decreases (at the lower extreme of the $1\,\sigma$ interval we have C/O $= 0.002$). New observations, that can allow us to detect the presence of secondary carbon-bearing species, could help to better constrain the C/O ratio probability distribution.

For what concerns the temperature, the retrieval converges at $T_0 = 897^{+162}_{-113}\,\mathrm{K}$. This is about half the estimated equilibrium temperature (see Table 4.1). It is worth noting that with transmission spectroscopy we only probe a small fraction of the atmosphere (i.e. the terminator) between the two hemispheres of planets. Since hot Jupiters are expected to be tidally locked due to their proximity to the host stars, the average temperatures of the two faces of these planets can be very different ($\Delta T \sim 100 - 1\,000\,\mathrm{K}$, Heng and Showman 2015). As a consequence, the estimated equilibrium temperature could not be representative of the average temperature at the terminator, which is strongly dependent on the atmospheric circulation. In addition, even assuming that the equilibrium temperature is representative of the atmospheric layers where most of the absorption occurs, it is worth noting that retrieving a temperature value lower than the expected equilibrium temperature has proved to be a common output when 1D atmospheric models are used to fit transmission spectra (e.g. MacDonald et al. 2020 and references therein, Boucher et al. 2023, Xue et al. 2024). This effect could be due to possible asymmetries in the two regions (i.e. the morning and evening one) of the terminator (MacDonald et al., 2020). However, these differences can be explored effectively only

through at least a 2D atmospheric model and with a higher-quality dataset.

As can be seen in Table 4.5, also the atmospheric retrieval in the "free-chemistry" scenario converges to K_p and V_{rest} values in accordance with those found by the chemical equilibrium retrieval at $< 1\,\sigma$. Also, the retrieved value of T_0 is in accordance with the value retrieved in the former scenario at $1\,\sigma$. For H_2O we retrieve a volume mixing ratio of $\log_{10}(\mathrm{VMR}_{H_2O}) = -2.07^{+0.53}_{-0.72}$, in accordance at $1\,\sigma$ level with what is predicted assuming an isothermal atmosphere in chemical equilibrium at the temperature, C/O ratio and metallicity retrieved in the chemical equilibrium scenario (i.e. $\log_{10}(\mathrm{VMR}_{H_2O}) = -2.31$), while for the other chemical species we only find upper limits on the abundances, in accordance with the non-detections we find with the CCF analysis of our dataset.

KELT-23 Ab

In Fig. 4.6 we report the corner plots with retrieved posterior distributions of the fitted atmospheric parameters for KELT-23 Ab under the chemical-equilibrium assumption.

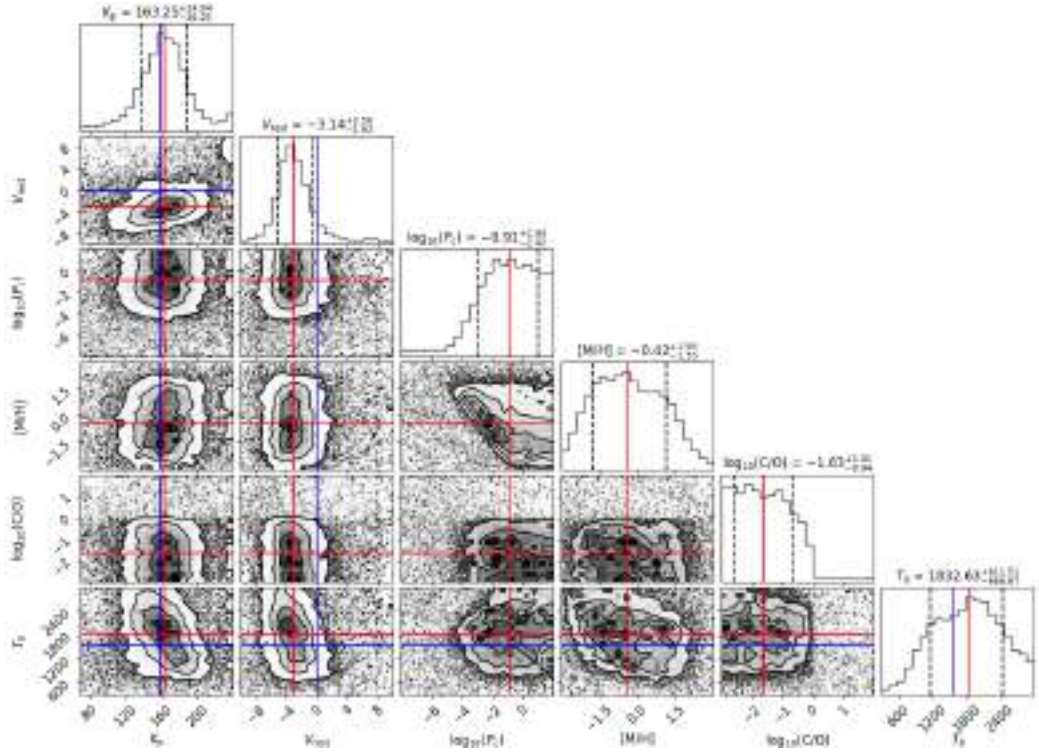

Figure 4.6: Posterior distributions for all the parameters of the chemical-equilibrium retrieval, for KELT-23 Ab. Off-diagonal plots report the 2D posterior distribution for pairs of parameters with the $1\,\sigma$-, $2\,\sigma$-, and $3\,\sigma$-confidence intervals. On-diagonal plots report the posterior distributions of each parameter marginalised over the remaining parameters. The blue lines represent the predicted values for some parameters and the red lines represent the median of the posterior distributions.

In the case of KELT-23 Ab, the atmospheric retrieval converges to a value of K_p compatible with the expected one at $< 1\,\sigma$ and to a V_{rest} value lower than $0\,\mathrm{km\,s^{-1}}$ (i.e. $V_{rest} = -3.14^{+2.50}_{-1.93}\,\mathrm{km\,s^{-1}}$), confirming the residual blueshift of the signal visible in the CCF peak in the $K_p - V_{rest}$ map (Fig. 4.4, right panel). Also for KELT-23 Ab, we find a lower limit on the cloud-top pressure but, in this case, it is at a lower pressure $P_c \geq 0.026\,\mathrm{mbar}$ (at $2\,\sigma$ level). For KELT-23 Ab the posterior distributions of the fitted parameters are less constrained with respect to the case of KELT-8 b, probably due

to the lower S/N of the observations (as it can be seen in Table 4.2). Indeed, for what concerns the chemical parameters, the metallicity posterior distribution is broader and we observe a larger degeneracy between the $\log_{10}(P_c)$ and [M/H]. However, we are still able to place a first constraint on the metallicity of the atmosphere: the $1\,\sigma$ interval around the retrieved median value ranges from a sub-solar ([M/H] $= -1.77$ dex) to a super-solar metallicity ([M/H] $= 1.14$ dex), with a median sub-solar metallicity value ([M/H] $= -0.42$ dex), that corresponds to 0.48 times the stellar metallicity (i.e. [Fe/H] $= -0.105^{+0.078}_{-0.077}$ dex). For the C/O ratio, also in this case, due to the lack of detection of carbon-bearing species in our dataset, we are only able to retrieve an upper limit, in particular, we measure a sub-unity C/O ratio (i.e. C/O ≤ 0.78 at $2\,\sigma$ level). The constraint on the retrieved temperature is broad and even if the median retrieved temperature is higher than the expected equilibrium one, there is compatibility at the $1\,\sigma$ level. As can be seen in Table 4.5, the atmospheric retrieval in the "free-chemistry" scenario converges to a K_p that is in accordance with the predicted value and with the value found in the chemical equilibrium scenario at $1\,\sigma$. From both atmospheric retrievals in the two analysed scenarios, we do not find evidence for the $\sim 20\,\mathrm{km\,s^{-1}}$ shift in K_p visible in the $K_p - V_{rest}$ map, probably because between the peak of the CCF signal and the CCF value at the expected K_p there is a small S/N difference of 0.5, making the peak shift statistically non-significant. However, it is interesting to note that a K_p shift of $\sim 20\,\mathrm{km}^{-1}$ is very similar to the expected shift predicted by Eq. (7) in Wardenier et al. (2023) due to the planetary rotation during the transit. Indeed, the predicted K_p shift is $\Delta K_p = -21.6\,\mathrm{km\,s^{-1}}$ for the equatorial rotation velocity of KELT-23 Ab ($V_{eq} = 2.98\,\mathrm{km\,s^{-1}}$, in case of synchronous rotation), so we cannot exclude that the observed shift is a hint of planetary rotation but we think that other measurements are needed to retrieve this dynamical effect in a statistically robust way. The shift in V_{rest} (i.e. $V_{rest} = -3.88^{+1.86}_{-1.40}\,\mathrm{km\,s^{-1}}$) is in accordance at $< 1\,\sigma$ with the value found assuming the chemical equilibrium and confirms a global blueshift of the atmospheric signal of KELT-23 Ab.
Also in this case the retrieved reference temperature is in accordance with the value retrieved in the chemical equilibrium scenario at $1\,\sigma$ level. In the case of KELT-23 Ab, we retrieved a volume mixing ratio of H_2O equal to $\log_{10}(\mathrm{VMR}_{H_2O}) = -2.26^{+0.75}_{-1.24}$, in accordance at $1\,\sigma$ level with what is predicted assuming an isothermal atmosphere in chemical equilibrium at the temperature, C/O ratio and metallicity retrieved in the chemical equilibrium scenario (i.e. $\log_{10}(\mathrm{VMR}_{H_2O}) = -3.52$) and, also in this case, we can only put upper limits on the abundances of other secondary chemical-species that we did not detect in cross-correlation in our dataset.

4.4 Discussion

4.4.1 KELT-8 b and KELT-23 Ab atmospheric properties

The two hot Jupiters analysed in this work have an atmosphere in which water vapour is the dominant secondary species. In particular, considering the $1\,\sigma$ interval of the water VMR, for KELT-8 b we measured an abundance of water between 0.2% and 3%, with a median value of 0.9%, while for KELT-23 Ab we measured an abundance of water between 0.03% and 3%, with a median value of 0.5%. Even if the constraints on KELT-23 Ab atmospheric metallicity are broader than those on KELT-8 b, the median value of the distribution is about one order of magnitude smaller, implying an average lower abundance of volatile heavy elements (e.g. oxygen, carbon) in accordance with the lower abundance of water vapour. While we identified the H_2O signature in cross-correlation

for both targets, we did not observe the presence of other secondary species in our dataset. This pushes the retrieved C/O ratio to lower values and, by being unable to measure the abundance of carbon-bearing species, we had only retrieved upper limits.

This first atmospheric analysis of KELT-8 b and KELT-23 Ab reveals two O-rich atmospheres, with a sub-solar C/O ratio for KELT-8 b and a sub-unity C/O ratio for KELT-23 Ab, at $2\,\sigma$ level. Assuming an atmosphere in chemical equilibrium at $T_{\rm eq}$ for the two planets and with C/O ratio upper limits we find, water is expected to be the most abundant secondary species in the atmosphere of hot Jupiters (e.g., Madhusudhan 2012, Moses 2014), while the formation of hydrocarbons like C_2H_2 and HCN is not favoured by the under-abundance of carbon, in accordance with the non-detection we found. In this scenario, the most abundant carbon-bearing species is expected to be CO, whose formation is favoured with respect to CH_4. We found no evidence for CO in our dataset. Since most of the CO absorption is concentrated in two absorption bands (one centered at 1 600 nm and one at 2 400 nm), we also tried to probe the presence of CO by using only GIANO-B orders in which these two bands fall (i.e. orders number 0, 1, 14, 15, 16, 17, with the exclusion of 15 for KELT-23 Ab) but, also in this case, we did not find any significant signal at the expected planetary RV. In order to further check our ability to detect the CO signal, for both targets we also performed a set of injection and retrieval tests with the CO single-species model built with different volume mixing ratios (i.e. $\log_{10}(\mathrm{VMR_{CO}}) = -2, -3, -4$) at the T_0 found by the chemical-equilibrium retrieval. In particular, for each trial VMR, we injected the model into the data with an RV shift of $-15\,\mathrm{km\,s^{-1}}$ with respect to the RV from Eq. (1.23). To avoid possible spurious correlation, we repeated the telluric removal procedure and the CCF analysis using the whole spectral range and built the $K_{\rm p} - V_{\rm rest}$ maps to search for the injected signal. For KELT-8 b, we were able to recover the injected signal with an S/N ≥ 3 for the case of $\log_{10}(\mathrm{VMR_{CO}}) = -2$, -3, -4, while for KELT-23 Ab we were not able to recover the injected signal with an S/N ≥ 3 in any case. These indicative tests are in accordance with the upper limits on the abundance of CO that we reported in Table 4.5 for both planets. It is worth noting that the expected CO abundance assuming chemical equilibrium (with the retrieved atmospheric parameters) is $\log_{10}(\mathrm{VMR_{CO}}) = -4.3$ and -5.1, for KELT-8 b and KELT-23 Ab, respectively. These values are well below the upper limits we found. Indeed, the non-detection of the other probed chemical species less abundant than water does not exclude that these species are present in the atmosphere of the two targets and that their lower signal may be detectable with more observations at both high- and low-spectral resolution.

Hot Jupiters are expected to be tidally locked due to their proximity to their host stars. The high-temperature gradient between the day side and the night side of these planets can induce the presence of strong atmospheric dynamical effects (e.g super-rotating equatorial jet streams and day-to-night side winds) spreading the heat around the planets (Heng and Showman, 2015, Showman and Polvani, 2011). The possible presence of day-to-night side winds (with speeds of a few $\mathrm{km\,s^{-1}}$), transporting atmospheric gases across the terminator from the sub-stellar point towards the colder side of the planet (i.e. towards the observer during the planetary transit), introduces a blueshift of the atmospheric transmission signal. Looking at the signal of H_2O for KELT-23 Ab, we measured a residual blueshift of the signal that can be explained by the presence of a day-to-night wind on this planet with a speed of $V_{\rm wind} = -3.88^{+1.86}_{-1.40}\,\mathrm{km\,s^{-1}}$ (the most precise value among the two retrieved), a value in line with the typical wind speed measured on other hot Jupiters (e.g. Brogi et al. 2016, Line et al. 2021, Nortmann et al. 2024, Snellen et al. 2010). Both targets orbit around G2 V stars

but, considering the orbits, KELT-8 b receives 25% less flux from its host star than KELT-23 Ab. Therefore, the effects due to the redistribution of heat in the atmosphere could be less intense because the amount of stellar energy received is less. However, this does not exclude the possible presence of large-scale circulation effects on KELT-8 b that redistribute the incoming energy across the atmosphere and planetary interior. Indeed, complex atmospheric dynamical effects, described by, e.g., Wardenier et al. (2023) and Weiner Mansfield et al. (2024), can be a possible explanation also for the observed residual redshift of the atmospheric signal of KELT-8 b.

However, it is worth noting that, besides the atmospheric dynamical effects, which could be effectively studied with more precise measurements, by observing the signal of other chemical species populating different atmospheric layers and by employing more realistic atmospheric models (e.g. Beltz et al. 2023, Gandhi et al. 2022, Nortmann et al. 2024, Wardenier et al. 2023), also a small orbital eccentricity can produce the residual Doppler shift of the signal observed for both planets. Indeed, it is possible to obtain a residual radial-velocity shift of the signal between $-10\,\mathrm{km\,s^{-1}} < V_{\mathrm{rest}} < 10\,\mathrm{km\,s^{-1}}$ by considering a small orbital eccentricity value $e \sim 0.01 - 0.05$ (below the upper limit reported in the literature for both planets) and different values of the planetary argument of periastron, ω_{p}. So, even though for KELT-8 b and KELT-23 Ab there is not robust evidence for an eccentric orbit in the literature, a small residual eccentricity remains a possible explanation for the observed atmospheric signal Doppler shift.

4.4.2 Possible formation scenarios for the two planets

By measuring the abundances of the different chemical species populating the atmosphere of an exoplanet, it is possible to constrain its formation and evolution paths. Indeed, observables like the atmospheric elemental abundance ratios (e.g. C/O and N/O) and the metallicity depend on the planet formation location into the protoplanetary disk, the accretion mechanisms that enriched the planet atmosphere with heavy elements, and the migration mechanisms that led to the current orbital configuration of the planetary system (e.g. Madhusudhan 2019, Mordasini et al. 2016, Pacetti et al. 2022).

Even though, in our work, we only detect the presence of H_2O, we estimate its abundance and place constraints on the planetary atmospheric metallicity and upper limits on the C/O ratio for both targets. Therefore, we can try to make preliminary inferences on possible formation scenarios for the two planets. Of course, with more precise future measurements of the atmospheric composition, it would be possible to put stronger constraints on the planetary formation and evolution paths followed by both targets.

The observed enrichment in the two giant planets suggests the accretion of the disk gas as the source of their atmospheric metallicity (e.g. Pacetti et al., 2022, Turrini et al., 2021). It also suggests that the possible sequestration of O by rock-forming elements (Fonte et al., 2023) should be limited, meaning that the abundance of H_2O provides a proxy for the bulk abundance of O. This scenario would be confirmed by the non-detection of abundant rock-forming elements in future analyses. The super-solar mixing ratio estimated for H_2O in both planets argues for the accretion of high-metallicity gas enriched by the sublimation of volatile species from drifting pebbles (e.g. Booth and Ilee, 2019, Schneider and Bitsch, 2021). Finally, the non-detection of C and N species and the upper limits to the C/O ratios of both planets (see below for discussion) point to the accretion of gas from a disk region enriched primarily in O.

Focusing on KELT-8 b, the availability of stellar abundances from the Hypatia Catalog Database (Hinkel et al., 2014) enables for a more detailed analysis. The host star exhibits a super-solar metallicity and a slightly sub-solar C/O ratio ($\sim$ 0.51). Comparing these with our retrieved parameters reveals that the giant planet is enriched in heavy elements by a factor of about 3 compared to its host star, with a sub-stellar upper limit for the normalised C/O ratio (< 0.59). This sub-stellar C/O ratio, combined with a super-stellar VMR for H_2O, suggests that the planet has accreted gas more enriched in oxygen than carbon, consistent with gas accretion from within the H_2O snowline. In particular, the Hypatia Catalog Database reports that the [O/H] of KELT-8 is 0.2 dex, meaning that it is 1.58 times higher than the solar one. The estimated VMR for H_2O then points to a $\sim 7\times$ enrichment in O with respect to the star, which is compatible with the estimated super-stellar metallicity. Specifically, in a solar-like mixture, O accounts for about 45% of the mass of heavy elements (Lodders, 2010), meaning that a $\sim 7\times$ enrichment in O causes a $3\times$ enrichment in metallicity, consistently with the estimated value.

The lack of compositional data on KELT-23 A and the large uncertainties affecting the planetary metallicity prevent us from refining the discussion as in the case of KELT-8 b. Based on the correlations between stellar metallicity and composition discussed in da Silva et al. (2024), however, the average C/O values for stars, whose metallicities fall in the uncertainty range of KELT-23 A's [Fe/H], are expected to vary between 0.45 and 0.65. While the estimated upper limit to the C/O ratio of KELT-23 Ab does not allow to rule out super-stellar values, it is broadly consistent with the accretion of O-enriched gas across the snowline of H_2O as discussed for KELT-8 b. This scenario would suggest planetary metallicity values higher than the one reported in Table 4.4. Similarly to what we discussed for KELT-8 b, if we assume a solar-like mixture, the O enrichment suggested by the H_2O VMR would point to a planetary metallicity [M/H] of the order of 0.5 dex that, while higher, is compatible within $1\,\sigma$ with the estimated atmospheric value.

Finally, it is worth noting that in order to completely understand the formation and orbital evolution path followed by KELT-23 Ab, it is necessary to take into consideration also the presence of the outer stellar companion in a wide orbit. Indeed, under some conditions, eccentric orbital interactions with a distant companion star via Kozai–Lidov oscillations (Kozai, 1962) can lead to a giant planet migration towards its host star and subsequent orbital circularisation through tidal friction (Fabrycky and Tremaine, 2007). In order to effectively consider the magnitude of such effects in the KELT-23 Ab case, more data about the orbital configuration of the KELT-23 system and the physical characteristics of the outer stellar body are needed.

4.5 Summary and Conclusions

In this work, we searched for the atmospheric signal of the two hot Jupiters KELT-8 b and KELT-23 Ab, and started exploring their chemical and physical properties under the simplest assumption (i.e. 1D isothermal atmosphere), in order to enlarge the sample of known hot Jupiters with atmospheric detection and characterisation.

We performed our study by analysing one transit observation for each target taken with the NIR GIANO-B high-resolution ($R \approx 50\,000$) spectrograph mounted at the 3.58 m TNG telescope. By cross-correlating data with atmospheric transmission template models, we detect the signal of H_2O for both planets, with a CCF peak value corresponding to S/N = 6.6 and S/N = 4.2 for

KELT-8 b and KELT-23 Ab, respectively, while finding no significant signal for the other probed chemical species. This constitutes the first observation of the atmospheric signal from KELT-8 b and KELT-23 Ab.

We explored the chemical and physical properties of the two atmospheres in a Bayesian framework. In particular, we ran two retrievals for both planets: a retrieval assuming chemical equilibrium and a "free-chemistry" retrieval. Both the retrievals point towards an atmosphere rich in H_2O (from $\sim 0.1\%$ to $\sim 1\%$) for both targets.

For KELT-8 b, in the chemical-equilibrium scenario, we find an atmospheric metallicity of $[M/H] = 0.77^{+0.61}_{-0.89}$ dex, which corresponds to 3.2 times the stellar metallicity, while for the C/O ratio, we can place a sub-solar upper limit at C/O ≤ 0.30 (at $2\,\sigma$ confidence level). In the "free-chemistry" scenario, we can constrain an H_2O abundance of $\log_{10}(\mathrm{VMR}_{H_2O}) = -2.07^{+0.53}_{-0.72}$, in accordance with the prediction of chemical-equilibrium, while for the other probed chemical species we put upper limits on their abundance.

For KELT-23 Ab, the posterior distributions of the parameters are broader than the ones retrieved for KELT-8 b, probably due to the lower S/N of the dataset. Indeed, in the case of KELT-23 Ab, we find an atmospheric metallicity that ranges from a sub- to super-solar metallicity in the $1\,\sigma$ confidence interval, with a sub-solar median value ($[M/H] = -0.42^{+1.56}_{-1.35}$ dex), that corresponds to 0.48 times the stellar metallicity. For the atmosphere of KELT-23 Ab, we put a sub-unity C/O ratio upper limit (C/O ≤ 0.78 at $2\,\sigma$ level). The "free-chemistry" retrieval converges to an H_2O abundance of $\log_{10}(\mathrm{VMR}_{H_2O}) = -2.26^{+0.75}_{-1.24}$, in agreement with the prediction of chemical equilibrium and, also in this case, we place upper limits on the abundance of the other probed chemical species.

Comparing the atmospheric chemical characteristics with those of the host stars, we obtained indications of the formation mechanisms of the two hot Jupiters. In particular, the constraints on VMR_{H_2O} and the upper limits on the C/O ratio suggest for both planets the accretion of O-rich gas. This, in turn, points to an accretion of gaseous material that occurred within the H_2O snowline in a pebble-rich disk where the gas phase is enriched in oxygen due to sublimation of water ice from the inward-drifting pebbles.

With our analysis, we offer a preliminary investigation of the atmospheric properties of KELT-8 b and KELT-23 Ab. New measurements of atmospheric spectra of both targets could allow us to detect the presence of other secondary species other than refine the current H_2O abundance and, thus, place stronger constraints on the metallicity and the C/O ratio posterior distributions. We stress that our main goal was not to give a fully comprehensive picture of the chemical and physical phenomena occurring in the atmosphere of the two targets but to provide a first general characterisation of the main properties of the two atmospheres under simple assumptions. Even if more complex 2- and 3-dimensional atmospheric models (including, e.g., global circulation and limb asymmetries, more parametrised temperature profiles, and different chemical scenarios) would certainly provide a more realistic description of the chemical and physical properties of the atmosphere of the two targets, this is beyond the scope of this work, also given the limited amount of data available for both targets.

Our analysis based on only one transit observation for each target shows that these two planets, whose atmospheres were unstudied before this work, are very interesting targets for atmospheric investigations and that it is worth observing them with higher diameter instruments both at high resolution from the ground and at low resolution from space with HST and JWST.

Role of the Ph.D. candidate in the work

As the leading author of this work, carried out with Dr. Paolo Giacobbe and submitted to A&A as Basilicata et al. (2024b), I coordinated the effort of the whole team. In particular, I reduced and analysed GIANO-B data, while Dr. Paolo Giacobbe, who supervised the work giving important advices, performed the atmospheric retrievals, by using a pipeline developed by him and Mr. Francesco Amadori. I discussed the results of the atmospheric analysis, while the discussion about the formation of the two planets was carried out by Dr. Elenia Pacetti and Dr. Diego Turrini. Finally, the updated analysis of the KELT-8 stellar parameters was performed by Dr. Martina Baratella, Dr. Katia Biazzo, and Dr. Aldo S. Bonomo.

Chapter 5

Preliminary results of the investigation of the atmospheric signal of the two hot Jupiters WASP-13 b and HAT-P-1 b

In this chapter, I show the preliminary results of the analysis reported in a paper currently in preparation (Basilicata et al., in prep.). In this work, we searched for the atmospheric signal of the two hot Jupiters WASP-13 b and HAT-P-1 b, for the first time at high resolution.

Studying the atmosphere of hot Jupiters is important to understand their formation and evolution processes, as well as to probe atmospheric environments that we do not find in our Solar System. The two hot Jupiters WASP-13 b and HAT-P-1 b are valid targets for atmospheric investigation, thanks to their inflated hot atmospheres ($T \sim 1\,300 - 1\,500$ K). In this work, we use high-resolution spectroscopy in the near-infrared (NIR), to search for the atmospheric signal of WASP-13 b, for the first time, and to probe the atmosphere of HAT-P-1 b, for the first time at high resolution. For each target, we analysed the atmospheric transmission spectra with the NIR GIANO-B spectrograph at the TNG. In particular, for WASP-13 b, we used data of one transit observation while, for HAT-P-1 b, we used data collected during two transits. We adopted a data-reduction approach similar to the one adopted in the analysis reported in Chapter 4 and searched for the atmospheric signal of the targets by cross-correlating single-species template atmospheric models with data. We first searched for the signal of water vapour (H_2O), as it is expected to be the most abundant secondary species in the atmosphere of hot giant planets under a broad range of atmospheric conditions. Then, we searched for the signals of other molecular species which are common in the atmosphere of this type of planets. In this preliminary analysis, we do not detect the signal of H_2O in either atmosphere, even when combining the two datasets of HAT-P-1 b. We do not detect the signal of the other probed chemical species, but only find a possible hint of the presence of CO in the atmosphere of WASP-13 b, whose signal needs to be confirmed with further studies. In conclusion, in our preliminary analysis, we do not detect the atmospheric signal of the two targets. The analysis is still ongoing and in the final section of this chapter, we describe the future steps we plan to refine it.

5.1 Introduction

Hot Jupiters and ultra-hot Jupiters are the most suitable targets for atmospheric characterisation, as described in previous sections. Indeed, their hot ($T \geq 1\,000\,\mathrm{K}$) inflated atmospheres produce the highest atmospheric signal (see Eq. 1.19 and Eq. 1.21). Characterising the chemical and physical properties of their atmospheres can improve our understanding of the mechanisms behind their formation and evolution (e.g. Dawson and Johnson 2018, Madhusudhan 2019).

In this context, we employed high-resolution spectroscopy (HRS, see Birkby 2018, for a review) to search for an atmospheric signal from the two hot Jupiters WASP-13 b (Skillen et al., 2009) and HAT-P-1 b (Bakos et al., 2007), which both orbit Sun-like stars. WASP-13 b was discovered using data from the Wide Angle Search for Planets survey (WASP, Pollacco et al. 2006), while HAT-P-1 b was discovered using data from the Hungarian Automated Telescope Network survey (HATNet, Bakos et al. 2004). Both targets were confirmed with photometric and spectroscopic follow-up observations. HAT-P-1 b orbits around a star (ADS 16402 B) that is a member of a wide binary system, composed of a pair of G0 V stars (i.e. ADS 16402 A and ADS 16402 B), with a projected separation of $\simeq 1550\,\mathrm{au}$ (Bakos et al., 2007). In Table 5.1[1], we report a summary of the physical and orbital parameters of the two planetary systems.

Both planets are puffier versions of Jupiter, indeed both have a larger radius ($\sim 1.2\,R_\mathrm{J}$) but a smaller mass ($\sim 0.36\,M_\mathrm{J}$ and $\sim 0.52\,M_\mathrm{J}$, for WASP-13 b and HAT-P-1 b, respectively). The two inflated atmospheres have an atmospheric scale height of $H_\mathrm{s} = 883\,\mathrm{km}$ and $H_\mathrm{s} = 542\,\mathrm{km}$ (assuming an atmospheric mean molecular weight of $\mu = 2.3\,\mathrm{g\,mol^{-1}}$), for WASP-13 b and HAT-P-1 b, respectively. Combining these values with those of the stellar radii, we obtain an expected atmospheric transmission signal amplitude of $\Delta = 124\,\mathrm{ppm}$ and $\Delta = 140\,\mathrm{ppm}$, for WASP-13 b and HAT-P-1 b, respectively. Even if these two hot Jupiters are ideal targets for atmospheric studies, for WASP-13 b there are no atmospheric studies in the literature, while for HAT-P-1 b there are no atmospheric studies in the literature performed with high-resolution spectroscopy. Indeed, for what concerns the near-infrared (NIR), the atmosphere of HAT-P-1 b has been investigated only with low-resolution HST/WFC3 data (Wakeford et al., 2013), which indicate the presence of water vapour (H_2O) in its atmosphere.

In this work, we present the preliminary results of the first investigation of the atmosphere of WASP-13 b and HAT-P-1 b with high-resolution spectroscopy. In Sect. 5.2 we describe the observations, the data reduction process, and the analysis we performed for the atmospheric characterisation of the targets. In Sect. 5.3 we report the preliminary results, while in Sect. 5.4 we discuss them and present our conclusions and future steps of the analysis.

[1]The symbols of the parameters listed in the table have the following meanings: $M_\star$ - stellar mass; $R_\star$ - stellar radius; T_eff - stellar effective temperature; [Fe/H] - stellar metallicity; $\log g$ - logarithm of stellar surface gravity; V_sys - systemic radial velocity; H - apparent magnitude in the photometric H band; M_p - planetary mass; R_p - planetary radius; ρ_p - planetary mean density; T_eq - planetary equilibrium temperature; P_orb - orbital period; T_0 - transit epoch; T_{14} - transit duration; i - orbital inclination; e - orbital eccentricity; a - orbital semi-major axis; K_p - planetary radial-velocity semi-amplitude. The left reference numbers are for the parameters of the WASP-13 system, and the right ones for those of the HAT-P-1 system. The references of the values in the table are: 1. Ehrenreich and Désert (2011); 2. Ment et al. (2018); 3. Stassun et al. (2019); 4. Gaia Collaboration et al. (2023); 5. Bonomo et al. (2017); 6. Cutri et al. (2003); 7. Stassun et al. (2017); 8. Southworth (2012), 9. Nikolov et al. (2014); 10. Kokori et al. (2023); 11. Brothwell et al. (2014).

Table 5.1: Main physical and orbital parameters of the WASP-13 and HAT-P-1 systems.

Parameter	WASP-13	HAT-P-1	References
Stellar Parameters			
Spectral Class	G1 V	G0 V	1, 2
$M_\star$ [$M_\odot$]	$1.08^{+0.13}_{-0.14}$	$1.13^{+0.19}_{-0.11}$	3, 3
$R_\star$ [$R_\odot$]	$1.58^{+0.10}_{-0.08}$	$1.178^{+0.064}_{-0.039}$	3, 3
$T_{\rm eff}$ [K]	$5\,914^{+147}_{-144}$	$6\,051^{+127}_{-86}$	3, 3
[Fe/H] [dex]	0.0 ± 0.1	0.158 ± 0.007	3, 3
$\log g$ [$\log_{10}$, cgs]	$4.070^{+0.083}_{-0.089}$	$4.347^{+0.067}_{-0.091}$	3, 3
$V_{\rm sys}$ [km s^{-1}]	10.00 ± 0.20	-2.64 ± 0.23	4, 4
Parallax [mas]	4.331 ± 0.020	6.244 ± 0.015	4, 4
Distance [pc]	230.9 ± 1.1	160.15 ± 0.38	4, 4
Age [Gyr]	$5.0^{+2.6}_{-1.7}$	$2.7^{+2.5}_{-2.0}$	5, 5
H	9.182 ± 0.016	8.923 ± 0.030	6, 6
Planetary Parameters			
$M_{\rm p}$ [$M_{\rm J}$]	0.36 ± 0.09	0.525 ± 0.026	7, 5
$R_{\rm p}$ [$R_{\rm J}$]	1.22 ± 0.14	1.242 ± 0.053	7, 5
$M_{\rm p}$ [$M_\oplus$]	114 ± 29	167 ± 8	7, 5
$R_{\rm p}$ [$R_\oplus$]	13.7 ± 1.6	13.92 ± 0.59	7, 5
$\rho_{\rm p}$ [g cm^{-3}]	0.26 ± 0.11	0.363 ± 0.050	7, 5
$T_{\rm eq}$ [K]	$1\,531 \pm 37$	$1\,322^{+14}_{-15}$	8, 9
$P_{\rm orb}$ [days]	$4.35301101 \pm 0.00000066$	$4.46529913 \pm 0.00000037$	10, 10
T_0 [BJD$_{\rm TDB}$]	$2\,457\,077.30360 \pm 0.00028$	$2\,456\,476.03405 \pm 0.00019$	10, 10
T_{14} [hr]	4.003 ± 0.024	$2.850^{+0.012}_{-0.013}$	11, 9
i [deg]	85.43 ± 0.29	85.634 ± 0.056	7, 9
e	≤ 0.016	≤ 0.011	5, 5
a [au]	0.0557 ± 0.0018	$0.0553^{+0.0012}_{-0.0013}$	8, 5
$K_{\rm p}$ [km s^{-1}]	174 ± 50	134 ± 24	7, 5

5.2 Methods

5.2.1 Observations and data reduction

Both targets were observed simultaneously by the two high-resolution spectrographs GIANO-B (wavelength range: $950 - 2\,450$ nm, spectral resolving power $R \approx 50\,000$) and HARPS-N (wavelength range: $383 - 693$ nm, $R \approx 115\,000$) in the GIARPS configuration (Claudi et al., 2017) at the Telescopio Nazionale Galileo (TNG), as part of the Global Architecture of Planetary Systems (GAPS) Project[2]. Both targets were observed in the nodding ABAB observing mode (described in Sect. 2.1), allowing an optimal subtraction of detector and thermal background noise.
For this analysis, we only used the NIR data from GIANO-B, as we were primarily interested in estimating the volatile content of the atmospheres through molecular signatures.

For WASP-13 b, data from two transit observations were available (i.e. 26 December 2019 and 04 January 2022), but only data from the second transit were used for this analysis since the first transit was observed only partially due to instrumental problems. On 04 January 2022, 68 spectra (with exposure time per spectra of $t_{\rm exp} = 200$ s) were available. The pre-transit and transit-ingress data were missing, but $\sim 90\%$ of the transit was available and observed at low airmass (mean airmass $AM = 1.02$).

For HAT-P-1 b, data from two transit observations were available (i.e. 30 August 2019 and 31 July 2021). For each night, 64 spectra with $t_{\rm exp} = 200$ s were taken. The target was observed at a mean airmass $AM = 1.04$ and $AM = 1.08$, on the first and second night, respectively. On the second observing night mild calima (see Sect. 4.2.1) was present. A schematic log of the observations is reported in Table 5.2.

Table 5.2: Log of the GIANO-B observations of the transits of WASP-13 b and HAT-P-1 b.[a]

Target	Night	Airmass	$N_{\rm obs}$	$t_{\rm exp}$ [s]	$(\mathrm{S/N})_{\rm avg}$	$(\mathrm{S/N})_{\rm min}$ to $(\mathrm{S/N})_{\rm max}$
WASP-13 b	04 January 2022	$1.11 \rightarrow 1.00 \rightarrow 1.06$	68	200	18	$4 - 32$
HAT-P-1 b	30 August 2019	$1.12 \rightarrow 1.02 \rightarrow 1.03$	64	200	30	$1 - 55$
HAT-P-1 b	31 July 2021	$1.21 \rightarrow 1.02$	64	200	26	$1 - 47$

Notes. [(a)] From left to right we report: the date at the start of the observing night; the airmass during the planetary transit; the number of observed spectra $N_{\rm obs}$; the exposure time per spectrum $t_{\rm exp}$; the signal-to-noise ratio averaged across the whole spectral range $(\mathrm{S/N})_{\rm avg}$; the range of signal-to-noise ratios $(\mathrm{S/N})_{\rm min}$ to $(\mathrm{S/N})_{\rm max}$ in the individual spectral orders.

Following the methods explained in Chapters 3 and 4, the raw spectra were dark-subtracted, extracted, and calibrated in wavelength, using the GOFIO pipeline Python-3 version (Rainer et al., 2018). As explained in previous chapters, the wavelength calibration performed by GOFIO is based on observing the spectrum of a U-Ne lamp as a template at the end of each observing night, but the pixel-wavelength solution is not sufficiently accurate for our kind of analysis and is expected to shift and jitter during the observations due to the mechanical instability of the instrument. In order to correct the spectral drift of the instrument, we aligned all the spectra of a single night to a common reference frame via cross-correlation with a time-averaged observed spectrum of the target used as a template. Thanks to this correction, we achieved a residual shift of the spectra well below $0.3\,\mathrm{km\,s^{-1}}$ (approximately 1/10th of a pixel) for most of the spectral orders. Finally, we refined the wavelength calibration by matching the position of a set of telluric lines in the time-averaged

[2] `https://theglobalarchitectureofplanetarysystems.wordpress.com/`

observed spectrum with a high-resolution atmospheric transmission model of the Earth generated via the ESO Sky Model Calculator (Noll et al., 2012) and solving for the pixel-wavelength relation with a fourth-order polynomial fit.

The GIANO-B spectral range covers the Y, J, H, K bands in 50 spectral orders and for this analysis, we adopted the same approach we described in Sect. 4.2.1 for what concerns the spectral orders to discard. In particular, we excluded a fixed set of spectral orders dominated by tellurics (8-11,23-26,34-37) and the Y band (orders 38-49) in which GIANO-B has a characteristic drop of throughput. Finally, in each observing night, we excluded a few orders with high residual drift or for which the refined wavelength calibration procedure failed (i.e. orders number 0,3,4,13,22,27,28,30,31 for the night of WASP-13 b, and orders number 20,22,30 and 18,19,22,30 for the first and the second night of HAT-P-1 b, respectively). In this way, we used a spectral range that is as uniform as possible among the nights and in which the differences are mainly due to the stability of the pixel-wavelength solution, which for a few orders depends on the S/N of the observations.

5.2.2 Telluric and stellar spectra removal procedure

In order to remove telluric and stellar contamination we employed a principal component analysis (PCA) on each $M \times N$ ($M = 64 - 68$ spectra, $N = 2048$ pixels) data matrix associated with each spectral order, following the methods described in Sect. 4.2.2. Also in this analysis, in order to choose the appropriate number of principal components to remove, we iteratively computed the standard deviation (σ) of the residuals by gradually increasing the number of components removed from the data and measured its relative variation for each step: $\Delta\sigma = \frac{\sigma_{i-1}-\sigma_i}{\sigma_{i-1}}$, with i = the i-th number of principal components removed. As can be seen from Fig. 5.1, the $\Delta\sigma$ of the residuals gradually decreases when the number of principal components removed increases, down to a plateau, as expected. In order to compute the minimum number of components at which the σ does not change in a significative way (i.e. the plateau is reached), we studied the relative variation of $\Delta\sigma$ (indicated with the symbol δ) and, also for this analysis, we selected the minimum number of principal components for which $-0.1 < \delta < 0$ for all the spectral orders. In this way, we selected 9 components for the dataset of WASP-13 b and 8 components for both the datasets of HAT-P-1 b.

Once we applied the telluric removal procedure, we visually inspected the map of cross-correlation function (CCF) values as a function of the planetary orbital phase, computed by cross-correlating each of the three datasets with the models of water that we used for the CCF analysis (see Sect. 5.2.3), as a further check. As it is visible from Fig. 5.2, there is no spurious cross-correlation at radial-velocity RV$= 0\,\mathrm{km\,s^{-1}}$ (i.e. the RV of the telluric signal measured in the observed rest-frame), for any of the three cases.

It is worth noting that due to the combined effect of Earth's velocity around the barycenter of the Solar System (barycentric velocity) and velocity of the centre of mass of the star-planet systems with respect to the Earth (systemic velocity), the planetary signal of HAT-P-1 b is shifted relatively far from the telluric rest-frame in terms of RV during most of the transit (at the mid-transit point the observed planetary signal has an RV$\sim -12\,\mathrm{km\,s^{-1}}$ and RV$\sim -21\,\mathrm{km\,s^{-1}}$, for the first and second transit of HAT-P-1 b, respectively) and thus it is less affected by the telluric contamination.

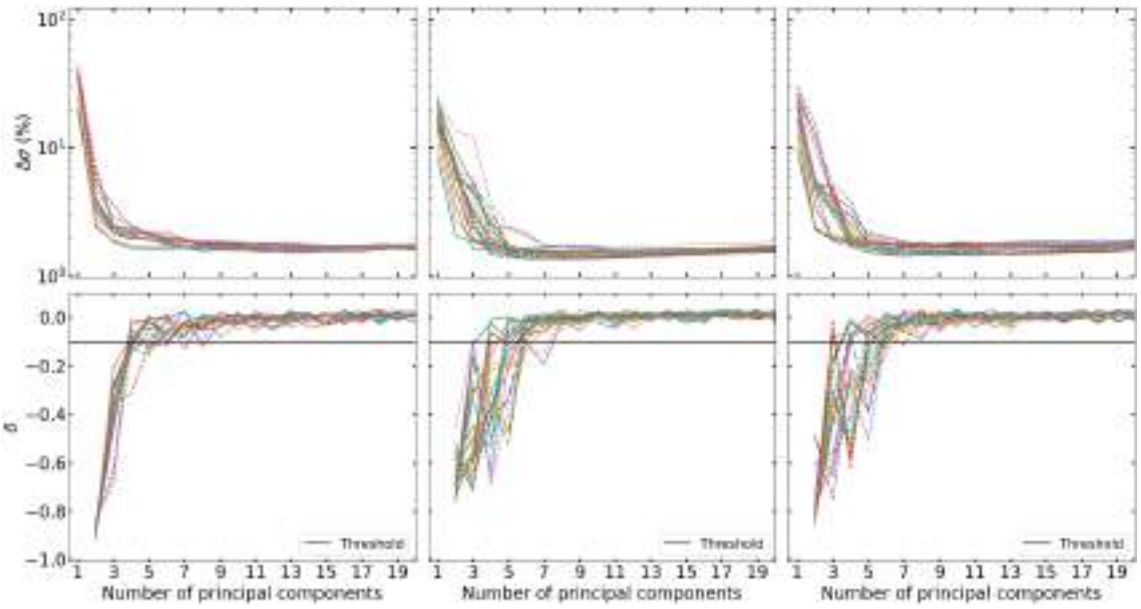

Figure 5.1: Variation of the standard deviation (σ) of the residuals as a function of the number of principal components removed via PCA, for the WASP-13 b dataset (left panels) and the HAT-P-1 b dataset of the first (middle panels) and second (right panels) night. Top panels: relative variation $\Delta\sigma$ of the standard deviation of the residuals (expressed in percentage value and reported in logarithmic scale for a better visualisation) in the different spectral orders (coloured solid and dashed lines). Bottom panels: relative variation of $\Delta\sigma$ (δ) in the different spectral orders (coloured solid and dashed lines). The solid black horizontal line represents the -0.1 threshold on δ used to identify the minimum number of principal components to select in order to remove the telluric and stellar contamination.

5.2.3 Searching for atmospheric signals through cross-correlation analysis

In order to measure the atmospheric signal of the two targets, we first searched for the presence of H_2O, the most common primary molecular species in hot-giant planets' atmosphere in a large range of atmospheric temperatures (Madhusudhan, 2012). We built a single-species model for each planet using the petitRADTRANS code (Mollière et al., 2019), assuming an isothermal atmosphere at the equilibrium temperature reported in Table 5.1, dominated by hydrogen and helium, with constant-with-altitude volume-mixing-ratios (VMRs) for hydrogen ($\mathrm{VMR_{H_2}} = 0.855$), helium ($\mathrm{VMR_{He}} = 0.145$), and water ($\mathrm{VMR_{H_2O}} = 10^{-3}$). Although single-species models do not represent any specific chemical scenario, this was the simplest framework we could adopt to probe the presence of chemical species in addition to H_2 and He. After having searched for the presence of H_2O, we also searched for other chemical species common in the atmospheres of hot Jupiters (i.e. CO, CH_4, CO_2, NH_3, HCN, C_2H_2), building a single-species model as described above for each molecular species. See Table 4.3 for the line-lists adopted to build these models.

To search for the atmospheric signal of WASP-13 b and HAT-P-1 b, we cross-correlated the models with the data of each night. The CCF was evaluated by shifting the model in wavelength on a fixed grid of RV lags (Eq. 4.2) ranging from $-270\,\mathrm{km\,s^{-1}}$ to $+270\,\mathrm{km\,s^{-1}}$, in steps of $0.1\,\mathrm{km\,s^{-1}}$. The numeric computation was performed using the C_CORRELATE PXY(L) IDL function[3], with null lag ($L = 0$), since the RV lags were applied to the wavelength array associated with the model. For each lag, the model was interpolated (via spline interpolation) on the same wavelength array of data before computing the CCF. The CCFs calculated for each spectral order were co-added to

[3] `https://www.nv5geospatialsoftware.com/docs/C_CORRELATE.html`

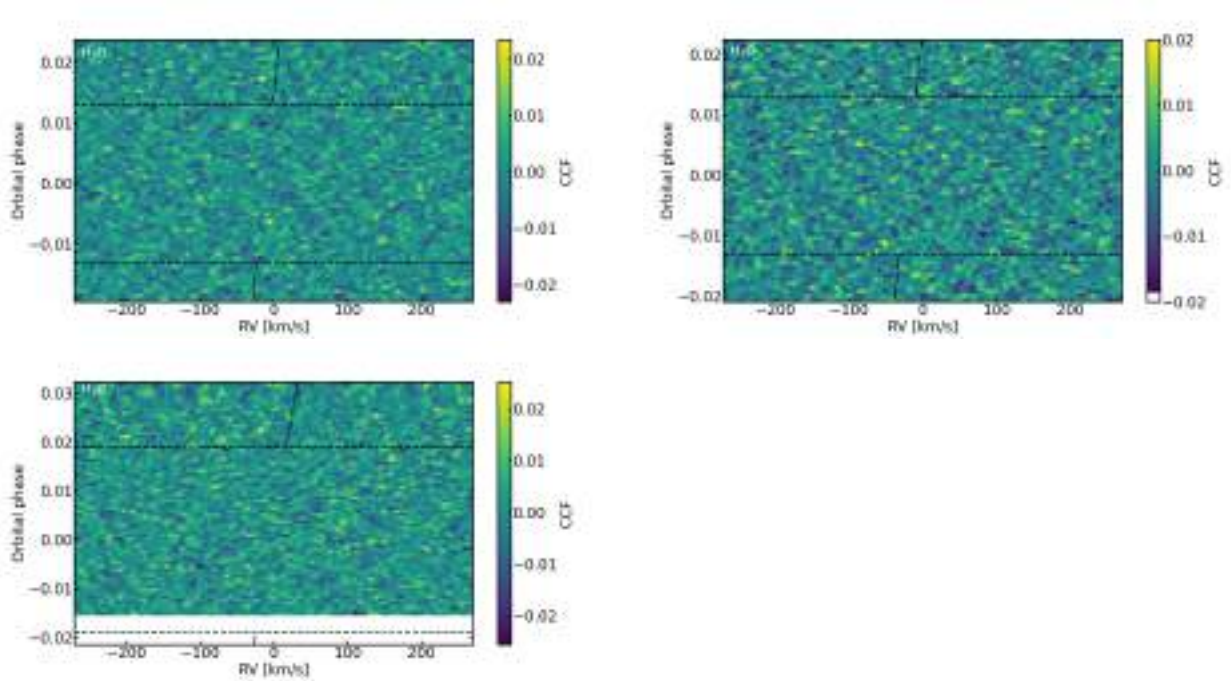

Figure 5.2: Example of CCF values as a function of the orbital phase computed by cross-correlating the model containing only H_2O with the data from the first (top-left panel) and second (top-right panel) night of HAT-P-1 b, and data from the single night (bottom-left panel) of WASP-13 b. The horizontal dashed lines represent the transit ingress and egress while the dash-dotted line represents the expected CCF peak trail due to the planetary motion, as measured in the observer rest frame. The expected CCF peak trail in transit is not represented for clarity. As it is visible, no telluric residuals are visible by eye at $RV = 0\,km\,s^{-1}$ in the three datasets. The white horizontal band in the bottom-left panel corresponds to a lack of pre-transit/transit-ingress spectra.

obtain a single CCF for each exposure of each night.

Following the methods described in Sect. 4.2.4, we assumed that the Doppler shift of the atmospheric signal, as observed from the Earth, can be expressed as a function of three RVs (see Eq. 1.23) and assumed a circular orbit for both targets (Bonomo et al., 2017). We built the $K_p - V_{rest}$ maps exploring a range of planetary RV semi-amplitudes K_p (defined in Eq. 1.26) that spans from $0\,km\,s^{-1}$ to $270\,km\,s^{-1}$ in steps of $1.0\,km\,s^{-1}$. The expected planetary RV semi-amplitudes are $K_p = 174 \pm 50$ and $K_p = 134 \pm 24$, for WASP-13 b and HAT-P-1 b, respectively. In order to build these maps, we binned the CCF values in RV using a bin width of $3.1\,km\,s^{-1}$ and took the median of the CCF values in each RV bin as the value of the CCF associated with each bin, before co-adding the CCF values in phase for each trial K_p.

5.3 Results

In Fig. 5.3, we report the S/N $K_p - V_{rest}$ maps obtained by cross-correlating the H_2O model with WASP-13 b and HAT-P-1 b data. For HAT-P-1 b, we show both the S/N $K_p - V_{rest}$ map obtained by using single-night data and by combining the data from the two observing nights. In order to build these maps, we divided the CCF values by the standard deviation of the noise far ($|V_{rest}| \geq 25\,km\,s^{-1}$) from the peak.

As it can be seen from Fig. 5.3, for WASP-13 b, we do not detect any significant signal (S/N≥ 3) around the expected planetary RV. In the S/N $K_p - V_{rest}$ map of the H_2O model, there is a spurious

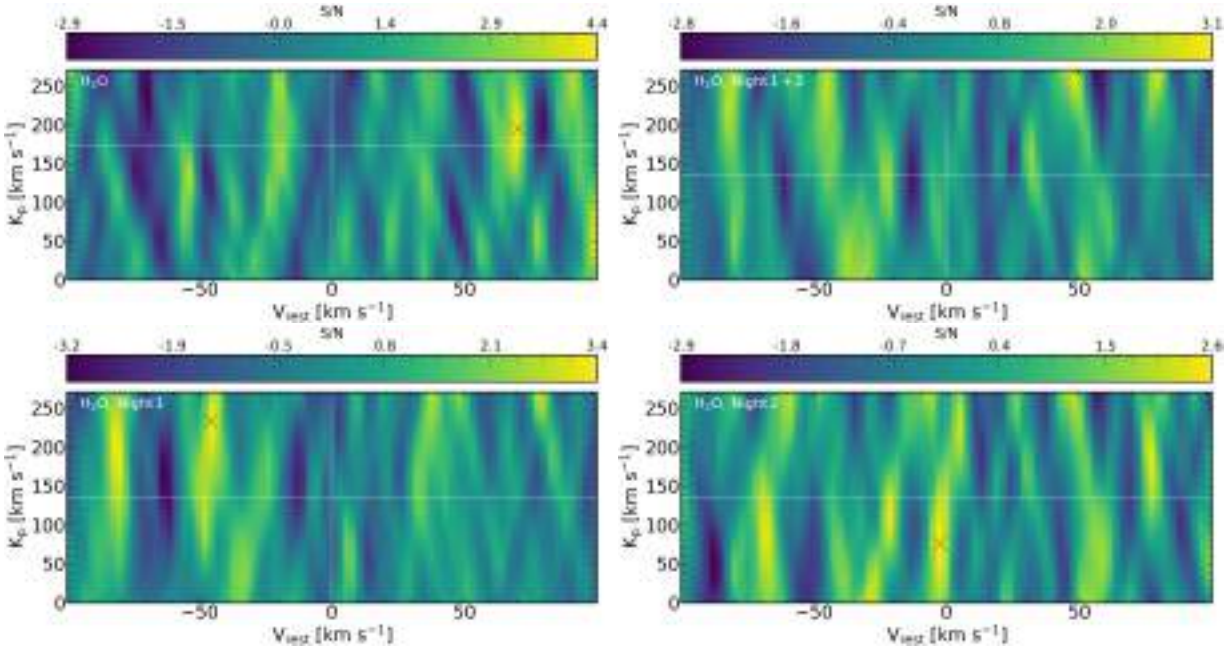

Figure 5.3: (S/N) $K_\mathrm{p} - V_\mathrm{rest}$ maps. These maps are built by cross-correlating a single-species model of H_2O with data from the single night of WASP-13 b (top-left panel) and data from the first (bottom-left panel) and second (bottom-right panel) night of HAT-P-1 b (right panel), as described in the text. We also report the (S/N) $K_\mathrm{p} - V_\mathrm{rest}$ map obtained by combining the data from the two observing nights of HAT-P-1 b (top-right panel). The maps are computed by dividing the CCF values by the standard deviation of the noise far ($|V_\mathrm{rest}| \geq 25\,\mathrm{km\,s^{-1}}$) from the peak. The horizontal (vertical) white dashed lines represent the expected K_p (V_rest) of the atmospheric signal. The black "×" marks denote the cross-correlation maximum in each plot.

peak of the signal at $V_\mathrm{rest} \sim 70\,\mathrm{km\,s^{-1}}$ and $K_\mathrm{p} \sim 195\,\mathrm{km\,s^{-1}}$. This signal can have different possible origins. For example, it could be due to cross-correlation with telluric residuals not entirely corrected by PCA. However, this hypothesis does not seem probable, since the RV of the signal is too high with respect to the RV of telluric lines, as measured inside the planetary rest-frame ($\sim 3\,\mathrm{km\,s^{-1}}$). In addition, by being the telluric signal stationary in the observer rest-frame, it is expected to be observed at low K_p ($\sim 0\,\mathrm{km\,s^{-1}}$). Another possible explanation is the presence of aliasing, that is a systematic artefact of CCFs due to either auto-correlation of the model with the searched species or correlations with alternative species in the spectrum, (see Borsato et al. 2023, and references therein). However, it is worth noting that we do not see multiple CCF peaks at different RVs (as typical of aliasing), but only a single one. Therefore, further analyses are needed to investigate the possible origin of this spurious peak.

For what concerns HAT-P-1 b, looking at the $K_\mathrm{p} - V_\mathrm{rest}$ maps we do not find any significant signal around the expected planetary RV. In particular, on both nights, the CCF signal has a maximum S/N ~ 3 without any significant peak at the expected position. Even if, in the second night, a peak of the signal is visible at $K_\mathrm{p} = 76\,\mathrm{km\,s^{-1}}$ and $V_\mathrm{rest} = 2.7\,\mathrm{km\,s^{-1}}$ (compatible with the expected RV at $< 3\,\sigma$), it is not statistically significant (S/N= 2.6) and thus cannot be considered as an atmospheric signature. When the data from the two nights are combined, we do not observe any significant signal around the expected planetary RV and the map does not show any spurious significant cross-correlation peak.

We do not find any significant signal for the other testes molecular species in both the dataset of WASP-13 b and HAT-P-1 b. We searched for all the other molecular species using the same set

of spectral orders (see Sect. 5.2.1). However, the CO has absorption features in only two spectral bands (one centered at 1 600 nm and one at 2 400 nm), considering the GIANO-B wavelength range. Therefore, we also searched for the signal of CO by using only orders covering these bands (i.e. orders number 1,14,15,16,17). In this case, a significant signal around the expected planetary RV is visible in the $K_p - V_{rest}$ map of the CO for WASP-13 b (see Fig. 5.4). Even if the peak of the signal is shifted at a K_p higher than the expected one ($K_p > 250\,km\,s^{-1}$), at the expected planetary RV the CCF signal has an S/N= 5.2 (i.e. an S/N only 0.7 unities smaller than the S/N of the peak). In Fig. 5.4, we also show the CCF values as a function of the planetary orbital phase, computed by cross-correlating the CO model with data, in order to visually check the possible presence of spurious cross-correlation with the stellar spectrum that could produce the signal we observe. As it is visible, we do not see by eye the presence of spurious cross-correlation at the stellar RV. However, since the most significant signal in the $K_p - V_{rest}$ map is not centered around the planetary RV, we do not consider this as a detection, but as a possible hint of the presence of CO, that must be confirmed with future studies (see Sect. 5.4).

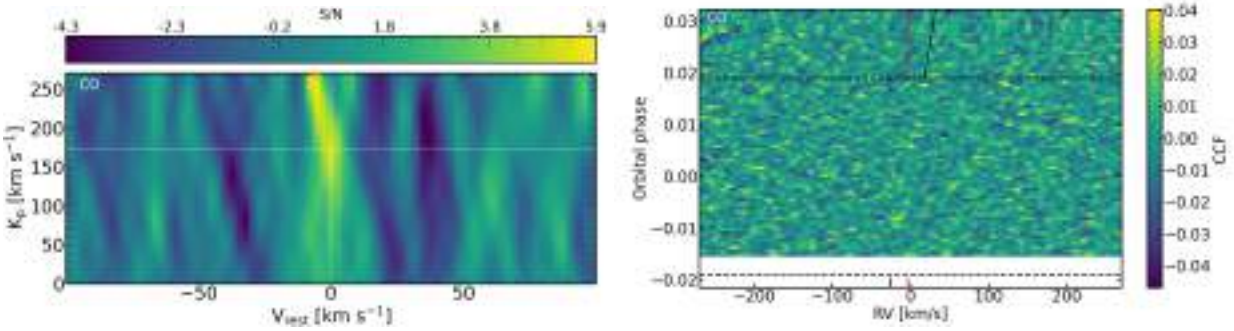

Figure 5.4: CCF analysis of the atmospheric CO signal. Left-panel: (S/N) $K_p - V_{rest}$ map obtained by cross-correlating a single-species model of CO with data from the single night of WASP-13 b. The meaning of the symbols is the same as that reported in Fig. 5.3. As it can be seen, the CCF peak (S/N = 5.9) is shifted with respect to the expected planetary RV and, at the expected position in the $K_p - V_{rest}$ map, the CCF has an S/N= 5.2. Right-panel: CCF values as a function of the orbital phase computed by cross-correlating the model containing only CO with the data from the single night of WASP-13 b. The meaning of the symbols is the same as that reported in Fig. 5.2, with the addition that the red dash-dotted line represents the expected RV of the stellar signal, as measured in the observer rest frame. As it is visible, no spurious cross-correlations are visible by eye at the stellar RV.

5.4 Discussion and future steps of the analysis

In this work, we reported a preliminary analysis of the atmospheric investigation of the two hot Jupiters WASP-13 b and HAT-P-1 b, at high spectral resolution.

We applied a data reduction and analysis approach similar to that used for the analysis of KELT-8 b and KELT-23 Ab, reported in Chapter 4. By performing a CCF analysis on data of a single transit of WASP-13 b and of two transits of HAT-P-1 b, we do not measure the atmospheric signal of the two targets. Indeed, we do not find evidence for the presence of the signal of H_2O and of the other probed species by cross-correlating single-species models with data. Only for WASP-13 b, we find a signal that could hint at the presence of CO in the atmosphere of the target.

In order to interpret our results, we considered the atmosphere of both targets to be in chemical

equilibrium. In particular, for the atmosphere of WASP-13 b we assumed a stellar metallicity (see Table 5.1), and a stellar carbon-to-oxygen (C/O) ratio (i.e. C/O = 0.45, from the Hypatia Catalog Database, Hinkel et al. 2014). Also for the atmosphere of HAT-P-1 b, we assumed a stellar metallicity (see Table 5.1), and a stellar C/O ratio (i.e. C/O = 0.62, from the Hypatia Catalog Database). Finally, for each target, we assumed an isothermal atmosphere at the equilibrium temperature reported in Table 5.1. Under these assumptions, we derived the volume-mixing-ratios (VMRs) of each chemical species as a function of atmospheric pressure, using the chemical network Chemcat[4] (Cubillos et al. in prep.). In Fig. 5.5, we plot the derived VMRs of different chemical species as a function of the atmospheric pressure for the atmosphere of both targets. As is visible, and as expected considering the equilibrium temperature and the assumed C/O ratios of the targets (Madhusudhan, 2012), the most abundant molecular species, after H_2, are H_2O and CO, as the formation of CO is favoured with respect to CH_4 for temperatures higher than $T \sim 1\,300$ K. For each planet, the abundances of H_2O and CO are similar to each other, with the abundance of CO being slightly higher than that of H_2O in the case of HAT-P-1 b. Indeed, $\mathrm{VMR}_{H_2O} \sim 0.00046$ and $\mathrm{VMR}_{CO} \sim 0.00038$, for WASP-13 b, while $\mathrm{VMR}_{H_2O} \sim 0.00046$ and $\mathrm{VMR}_{CO} \sim 0.00075$, for HAT-P-1 b. Among the probed molecular species, CO_2 is expected to be the third most abundant species, but with a VMR $\sim 10^{-3}$ times lower than those of H_2O and CO.

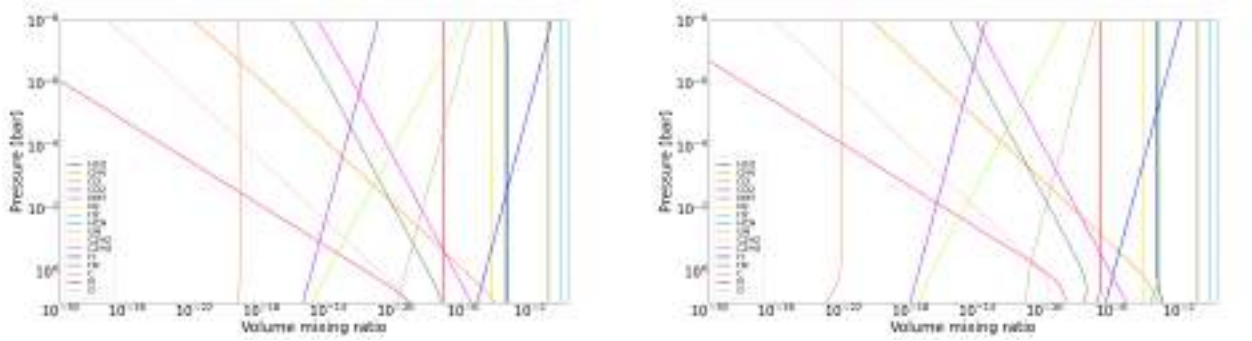

Figure 5.5: VMRs of different chemical species as a function of atmospheric pressure, for the atmosphere of WASP-13 b (left panel) and HAT-P-1 b (right panel). The VMRs are computed assuming an isothermal atmosphere in chemical equilibrium with the parameters reported in the text. As it can be seen, H_2O and CO are expected to be the most abundant molecular species after H_2, in both atmospheres.

From this indicative simulation, we expect the signals of H_2O and CO to be stronger than those of the other molecules and, thus, easier to detect. For what concerns the hint of the presence of CO, which we find in the atmosphere of WASP-13 b, it is in accordance with this scenario. However, it is worth noting that, if we assume a planetary origin for this signal, the high RV shift of the peak of the signal would be difficult to explain with the presence of atmospheric dynamical effects only. Indeed, for example, assuming a synchronous rotation for WASP-13 b, the possible K_p shift due to atmospheric rotation would be of about $\Delta K_\mathrm{p} = 12\,\mathrm{km\,s^{-1}}$, according to Eq. (7) in Wardenier et al. (2023), which is a small quantity compared to the observed shift ($\Delta K_\mathrm{p} \sim 100\,\mathrm{km\,s^{-1}}$). For these reasons, we conservatively consider it as a non-detection and suggest confirming the possible presence of CO with further analyses.

In conclusion, we do not detect the atmospheric signal of the two hot Jupiters WASP-13 b and HAT-P-1 b, with our preliminary CCF analysis of high-resolution GIANO-B data. Our non-detection

[4] `https://chemcat.readthedocs.io/en/main/chemistry_tutorial.html`

of H_2O in the atmosphere of HAT-P-1 b does not confirm the detection obtained at low resolution. However, we want to underline that our non-detection does not exclude that this chemical species, as well as the other probed ones, is present in the atmosphere of the two targets. With the CCF analysis alone, we are not able to put upper limits on the abundance of the chemical species present in the atmosphere of WASP-13 b and HAT-P-1 b, but we can have first indications about the strength of the atmospheric signal of the two targets. The analysis is still ongoing in order to better understand the origin of our non-detections and to exclude possible observing and/or instrumental problems that occurred during the collection of the data, that could have impacted our analysis. In order to fulfil these aims, as the next steps of this analysis, we will perform injection and retrieval tests with different models (e.g. single-species models of H_2O and CO, with different VMRs), in order to further check our ability to detect the signals of the dominant secondary molecular species. We will also perform a CCF analysis employing multiple-species models (e.g. transmission spectrum models obtained assuming an atmosphere in chemical equilibrium), in order to test the possibility that the single-species models used in this analysis are not sufficiently adequate to probe the atmosphere of these two targets. Another step of this analysis will be to analyse also the visible data collected by HARPS-N during the three transits, in order to measure the atmospheric signal of the targets through the detection of atomic species and to cross-check the presence of observing problems. Finally, in the future, we plan to observe again both targets in order to refine our analysis with new data, both with GIANO-B and with other high-resolution NIR instruments (e.g. CARMENES).

Role of the Ph.D. candidate in the work

As the leading author of this work (in preparation), I coordinated the work and performed the preliminary cross-correlation analysis, under the supervision of Dr. Paolo Giacobbe. Regarding the future developments of this work, I will carry out the various tests we planned.

Chapter 6

Conclusions

In this chapter, I report a summary and the main conclusions of the results achieved in the works presented in this Ph.D. thesis and present the studies that could be carried out in the near future in line with the ones conducted during my three years of Ph.D. studies.

6.1 Summary of the results achieved

In this thesis, I reported the analysis of the transmission spectra of the atmosphere of five hot giant exoplanets, obtained with the near-Infrared (NIR) GIANO-B high-resolution spectrograph, mounted at the Telescopio Nazionale Galileo (TNG). These analyses, reported from Chapter 3 to Chapter 5, resulted in a published paper (Basilicata et al., 2024a), a submitted paper (Basilicata et al., 2024b), and a paper currently in preparation (Basilicata et al., in prep.).

In particular, in Chapter 3, I reported the analysis of high-resolution observations of the atmosphere of the warm Neptune HAT-P-11 b. Warm Neptunes are difficult targets for atmospheric studies, due to their relatively small radii and low temperatures, which result in a reduced atmospheric scale height. However, HAT-P-11 b is a remarkable target for atmospheric characterisation, because of the large brightness of its host star ($V = 9.46\,\mathrm{mag}$; $H = 7.13\,\mathrm{mag}$). In this work, we first reviewed the physical and architectural properties of the HAT-P-11 planetary system, by analysing transits and occultations of HAT-P-11 b from the *Kepler* data set as well as HIRES at Keck archival radial-velocity data. In this work, we measure a radius of $R_\mathrm{p} = 0.4466 \pm 0.0059\,R_\mathrm{J}$, a mass of $M_\mathrm{p} = 0.0787 \pm 0.0048\,M_\mathrm{J}$, and an orbital eccentricity of $e = 0.2577^{+0.0033}_{-0.0025}$, for HAT-P-11 b. These values are in agreement with those in the literature. We also find an alternative explanation to the long-period radial-velocity signal of HAT-P-11 previously attributed to the HAT-P-11 c planet (Yee et al., 2018). In particular, we suggest that it is likely due to the stellar magnetic activity cycle. Probing the atmosphere of HAT-P-11 b, we detect the presence of H_2O (with an S/N of 5.1 and a significance of $3.4\,\sigma$) and of NH_3 (with an S/N of 5.3 and a significance of $5.0\,\sigma$). We also tentatively detect the presence of CO_2 and CH_4, with an S/N of 3.0 and 4.8, and a significance of 3.2 σ and 2.6 σ, respectively. The significance of the detections was computed by performing a Welch *t-test* on two samples of CCF values: the former far ($|V_\mathrm{rest}| > 25\,\mathrm{km\,s^{-1}}$) from the planet's rest-frame velocity and the latter near to it ($|V_\mathrm{rest}| < 3\,\mathrm{km\,s^{-1}}$). The robustness of these detections was evaluated by performing different statistical analyses.

In conclusion, these results confirm the detection of H_2O obtained at low resolution and constitute

the first detection of NH_3 in the atmosphere of a warm Neptune. They also constitute the first simultaneous observation of multiple molecular species in the atmosphere of this type of planets. With our results, we started exploring plausible chemical conditions for the atmosphere of HAT-P-11 b. In particular, our models suggest two scenarios more in line with the observations: the first model describes an atmosphere in chemical equilibrium with super-solar metallicity and enhanced C/O and N/O ratios relative to solar values; the second model describes an atmosphere with disequilibrium chemistry (i.e. NH_3 vertical quenching), lower metallicity, and C/O and N/O ratios close to solar values. Finally, we also show how a small error ($\approx 1\%$) on the eccentricity and argument of periastron parameters translates into a large uncertainty ($\approx 25\%$) on the retreived K_p parameter. It is important to take into account this last result for future investigation of atmospheric dynamical effects.

In Chapter 4, I report the analysis of the atmospheres of the two hot Jupiters KELT-8 b and KELT-23 Ab. Even if they are valid targets for atmospheric characterisation, there are no atmospheric studies in the literature for either planet. Therefore, in this work, we searched for the atmospheric signature of both planets for the first time. In order to do this, we first searched for the presence of H_2O, the most common molecular species in the atmosphere of hot giant planets under a broad range of physical and chemical conditions. We detect the signal of H_2O in both the atmospheres of KELT-8 b and KELT-23 Ab, with an S/N = 6.6 and S/N = 4.2, respectively. We also searched for the presence of other secondary species common in the atmosphere of this type of planets but we do not detect any of them. We also performed a preliminary characterisation of atmospheric chemical and physical properties, under simple assumptions (i.e. one-dimensional isothermal atmospheres). In order to do this, we run two different retrievals for each target: a retrieval assuming chemical equilibrium and a "free-chemistry" retrieval, in which the abundance of each molecule could vary freely. With this analysis, we determine constraints on the chemical conditions of the two atmospheres, for the first time. In particular, in the case of KELT-8 b, we determine a water volume mixing ratio of $\log_{10}(\mathrm{VMR}_{H_2O}) = -2.07^{+0.53}_{-0.72}$, a metallicity [M/H] $= 0.77^{+0.61}_{-0.89}$ dex, and a sub-solar C/O ratio (C/O ≤ 0.30, at $2\,\sigma$). For KELT-23 Ab, we find $\log_{10}(\mathrm{VMR}_{H_2O}) = -2.26^{+0.75}_{-1.24}$, a metallicity [M/H] $= -0.42^{+1.56}_{-1.35}$ dex, and a C/O ratio ≤ 0.78 (at $2\,\sigma$). Comparing the retrieved chemical properties of the atmospheres of the two planets with those of the host stars, we suggest a formation scenario for each target. In particular, we find that for both planets, the accretion of gaseous material occurred within the H_2O snowline in a pebble-rich disk, enriched in oxygen due to sublimation of water ice from the inward-drifting pebbles.
In conclusion, we report the detection of the atmospheric signal of KELT-8 b and KELT-23 Ab, through the measurement of the signal of H_2O. We also report the first preliminary characterisation of the chemical-physical properties of the atmospheres of the two targets, that allows to put first constraints on the chemical composition of the two atmospheres and to infer important information about the formation mechanisms behind the two hot Jupiters. Finally, our analysis of only one transit observation for each target shows that these two planets are very interesting targets for atmospheric investigations and that it is worth observing them with more powerful instruments, in order to improve our knowledge about their atmospheres and their formation.

In Chapter 5, I report the preliminary results of the first atmospheric study of WASP-13 b and the first high-resolution investigation of the atmosphere of HAT-P-1 b. We adopted a data-reduction approach similar to that reported in Chapter 4 and searched for the atmospheric signal of the targets by cross-correlating data of one transit observation (for WASP-13 b) and of two transit observations

(for HAT-P-1 b), with single-species atmospheric models. We first searched for the signal of H_2O, but our preliminary results do not show any significant signal at the expected planetary radial velocity, for either target. We also searched for the presence of other molecular species, common in the atmosphere of hot giant planets, but we do not detect any of them in the atmosphere of the two planets. We only find a possible hint of the presence of CO in the atmosphere of WASP-13 b, whose signal needs to be confirmed with further studies. We also computed the expected abundances of different chemical species, for the atmosphere of each of the two targets, under the assumption of an isothermal atmosphere in chemical equilibrium, with the metallicities and C/O ratios of the respective host stars. For both planets, we find that the most abundant secondary tracers are H_2O and CO, with abundances similar to each other. This simple chemical scenario has to be confirmed with further analyses.
In conclusion, with our preliminary analysis we do not detect the atmospheric signal of WASP-13 b and HAT-P-1 b, not confirming the detection of H_2O obtained at low resolution for the latter. We find a possible hint of the presence of CO in the atmosphere of WASP-13 b which, if confirmed, would be in accordance with the prediction from chemical equilibrium. The analysis is still ongoing and we plan to perform further tests and observations in order to refine our analysis and to understand the origin of the non-detections.

6.2 Future perspectives

In my Ph.D. thesis, I have studied the transmission spectrum of several exoplanets, including hot Neptunes and hot Jupiters. These analyses have contributed to a better characterisation and understanding of their atmospheres. I plan further investigations associated with this research line in the near future, in order to understand other aspects of these atmospheres and improve our knowledge about hot giant planets.

For what it concerns the future perspectives of the works reported in this thesis, the near-future plans are described in the following. In particular, the next step of the study of HAT-P-11 b is to analyse new observations gathered by GIANO-B and by other instruments (e.g. CARMENES), in order to increase the S/N of the detections, to independently confirm the results we obtain and to find conclusive evidence of the presence of CH_4 and CO_2 in the atmosphere of the target. We also plan to perform atmospheric retrieval analyses in a Bayesian framework, in order to identify which chemical scenario better describes the atmosphere of HAT-P-11 b among the two proposed and to constrain the chemical and physical conditions of its atmosphere, on a statistically robust base. With this future analysis, we will also be able to suggest plausible formation mechanisms for this target. For what it concerns the analysis of KELT-8 b and KELT-23 Ab, we show that these two hot Jupiters are remarkable targets for further atmospheric investigations. Indeed, we plan to observe them with both high-resolution instruments from the ground (e.g. CRIRES$^+$) and low-resolution instruments from space (i.e. HST and JWST). These future observations will allow us to better characterise the atmospheric properties of the two hot Jupiters and to put stronger constraints on the chemical composition of the two planets, through the detection of secondary species other than H_2O. We also plan to perform atmospheric retrieval analyses by using more complex atmospheric models, which keep into account the three-dimensionality of the planets, in order to investigate possible asymmetries between the two regions of the terminator (i.e. the morning and the evening one) and,

more in general, to better characterise the atmospheric dynamics of the two hot Jupiters.
Finally, the near-future steps of the analysis of the atmospheres of WASP-13 b and HAT-P-1 b will be focused on understanding the origin of our non-detections and excluding possible observing and/or instrumental problems that occurred during the collection of the data, that could have impacted our analysis. In particular, we plan to perform different tests of injection and retrieval of artificial atmospheric signals in order to check our ability to detect them with the available datasets. We plan to build atmospheric models with different complexity to explore how this aspect affects the detection of the atmospheric signal of the two planets. We also plan to observe these two targets again, both with GIANO-B and with other high-resolution instruments, in order to increase the S/N of the observations and to cross-check the presence of possible systematic effects in our preliminary analysis.

In general, as a future perspective of this research line, I plan to enlarge the number of hot giant planets with atmospheric characterisation, searching for the atmospheric signal of planets for which there are not atmospheric studies in the literature. I also plan to refine the analysis of already studied targets with future observations both with GIANO-B and with other high-resolution instruments, with the aim of improving our knowledge about their atmospheric chemical and physical properties. These two future steps will allow us to perform more precise population studies of the atmospheres of hot giant planets, which can allow us to better understand the main mechanisms driving their atmospheres and their formation and evolution processes. In this context, I plan to extend the investigation of the atmospheric properties of exoplanets by also performing atmospheric studies in emission, since this kind of observations can bring important information about the three-dimensional thermal structure and the radiative state of exoatmospheres.
I also plan to improve my knowledge of the data analysis of spectra gathered with low-resolution instruments, in order to combine the information that can be extracted from both the high-resolution and low-resolution observations of the same target. This will result in more precise and accurate constraints on both the atmospheric properties and the formation/migration mechanisms of exoplanets.

The works presented in this Ph.D. thesis contribute to improve our comprehension of exoplanetary atmospheres and test the capabilities of the high-resolution spectroscopy technique.
The future is bright for the atmospheric characterisation of exoplanets both at high- and low-resolution. For what it concerns high-resolution, future new-generation extremely large telescopes (e.g. the European Extremely Large Telescope, E-ELT) will allow the detection of the faint atmospheric signal of terrestrial planets. Therefore, refining this technique by studying hot giant planet atmospheres today, will allow us to detect possible biosignatures in the atmosphere of Earth-like planets in the future and, thus, to possibly answer the deep question reported at the beginning of this thesis work: are we alone in the Universe?

Bibliography

N. A-thano, S. Awiphan, I.-G. Jiang, E. Kerins, A. Priyadarshi, I. McDonald, Y. C. Joshi, T. Chulikorn, J. J. C. Hayes, S. Charles, C.-K. Huang, R. Rattanamala, L.-C. Yeh, and V. S. Dhillon. Revisiting the Transit Timing and Atmosphere Characterization of the Neptune-mass Planet HAT-P-26 b. *arXiv e-prints*, art. arXiv:2303.03610, Mar. 2023. doi: 10.48550/arXiv.2303.03610.

R. Allart, V. Bourrier, C. Lovis, D. Ehrenreich, J. J. Spake, A. Wyttenbach, L. Pino, F. Pepe, D. K. Sing, and A. Lecavelier des Etangs. Spectrally resolved helium absorption from the extended atmosphere of a warm Neptune-mass exoplanet. *Science*, 362(6421):1384–1387, Dec. 2018. doi: 10.1126/science.aat5879.

F. J. Alonso-Floriano, A. Sánchez-López, I. A. G. Snellen, M. López-Puertas, E. Nagel, P. J. Amado, F. F. Bauer, J. A. Caballero, S. Czesla, L. Nortmann, E. Pallé, M. Salz, A. Reiners, I. Ribas, A. Quirrenbach, J. Aceituno, G. Anglada-Escudé, V. J. S. Béjar, E. W. Guenther, T. Henning, A. Kaminski, M. Kürster, M. Lampón, L. M. Lara, D. Montes, J. C. Morales, L. Tal-Or, J. H. M. M. Schmitt, M. R. Zapatero Osorio, and M. Zechmeister. Multiple water band detections in the CARMENES near-infrared transmission spectrum of HD 189733 b. *Astronomy & Astrophysics*, 621:A74, Jan. 2019. doi: 10.1051/0004-6361/201834339.

M. Asplund, N. Grevesse, A. J. Sauval, and P. Scott. The Chemical Composition of the Sun. *Annual Review of Astronomy and Astrophysics*, 47(1):481–522, Sept. 2009. doi: 10.1146/annurev.astro.46.060407.145222.

M. Asplund, A. M. Amarsi, and N. Grevesse. The chemical make-up of the Sun: A 2020 vision. *Astronomy & Astrophysics*, 653:A141, Sept. 2021. doi: 10.1051/0004-6361/202140445.

G. Bakos, R. W. Noyes, G. Kovács, K. Z. Stanek, D. D. Sasselov, and I. Domsa. Wide-Field Millimagnitude Photometry with the HAT: A Tool for Extrasolar Planet Detection. *Publications of the Astronomical Society of the Pacific*, 116(817):266–277, Mar. 2004. doi: 10.1086/382735.

G. Á. Bakos, R. W. Noyes, G. Kovács, D. W. Latham, D. D. Sasselov, G. Torres, D. A. Fischer, R. P. Stefanik, B. Sato, J. A. Johnson, A. Pál, G. W. Marcy, R. P. Butler, G. A. Esquerdo, K. Z. Stanek, J. Lázár, I. Papp, P. Sári, and B. Sipőcz. HAT-P-1b: A Large-Radius, Low-Density Exoplanet Transiting One Member of a Stellar Binary. *Astrophysical Journal*, 656(1):552–559, Feb. 2007. doi: 10.1086/509874.

G. Á. Bakos, G. Torres, A. Pál, J. Hartman, G. Kovács, R. W. Noyes, D. W. Latham, D. D. Sasselov, B. Sipőcz, G. A. Esquerdo, D. A. Fischer, J. A. Johnson, G. W. Marcy, R. P. Butler, H. Isaacson, A. Howard, S. Vogt, G. Kovács, J. Fernandez, A. Moór, R. P. Stefanik, J. Lázár, I. Papp, and

P. Sári. HAT-P-11b: A Super-Neptune Planet Transiting a Bright K Star in the Kepler Field. *The Astrophysical Journal*, 710(2):1724–1745, Feb. 2010. doi: 10.1088/0004-637X/710/2/1724.

P. Ballerini, G. Micela, A. F. Lanza, and I. Pagano. Multiwavelength flux variations induced by stellar magnetic activity: effects on planetary transits. *Astronomy & Astrophysics*, 539:A140, Mar. 2012. doi: 10.1051/0004-6361/201117102.

A. Banzatti, I. Pascucci, A. D. Bosman, P. Pinilla, C. Salyk, G. J. Herczeg, K. M. Pontoppidan, I. Vazquez, A. Watkins, S. Krijt, N. Hendler, and F. Long. Hints for icy pebble migration feeding an oxygen-rich chemistry in the inner planet-forming region of disks. *The Astrophysical Journal*, 903(2):124, nov 2020. doi: 10.3847/1538-4357/abbc1a. URL `https://dx.doi.org/10.3847/1538-4357/abbc1a`.

R. J. Barber, J. K. Strange, C. Hill, O. L. Polyansky, G. C. Mellau, S. N. Yurchenko, and J. Tennyson. ExoMol line lists – III. An improved hot rotation-vibration line list for HCN and HNC. *Monthly Notices of the Royal Astronomical Society*, 437(2):1828–1835, 11 2013. ISSN 0035-8711. doi: 10.1093/mnras/stt2011. URL `https://doi.org/10.1093/mnras/stt2011`.

M. Basilicata, P. Giacobbe, A. S. Bonomo, G. Scandariato, M. Brogi, V. Singh, A. Di Paola, L. Mancini, A. Sozzetti, A. F. Lanza, P. E. Cubillos, M. Damasso, S. Desidera, K. Biazzo, A. Bignamini, F. Borsa, L. Cabona, I. Carleo, A. Ghedina, G. Guilluy, A. Maggio, G. Mainella, G. Micela, E. Molinari, M. Molinaro, D. Nardiello, M. Pedani, L. Pino, E. Poretti, J. Southworth, M. Stangret, and D. Turrini. The GAPS Programme at TNG. LV. Multiple molecular species in the atmosphere of HAT-P-11 b and review of the HAT-P-11 planetary system. *Astronomy & Astrophysics*, 686:A127, June 2024a. doi: 10.1051/0004-6361/202347659.

M. Basilicata, P. Giacobbe, M. Brogi, and al. The GAPS Programme at TNG. TBD. Detection of water and preliminary characterisation of the atmospheres of the two hot Jupiters KELT-8 b and KELT-23 Ab. *Astronomy & Astrophysics*, Submitted (article reference: AA52733-24), 2024b.

T. G. Beatty, N. Madhusudhan, R. Pogge, S. M. Chung, A. Bierlya, B. S. Gaudi, and D. W. Latham. The Broadband and Spectrally Resolved H-band Eclipse of KELT-1b and the Role of Surface Gravity in Stratospheric Inversions in Hot Jupiters. *Astronomical Journal*, 154(6):242, Dec. 2017. doi: 10.3847/1538-3881/aa94cf.

B. Béky, D. M. Kipping, and M. J. Holman. SPOTROD: a semi-analytic model for transits of spotted stars. *Monthly Notices of the Royal Astronomical Society*, 442(4):3686–3699, Aug. 2014. doi: 10.1093/mnras/stu1061.

H. Beltz, E. Rauscher, E. M.-R. Kempton, I. Malsky, and A. B. Savel. Magnetic effects and 3d structure in theoretical high-resolution transmission spectra of ultrahot jupiters: the case of wasp-76b. *The Astronomical Journal*, 165(6):257, may 2023. doi: 10.3847/1538-3881/acd24d. URL `https://dx.doi.org/10.3847/1538-3881/acd24d`.

B. Benneke and S. Seager. How to Distinguish between Cloudy Mini-Neptunes and Water/Volatile-dominated Super-Earths. *Astrophysical Journal*, 778(2):153, Dec. 2013. doi: 10.1088/0004-637X/778/2/153.

B. Benneke, I. Wong, C. Piaulet, H. A. Knutson, J. Lothringer, C. V. Morley, I. J. M. Crossfield, P. Gao, T. P. Greene, C. Dressing, D. Dragomir, A. W. Howard, P. R. McCullough, E. M. R. Kempton, J. J. Fortney, and J. Fraine. Water Vapor and Clouds on the Habitable-zone Sub-Neptune Exoplanet K2-18b. *The Astrophysical Journal Letters*, 887(1):L14, Dec. 2019. doi: 10.3847/2041-8213/ab59dc.

S. Bertocco, D. Goz, L. Tornatore, A. Ragagnin, G. Maggio, F. Gasparo, C. Vuerli, G. Taffoni, and M. Molinaro. INAF Trieste Astronomical Observatory Information Technology Framework. In R. Pizzo, E. R. Deul, J. D. Mol, J. de Plaa, and H. Verkouter, editors, *Astronomical Data Analysis Software and Systems XXIX*, volume 527 of *Astronomical Society of the Pacific Conference Series*, page 303, Jan. 2020.

B. Bézard, B. Charnay, and D. Blain. Methane as a dominant absorber in the habitable-zone sub-Neptune K2-18 b. *Nature Astronomy*, 6:537–540, May 2022. doi: 10.1038/s41550-022-01678-z.

K. Biazzo, V. D'Orazi, S. Desidera, D. Turrini, S. Benatti, R. Gratton, L. Magrini, A. Sozzetti, M. Baratella, A. S. Bonomo, F. Borsa, R. Claudi, E. Covino, M. Damasso, M. P. Di Mauro, A. F. Lanza, A. Maggio, L. Malavolta, J. Maldonado, F. Marzari, G. Micela, E. Poretti, F. Vitello, L. Affer, A. Bignamini, I. Carleo, R. Cosentino, A. F. M. Fiorenzano, P. Giacobbe, A. Harutyunyan, G. Leto, L. Mancini, E. Molinari, M. Molinaro, D. Nardiello, V. Nascimbeni, I. Pagano, M. Pedani, G. Piotto, M. Rainer, and G. Scandariato. The GAPS Programme at TNG. XXXV. Fundamental properties of transiting exoplanet host stars. *Astronomy & Astrophysics*, 664:A161, Aug. 2022. doi: 10.1051/0004-6361/202243467.

C. Bilger, P. Rimmer, and C. Helling. Small hydrocarbon molecules in cloud-forming brown dwarf and giant gas planet atmospheres. *Monthly Notices of the Royal Astronomical Society*, 435(3): 1888–1903, Nov. 2013. doi: 10.1093/mnras/stt1378.

J. L. Birkby. Exoplanet Atmospheres at High Spectral Resolution. *arXiv e-prints*, art. arXiv:1806.04617, June 2018.

J. L. Birkby, R. J. de Kok, M. Brogi, E. J. W. de Mooij, H. Schwarz, S. Albrecht, and I. A. G. Snellen. Detection of water absorption in the day side atmosphere of HD 189733 b using ground-based high-resolution spectroscopy at 3.2μm. *Monthly Notices of the Royal Astronomical Society: Letters*, 436(1):L35–L39, 08 2013. ISSN 1745-3925. doi: 10.1093/mnrasl/slt107. URL `https://doi.org/10.1093/mnrasl/slt107`.

J. L. Birkby, R. J. de Kok, M. Brogi, H. Schwarz, and I. A. G. Snellen. Discovery of Water at High Spectral Resolution in the Atmosphere of 51 Peg b. *The Astronomical Journal*, 153(3):138, Mar. 2017. doi: 10.3847/1538-3881/aa5c87.

B. Bitsch, A. D. Schneider, and L. Kreidberg. How drifting and evaporating pebbles shape giant planets. III. The formation of WASP-77A b and τ Boötis b. *Astronomy & Astrophysics*, 665:A138, Sept. 2022. doi: 10.1051/0004-6361/202243345.

D. Blain, R. Landman, P. Mollière, and J. Dittmann. Four HD 209458 b transits through CRIRES+: Detection of H_2O and non-detections of C_2H_2, CH_4, and HCN. *Astronomy & Astrophysics*, 690: A63, Oct. 2024. doi: 10.1051/0004-6361/202450767.

J. Blecic, I. Dobbs-Dixon, and T. Greene. The Implications of 3D Thermal Structure on 1D Atmospheric Retrieval. *Astrophysical Journal*, 848(2):127, Oct. 2017. doi: 10.3847/1538-4357/aa8171.

A. S. Bonomo, A. Sozzetti, A. Santerne, M. Deleuil, J. M. Almenara, G. Bruno, R. F. Díaz, G. Hébrard, and C. Moutou. Improved parameters of seven Kepler giant companions characterized with SOPHIE and HARPS-N. *Astronomy & Astrophysics*, 575:A85, Mar. 2015. doi: 10.1051/0004-6361/201323042.

A. S. Bonomo, S. Desidera, S. Benatti, F. Borsa, S. Crespi, M. Damasso, A. F. Lanza, A. Sozzetti, G. Lodato, F. Marzari, C. Boccato, R. U. Claudi, R. Cosentino, E. Covino, R. Gratton, A. Maggio, G. Micela, E. Molinari, I. Pagano, G. Piotto, E. Poretti, R. Smareglia, L. Affer, K. Biazzo, A. Bignamini, M. Esposito, P. Giacobbe, G. Hébrard, L. Malavolta, J. Maldonado, L. Mancini, A. Martinez Fiorenzano, S. Masiero, V. Nascimbeni, M. Pedani, M. Rainer, and G. Scandariato. The GAPS Programme with HARPS-N at TNG . XIV. Investigating giant planet migration history via improved eccentricity and mass determination for 231 transiting planets. *Astronomy & Astrophysics*, 602:A107, June 2017. doi: 10.1051/0004-6361/201629882.

A. S. Bonomo, X. Dumusque, A. Massa, A. Mortier, R. Bongiolatti, L. Malavolta, A. Sozzetti, L. A. Buchhave, M. Damasso, R. D. Haywood, A. Morbidelli, D. W. Latham, E. Molinari, F. Pepe, E. Poretti, S. Udry, L. Affer, W. Boschin, D. Charbonneau, R. Cosentino, M. Cretignier, A. Ghedina, E. Lega, M. López-Morales, M. Margini, A. F. Martínez Fiorenzano, M. Mayor, G. Micela, M. Pedani, M. Pinamonti, K. Rice, D. Sasselov, R. Tronsgaard, and A. Vanderburg. Cold Jupiters and improved masses in 38 Kepler and K2 small planet systems from 3661 HARPS-N radial velocities. No excess of cold Jupiters in small planet systems. *Astronomy & Astrophysics*, 677:A33, Sept. 2023. doi: 10.1051/0004-6361/202346211.

R. A. Booth and J. D. Ilee. Planet-forming material in a protoplanetary disc: the interplay between chemical evolution and pebble drift. *Monthly Notices of the Royal Astronomical Society*, 487(3): 3998–4011, Aug. 2019. doi: 10.1093/mnras/stz1488.

F. Borsa, G. Scandariato, M. Rainer, A. Bignamini, A. Maggio, E. Poretti, A. F. Lanza, M. P. Di Mauro, S. Benatti, K. Biazzo, A. S. Bonomo, M. Damasso, M. Esposito, R. Gratton, L. Affer, M. Barbieri, C. Boccato, R. U. Claudi, R. Cosentino, E. Covino, S. Desidera, A. F. M. Fiorenzano, D. Gandolfi, A. Harutyunyan, J. Maldonado, G. Micela, P. Molaro, E. Molinari, I. Pagano, I. Pillitteri, G. Piotto, E. Shkolnik, R. Silvotti, R. Smareglia, J. Southworth, A. Sozzetti, and B. Stelzer. The GAPS programme with HARPS-N at TNG. VII. Putting exoplanets in the stellar context: magnetic activity and asteroseismology of <ASTROBJ>τ Bootis A</ASTROBJ>. *Astronomy & Astrophysics*, 578:A64, June 2015. doi: 10.1051/0004-6361/201525741.

N. W. Borsato, H. J. Hoeijmakers, B. Prinoth, B. Thorsbro, R. Forsberg, D. Kitzmann, K. Jones, and K. Heng. The Mantis Network. III. Expanding the limits of chemical searches within ultra-hot Jupiters: New detections of Ca I, V I, Ti I, Cr I, Ni I, Sr II, Ba II, and Tb II in KELT-9 b. *Astronomy & Astrophysics*, 673:A158, May 2023. doi: 10.1051/0004-6361/202245121.

W. J. Borucki and A. L. Summers. The photometric method of detecting other planetary systems. *Icarus*, 58(1):121–134, Apr. 1984. doi: 10.1016/0019-1035(84)90102-7.

W. J. Borucki, D. Koch, G. Basri, N. Batalha, T. Brown, D. Caldwell, J. Caldwell, J. Christensen-Dalsgaard, W. D. Cochran, E. DeVore, E. W. Dunham, A. K. Dupree, T. N. Gautier, J. C. Geary, R. Gilliland, A. Gould, S. B. Howell, J. M. Jenkins, Y. Kondo, D. W. Latham, G. W. Marcy, S. Meibom, H. Kjeldsen, J. J. Lissauer, D. G. Monet, D. Morrison, D. Sasselov, J. Tarter, A. Boss, D. Brownlee, T. Owen, D. Buzasi, D. Charbonneau, L. Doyle, J. Fortney, E. B. Ford, M. J. Holman, S. Seager, J. H. Steffen, W. F. Welsh, J. Rowe, H. Anderson, L. Buchhave, D. Ciardi, L. Walkowicz, W. Sherry, E. Horch, H. Isaacson, M. E. Everett, D. Fischer, G. Torres, J. A. Johnson, M. Endl, P. MacQueen, S. T. Bryson, J. Dotson, M. Haas, J. Kolodziejczak, J. Van Cleve, H. Chandrasekaran, J. D. Twicken, E. V. Quintana, B. D. Clarke, C. Allen, J. Li, H. Wu, P. Tenenbaum, E. Verner, F. Bruhweiler, J. Barnes, and A. Prsa. Kepler Planet-Detection Mission: Introduction and First Results. *Science*, 327(5968):977, Feb. 2010. doi: 10.1126/science.1185402.

A. Borysow. Collision-induced absorption coefficients of H_2 pairs at temperatures from 60 K to 1000 K. *Astronomy & Astrophysics*, 390:779–782, Aug. 2002. doi: 10.1051/0004-6361:20020555.

A. Borysow and L. Frommhold. Collision-induced Infrared Spectra of H 2-He Pairs at Temperatures from 18 to 7000 K. II. Overtone and Hot Bands. *The Astrophysical Journal*, 341:549, June 1989. doi: 10.1086/167515.

A. Borysow, L. Frommhold, and M. Moraldi. Collision-induced Infrared Spectra of H 2-He Pairs Involving 0 1 Vibrational Transitions and Temperatures from 18 to 7000 K. *The Astrophysical Journal*, 336:495, Jan. 1989. doi: 10.1086/167027.

A. Borysow, U. G. Jorgensen, and Y. Fu. High-temperature (1000-7000 K) collision-induced absorption of H"2 pairs computed from the first principles, with application to cool and dense stellar atmospheres. *Journal of Quantitative Spectroscopy and Radiative Transfer*, 68:235–255, Feb. 2001. doi: 10.1016/S0022-4073(00)00023-6.

J. Borysow, L. Frommhold, and G. Birnbaum. Collision-induced Rototranslational Absorption Spectra of H 2-He Pairs at Temperatures from 40 to 3000 K. *The Astrophysical Journal*, 326:509, Mar. 1988. doi: 10.1086/166112.

A. Boucher, A. Darveau-Bernier, S. Pelletier, D. Lafrenière, É. Artigau, N. J. Cook, R. Allart, M. Radica, R. Doyon, B. Benneke, L. Arnold, X. Bonfils, V. Bourrier, R. Cloutier, J. Gomes da Silva, E. Deibert, X. Delfosse, J.-F. Donati, D. Ehrenreich, P. Figueira, T. Forveille, P. Fouqué, J. Gagné, E. Gaidos, G. Hébrard, R. Jayawardhana, B. Klein, C. Lovis, J. H. C. Martins, E. Martioli, C. Moutou, and N. C. Santos. Characterizing Exoplanetary Atmospheres at High Resolution with SPIRou: Detection of Water on HD 189733 b. *Astronomical Journal*, 162(6):233, Dec. 2021. doi: 10.3847/1538-3881/ac1f8e.

A. Boucher, D. Lafreniére, S. Pelletier, A. Darveau-Bernier, M. Radica, R. Allart, É. Artigau, N. J. Cook, F. Debras, R. Doyon, E. Gaidos, B. Benneke, C. Cadieux, A. Carmona, R. Cloutier, P. Cortés-Zuleta, N. B. Cowan, X. Delfosse, J.-F. Donati, P. Fouqué, T. Forveille, K. Grankin, G. Hébrard, J. H. C. Martins, E. Martioli, A. Masson, and S. Vinatier. CO or no CO? Narrowing the CO abundance constraint and recovering the H_2O detection in the atmosphere of WASP-127 b using SPIRou. *Monthly Notices of the Royal Astronomical Society*, 522(4):5062–5083, July 2023. doi: 10.1093/mnras/stad1247.

V. Bourrier and A. Lecavelier des Etangs. 3D model of hydrogen atmospheric escape from HD 209458b and HD 189733b: radiative blow-out and stellar wind interactions. *Astronomy & Astrophysics*, 557:A124, Sept. 2013. doi: 10.1051/0004-6361/201321551.

V. Bozza, L. Mancini, and A. Sozzetti. *Astrophysics of Exoplanetary Atmospheres*, volume 450. Springer, 2018. doi: 10.1007/978-3-319-89701-1.

J. Brande, I. J. M. Crossfield, L. Kreidberg, A. Oklopčić, A. S. Polanski, T. Barman, B. Benneke, J. L. Christiansen, D. Dragomir, D. Foreman-Mackey, J. J. Fortney, T. P. Greene, A. W. Howard, H. A. Knutson, J. D. Lothringer, T. Mikal-Evans, and C. V. Morley. A Mirage or an Oasis? Water Vapor in the Atmosphere of the Warm Neptune TOI-674 b. *The Astronomical Journal*, 164(5): 197, Nov. 2022. doi: 10.3847/1538-3881/ac8b7e.

T. D. Brandt. The Hipparcos-Gaia Catalog of Accelerations. *The Astrophysical Journal Supplement Series*, 239(2):31, Dec. 2018. doi: 10.3847/1538-4365/aaec06.

T. D. Brandt. The Hipparcos-Gaia Catalog of Accelerations: Gaia EDR3 Edition. *The Astrophysical Journal Supplement Series*, 254(2):42, June 2021. doi: 10.3847/1538-4365/abf93c.

Brogi, Giacobbe, P., Guilluy, G., de Kok, R. J., Sozzetti, A., Mancini, L., and Bonomo, A. S. Exoplanet atmospheres with giano - i. water in the transmission spectrum of hd 189 733 b. *Astronomy & Astrophysics*, 615:A16, 2018. doi: 10.1051/0004-6361/201732189. URL `https://doi.org/10.1051/0004-6361/201732189`.

M. Brogi and M. R. Line. Retrieving Temperatures and Abundances of Exoplanet Atmospheres with High-resolution Cross-correlation Spectroscopy. *The Astronomical Journal*, 157(3):114, Mar. 2019a. doi: 10.3847/1538-3881/aaffd3.

M. Brogi and M. R. Line. Retrieving Temperatures and Abundances of Exoplanet Atmospheres with High-resolution Cross-correlation Spectroscopy. *Astronomical Journal*, 157(3):114, Mar. 2019b. doi: 10.3847/1538-3881/aaffd3.

M. Brogi, I. A. G. Snellen, R. J. de Kok, S. Albrecht, J. Birkby, and E. J. W. de Mooij. The signature of orbital motion from the dayside of the planet τ Boötis b. *Nature*, 486(7404):502–504, June 2012. doi: 10.1038/nature11161.

M. Brogi, I. A. G. Snellen, R. J. de Kok, S. Albrecht, J. L. Birkby, and E. J. W. de Mooij. DETECTION OF MOLECULAR ABSORPTION IN THE DAYSIDE OF EXOPLANET 51 PEGASI b? *The Astrophysical Journal*, 767(1):27, mar 2013. doi: 10.1088/0004-637x/767/1/27. URL `https://doi.org/10.1088/0004-637x/767/1/27`.

M. Brogi, R. J. de Kok, J. L. Birkby, H. Schwarz, and I. A. G. Snellen. Carbon monoxide and water vapor in the atmosphere of the non-transiting exoplanet HD 179949 b. *Astronomy & Astrophysics*, 565:A124, May 2014. doi: 10.1051/0004-6361/201423537.

M. Brogi, R. J. de Kok, S. Albrecht, I. A. G. Snellen, J. L. Birkby, and H. Schwarz. Rotation and Winds of Exoplanet HD 189733 b Measured with High-dispersion Transmission Spectroscopy. *Astrophysical Journal*, 817(2):106, Feb. 2016. doi: 10.3847/0004-637X/817/2/106.

M. Brogi, M. Line, J. Bean, J. M. Désert, and H. Schwarz. A Framework to Combine Low- and High-resolution Spectroscopy for the Atmospheres of Transiting Exoplanets. *Astrophysical Journal Letters*, 839(1):L2, Apr. 2017. doi: 10.3847/2041-8213/aa6933.

M. Brogi, V. Emeka-Okafor, M. R. Line, S. Gandhi, L. Pino, E. M. R. Kempton, E. Rauscher, V. Parmentier, J. L. Bean, G. N. Mace, N. B. Cowan, E. Shkolnik, J. P. Wardenier, M. Mansfield, L. Welbanks, P. Smith, J. J. Fortney, J. L. Birkby, J. A. Zalesky, L. Dang, J. Patience, and J.-M. Désert. The Roasting Marshmallows Program with IGRINS on Gemini South I: Composition and Climate of the Ultrahot Jupiter WASP-18 b. *Astronomical Journal*, 165(3):91, Mar. 2023. doi: 10.3847/1538-3881/acaf5c.

R. D. Brothwell, C. A. Watson, G. Hébrard, A. H. M. J. Triaud, H. M. Cegla, A. Santerne, E. Hébrard, D. R. Anderson, D. Pollacco, E. K. Simpson, F. Bouchy, D. J. A. Brown, Y. G. M. Chew, A. Collier Cameron, D. J. Armstrong, S. C. C. Barros, J. Bento, J. Bochinski, V. Burwitz, R. Busuttil, L. Delrez, A. P. Doyle, F. Faedi, A. Fumel, M. Gillon, C. A. Haswell, C. Hellier, E. Jehin, U. Kolb, M. Lendl, C. Liebig, P. F. L. Maxted, J. McCormac, G. R. M. Miller, A. J. Norton, F. Pepe, D. Queloz, J. Rodríguez, D. Ségransan, I. Skillen, B. Smalley, K. G. Stassun, S. Udry, R. G. West, and P. J. Wheatley. A window on exoplanet dynamical histories: Rossiter-McLaughlin observations of WASP-13b and WASP-32b. *Monthly Notices of the Royal Astronomical Society*, 440(4):3392–3401, June 2014. doi: 10.1093/mnras/stu520.

A. Burrows, M. S. Marley, and C. M. Sharp. The Near-Infrared and Optical Spectra of Methane Dwarfs and Brown Dwarfs. *The Astrophysical Journal*, 531(1):438–446, Mar. 2000. doi: 10.1086/308462.

I. Carleo, P. Giacobbe, G. Guilluy, P. E. Cubillos, A. S. Bonomo, A. Sozzetti, M. Brogi, S. Gandhi, L. Fossati, D. Turrini, K. Biazzo, F. Borsa, A. F. Lanza, L. Malavolta, A. Maggio, L. Mancini, G. Micela, L. Pino, E. Poretti, M. Rainer, G. Scandariato, E. Schisano, G. Andreuzzi, A. Bignamini, R. Cosentino, A. Fiorenzano, A. Harutyunyan, E. Molinari, M. Pedani, S. Redfield, and H. Stoev. The GAPS programme at TNG XXXIX. multiple molecular species in the atmosphere of the warm giant planet WASP-80 b unveiled at high resolution with GIANO-b. *The Astronomical Journal*, 164(3):101, aug 2022. doi: 10.3847/1538-3881/ac80bf. URL `https://doi.org/10.3847/1538-3881/ac80bf`.

A. L. Carter, E. M. May, N. Espinoza, L. Welbanks, E. Ahrer, L. Alderson, R. Brahm, A. D. Feinstein, D. Grant, M. Line, G. Morello, R. O'Steen, M. Radica, Z. Rustamkulov, K. B. Stevenson, J. D. Turner, M. K. Alam, D. R. Anderson, N. M. Batalha, M. P. Battley, D. Bayliss, J. L. Bean, B. Benneke, Z. K. Berta-Thompson, J. Brande, E. M. Bryant, M. R. Burleigh, L. Coulombe, I. J. M. Crossfield, M. Damiano, J. M. Désert, L. Flagg, S. Gill, J. Inglis, J. Kirk, H. Knutson, L. Kreidberg, M. López Morales, M. Mansfield, S. E. Moran, C. A. Murray, M. C. Nixon, D. J. M. Petit dit de la Roche, B. V. Rackham, E. Schlawin, D. K. Sing, H. R. Wakeford, N. L. Wallack, P. J. Wheatley, S. Zieba, K. Aggarwal, J. K. Barstow, T. J. Bell, J. Blecic, C. Caceres, N. Crouzet, P. E. Cubillos, T. Daylan, M. de Val-Borro, L. Decin, J. J. Fortney, N. P. Gibson, K. Heng, R. Hu, E. M. R. Kempton, P. Lagage, J. D. Lothringer, J. Lustig-Yaeger, L. Mancini, N. J. Mayne, L. C. Mayorga, K. Molaverdikhani, E. Nasedkin, K. Ohno, V. Parmentier, D. Powell, S. Redfield, P. Roy,

J. Taylor, and X. Zhang. A benchmark JWST near-infrared spectrum for the exoplanet WASP-39 b. *Nature Astronomy*, 8:1008–1019, Aug. 2024. doi: 10.1038/s41550-024-02292-x.

N. Casasayas-Barris, E. Palle, G. Nowak, F. Yan, L. Nortmann, and F. Murgas. Detection of sodium in the atmosphere of WASP-69b. *Astronomy & Astrophysics*, 608:A135, Dec. 2017. doi: 10.1051/0004-6361/201731956.

F. Castelli and R. L. Kurucz. New Grids of ATLAS9 Model Atmospheres. In N. Piskunov, W. W. Weiss, and D. F. Gray, editors, *Modelling of Stellar Atmospheres*, volume 210, page A20, Jan. 2003. doi: 10.48550/arXiv.astro-ph/0405087.

Y. Chachan, H. A. Knutson, P. Gao, T. Kataria, I. Wong, G. W. Henry, B. Benneke, M. Zhang, J. Barstow, J. L. Bean, T. Mikal-Evans, N. K. Lewis, M. Mansfield, M. López-Morales, N. Nikolov, D. K. Sing, and H. Wakeford. A Hubble PanCET Study of HAT-P-11b: A Cloudy Neptune with a Low Atmospheric Metallicity. *The Astronomical Journal*, 158(6):244, Dec. 2019. doi: 10.3847/1538-3881/ab4e9a.

D. Charbonneau, T. M. Brown, D. W. Latham, and M. Mayor. Detection of Planetary Transits Across a Sun-like Star. *Astrophysical Journal Letters*, 529(1):L45–L48, Jan. 2000. doi: 10.1086/312457.

D. Charbonneau, T. M. Brown, R. W. Noyes, and R. L. Gilliland. Detection of an Extrasolar Planet Atmosphere. *Astrophysical Journal*, 568(1):377–384, Mar. 2002. doi: 10.1086/338770.

D. Charbonneau, L. E. Allen, S. T. Megeath, G. Torres, R. Alonso, T. M. Brown, R. L. Gilliland, D. W. Latham, G. Mandushev, F. T. O'Donovan, and A. Sozzetti. Detection of Thermal Emission from an Extrasolar Planet. *Astrophysical Journal*, 626(1):523–529, June 2005. doi: 10.1086/429991.

L. Chatziastros, B. Bitsch, and A. D. Schneider. Constraining the formation history of the HAT-P-11 system by atmospheric abundances. *arXiv e-prints*, art. arXiv:2310.12797, Oct. 2023. doi: 10.48550/arXiv.2310.12797.

G. Chen, N. Casasayas-Barris, E. Pallé, L. Welbanks, N. Madhusudhan, R. Luque, and F. Murgas. Detection of Na in WASP-21b's lower and upper atmosphere. *Astronomy & Astrophysics*, 642: A54, Oct. 2020a. doi: 10.1051/0004-6361/202038661.

G. Chen, N. Casasayas-Barris, E. Pallé, F. Yan, M. Stangret, H. M. Cegla, R. Allart, and C. Lovis. Detection of Na, K, and Hα absorption in the atmosphere of WASP-52b using ESPRESSO. *Astronomy & Astrophysics*, 635:A171, Mar. 2020b. doi: 10.1051/0004-6361/201936986.

K. L. Chubb, J. Tennyson, and S. N. Yurchenko. ExoMol molecular line lists – XXXVII. Spectra of acetylene. *Monthly Notices of the Royal Astronomical Society*, 493(2):1531–1545, 01 2020. ISSN 0035-8711. doi: 10.1093/mnras/staa229. URL `https://doi.org/10.1093/mnras/staa229`.

R. Claudi, S. Benatti, I. Carleo, A. Ghedina, J. Guerra, G. Micela, E. Molinari, E. Oliva, M. Rainer, A. Tozzi, C. Baffa, A. Baruffolo, N. Buchschacher, M. Cecconi, R. Cosentino, D. Fantinel, L. Fini, F. Ghinassi, E. Giani, E. Gonzalez, M. Gonzalez, R. Gratton, A. Harutyunyan, N. Hernandez, M. Lodi, L. Malavolta, J. Maldonado, L. Origlia, N. Sanna, J. Sanjuan, S. Scuderi, U. Seemann, A. Sozzetti, H. Perez Ventura, M. Hernandez Diaz, A. Galli, C. Gonzalez, L. Riverol, and C. Riverol.

GIARPS@TNG: GIANO-B and HARPS-N together for a wider wavelength range spectroscopy. *European Physical Journal Plus*, 132(8):364, Aug. 2017. doi: 10.1140/epjp/i2017-11647-9.

P. A. Coles, S. N. Yurchenko, and J. Tennyson. ExoMol molecular line lists – XXXV. A rotation-vibration line list for hot ammonia. *Monthly Notices of the Royal Astronomical Society*, 490(4): 4638–4647, 11 2019. ISSN 0035-8711. doi: 10.1093/mnras/stz2778. URL `https://doi.org/10.1093/mnras/stz2778`.

D. Cont, F. Yan, A. Reiners, L. Nortmann, K. Molaverdikhani, E. Pallé, T. Henning, I. Ribas, A. Quirrenbach, J. A. Caballero, P. J. Amado, S. Czesla, F. Lesjak, M. López-Puertas, P. Mollière, D. Montes, G. Morello, E. Nagel, S. Pedraz, and A. Sánchez-López. Atmospheric characterization of the ultra-hot Jupiter WASP-33b. Detection of Ti and V emission lines and retrieval of a broadened line profile. *Astronomy & Astrophysics*, 668:A53, Dec. 2022. doi: 10.1051/0004-6361/202244277.

C. S. Cooper and A. P. Showman. Dynamics and disequilibrium carbon chemistry in hot jupiter atmospheres, with application to hd 209458b. *The Astrophysical Journal*, 649(2):1048, oct 2006. doi: 10.1086/506312. URL `https://dx.doi.org/10.1086/506312`.

R. Cosentino, C. Lovis, F. Pepe, A. Collier Cameron, D. W. Latham, E. Molinari, S. Udry, N. Bezawada, M. Black, A. Born, N. Buchschacher, D. Charbonneau, P. Figueira, M. Fleury, A. Galli, A. Gallie, X. Gao, A. Ghedina, C. Gonzalez, M. Gonzalez, J. Guerra, D. Henry, K. Horne, I. Hughes, D. Kelly, M. Lodi, D. Lunney, C. Maire, M. Mayor, G. Micela, M. P. Ordway, J. Peacock, D. Phillips, G. Piotto, D. Pollacco, D. Queloz, K. Rice, C. Riverol, L. Riverol, J. San Juan, D. Sasselov, D. Segransan, A. Sozzetti, D. Sosnowska, B. Stobie, A. Szentgyorgyi, A. Vick, and L. Weber. Harps-N: the new planet hunter at TNG. In I. S. McLean, S. K. Ramsay, and H. Takami, editors, *Ground-based and Airborne Instrumentation for Astronomy IV*, volume 8446 of *Society of Photo-Optical Instrumentation Engineers (SPIE) Conference Series*, page 84461V, Sept. 2012. doi: 10.1117/12.925738.

B. Courcol, F. Bouchy, and M. Deleuil. An upper boundary in the mass-metallicity plane of exo-Neptunes. *Monthly Notices of the Royal Astronomical Society*, 461(2):1841–1849, Sept. 2016. doi: 10.1093/mnras/stw1049.

N. B. Cowan and E. Agol. The Statistics of Albedo and Heat Recirculation on Hot Exoplanets. *The Astrophysical Journal*, 729(1):54, Mar. 2011. doi: 10.1088/0004-637X/729/1/54.

I. J. M. Crossfield. Observations of Exoplanet Atmospheres. *Publications of the Astronomical Society of the Pacific*, 127(956):941, Oct. 2015. doi: 10.1086/683115.

P. E. Cubillos. An Algorithm to Compress Line-transition Data for Radiative-transfer Calculations. *The Astrophysical Journal*, 850(1):32, Nov. 2017. doi: 10.3847/1538-4357/aa9228.

P. E. Cubillos and J. Blecic. The PYRAT BAY framework for exoplanet atmospheric modelling: a population study of Hubble/WFC3 transmission spectra. *Monthly Notices of the Royal Astronomical Society*, 505(2):2675–2702, Aug. 2021. doi: 10.1093/mnras/stab1405.

P. E. Cubillos, J. Harrington, J. Blecic, M. D. Himes, P. M. Rojo, T. J. Loredo, N. B. Lust, R. C. Challener, A. J. Foster, M. M. Stemm, A. S. D. Foster, and S. D. Blumenthal. An Open-source

Bayesian Atmospheric Radiative Transfer (BART) Code. II. The TRANSIT Radiative Transfer Module and Retrieval of HAT-P-11b. *The Planetary Science Journal*, 3(4):81, Apr. 2022. doi: 10.3847/PSJ/ac348b.

R. M. Cutri, M. F. Skrutskie, S. van Dyk, C. A. Beichman, J. M. Carpenter, T. Chester, L. Cambresy, T. Evans, J. Fowler, J. Gizis, E. Howard, J. Huchra, T. Jarrett, E. L. Kopan, J. D. Kirkpatrick, R. M. Light, K. A. Marsh, H. McCallon, S. Schneider, R. Stiening, M. Sykes, M. Weinberg, W. A. Wheaton, S. Wheelock, and N. Zacarias. VizieR Online Data Catalog: 2MASS All-Sky Catalog of Point Sources (Cutri+ 2003). *VizieR Online Data Catalog*, art. II/246, June 2003.

R. M. Cutri, E. L. Wright, T. Conrow, J. W. Fowler, P. R. M. Eisenhardt, C. Grillmair, J. D. Kirkpatrick, F. Masci, H. L. McCallon, S. L. Wheelock, S. Fajardo-Acosta, L. Yan, D. Benford, M. Harbut, T. Jarrett, S. Lake, D. Leisawitz, M. E. Ressler, S. A. Stanford, C. W. Tsai, F. Liu, G. Helou, A. Mainzer, D. Gettngs, A. Gonzalez, D. Hoffman, K. A. Marsh, D. Padgett, M. F. Skrutskie, R. Beck, M. Papin, and M. Wittman. VizieR Online Data Catalog: AllWISE Data Release (Cutri+ 2013). VizieR On-line Data Catalog: II/328. Originally published in: IPAC/Caltech (2013), Feb. 2013.

R. da Silva, C. Danielski, E. Delgado Mena, L. Magrini, D. Turrini, K. Biazzo, M. Tsantaki, M. Rainer, K. G. Helminiak, S. Benatti, V. Adibekyan, N. Sanna, S. Sousa, G. Casali, and M. Van der Swaelmen. Ariel stellar characterisation. II. Chemical abundances of carbon, nitrogen, and oxygen for 181 planet-host FGK dwarf stars. *Astronomy & Astrophysics*, 688:A193, Aug. 2024. doi: 10.1051/0004-6361/202450604.

R. I. Dawson and J. A. Johnson. Origins of Hot Jupiters. *Annual Review of Astronomy and Astrophysics*, 56:175–221, Sept. 2018. doi: 10.1146/annurev-astro-081817-051853.

de Kok, Brogi, M., Snellen, I.A.G., Birkby, J., Albrecht, S., and de Mooij, E.J.W. Detection of carbon monoxide in the high-resolution day-side spectrum of the exoplanet hd 189733b. *Astronomy & Astrophysics*, 554:A82, 2013. doi: 10.1051/0004-6361/201321381. URL `https://doi.org/10.1051/0004-6361/201321381`.

D. Deming, S. Seager, L. J. Richardson, and J. Harrington. Infrared radiation from an extrasolar planet. *Nature*, 434(7034):740–743, Mar. 2005. doi: 10.1038/nature03507.

B.-O. Demory, M. Gillon, J. de Wit, N. Madhusudhan, E. Bolmont, K. Heng, T. Kataria, N. Lewis, R. Hu, J. Krick, V. Stamenković, B. Benneke, S. Kane, and D. Queloz. A map of the large day-night temperature gradient of a super-Earth exoplanet. *Nature*, 532(7598):207–209, Apr. 2016. doi: 10.1038/nature17169.

J. Eastman. EXOFASTv2: Generalized publication-quality exoplanet modeling code. Astrophysics Source Code Library, record ascl:1710.003, Oct. 2017.

J. Eastman, B. S. Gaudi, and E. Agol. Exofast: A fast exoplanetary fitting suite in idl. *Publications of the Astronomical Society of the Pacific*, 125(923):83, jan 2013. doi: 10.1086/669497. URL `https://dx.doi.org/10.1086/669497`.

J. D. Eastman, J. E. Rodriguez, E. Agol, K. G. Stassun, T. G. Beatty, A. Vanderburg, B. S. Gaudi, K. A. Collins, and R. Luger. EXOFASTv2: A public, generalized, publication-quality exoplanet modeling code. *arXiv e-prints*, art. arXiv:1907.09480, July 2019.

D. Ehrenreich and J. M. Désert. Mass-loss rates for transiting exoplanets. *Astronomy & Astrophysics*, 529:A136, May 2011. doi: 10.1051/0004-6361/201016356.

D. Ehrenreich, C. Lovis, R. Allart, M. R. Zapatero Osorio, F. Pepe, S. Cristiani, R. Rebolo, N. C. Santos, F. Borsa, O. Demangeon, X. Dumusque, J. I. González Hernández, N. Casasayas-Barris, D. Ségransan, S. Sousa, M. Abreu, V. Adibekyan, M. Affolter, C. Allende Prieto, Y. Alibert, M. Aliverti, D. Alves, M. Amate, G. Avila, V. Baldini, T. Bandy, W. Benz, A. Bianco, É. Bolmont, F. Bouchy, V. Bourrier, C. Broeg, A. Cabral, G. Calderone, E. Pallé, H. M. Cegla, R. Cirami, J. M. P. Coelho, P. Conconi, I. Coretti, C. Cumani, G. Cupani, H. Dekker, B. Delabre, S. Deiries, V. D'Odorico, P. Di Marcantonio, P. Figueira, A. Fragoso, L. Genolet, M. Genoni, R. Génova Santos, N. Hara, I. Hughes, O. Iwert, F. Kerber, J. Knudstrup, M. Landoni, B. Lavie, J.-L. Lizon, M. Lendl, G. Lo Curto, C. Maire, A. Manescau, C. J. A. P. Martins, D. Mégevand, A. Mehner, G. Micela, A. Modigliani, P. Molaro, M. Monteiro, M. Monteiro, M. Moschetti, E. Müller, N. Nunes, L. Oggioni, A. Oliveira, G. Pariani, L. Pasquini, E. Poretti, J. L. Rasilla, E. Redaelli, M. Riva, S. Santana Tschudi, P. Santin, P. Santos, A. Segovia Milla, J. V. Seidel, D. Sosnowska, A. Sozzetti, P. Spanò, A. Suárez Mascareño, H. Tabernero, F. Tenegi, S. Udry, A. Zanutta, and F. Zerbi. Nightside condensation of iron in an ultrahot giant exoplanet. *Nature*, 580(7805):597–601, Apr. 2020. doi: 10.1038/s41586-020-2107-1.

C. Eistrup and T. Henning. Chemical evolution in ices on drifting, planet-forming pebbles. *Astronomy & Astrophysics*, 667:A160, Nov. 2022. doi: 10.1051/0004-6361/202243982.

C. Eistrup, C. Walsh, and E. F. van Dishoeck. Setting the volatile composition of (exo)planet-building material. Does chemical evolution in disk midplanes matter? *Astronomy & Astrophysics*, 595:A83, Nov. 2016. doi: 10.1051/0004-6361/201628509.

C. Eistrup, L. I. Cleeves, and S. Krijt. Chemical evolution in planet-forming regions with growing grains. *Astronomy & Astrophysics*, 667:A121, Nov. 2022. doi: 10.1051/0004-6361/202243981.

N. V. Erkaev, Y. N. Kulikov, H. Lammer, F. Selsis, D. Langmayr, G. F. Jaritz, and H. K. Biernat. Roche lobe effects on the atmospheric loss from "Hot Jupiters". *Astronomy & Astrophysics*, 472 (1):329–334, Sept. 2007. doi: 10.1051/0004-6361:20066929.

E. Esparza-Borges, M. López-Morales, J. I. Adams Redai, E. Pallé, J. Kirk, N. Casasayas-Barris, N. E. Batalha, B. V. Rackham, J. L. Bean, S. L. Casewell, L. Decin, L. A. Dos Santos, A. García Muñoz, J. Harrington, K. Heng, R. Hu, L. Mancini, K. Molaverdikhani, G. Morello, N. K. Nikolov, M. C. Nixon, S. Redfield, K. B. Stevenson, H. R. Wakeford, M. K. Alam, B. Benneke, J. Blecic, N. Crouzet, T. Daylan, J. Inglis, L. Kreidberg, D. J. M. Petit dit de la Roche, and J. D. Turner. Detection of Carbon Monoxide in the Atmosphere of WASP-39b Applying Standard Cross-correlation Techniques to JWST NIRSpec G395H Data. *Astrophysical Journal Letters*, 955 (1):L19, Sept. 2023. doi: 10.3847/2041-8213/acf27b.

N. Espinoza, M. E. Steinrueck, J. Kirk, R. J. MacDonald, A. B. Savel, K. Arnold, E. M. R. Kempton, M. M. Murphy, L. Carone, M. Zamyatina, D. A. Lewis, D. Samra, S. Kiefer, E. Rauscher, D. Christie, N. Mayne, C. Helling, Z. Rustamkulov, V. Parmentier, E. M. May, A. L. Carter, X. Zhang, M. López-Morales, N. Allen, J. Blecic, L. Decin, L. Mancini, K. Molaverdikhani, B. V. Rackham, E. Palle, S.-M. Tsai, E.-M. Ahrer, J. L. Bean, I. J. M. Crossfield, D. Haegele, E. Hébrard, L. Kreidberg, D. Powell, A. D. Schneider, L. Welbanks, P. Wheatley, R. Brahm, and N. Crouzet. Inhomogeneous terminators on the exoplanet WASP-39 b. *Nature*, 632(8027):1017–1020, Aug. 2024. doi: 10.1038/s41586-024-07768-4.

T. M. Evans, D. K. Sing, H. R. Wakeford, N. Nikolov, G. E. Ballester, B. Drummond, T. Kataria, N. P. Gibson, D. S. Amundsen, and J. Spake. Detection of H_2O and Evidence for TiO/VO in an Ultra-hot Exoplanet Atmosphere. *Astrophysical Journal Letters*, 822(1):L4, May 2016. doi: 10.3847/2041-8205/822/1/L4.

T. M. Evans, D. K. Sing, J. M. Goyal, N. Nikolov, M. S. Marley, K. Zahnle, G. W. Henry, J. K. Barstow, M. K. Alam, J. Sanz-Forcada, T. Kataria, N. K. Lewis, P. Lavvas, G. E. Ballester, L. Ben-Jaffel, S. D. Blumenthal, V. Bourrier, B. Drummond, A. García Muñoz, M. López-Morales, P. Tremblin, D. Ehrenreich, H. R. Wakeford, L. A. Buchhave, A. Lecavelier des Etangs, É. Hébrard, and M. H. Williamson. An Optical Transmission Spectrum for the Ultra-hot Jupiter WASP-121b Measured with the Hubble Space Telescope. *Astronomical Journal*, 156(6):283, Dec. 2018. doi: 10.3847/1538-3881/aaebff.

D. Fabrycky and S. Tremaine. Shrinking Binary and Planetary Orbits by Kozai Cycles with Tidal Friction. *Astrophysical Journal*, 669(2):1298–1315, Nov. 2007. doi: 10.1086/521702.

R. Follert, R. J. Dorn, E. Oliva, J. L. Lizon, A. Hatzes, N. Piskunov, A. Reiners, U. Seemann, E. Stempels, U. Heiter, T. Marquart, M. Lockhart, G. Anglada-Escude, T. Löwinger, D. Baade, J. Grunhut, P. Bristow, B. Klein, Y. Jung, D. J. Ives, F. Kerber, E. Pozna, J. Paufique, H. U. Kaeufl, L. Origlia, E. Valenti, D. Gojak, M. Hilker, L. Pasquini, A. Smette, and J. Smoker. CRIRES+: a cross-dispersed high-resolution infrared spectrograph for the ESO VLT. In S. K. Ramsay, I. S. McLean, and H. Takami, editors, *Ground-based and Airborne Instrumentation for Astronomy V*, volume 9147 of *Society of Photo-Optical Instrumentation Engineers (SPIE) Conference Series*, page 914719, July 2014. doi: 10.1117/12.2054197.

S. Fonte, D. Turrini, E. Pacetti, E. Schisano, S. Molinari, D. Polychroni, R. Politi, and Q. Changeat. Oxygen depletion in giant planets with different formation histories. *Monthly Notices of the Royal Astronomical Society*, 520(3):4683–4695, Apr. 2023. doi: 10.1093/mnras/stad245.

E. B. Ford. Improving the Efficiency of Markov Chain Monte Carlo for Analyzing the Orbits of Extrasolar Planets. *Astrophysical Journal*, 642(1):505–522, May 2006. doi: 10.1086/500802.

D. Foreman-Mackey, D. W. Hogg, D. Lang, and J. Goodman. emcee: The MCMC Hammer. *Publications of the Astronomical Society of the Pacific*, 125(925):306, Mar. 2013. doi: 10.1086/670067.

J. Fraine, D. Deming, B. Benneke, H. Knutson, A. Jordán, N. Espinoza, N. Madhusudhan, A. Wilkins, and K. Todorov. Water vapour absorption in the clear atmosphere of a Neptune-sized exoplanet. *Nature*, 513(7519):526–529, Sept. 2014. doi: 10.1038/nature13785.

B. J. Fulton, K. A. Collins, B. S. Gaudi, K. G. Stassun, J. Pepper, T. G. Beatty, R. J. Siverd, K. Penev, A. W. Howard, C. Baranec, G. Corfini, J. D. Eastman, J. Gregorio, N. M. Law, M. B. Lund, T. E. Oberst, M. T. Penny, R. Riddle, J. E. Rodriguez, D. J. Stevens, R. Zambelli, C. Ziegler, A. Bieryla, G. D'Ago, D. L. DePoy, E. L. N. Jensen, J. F. Kielkopf, D. W. Latham, M. Manner, J. Marshall, K. K. McLeod, and P. A. Reed. KELT-8b: A Highly Inflated Transiting Hot Jupiter and a New Technique for Extracting High-precision Radial Velocities from Noisy Spectra. *Astrophysical Journal*, 810(1):30, Sept. 2015. doi: 10.1088/0004-637X/810/1/30.

B. J. Fulton, E. A. Petigura, A. W. Howard, H. Isaacson, G. W. Marcy, P. A. Cargile, L. Hebb, L. M. Weiss, J. A. Johnson, T. D. Morton, E. Sinukoff, I. J. M. Crossfield, and L. A. Hirsch. The California-Kepler Survey. III. A Gap in the Radius Distribution of Small Planets. *Astronomical Journal*, 154(3):109, Sept. 2017. doi: 10.3847/1538-3881/aa80eb.

Gaia Collaboration, A. G. A. Brown, A. Vallenari, T. Prusti, J. H. J. de Bruijne, C. Babusiaux, C. A. L. Bailer-Jones, M. Biermann, D. W. Evans, L. Eyer, F. Jansen, C. Jordi, S. A. Klioner, U. Lammers, L. Lindegren, X. Luri, F. Mignard, C. Panem, D. Pourbaix, S. Randich, P. Sartoretti, H. I. Siddiqui, C. Soubiran, F. van Leeuwen, N. A. Walton, F. Arenou, U. Bastian, M. Cropper, R. Drimmel, D. Katz, M. G. Lattanzi, J. Bakker, C. Cacciari, J. Castañeda, L. Chaoul, N. Cheek, F. De Angeli, C. Fabricius, R. Guerra, B. Holl, E. Masana, R. Messineo, N. Mowlavi, K. Nienartowicz, P. Panuzzo, J. Portell, M. Riello, G. M. Seabroke, P. Tanga, F. Thévenin, G. Gracia-Abril, G. Comoretto, M. Garcia-Reinaldos, D. Teyssier, M. Altmann, R. Andrae, M. Audard, I. Bellas-Velidis, K. Benson, J. Berthier, R. Blomme, P. Burgess, G. Busso, B. Carry, A. Cellino, G. Clementini, M. Clotet, O. Creevey, M. Davidson, J. De Ridder, L. Delchambre, A. Dell'Oro, C. Ducourant, J. Fernández-Hernández, M. Fouesneau, Y. Frémat, L. Galluccio, M. García-Torres, J. González-Núñez, J. J. González-Vidal, E. Gosset, L. P. Guy, J. L. Halbwachs, N. C. Hambly, D. L. Harrison, J. Hernández, D. Hestroffer, S. T. Hodgkin, A. Hutton, G. Jasniewicz, A. Jean-Antoine-Piccolo, S. Jordan, A. J. Korn, A. Krone-Martins, A. C. Lanzafame, T. Lebzelter, W. Löffler, M. Manteiga, P. M. Marrese, J. M. Martín-Fleitas, A. Moitinho, A. Mora, K. Muinonen, J. Osinde, E. Pancino, T. Pauwels, J. M. Petit, A. Recio-Blanco, P. J. Richards, L. Rimoldini, A. C. Robin, L. M. Sarro, C. Siopis, M. Smith, A. Sozzetti, M. Süveges, J. Torra, W. van Reeven, U. Abbas, A. Abreu Aramburu, S. Accart, C. Aerts, G. Altavilla, M. A. Álvarez, R. Alvarez, J. Alves, R. I. Anderson, A. H. Andrei, E. Anglada Varela, E. Antiche, T. Antoja, B. Arcay, T. L. Astraatmadja, N. Bach, S. G. Baker, L. Balaguer-Núñez, P. Balm, C. Barache, C. Barata, D. Barbato, F. Barblan, P. S. Barklem, D. Barrado, M. Barros, M. A. Barstow, S. Bartholomé Muñoz, J. L. Bassilana, U. Becciani, M. Bellazzini, A. Berihuete, S. Bertone, L. Bianchi, O. Bienaymé, S. Blanco-Cuaresma, T. Boch, C. Boeche, A. Bombrun, R. Borrachero, D. Bossini, S. Bouquillon, G. Bourda, A. Bragaglia, L. Bramante, M. A. Breddels, A. Bressan, N. Brouillet, T. Brüsemeister, E. Brugaletta, B. Bucciarelli, A. Burlacu, D. Busonero, A. G. Butkevich, R. Buzzi, E. Caffau, R. Cancelliere, G. Cannizzaro, T. Cantat-Gaudin, R. Carballo, T. Carlucci, J. M. Carrasco, L. Casamiquela, M. Castellani, A. Castro-Ginard, P. Charlot, L. Chemin, A. Chiavassa, G. Cocozza, G. Costigan, S. Cowell, F. Crifo, M. Crosta, C. Crowley, J. Cuypers, C. Dafonte, Y. Damerdji, A. Dapergolas, P. David, M. David, P. de Laverny, F. De Luise, R. De March, D. de Martino, R. de Souza, A. de Torres, J. Debosscher, E. del Pozo, M. Delbo, A. Delgado, H. E. Delgado, P. Di Matteo, S. Diakite, C. Diener, E. Distefano, C. Dolding, P. Drazinos, J. Durán, B. Edvardsson, H. Enke, K. Eriksson, P. Esquej, G. Eynard Bontemps,

C. Fabre, M. Fabrizio, S. Faigler, A. J. Falcão, M. Farràs Casas, L. Federici, G. Fedorets, P. Fernique, F. Figueras, F. Filippi, K. Findeisen, A. Fonti, E. Fraile, M. Fraser, B. Frézouls, M. Gai, S. Galleti, D. Garabato, F. García-Sedano, A. Garofalo, N. Garralda, A. Gavel, P. Gavras, J. Gerssen, R. Geyer, P. Giacobbe, G. Gilmore, S. Girona, G. Giuffrida, F. Glass, M. Gomes, M. Granvik, A. Gueguen, A. Guerrier, J. Guiraud, R. Gutiérrez-Sánchez, R. Haigron, D. Hatzidimitriou, M. Hauser, M. Haywood, U. Heiter, A. Helmi, J. Heu, T. Hilger, D. Hobbs, W. Hofmann, G. Holland, H. E. Huckle, A. Hypki, V. Icardi, K. Janßen, G. Jevardat de Fombelle, P. G. Jonker, Á. L. Juhász, F. Julbe, A. Karampelas, A. Kewley, J. Klar, A. Kochoska, R. Kohley, K. Kolenberg, M. Kontizas, E. Kontizas, S. E. Koposov, G. Kordopatis, Z. Kostrzewa-Rutkowska, P. Koubsky, S. Lambert, A. F. Lanza, Y. Lasne, J. B. Lavigne, Y. Le Fustec, C. Le Poncin-Lafitte, Y. Lebreton, S. Leccia, N. Leclerc, I. Lecoeur-Taibi, H. Lenhardt, F. Leroux, S. Liao, E. Licata, H. E. P. Lindstrøm, T. A. Lister, E. Livanou, A. Lobel, M. López, S. Managau, R. G. Mann, G. Mantelet, O. Marchal, J. M. Marchant, M. Marconi, S. Marinoni, G. Marschalkó, D. J. Marshall, M. Martino, G. Marton, N. Mary, D. Massari, G. Matijevič, T. Mazeh, P. J. McMillan, S. Messina, D. Michalik, N. R. Millar, D. Molina, R. Molinaro, L. Molnár, P. Montegriffo, R. Mor, R. Morbidelli, T. Morel, D. Morris, A. F. Mulone, T. Muraveva, I. Musella, G. Nelemans, L. Nicastro, L. Noval, W. O'Mullane, C. Ordénovic, D. Ordóñez-Blanco, P. Osborne, C. Pagani, I. Pagano, F. Pailler, H. Palacin, L. Palaversa, A. Panahi, M. Pawlak, A. M. Piersimoni, F. X. Pineau, E. Plachy, G. Plum, E. Poggio, E. Poujoulet, A. Prša, L. Pulone, E. Racero, S. Ragaini, N. Rambaux, M. Ramos-Lerate, S. Regibo, C. Reylé, F. Riclet, V. Ripepi, A. Riva, A. Rivard, G. Rixon, T. Roegiers, M. Roelens, M. Romero-Gómez, N. Rowell, F. Royer, L. Ruiz-Dern, G. Sadowski, T. Sagristà Sellés, J. Sahlmann, J. Salgado, E. Salguero, N. Sanna, T. Santana-Ros, M. Sarasso, H. Savietto, M. Schultheis, E. Sciacca, M. Segol, J. C. Segovia, D. Ségransan, I. C. Shih, L. Siltala, A. F. Silva, R. L. Smart, K. W. Smith, E. Solano, F. Solitro, R. Sordo, S. Soria Nieto, J. Souchay, A. Spagna, F. Spoto, U. Stampa, I. A. Steele, H. Steidelmüller, C. A. Stephenson, H. Stoev, F. F. Suess, J. Surdej, L. Szabados, E. Szegedi-Elek, D. Tapiador, F. Taris, G. Tauran, M. B. Taylor, R. Teixeira, D. Terrett, P. Teyssandier, W. Thuillot, A. Titarenko, F. Torra Clotet, C. Turon, A. Ulla, E. Utrilla, S. Uzzi, M. Vaillant, G. Valentini, V. Valette, A. van Elteren, E. Van Hemelryck, M. van Leeuwen, M. Vaschetto, A. Vecchiato, J. Veljanoski, Y. Viala, D. Vicente, S. Vogt, C. von Essen, H. Voss, V. Votruba, S. Voutsinas, G. Walmsley, M. Weiler, O. Wertz, T. Wevers, Ł. Wyrzykowski, A. Yoldas, M. Žerjal, H. Ziaeepour, J. Zorec, S. Zschocke, S. Zucker, C. Zurbach, and T. Zwitter. Gaia Data Release 2. Summary of the contents and survey properties. *Astronomy & Astrophysics*, 616:A1, Aug. 2018. doi: 10.1051/0004-6361/201833051.

Gaia Collaboration, A. Vallenari, A. G. A. Brown, T. Prusti, J. H. J. de Bruijne, F. Arenou, C. Babusiaux, M. Biermann, O. L. Creevey, C. Ducourant, D. W. Evans, L. Eyer, R. Guerra, A. Hutton, C. Jordi, S. A. Klioner, U. L. Lammers, L. Lindegren, X. Luri, F. Mignard, C. Panem, D. Pourbaix, S. Randich, P. Sartoretti, C. Soubiran, P. Tanga, N. A. Walton, C. A. L. Bailer-Jones, U. Bastian, R. Drimmel, F. Jansen, D. Katz, M. G. Lattanzi, F. van Leeuwen, J. Bakker, C. Cacciari, J. Castañeda, F. De Angeli, C. Fabricius, M. Fouesneau, Y. Frémat, L. Galluccio, A. Guerrier, U. Heiter, E. Masana, R. Messineo, N. Mowlavi, C. Nicolas, K. Nienartowicz, F. Pailler, P. Panuzzo, F. Riclet, W. Roux, G. M. Seabroke, R. Sordo, F. Thévenin, G. Gracia-Abril, J. Portell, D. Teyssier, M. Altmann, R. Andrae, M. Audard, I. Bellas-Velidis, K. Benson, J. Berthier, R. Blomme, P. W. Burgess, D. Busonero, G. Busso, H. Cánovas, B. Carry, A. Cellino, N. Cheek, G. Clementini,

Y. Damerdji, M. Davidson, P. de Teodoro, M. Nuñez Campos, L. Delchambre, A. Dell'Oro, P. Esquej, J. Fernández-Hernández, E. Fraile, D. Garabato, P. García-Lario, E. Gosset, R. Haigron, J. L. Halbwachs, N. C. Hambly, D. L. Harrison, J. Hernández, D. Hestroffer, S. T. Hodgkin, B. Holl, K. Janßen, G. Jevardat de Fombelle, S. Jordan, A. Krone-Martins, A. C. Lanzafame, W. Löffler, O. Marchal, P. M. Marrese, A. Moitinho, K. Muinonen, P. Osborne, E. Pancino, T. Pauwels, A. Recio-Blanco, C. Reylé, M. Riello, L. Rimoldini, T. Roegiers, J. Rybizki, L. M. Sarro, C. Siopis, M. Smith, A. Sozzetti, E. Utrilla, M. van Leeuwen, U. Abbas, P. Ábrahám, A. Abreu Aramburu, C. Aerts, J. J. Aguado, M. Ajaj, F. Aldea-Montero, G. Altavilla, M. A. Álvarez, J. Alves, F. Anders, R. I. Anderson, E. Anglada Varela, T. Antoja, D. Baines, S. G. Baker, L. Balaguer-Núñez, E. Balbinot, Z. Balog, C. Barache, D. Barbato, M. Barros, M. A. Barstow, S. Bartolomé, J. L. Bassilana, N. Bauchet, U. Becciani, M. Bellazzini, A. Berihuete, M. Bernet, S. Bertone, L. Bianchi, A. Binnenfeld, S. Blanco-Cuaresma, A. Blazere, T. Boch, A. Bombrun, D. Bossini, S. Bouquillon, A. Bragaglia, L. Bramante, E. Breedt, A. Bressan, N. Brouillet, E. Brugaletta, B. Bucciarelli, A. Burlacu, A. G. Butkevich, R. Buzzi, E. Caffau, R. Cancelliere, T. Cantat-Gaudin, R. Carballo, T. Carlucci, M. I. Carnerero, J. M. Carrasco, L. Casamiquela, M. Castellani, A. Castro-Ginard, L. Chaoul, P. Charlot, L. Chemin, V. Chiaramida, A. Chiavassa, N. Chornay, G. Comoretto, G. Contursi, W. J. Cooper, T. Cornez, S. Cowell, F. Crifo, M. Cropper, M. Crosta, C. Crowley, C. Dafonte, A. Dapergolas, M. David, P. David, P. de Laverny, F. De Luise, R. De March, J. De Ridder, R. de Souza, A. de Torres, E. F. del Peloso, E. del Pozo, M. Delbo, A. Delgado, J. B. Delisle, C. Demouchy, T. E. Dharmawardena, P. Di Matteo, S. Diakite, C. Diener, E. Distefano, C. Dolding, B. Edvardsson, H. Enke, C. Fabre, M. Fabrizio, S. Faigler, G. Fedorets, P. Fernique, A. Fienga, F. Figueras, Y. Fournier, C. Fouron, F. Fragkoudi, M. Gai, A. Garcia-Gutierrez, M. Garcia-Reinaldos, M. García-Torres, A. Garofalo, A. Gavel, P. Gavras, E. Gerlach, R. Geyer, P. Giacobbe, G. Gilmore, S. Girona, G. Giuffrida, R. Gomel, A. Gomez, J. González-Núñez, I. González-Santamaría, J. J. González-Vidal, M. Granvik, P. Guillout, J. Guiraud, R. Gutiérrez-Sánchez, L. P. Guy, D. Hatzidimitriou, M. Hauser, M. Haywood, A. Helmer, A. Helmi, M. H. Sarmiento, S. L. Hidalgo, T. Hilger, N. Hładczuk, D. Hobbs, G. Holland, H. E. Huckle, K. Jardine, G. Jasniewicz, A. Jean-Antoine Piccolo, Ó. Jiménez-Arranz, A. Jorissen, J. Juaristi Campillo, F. Julbe, L. Karbevska, P. Kervella, S. Khanna, M. Kontizas, G. Kordopatis, A. J. Korn, Á. Kóspál, Z. Kostrzewa-Rutkowska, K. Kruszyńska, M. Kun, P. Laizeau, S. Lambert, A. F. Lanza, Y. Lasne, J. F. Le Campion, Y. Lebreton, T. Lebzelter, S. Leccia, N. Leclerc, I. Lecoeur-Taibi, S. Liao, E. L. Licata, H. E. P. Lindstrøm, T. A. Lister, E. Livanou, A. Lobel, A. Lorca, C. Loup, P. Madrero Pardo, A. Magdaleno Romeo, S. Managau, R. G. Mann, M. Manteiga, J. M. Marchant, M. Marconi, J. Marcos, M. M. S. Marcos Santos, D. Marín Pina, S. Marinoni, F. Marocco, D. J. Marshall, L. Martin Polo, J. M. Martín-Fleitas, G. Marton, N. Mary, A. Masip, D. Massari, A. Mastrobuono-Battisti, T. Mazeh, P. J. McMillan, S. Messina, D. Michalik, N. R. Millar, A. Mints, D. Molina, R. Molinaro, L. Molnár, G. Monari, M. Monguió, P. Montegriffo, A. Montero, R. Mor, A. Mora, R. Morbidelli, T. Morel, D. Morris, T. Muraveva, C. P. Murphy, I. Musella, Z. Nagy, L. Noval, F. Ocaña, A. Ogden, C. Ordenovic, J. O. Osinde, C. Pagani, I. Pagano, L. Palaversa, P. A. Palicio, L. Pallas-Quintela, A. Panahi, S. Payne-Wardenaar, X. Peñalosa Esteller, A. Penttilä, B. Pichon, A. M. Piersimoni, F. X. Pineau, E. Plachy, G. Plum, E. Poggio, A. Prša, L. Pulone, E. Racero, S. Ragaini, M. Rainer, C. M. Raiteri, N. Rambaux, P. Ramos, M. Ramos-Lerate, P. Re Fiorentin, S. Regibo, P. J. Richards, C. Rios Diaz, V. Ripepi, A. Riva, H. W. Rix,

G. Rixon, N. Robichon, A. C. Robin, C. Robin, M. Roelens, H. R. O. Rogues, L. Rohrbasser, M. Romero-Gómez, N. Rowell, F. Royer, D. Ruz Mieres, K. A. Rybicki, G. Sadowski, A. Sáez Núñez, A. Sagristà Sellés, J. Sahlmann, E. Salguero, N. Samaras, V. Sanchez Gimenez, N. Sanna, R. Santoveña, M. Sarasso, M. Schultheis, E. Sciacca, M. Segol, J. C. Segovia, D. Ségransan, D. Semeux, S. Shahaf, H. I. Siddiqui, A. Siebert, L. Siltala, A. Silvelo, E. Slezak, I. Slezak, R. L. Smart, O. N. Snaith, E. Solano, F. Solitro, D. Souami, J. Souchay, A. Spagna, L. Spina, F. Spoto, I. A. Steele, H. Steidelmüller, C. A. Stephenson, M. Süveges, J. Surdej, L. Szabados, E. Szegedi-Elek, F. Taris, M. B. Taylor, R. Teixeira, L. Tolomei, N. Tonello, F. Torra, J. Torra, G. Torralba Elipe, M. Trabucchi, A. T. Tsounis, C. Turon, A. Ulla, N. Unger, M. V. Vaillant, E. van Dillen, W. van Reeven, O. Vanel, A. Vecchiato, Y. Viala, D. Vicente, S. Voutsinas, M. Weiler, T. Wevers, Ł. Wyrzykowski, A. Yoldas, P. Yvard, H. Zhao, J. Zorec, S. Zucker, and T. Zwitter. Gaia Data Release 3. Summary of the content and survey properties. *Astronomy & Astrophysics*, 674:A1, June 2023. doi: 10.1051/0004-6361/202243940.

S. Gandhi, A. Kesseli, I. Snellen, M. Brogi, J. P. Wardenier, V. Parmentier, L. Welbanks, and A. B. Savel. Spatially resolving the terminator: variation of Fe, temperature, and winds in WASP-76 b across planetary limbs and orbital phase. *Monthly Notices of the Royal Astronomical Society*, 515 (1):749–766, Sept. 2022. doi: 10.1093/mnras/stac1744.

S. Gandhi, A. Kesseli, Y. Zhang, A. Louca, I. Snellen, M. Brogi, Y. Miguel, N. Casasayas-Barris, S. Pelletier, R. Landman, C. Maguire, and N. P. Gibson. Retrieval Survey of Metals in Six Ultrahot Jupiters: Trends in Chemistry, Rain-out, Ionization, and Atmospheric Dynamics. *Astronomical Journal*, 165(6):242, June 2023. doi: 10.3847/1538-3881/accd65.

P. Gao, H. R. Wakeford, S. E. Moran, and V. Parmentier. Aerosols in Exoplanet Atmospheres. *Journal of Geophysical Research (Planets)*, 126(4):e06655, Apr. 2021. doi: 10.1029/2020JE006655.

J. P. Gardner, J. C. Mather, M. Clampin, R. Doyon, M. A. Greenhouse, H. B. Hammel, J. B. Hutchings, P. Jakobsen, S. J. Lilly, K. S. Long, J. I. Lunine, M. J. McCaughrean, M. Mountain, J. Nella, G. H. Rieke, M. J. Rieke, H.-W. Rix, E. P. Smith, G. Sonneborn, M. Stiavelli, H. S. Stockman, R. A. Windhorst, and G. S. Wright. The James Webb Space Telescope. *Space Science Reviews*, 123(4):485–606, Apr. 2006. doi: 10.1007/s11214-006-8315-7.

A. Gelman and D. B. Rubin. Inference from Iterative Simulation Using Multiple Sequences. *Statistical Science*, 7:457–472, Jan. 1992. doi: 10.1214/ss/1177011136.

P. Giacobbe, M. Brogi, S. Gandhi, P. E. Cubillos, A. S. Bonomo, A. Sozzetti, L. Fossati, G. Guilluy, I. Carleo, M. Rainer, A. Harutyunyan, F. Borsa, L. Pino, V. Nascimbeni, S. Benatti, K. Biazzo, A. Bignamini, K. L. Chubb, R. Claudi, R. Cosentino, E. Covino, M. Damasso, S. Desidera, A. F. M. Fiorenzano, A. Ghedina, A. F. Lanza, G. Leto, A. Maggio, L. Malavolta, J. Maldonado, G. Micela, E. Molinari, I. Pagano, M. Pedani, G. Piotto, E. Poretti, G. Scandariato, S. N. Yurchenko, D. Fantinel, A. Galli, M. Lodi, N. Sanna, and A. Tozzi. Five carbon- and nitrogen-bearing species in a hot giant planet's atmosphere. *Nature*, 592(7853):205–208, Apr. 2021. doi: 10.1038/s41586-021-03381-x.

N. P. Gibson, S. Merritt, S. K. Nugroho, P. E. Cubillos, E. J. W. de Mooij, T. Mikal-Evans, L. Fossati, J. Lothringer, N. Nikolov, D. K. Sing, J. J. Spake, C. A. Watson, and J. Wilson. Detection of Fe

I in the atmosphere of the ultra-hot Jupiter WASP-121b, and a new likelihood-based approach for Doppler-resolved spectroscopy. *Monthly Notices of the Royal Astronomical Society*, 493(2): 2215–2228, Apr. 2020. doi: 10.1093/mnras/staa228.

S. K. Grunblatt, A. W. Howard, and R. D. Haywood. Determining the Mass of Kepler-78b with Nonparametric Gaussian Process Estimation. *The Astrophysical Journal*, 808(2):127, Aug. 2015. doi: 10.1088/0004-637X/808/2/127.

T. Guillot. On the radiative equilibrium of irradiated planetary atmospheres. *Astronomy & Astrophysics*, 520:A27, Sept. 2010. doi: 10.1051/0004-6361/200913396.

G. Guilluy, A. Sozzetti, M. Brogi, A. S. Bonomo, P. Giacobbe, R. Claudi, and S. Benatti. Exoplanet atmospheres with GIANO. II. Detection of molecular absorption in the dayside spectrum of HD 102195b. *Astronomy & Astrophysics*, 625:A107, May 2019. doi: 10.1051/0004-6361/201834615.

G. Guilluy, P. Giacobbe, I. Carleo, P. E. Cubillos, A. Sozzetti, A. S. Bonomo, M. Brogi, S. Gandhi, L. Fossati, V. Nascimbeni, D. Turrini, E. Schisano, F. Borsa, A. F. Lanza, L. Mancini, A. Maggio, L. Malavolta, G. Micela, L. Pino, M. Rainer, A. Bignamini, R. Claudi, R. Cosentino, E. Covino, S. Desidera, A. Fiorenzano, A. Harutyunyan, V. Lorenzi, C. Knapic, E. Molinari, E. Pacetti, I. Pagano, M. Pedani, G. Piotto, and E. Poretti. The GAPS Programme at TNG. XXXVIII. Five molecules in the atmosphere of the warm giant planet WASP-69b detected at high spectral resolution. *Astronomy & Astrophysics*, 665:A104, Sept. 2022. doi: 10.1051/0004-6361/202243854.

G. Guilluy, V. Bourrier, Y. Jaziri, W. Dethier, D. Mounzer, P. Giacobbe, O. Attia, R. Allart, A. S. Bonomo, L. A. Dos Santos, M. Rainer, and A. Sozzetti. DREAM. III. A helium survey in exoplanets on the edge of the hot Neptune desert with GIANO-B at TNG. *Astronomy & Astrophysics*, 676:A130, Aug. 2023. doi: 10.1051/0004-6361/202346419.

E. Han, S. X. Wang, J. T. Wright, Y. K. Feng, M. Zhao, O. Fakhouri, J. I. Brown, and C. Hancock. Exoplanet orbit database. ii. updates to exoplanets.org. *Publications of the Astronomical Society of the Pacific*, 126(943):827, sep 2014. doi: 10.1086/678447. URL `https://dx.doi.org/10.1086/678447`.

R. J. Hargreaves, I. E. Gordon, M. Rey, A. V. Nikitin, V. G. Tyuterev, R. V. Kochanov, and L. S. Rothman. An Accurate, Extensive, and Practical Line List of Methane for the HITEMP Database. *Astrophysical Journal Supplement*, 247(2):55, Apr. 2020. doi: 10.3847/1538-4365/ab7a1a.

G. J. Harris, J. Tennyson, B. M. Kaminsky, Y. V. Pavlenko, and H. R. A. Jones. Improved HCN/HNC linelist, model atmospheres and synthetic spectra for WZ Cas. *Monthly Notices of the Royal Astronomical Society*, 367(1):400–406, Mar. 2006. doi: 10.1111/j.1365-2966.2005.09960.x.

G. J. Harris, F. C. Larner, J. Tennyson, B. M. Kaminsky, Y. V. Pavlenko, and H. R. A. Jones. A $H^{13}CN/HN^{13}C$ linelist, model atmospheres and synthetic spectra for carbon stars. *Monthly Notices of the Royal Astronomical Society*, 390(1):143–148, Oct. 2008. doi: 10.1111/j.1365-2966.2008.13642.x.

G. A. Hawker, N. Madhusudhan, S. H. C. Cabot, and S. Gandhi. Evidence for multiple molecular species in the hot jupiter HD 209458b. *The Astrophysical Journal*, 863(1):L11, aug 2018. doi: 10.3847/2041-8213/aac49d. URL `https://doi.org/10.3847/2041-8213/aac49d`.

K. Haynes, A. M. Mandell, N. Madhusudhan, D. Deming, and H. Knutson. Spectroscopic Evidence for a Temperature Inversion in the Dayside Atmosphere of Hot Jupiter WASP-33b. *Astrophysical Journal*, 806(2):146, June 2015. doi: 10.1088/0004-637X/806/2/146.

R. D. Haywood. *Hide and Seek: Radial-Velocity Searches for Planets around Active Stars*. PhD thesis, Saint Andrews University, UK, Nov. 2015.

R. D. Haywood, A. Collier Cameron, D. Queloz, S. C. C. Barros, M. Deleuil, R. Fares, M. Gillon, A. F. Lanza, C. Lovis, C. Moutou, F. Pepe, D. Pollacco, A. Santerne, D. Ségransan, and Y. C. Unruh. Planets and stellar activity: hide and seek in the CoRoT-7 system. *Monthly Notices of the Royal Astronomical Society*, 443(3):2517–2531, Sept. 2014. doi: 10.1093/mnras/stu1320.

K. Heng and A. P. Showman. Atmospheric Dynamics of Hot Exoplanets. *Annual Review of Earth and Planetary Sciences*, 43:509–540, May 2015. doi: 10.1146/annurev-earth-060614-105146.

K. Heng, J. M. Mendonça, and J.-M. Lee. Analytical Models of Exoplanetary Atmospheres. II. Radiative Transfer via the Two-stream Approximation. *The Astrophysical Journal Supplement Series*, 215(1):4, Nov. 2014. doi: 10.1088/0067-0049/215/1/4.

G. W. Henry, G. W. Marcy, R. P. Butler, and S. S. Vogt. A Transiting "51 Peg-like" Planet. *Astrophysical Journal Letters*, 529(1):L41–L44, Jan. 2000. doi: 10.1086/312458.

N. R. Hinkel, F. X. Timmes, P. A. Young, M. D. Pagano, and M. C. Turnbull. Stellar Abundances in the Solar Neighborhood: The Hypatia Catalog. *Astronomical Journal*, 148(3):54, Sept. 2014. doi: 10.1088/0004-6256/148/3/54.

H. J. Hoeijmakers, D. Ehrenreich, K. Heng, D. Kitzmann, S. L. Grimm, R. Allart, R. Deitrick, A. Wyttenbach, M. Oreshenko, L. Pino, P. B. Rimmer, E. Molinari, and L. Di Fabrizio. Atomic iron and titanium in the atmosphere of the exoplanet KELT-9b. *Nature*, 560(7719):453–455, Aug. 2018. doi: 10.1038/s41586-018-0401-y.

H. J. Hoeijmakers, D. Ehrenreich, D. Kitzmann, R. Allart, S. L. Grimm, J. V. Seidel, A. Wyttenbach, L. Pino, L. D. Nielsen, C. Fisher, P. B. Rimmer, V. Bourrier, H. M. Cegla, B. Lavie, C. Lovis, A. B. C. Patzer, J. W. Stock, F. A. Pepe, and K. Heng. A spectral survey of an ultra-hot Jupiter. Detection of metals in the transmission spectrum of KELT-9 b. *Astronomy & Astrophysics*, 627: A165, July 2019. doi: 10.1051/0004-6361/201935089.

E. Høg, C. Fabricius, V. V. Makarov, S. Urban, T. Corbin, G. Wycoff, U. Bastian, P. Schwekendiek, and A. Wicenec. The Tycho-2 catalogue of the 2.5 million brightest stars. *Astronomy & Astrophysics*, 355:L27–L30, Mar. 2000.

J. R. Holton. *An introduction to dynamic meteorology*. Academic Press, 1992.

A. W. Howard, G. W. Marcy, J. A. Johnson, D. A. Fischer, J. T. Wright, H. Isaacson, J. A. Valenti, J. Anderson, D. N. C. Lin, and S. Ida. The Occurrence and Mass Distribution of Close-in Super-Earths, Neptunes, and Jupiters. *Science*, 330(6004):653, Oct. 2010. doi: 10.1126/science.1194854.

A. W. Howard, G. W. Marcy, S. T. Bryson, J. M. Jenkins, J. F. Rowe, N. M. Batalha, W. J. Borucki, D. G. Koch, E. W. Dunham, I. Gautier, Thomas N., J. Van Cleve, W. D. Cochran, D. W.

Latham, J. J. Lissauer, G. Torres, T. M. Brown, R. L. Gilliland, L. A. Buchhave, D. A. Caldwell, J. Christensen-Dalsgaard, D. Ciardi, F. Fressin, M. R. Haas, S. B. Howell, H. Kjeldsen, S. Seager, L. Rogers, D. D. Sasselov, J. H. Steffen, G. S. Basri, D. Charbonneau, J. Christiansen, B. Clarke, A. Dupree, D. C. Fabrycky, D. A. Fischer, E. B. Ford, J. J. Fortney, J. Tarter, F. R. Girouard, M. J. Holman, J. A. Johnson, T. C. Klaus, P. Machalek, A. V. Moorhead, R. C. Morehead, D. Ragozzine, P. Tenenbaum, J. D. Twicken, S. N. Quinn, H. Isaacson, A. Shporer, P. W. Lucas, L. M. Walkowicz, W. F. Welsh, A. Boss, E. Devore, A. Gould, J. C. Smith, R. L. Morris, A. Prsa, T. D. Morton, M. Still, S. E. Thompson, F. Mullally, M. Endl, and P. J. MacQueen. Planet Occurrence within 0.25 AU of Solar-type Stars from Kepler. *Astrophysical Journal Supplement*, 201(2):15, Aug. 2012. doi: 10.1088/0067-0049/201/2/15.

X. Huang, D. W. Schwenke, R. S. Freedman, and T. J. Lee. Ames-2016 line lists for 13 isotopologues of co2: Updates, consistency, and remaining issues. *Journal of Quantitative Spectroscopy and Radiative Transfer*, 203:224–241, 2017. ISSN 0022-4073. doi: https://doi.org/10.1016/j.jqsrt.2017.04.026. URL `https://www.sciencedirect.com/science/article/pii/S0022407317300547`. HITRAN2016 Special Issue.

K. F. Huber, S. Czesla, and J. H. M. M. Schmitt. Discovery of the secondary eclipse of HAT-P-11 b. *Astronomy & Astrophysics*, 597:A113, Jan. 2017. doi: 10.1051/0004-6361/201629699.

P. Hut. Tidal evolution in close binary systems. *Astronomy & Astrophysics*, 99:126–140, June 1981.

T. L. John. Continuous absorption by the negative hydrogen ion reconsidered. *Astronomy & Astrophysics*, 193(1-2):189–192, Mar. 1988.

D. Johns, P. A. Reed, J. E. Rodriguez, J. Pepper, K. G. Stassun, K. Penev, B. S. Gaudi, J. Labadie-Bartz, B. J. Fulton, S. N. Quinn, J. D. Eastman, D. R. Ciardi, L. Hirsch, D. J. Stevens, C. P. Stevens, T. E. Oberst, D. H. Cohen, E. L. N. Jensen, P. Benni, J. Villanueva, Steven, G. Murawski, A. Bieryla, D. W. Latham, S. Vanaverbeke, F. Dubois, S. Rau, L. Logie, R. F. Rauenzahn, R. A. Wittenmyer, R. Zambelli, D. Bayliss, T. G. Beatty, K. A. Collins, K. D. Colón, I. A. Curtis, P. Evans, J. Gregorio, D. James, D. L. Depoy, M. C. Johnson, M. D. Joner, D. H. Kasper, S. Khakpash, J. F. Kielkopf, R. B. Kuhn, M. B. Lund, M. Manner, J. L. Marshall, K. K. McLeod, M. T. Penny, H. Relles, R. J. Siverd, D. C. Stephens, C. Stockdale, T.-G. Tan, M. Trueblood, P. Trueblood, and X. Yao. KELT-23Ab: A Hot Jupiter Transiting a Near-solar Twin Close to the TESS and JWST Continuous Viewing Zones. *Astronomical Journal*, 158(2):78, Aug. 2019. doi: 10.3847/1538-3881/ab24c7.

J. A. Johnson, K. M. Aller, A. W. Howard, and J. R. Crepp. Giant Planet Occurrence in the Stellar Mass-Metallicity Plane. *Publications of the Astronomical Society of the Pacific*, 122(894):905, Aug. 2010. doi: 10.1086/655775.

U. G. Jørgensen, D. Hammer, A. Borysow, and J. Falkesgaard. The atmospheres of cool, helium-rich white dwarfs. *Astronomy & Astrophysics*, 361:283–292, Sept. 2000.

JWST Transiting Exoplanet Community Early Release Science Team, E.-M. Ahrer, L. Alderson, N. M. Batalha, N. E. Batalha, J. L. Bean, T. G. Beatty, T. J. Bell, B. Benneke, Z. K. Berta-Thompson, A. L. Carter, I. J. M. Crossfield, N. Espinoza, A. D. Feinstein, J. J. Fortney, N. P.

Gibson, J. M. Goyal, E. M. R. Kempton, J. Kirk, L. Kreidberg, M. López-Morales, M. R. Line, J. D. Lothringer, S. E. Moran, S. Mukherjee, K. Ohno, V. Parmentier, C. Piaulet, Z. Rustamkulov, E. Schlawin, D. K. Sing, K. B. Stevenson, H. R. Wakeford, N. H. Allen, S. M. Birkmann, J. Brande, N. Crouzet, P. E. Cubillos, M. Damiano, J.-M. Désert, P. Gao, J. Harrington, R. Hu, S. Kendrew, H. A. Knutson, P.-O. Lagage, J. Leconte, M. Lendl, R. J. MacDonald, E. M. May, Y. Miguel, K. Molaverdikhani, J. I. Moses, C. A. Murray, M. Nehring, N. K. Nikolov, D. J. M. Petit dit de la Roche, M. Radica, P.-A. Roy, K. G. Stassun, J. Taylor, W. C. Waalkes, P. Wachiraphan, L. Welbanks, P. J. Wheatley, K. Aggarwal, M. K. Alam, A. Banerjee, J. K. Barstow, J. Blecic, S. L. Casewell, Q. Changeat, K. L. Chubb, K. D. Colón, L.-P. Coulombe, T. Daylan, M. de Val-Borro, L. Decin, L. A. Dos Santos, L. Flagg, K. France, G. Fu, A. García Muñoz, J. E. Gizis, A. Glidden, D. Grant, K. Heng, T. Henning, Y.-C. Hong, J. Inglis, N. Iro, T. Kataria, T. D. Komacek, J. E. Krick, E. K. H. Lee, N. K. Lewis, J. Lillo-Box, J. Lustig-Yaeger, L. Mancini, A. M. Mandell, M. Mansfield, M. S. Marley, T. Mikal-Evans, G. Morello, M. C. Nixon, K. Ortiz Ceballos, A. A. A. Piette, D. Powell, B. V. Rackham, L. Ramos-Rosado, E. Rauscher, S. Redfield, L. K. Rogers, M. T. Roman, G. M. Roudier, N. Scarsdale, E. L. Shkolnik, J. Southworth, J. J. Spake, M. E. Steinrueck, X. Tan, J. K. Teske, P. Tremblin, S.-M. Tsai, G. S. Tucker, J. D. Turner, J. A. Valenti, O. Venot, I. P. Waldmann, N. L. Wallack, X. Zhang, and S. Zieba. Identification of carbon dioxide in an exoplanet atmosphere. *Nature*, 614(7949):649–652, Feb. 2023. doi: 10.1038/s41586-022-05269-w.

H.-U. Kaeufl, P. Ballester, P. Biereichel, B. Delabre, R. Donaldson, R. Dorn, E. Fedrigo, G. Finger, G. Fischer, F. Franza, D. Gojak, G. Huster, Y. Jung, J.-L. Lizon, L. Mehrgan, M. Meyer, A. Moorwood, J.-F. Pirard, J. Paufique, E. Pozna, R. Siebenmorgen, A. Silber, J. Stegmeier, and S. Wegerer. CRIRES: a high-resolution infrared spectrograph for ESO's VLT. In A. F. M. Moorwood and M. Iye, editors, *Ground-based Instrumentation for Astronomy*, volume 5492 of *Society of Photo-Optical Instrumentation Engineers (SPIE) Conference Series*, pages 1218–1227, Sept. 2004. doi: 10.1117/12.551480.

D. Kasper, J. L. Bean, M. R. Line, A. Seifahrt, J. Stürmer, L. Pino, J.-M. Désert, and M. Brogi. Confirmation of iron emission lines and nondetection of tio on the dayside of kelt-9b with maroon-x. *The Astrophysical Journal Letters*, 921(1):L18, nov 2021. doi: 10.3847/2041-8213/ac30e1. URL `https://dx.doi.org/10.3847/2041-8213/ac30e1`.

D. Kasper, J. L. Bean, M. R. Line, A. Seifahrt, M. T. Brady, J. Lothringer, L. Pino, G. Fu, S. Pelletier, J. Stürmer, B. Benneke, M. Brogi, and J.-M. Désert. Unifying high- and low-resolution observations to constrain the dayside atmosphere of kelt-20b/mascara-2b. *The Astronomical Journal*, 165(1):7, dec 2022. doi: 10.3847/1538-3881/ac9f40. URL `https://dx.doi.org/10.3847/1538-3881/ac9f40`.

E. Keles, S. Czesla, K. Poppenhaeger, P. Hauschildt, T. A. Carroll, I. Ilyin, M. Baratella, M. Steffen, K. G. Strassmeier, A. S. Bonomo, B. S. Gaudi, T. Henning, M. C. Johnson, K. Molaverdikhani, V. Nascimbeni, J. Patience, A. Reiners, G. Scandariato, E. Schlawin, E. Shkolnik, D. Sicilia, A. Sozzetti, M. Mallonn, C. Veillet, J. Wang, and F. Yan. The PEPSI Exoplanet Transit Survey (PETS) - V. New Na D transmission spectra indicate a quieter atmosphere on HD 189733b. *Monthly Notices of the Royal Astronomical Society*, 530(4):4826–4838, June 2024. doi: 10.1093/mnras/stae1097.

P. Kervella, F. Arenou, F. Mignard, and F. Thévenin. Stellar and substellar companions of nearby stars from Gaia DR2. Binarity from proper motion anomaly. *Astronomy & Astrophysics*, 623:A72, Mar. 2019. doi: 10.1051/0004-6361/201834371.

P. Kervella, F. Arenou, and F. Thévenin. Stellar and substellar companions from Gaia EDR3. Proper-motion anomaly and resolved common proper-motion pairs. *Astronomy & Astrophysics*, 657:A7, Jan. 2022. doi: 10.1051/0004-6361/202142146.

A. Y. Kesseli, I. A. G. Snellen, N. Casasayas-Barris, P. Mollière, and A. Sánchez-López. An atomic spectral survey of wasp-76b: Resolving chemical gradients and asymmetries. *The Astronomical Journal*, 163(3):107, feb 2022. doi: 10.3847/1538-3881/ac4336. URL `https://dx.doi.org/10.3847/1538-3881/ac4336`.

D. M. Kipping. Efficient, uninformative sampling of limb darkening coefficients for two-parameter laws. *Monthly Notices of the Royal Astronomical Society*, 435(3):2152–2160, Nov. 2013. doi: 10.1093/mnras/stt1435.

H. A. Knutson, D. Charbonneau, L. E. Allen, J. J. Fortney, E. Agol, N. B. Cowan, A. P. Showman, C. S. Cooper, and S. T. Megeath. A map of the day-night contrast of the extrasolar planet HD 189733b. *Nature*, 447(7141):183–186, May 2007. doi: 10.1038/nature05782.

H. A. Knutson, D. Charbonneau, L. E. Allen, A. Burrows, and S. T. Megeath. The 3.6-8.0 μm Broadband Emission Spectrum of HD 209458b: Evidence for an Atmospheric Temperature Inversion. *Astrophysical Journal*, 673(1):526–531, Jan. 2008. doi: 10.1086/523894.

H. A. Knutson, B. Benneke, D. Deming, and D. Homeier. A featureless transmission spectrum for the Neptune-mass exoplanet GJ436b. *Nature*, 505(7481):66–68, Jan. 2014a. doi: 10.1038/nature12887.

H. A. Knutson, B. J. Fulton, B. T. Montet, M. Kao, H. Ngo, A. W. Howard, J. R. Crepp, S. Hinkley, G. Á. Bakos, K. Batygin, J. A. Johnson, T. D. Morton, and P. S. Muirhead. Friends of Hot Jupiters. I. A Radial Velocity Search for Massive, Long-period Companions to Close-in Gas Giant Planets. *The Astrophysical Journal*, 785(2):126, Apr. 2014b. doi: 10.1088/0004-637X/785/2/126.

A. Kokori, A. Tsiaras, B. Edwards, A. Jones, G. Pantelidou, G. Tinetti, L. Bewersdorff, A. Iliadou, Y. Jongen, G. Lekkas, A. Nastasi, E. Poultourtzidis, C. Sidiropoulos, F. Walter, A. Wünsche, R. Abraham, V. K. Agnihotri, R. Albanesi, E. Arce-Mansego, D. Arnot, M. Audejean, C. Aumasson, M. Bachschmidt, G. Baj, P. R. Barroy, A. A. Belinski, D. Bennett, P. Benni, K. Bernacki, L. Betti, A. Biagini, P. Bosch, P. Brandebourg, L. Brát, M. Bretton, S. M. Brincat, S. Brouillard, A. Bruzas, A. Bruzzone, R. A. Buckland, M. Caló, F. Campos, A. Carreño, J. A. Carrion Rodrigo, R. Casali, G. Casalnuovo, M. Cataneo, C. M. Chang, L. Changeat, V. Chowdhury, R. Ciantini, M. Cilluffo, J. F. Coliac, G. Conzo, M. Correa, G. Coulon, N. Crouzet, M. V. Crow, I. A. Curtis, D. Daniel, B. Dauchet, S. Dawes, M. Deldem, D. Deligeorgopoulos, G. Dransfield, R. Dymock, T. Eenmäe, N. Esseiva, P. Evans, C. Falco, R. G. Farfán, E. Fernández-Lajús, S. Ferratfiat, S. L. Ferreira, A. Ferretti, J. Fiołka, M. Fowler, S. R. Futcher, D. Gabellini, T. Gainey, J. Gaitan, P. Gajdoš, A. García-Sánchez, J. Garlitz, C. Gillier, C. Gison, J. Gonzales, D. Gorshanov, F. Grau Horta, G. Grivas, P. Guerra, T. Guillot, C. A. Haswell, T. Haymes, V. P. Hentunen, K. Hills, K. Hose,

T. Humbert, F. Hurter, T. Hynek, M. Irzyk, J. Jacobsen, A. L. Jannetta, K. Johnson, P. Jóźwik-Wabik, A. E. Kaeouach, W. Kang, H. Kiiskinen, T. Kim, Ü. Kivila, B. Koch, U. Kolb, H. Kučáková, S. P. Lai, D. Laloum, S. Lasota, L. A. Lewis, G. I. Liakos, F. Libotte, F. Lomoz, C. Lopresti, R. Majewski, A. Malcher, M. Mallonn, M. Mannucci, A. Marchini, J. M. Mari, A. Marino, G. Marino, J. C. Mario, J. B. Marquette, F. A. Martínez-Bravo, M. Mašek, P. Matassa, P. Michel, J. Michelet, M. Miller, E. Miny, D. Molina, T. Mollier, B. Monteleone, N. Montigiani, M. Morales-Aimar, F. Mortari, M. Morvan, L. V. Mugnai, G. Murawski, L. Naponiello, J. L. Naudin, R. Naves, D. Néel, R. Neito, S. Neveu, A. Noschese, Y. Öğmen, O. Ohshima, Z. Orbanic, E. P. Pace, C. Pantacchini, N. I. Paschalis, C. Pereira, I. Peretto, V. Perroud, M. Phillips, P. Pintr, J. B. Pioppa, J. Plazas, A. J. Poelarends, A. Popowicz, J. Purcell, N. Quinn, M. Raetz, D. Rees, F. Regembal, M. Rocchetto, P. F. Rocci, M. Rockenbauer, R. Roth, L. Rousselot, X. Rubia, N. Ruocco, E. Russo, M. Salisbury, F. Salvaggio, A. Santos, J. Savage, F. Scaggiante, D. Sedita, S. Shadick, A. F. Silva, N. Sioulas, V. Školník, M. Smith, M. Smolka, A. Solmaz, N. Stanbury, D. Stouraitis, T. G. Tan, M. Theusner, G. Thurston, F. P. Tifner, A. Tomacelli, A. Tomatis, J. Trnka, M. Tylšar, P. Valeau, J. P. Vignes, A. Villa, A. Vives Sureda, K. Vora, M. Vrašt'ák, D. Walliang, B. Wenzel, D. E. Wright, R. Zambelli, M. Zhang, and M. Zíbar. ExoClock Project. III. 450 New Exoplanet Ephemerides from Ground and Space Observations. *Astrophysical Journal Supplement*, 265(1):4, Mar. 2023. doi: 10.3847/1538-4365/ac9da4.

D. D. B. Koll and T. D. Komacek. Atmospheric Circulations of Hot Jupiters as Planetary Heat Engines. *Astrophysical Journal*, 853(2):133, Feb. 2018. doi: 10.3847/1538-4357/aaa3de.

Y. Kozai. Secular perturbations of asteroids with high inclination and eccentricity. *Astronomical Journal*, 67:591–598, Nov. 1962. doi: 10.1086/108790.

L. Kreidberg, M. R. Line, V. Parmentier, K. B. Stevenson, T. Louden, M. Bonnefoy, J. K. Faherty, G. W. Henry, M. H. Williamson, K. Stassun, T. G. Beatty, J. L. Bean, J. J. Fortney, A. P. Showman, J.-M. Désert, and J. Arcangeli. Global Climate and Atmospheric Composition of the Ultra-hot Jupiter WASP-103b from HST and Spitzer Phase Curve Observations. *Astronomical Journal*, 156(1):17, July 2018. doi: 10.3847/1538-3881/aac3df.

L. Kreidberg, P. Mollière, I. J. M. Crossfield, D. P. Thorngren, Y. Kawashima, C. V. Morley, B. Benneke, T. Mikal-Evans, D. Berardo, M. Kosiarek, V. Gorjian, D. R. Ciardi, J. L. Christiansen, D. Dragomir, C. D. Dressing, J. J. Fortney, B. J. Fulton, T. P. Greene, K. K. Hardegree-Ullman, A. W. Howard, S. B. Howell, H. Isaacson, J. E. Krick, J. H. Livingston, J. D. Lothringer, F. Y. Morales, E. A. Petigura, J. E. Rodriguez, J. E. Schlieder, and L. M. Weiss. Tentative Evidence for Water Vapor in the Atmosphere of the Neptune-Size Exoplanet HD 106315 c. *arXiv e-prints*, art. arXiv:2006.07444, June 2020. doi: 10.48550/arXiv.2006.07444.

R. L. Kurucz. Atlas: a Computer Program for Calculating Model Stellar Atmospheres. *SAO Special Report*, 309, Feb. 1970.

P. Lavvas, T. Koskinen, and R. V. Yelle. Electron Densities and Alkali Atoms in Exoplanet Atmospheres. *Astrophysical Journal*, 796(1):15, Nov. 2014. doi: 10.1088/0004-637X/796/1/15.

A. Lecavelier Des Etangs. A diagram to determine the evaporation status of extrasolar planets. *Astronomy & Astrophysics*, 461(3):1185–1193, Jan. 2007. doi: 10.1051/0004-6361:20065014.

A. Lecavelier des Etangs, A. Vidal-Madjar, J. C. McConnell, and G. Hébrard. Atmospheric escape from hot Jupiters. *Astronomy & Astrophysics*, 418:L1–L4, Apr. 2004. doi: 10.1051/0004-6361:20040106.

A. Lecavelier Des Etangs, F. Pont, A. Vidal-Madjar, and D. Sing. Rayleigh scattering in the transit spectrum of HD 189733b. *Astronomy & Astrophysics*, 481(2):L83–L86, Apr. 2008. doi: 10.1051/0004-6361:200809388.

N. K. Lewis, A. P. Showman, J. J. Fortney, M. S. Marley, R. S. Freedman, and K. Lodders. Atmospheric Circulation of Eccentric Hot Neptune GJ436b. *The Astrophysical Journal*, 720(1): 344–356, Sept. 2010. doi: 10.1088/0004-637X/720/1/344.

G. Li, I. E. Gordon, L. S. Rothman, Y. Tan, S.-M. Hu, S. Kassi, A. Campargue, and E. S. Medvedev. Rovibrational Line Lists for Nine Isotopologues of the CO Molecule in the X $^1\Sigma^+$ Ground Electronic State. *The Astrophysical Journal Supplement Series*, 216(1):15, Jan. 2015. doi: 10.1088/0067-0049/216/1/15.

M.-C. Liang, C. D. Parkinson, A. Y. T. Lee, Y. L. Yung, and S. Seager. Source of Atomic Hydrogen in the Atmosphere of HD 209458b. *Astrophysical Journal Letters*, 596(2):L247–L250, Oct. 2003. doi: 10.1086/379314.

M. Line, M. Brogi, P. Smith, J. Sanchez, E. Rauscher, M. Mansfield, J. Bean, V. Parmentier, and G. Mace. The Roasting Marshmallows Campaign with IGRINS on Gemini South: Characterizing the Composition and Climate of Transiting Exoplanets. In *American Astronomical Society Meeting Abstracts*, volume 243 of *American Astronomical Society Meeting Abstracts*, page 178.17, Feb. 2024.

M. R. Line, X. Zhang, G. Vasisht, V. Natraj, P. Chen, and Y. L. Yung. Information Content of Exoplanetary Transit Spectra: An Initial Look. *Astrophysical Journal*, 749(1):93, Apr. 2012. doi: 10.1088/0004-637X/749/1/93.

M. R. Line, M. Brogi, J. L. Bean, S. Gandhi, J. Zalesky, V. Parmentier, P. Smith, G. N. Mace, M. Mansfield, E. M. R. Kempton, J. J. Fortney, E. Shkolnik, J. Patience, E. Rauscher, J.-M. Désert, and J. P. Wardenier. A solar C/O and sub-solar metallicity in a hot Jupiter atmosphere. *Nature*, 598(7882):580–584, Oct. 2021. doi: 10.1038/s41586-021-03912-6.

K. Lodders. Solar System Abundances of the Elements. *Astrophysics and Space Science Proceedings*, 16:379, Jan. 2010. doi: 10.1007/978-3-642-10352-0_8.

K. Lodders and B. Fegley. Atmospheric Chemistry in Giant Planets, Brown Dwarfs, and Low-Mass Dwarf Stars. I. Carbon, Nitrogen, and Oxygen. *Icarus*, 155(2):393–424, Feb. 2002. doi: 10.1006/icar.2001.6740.

J. D. Lothringer, T. Barman, and T. Koskinen. Extremely Irradiated Hot Jupiters: Non-oxide Inversions, H^- Opacity, and Thermal Dissociation of Molecules. *Astrophysical Journal*, 866(1):27, Oct. 2018. doi: 10.3847/1538-4357/aadd9e.

T. Louden and P. J. Wheatley. Spatially Resolved Eastward Winds and Rotation of HD 189733b. *The Astrophysical Journal Letters*, 814(2):L24, Dec. 2015. doi: 10.1088/2041-8205/814/2/L24.

C. Lovis, X. Dumusque, N. C. Santos, F. Bouchy, M. Mayor, F. Pepe, D. Queloz, D. Ségransan, and S. Udry. The HARPS search for southern extra-solar planets. XXXI. Magnetic activity cycles in solar-type stars: statistics and impact on precise radial velocities. *arXiv e-prints*, art. arXiv:1107.5325, July 2011. doi: 10.48550/arXiv.1107.5325.

M. S. Lundkvist, H. Kjeldsen, S. Albrecht, G. R. Davies, S. Basu, D. Huber, A. B. Justesen, C. Karoff, V. Silva Aguirre, V. van Eylen, C. Vang, T. Arentoft, T. Barclay, T. R. Bedding, T. L. Campante, W. J. Chaplin, J. Christensen-Dalsgaard, Y. P. Elsworth, R. L. Gilliland, R. Handberg, S. Hekker, S. D. Kawaler, M. N. Lund, T. S. Metcalfe, A. Miglio, J. F. Rowe, D. Stello, B. Tingley, and T. R. White. Hot super-Earths stripped by their host stars. *Nature Communications*, 7:11201, Apr. 2016. doi: 10.1038/ncomms11201.

R. J. MacDonald, J. M. Goyal, and N. K. Lewis. Why Is it So Cold in Here? Explaining the Cold Temperatures Retrieved from Transmission Spectra of Exoplanet Atmospheres. *Astrophysical Journal Letters*, 893(2):L43, Apr. 2020. doi: 10.3847/2041-8213/ab8238.

N. Madhusudhan. C/O Ratio as a Dimension for Characterizing Exoplanetary Atmospheres. *The Astrophysical Journal*, 758(1):36, Oct. 2012. doi: 10.1088/0004-637X/758/1/36.

N. Madhusudhan. Exoplanetary Atmospheres: Key Insights, Challenges, and Prospects. *Annual Review of Astronomy and Astrophysics*, 57:617–663, Aug. 2019. doi: 10.1146/annurev-astro-081817-051846.

N. Madhusudhan and S. Seager. A Temperature and Abundance Retrieval Method for Exoplanet Atmospheres. *Astrophysical Journal*, 707(1):24–39, Dec. 2009. doi: 10.1088/0004-637X/707/1/24.

N. Madhusudhan, H. Knutson, J. J. Fortney, and T. Barman. Exoplanetary Atmospheres. In H. Beuther, R. S. Klessen, C. P. Dullemond, and T. Henning, editors, *Protostars and Planets VI*, page 739, Jan. 2014. doi: 10.2458/azu_uapress_9780816531240-ch032.

N. Madhusudhan, M. Agúndez, J. I. Moses, and Y. Hu. Exoplanetary Atmospheres—Chemistry, Formation Conditions, and Habitability. *Space Science Reviews*, 205(1-4):285–348, Dec. 2016. doi: 10.1007/s11214-016-0254-3.

N. Madhusudhan, B. Bitsch, A. Johansen, and L. Eriksson. Atmospheric signatures of giant exoplanet formation by pebble accretion. *Monthly Notices of the Royal Astronomical Society*, 469(4):4102–4115, 05 2017. ISSN 0035-8711. doi: 10.1093/mnras/stx1139. URL `https://doi.org/10.1093/mnras/stx1139`.

N. Madhusudhan, M. C. Nixon, L. Welbanks, A. A. A. Piette, and R. A. Booth. The interior and atmosphere of the habitable-zone exoplanet k2-18b. *The Astrophysical Journal Letters*, 891(1):L7, feb 2020. doi: 10.3847/2041-8213/ab7229. URL `https://dx.doi.org/10.3847/2041-8213/ab7229`.

N. Madhusudhan, A. A. A. Piette, and S. Constantinou. Habitability and Biosignatures of Hycean Worlds. *Astrophysical Journal*, 918(1):1, Sept. 2021. doi: 10.3847/1538-4357/abfd9c.

N. Madhusudhan, S. Sarkar, S. Constantinou, M. Holmberg, A. A. A. Piette, and J. I. Moses. Carbon-bearing Molecules in a Possible Hycean Atmosphere. *Astrophysical Journal Letters*, 956 (1):L13, Oct. 2023. doi: 10.3847/2041-8213/acf577.

M. C. Maimone, M. Brogi, A. Chiavassa, M. E. van den Ancker, C. F. Manara, J. Leconte, S. Gandhi, and W. Pluriel. Detecting H_2O with CRIRES+: WASP-20b. *Astronomy & Astrophysics*, 667: A106, Nov. 2022. doi: 10.1051/0004-6361/202244383.

C. Majeau, E. Agol, and N. B. Cowan. A Two-dimensional Infrared Map of the Extrasolar Planet HD 189733b. *Astrophysical Journal Letters*, 747(2):L20, Mar. 2012. doi: 10.1088/2041-8205/747/2/L20.

M. Malik, L. Grosheintz, J. M. Mendonça, S. L. Grimm, B. Lavie, D. Kitzmann, S.-M. Tsai, A. Burrows, L. Kreidberg, M. Bedell, J. L. Bean, K. B. Stevenson, and K. Heng. HELIOS: An Open-source, GPU-accelerated Radiative Transfer Code for Self-consistent Exoplanetary Atmospheres. *The Astronomical Journal*, 153(2):56, Feb. 2017. doi: 10.3847/1538-3881/153/2/56.

K. Mandel and E. Agol. Analytic Light Curves for Planetary Transit Searches. *The Astrophysical Journal Letters*, 580(2):L171–L175, Dec. 2002. doi: 10.1086/345520.

M. Mansfield, J. L. Bean, A. Oklopčić, L. Kreidberg, J.-M. Désert, E. M.-R. Kempton, M. R. Line, J. J. Fortney, G. W. Henry, M. Mallonn, K. B. Stevenson, D. Dragomir, R. Allart, and V. Bourrier. Detection of helium in the atmosphere of the exo-neptune hat-p-11b. *The Astrophysical Journal Letters*, 868(2):L34, nov 2018. doi: 10.3847/2041-8213/aaf166. URL `https://dx.doi.org/10.3847/2041-8213/aaf166`.

M. Mayor and D. Queloz. A Jupiter-mass companion to a solar-type star. *Nature*, 378(6555):355–359, Nov. 1995. doi: 10.1038/378355a0.

M. Mayor, F. Pepe, D. Queloz, F. Bouchy, G. Rupprecht, G. Lo Curto, G. Avila, W. Benz, J. L. Bertaux, X. Bonfils, T. Dall, H. Dekker, B. Delabre, W. Eckert, M. Fleury, A. Gilliotte, D. Gojak, J. C. Guzman, D. Kohler, J. L. Lizon, A. Longinotti, C. Lovis, D. Megevand, L. Pasquini, J. Reyes, J. P. Sivan, D. Sosnowska, R. Soto, S. Udry, A. van Kesteren, L. Weber, and U. Weilenmann. Setting New Standards with HARPS. *The Messenger*, 114:20–24, Dec. 2003.

D. B. McLaughlin. Some results of a spectrographic study of the Algol system. *The Astrophysical Journal*, 60:22–31, July 1924. doi: 10.1086/142826.

K. Ment, D. A. Fischer, G. Bakos, A. W. Howard, and H. Isaacson. Radial Velocities from the N2K Project: Six New Cold Gas Giant Planets Orbiting HD 55696, HD 98736, HD 148164, HD 203473, and HD 211810. *Astronomical Journal*, 156(5):213, Nov. 2018. doi: 10.3847/1538-3881/aae1f5.

N. Meunier, A. M. Lagrange, and S. Cuzacq. Activity time series of old stars from late F to early K. IV. Limits of the correction of radial velocities using chromospheric emission. *Astronomy & Astrophysics*, 632:A81, Dec. 2019. doi: 10.1051/0004-6361/201935348.

T. Mikal-Evans, N. Madhusudhan, J. Dittmann, M. N. Günther, L. Welbanks, V. Van Eylen, I. J. M. Crossfield, T. Daylan, and L. Kreidberg. Hubble Space Telescope Transmission Spectroscopy for the Temperate Sub-Neptune TOI-270 d: A Possible Hydrogen-rich Atmosphere Containing Water Vapor. *The Astronomical Journal*, 165(3):84, Mar. 2023. doi: 10.3847/1538-3881/aca90b.

P. Mollière, J. P. Wardenier, R. van Boekel, T. Henning, K. Molaverdikhani, and I. A. G. Snellen. petitRADTRANS. A Python radiative transfer package for exoplanet characterization and retrieval. *Astronomy & Astrophysics*, 627:A67, July 2019. doi: 10.1051/0004-6361/201935470.

M. Montalto, N. C. Santos, I. Boisse, G. Boué, P. Figueira, and S. Sousa. Exoplanet transmission spectroscopy: accounting for the eccentricity and the longitude of periastron. Superwinds in the upper atmosphere of HD 209458b? *Astronomy & Astrophysics*, 528:L17, Apr. 2011. doi: 10.1051/0004-6361/201116492.

C. Mordasini, R. van Boekel, P. Mollière, T. Henning, and B. Benneke. The Imprint of Exoplanet Formation History on Observable Present-day Spectra of Hot Jupiters. *Astrophysical Journal*, 832 (1):41, Nov. 2016. doi: 10.3847/0004-637X/832/1/41.

B. M. Morris, S. L. Hawley, L. Hebb, C. Sakari, J. R. A. Davenport, H. Isaacson, A. W. Howard, B. T. Montet, and E. Agol. Chromospheric Activity of HAT-P-11: An Unusually Active Planet-hosting K Star. *The Astrophysical Journal*, 848(1):58, Oct. 2017a. doi: 10.3847/1538-4357/aa8cca.

B. M. Morris, L. Hebb, J. R. A. Davenport, G. Rohn, and S. L. Hawley. The Starspots of HAT-P-11: Evidence for a Solar-like Dynamo. *The Astrophysical Journal*, 846(2):99, Sept. 2017b. doi: 10.3847/1538-4357/aa8555.

A. Mortier, N. C. Santos, A. Sozzetti, M. Mayor, D. Latham, X. Bonfils, and S. Udry. The frequency of giant planets around metal-poor stars. *Astronomy & Astrophysics*, 543:A45, July 2012. doi: 10.1051/0004-6361/201118651.

J. I. Moses. Chemical kinetics on extrasolar planets. *Philosophical Transactions of the Royal Society of London Series A*, 372(2014):20130073–20130073, Mar. 2014. doi: 10.1098/rsta.2013.0073.

J. I. Moses, C. Visscher, J. J. Fortney, A. P. Showman, N. K. Lewis, C. A. Griffith, S. J. Klippenstein, M. Shabram, A. J. Friedson, M. S. Marley, and R. S. Freedman. Disequilibrium Carbon, Oxygen, and Nitrogen Chemistry in the Atmospheres of HD 189733b and HD 209458b. *Astrophysical Journal*, 737(1):15, Aug. 2011. doi: 10.1088/0004-637X/737/1/15.

J. I. Moses, M. R. Line, C. Visscher, M. R. Richardson, N. Nettelmann, J. J. Fortney, T. S. Barman, K. B. Stevenson, and N. Madhusudhan. Compositional Diversity in the Atmospheres of Hot Neptunes, with Application to GJ 436b. *The Astrophysical Journal*, 777(1):34, Nov. 2013. doi: 10.1088/0004-637X/777/1/34.

F. Murtagh and A. Heck. *Multivariate Data Analysis*, volume 131. Springer, 1987. doi: 10.1007/978-94-009-3789-5.

V. Nascimbeni, G. Piotto, I. Pagano, G. Scandariato, E. Sani, and M. Fumana. The blue sky of GJ3470b: the atmosphere of a low-mass planet unveiled by ground-based photometry. *Astronomy & Astrophysics*, 559:A32, Nov. 2013. doi: 10.1051/0004-6361/201321971.

V. Nascimbeni, M. Mallonn, G. Scandariato, I. Pagano, G. Piotto, G. Micela, S. Messina, G. Leto, K. G. Strassmeier, S. Bisogni, and R. Speziali. Large Binocular Telescope view of the atmosphere of GJ1214b. *Astronomy & Astrophysics*, 579:A113, July 2015. doi: 10.1051/0004-6361/201425350.

N. Nikolov, D. K. Sing, F. Pont, A. S. Burrows, J. J. Fortney, G. E. Ballester, T. M. Evans, C. M. Huitson, H. R. Wakeford, P. A. Wilson, S. Aigrain, D. Deming, N. P. Gibson, G. W. Henry, H. Knutson, A. Lecavelier des Etangs, A. P. Showman, A. Vidal-Madjar, and K. Zahnle. Hubble Space Telescope hot Jupiter transmission spectral survey: a detection of Na and strong optical absorption in HAT-P-1b. *Monthly Notices of the Royal Astronomical Society*, 437(1):46–66, Jan. 2014. doi: 10.1093/mnras/stt1859.

S. Noll, W. Kausch, M. Barden, A. M. Jones, C. Szyszka, S. Kimeswenger, and J. Vinther. An atmospheric radiation model for Cerro Paranal. I. The optical spectral range. *Astronomy & Astrophysics*, 543:A92, July 2012. doi: 10.1051/0004-6361/201219040.

L. Nortmann, E. Pallé, M. Salz, J. Sanz-Forcada, E. Nagel, F. J. Alonso-Floriano, S. Czesla, F. Yan, G. Chen, I. A. G. Snellen, M. Zechmeister, J. H. M. M. Schmitt, M. López-Puertas, N. Casasayas-Barris, F. F. Bauer, P. J. Amado, J. A. Caballero, S. Dreizler, T. Henning, M. Lampón, D. Montes, K. Molaverdikhani, A. Quirrenbach, A. Reiners, I. Ribas, A. Sánchez-López, P. C. Schneider, and M. R. Zapatero Osorio. Ground-based detection of an extended helium atmosphere in the Saturn-mass exoplanet WASP-69b. *Science*, 362(6421):1388–1391, Dec. 2018. doi: 10.1126/science.aat5348.

L. Nortmann, F. Lesjak, F. Yan, D. Cont, S. Czesla, A. Lavail, A. D. Rains, E. Nagel, L. Boldt-Christmas, A. Hatzes, A. Reiners, N. Piskunov, O. Kochukhov, U. Heiter, D. Shulyak, M. Rengel, and U. Seemann. CRIRES$^+$ transmission spectroscopy of WASP-127b. Detection of the resolved signatures of a supersonic equatorial jet and cool poles in a hot planet. *arXiv e-prints*, art. arXiv:2404.12363, Apr. 2024. doi: 10.48550/arXiv.2404.12363.

S. K. Nugroho, H. Kawahara, K. Masuda, T. Hirano, T. Kotani, and A. Tajitsu. High-resolution Spectroscopic Detection of TiO and a Stratosphere in the Day-side of WASP-33b. *The Astronomical Journal*, 154(6):221, Dec. 2017. doi: 10.3847/1538-3881/aa9433.

S. K. Nugroho, H. Kawahara, N. P. Gibson, E. J. W. de Mooij, T. Hirano, T. Kotani, Y. Kawashima, K. Masuda, M. Brogi, J. L. Birkby, C. A. Watson, M. Tamura, K. Zwintz, H. Harakawa, T. Kudo, M. Kuzuhara, K. Hodapp, M. Ishizuka, S. Jacobson, M. Konishi, T. Kurokawa, J. Nishikawa, M. Omiya, T. Serizawa, A. Ueda, and S. Vievard. First Detection of Hydroxyl Radical Emission from an Exoplanet Atmosphere: High-dispersion Characterization of WASP-33b Using Subaru/IRD. *The Astrophysical Journal Letters*, 910(1):L9, Mar. 2021. doi: 10.3847/2041-8213/abec71.

K. I. Öberg, R. Murray-Clay, and E. A. Bergin. The Effects of Snowlines on C/O in Planetary Atmospheres. *The Astrophysical Journal Letters*, 743(1):L16, Dec. 2011. doi: 10.1088/2041-8205/743/1/L16.

L. Origlia, E. Oliva, C. Baffa, G. Falcini, E. Giani, F. Massi, P. Montegriffo, N. Sanna, S. Scuderi, M. Sozzi, A. Tozzi, I. Carleo, R. Gratton, F. Ghinassi, and M. Lodi. High resolution near IR spectroscopy with GIANO-TNG. In S. K. Ramsay, I. S. McLean, and H. Takami, editors, *Ground-based and Airborne Instrumentation for Astronomy V*, volume 9147 of *Society of Photo-Optical Instrumentation Engineers (SPIE) Conference Series*, page 91471E, July 2014. doi: 10.1117/12.2054743.

J. E. Owen and A. P. Jackson. Planetary evaporation by UV & X-ray radiation: basic hydrodynamics. *Monthly Notices of the Royal Astronomical Society*, 425(4):2931–2947, Oct. 2012. doi: 10.1111/j.1365-2966.2012.21481.x.

J. E. Owen and Y. Wu. Kepler Planets: A Tale of Evaporation. *Astrophysical Journal*, 775(2):105, Oct. 2013. doi: 10.1088/0004-637X/775/2/105.

E. Pacetti, D. Turrini, E. Schisano, S. Molinari, S. Fonte, R. Politi, P. Hennebelle, R. Klessen, L. Testi, and U. Lebreuilly. Chemical Diversity in Protoplanetary Disks and Its Impact on the Formation History of Giant Planets. *The Astrophysical Journal*, 937(1):36, Sept. 2022. doi: 10.3847/1538-4357/ac8b11.

P. Padovani and M. Cirasuolo. The Extremely Large Telescope. *Contemporary Physics*, 64(1):47–64, Jan. 2023. doi: 10.1080/00107514.2023.2266921.

E. Palle, K. Biazzo, E. Bolmont, P. Molliere, K. Poppenhaeger, J. Birkby, M. Brogi, G. Chauvin, A. Chiavassa, J. Hoeijmakers, E. Lellouch, C. Lovis, R. Maiolino, L. Nortmann, H. Parviainen, L. Pino, M. Turbet, J. Wender, S. Albrecht, S. Antoniucci, S. C. Barros, A. Beaudoin, B. Benneke, I. Boisse, A. S. Bonomo, F. Borsa, A. Brandeker, W. Brandner, L. A. Buchhave, A.-L. Cheffot, R. Deborde, F. Debras, R. Doyon, P. Di Marcantonio, P. Giacobbe, J. I. Gonzalez Hernandez, R. Helled, L. Kreidberg, P. Machado, J. Maldonado, A. Marconi, B. L. Canto Martins, A. Miceli, C. Mordasini, M. N'Diaye, A. Niedzielski, B. Nisini, L. Origlia, C. Peroux, A. G. M. Pietrow, E. Pinna, E. Rauscher, S. Reffert, P. Rousselot, N. Sanna, A. Simonnin, A. Suarez Mascareno, A. Zanutta, and M. Zechmeister. Ground-breaking Exoplanet Science with the ANDES spectrograph at the ELT. *arXiv e-prints*, art. arXiv:2311.17075, Nov. 2023. doi: 10.48550/arXiv.2311.17075.

C. Park, D. T. Jaffe, I.-S. Yuk, M.-Y. Chun, S. Pak, K.-M. Kim, M. Pavel, H. Lee, H. Oh, U. Jeong, C. K. Sim, H.-I. Lee, H. A. Nguyen Le, J. Strubhar, M. Gully-Santiago, J. S. Oh, S.-M. Cha, B. Moon, K. Park, C. Brooks, K. Ko, J.-Y. Han, J. Nah, P. C. Hill, S. Lee, S. Barnes, Y. S. Yu, K. Kaplan, G. Mace, H. Kim, J.-J. Lee, N. Hwang, and B.-G. Park. Design and early performance of IGRINS (Immersion Grating Infrared Spectrometer). In S. K. Ramsay, I. S. McLean, and H. Takami, editors, *Ground-based and Airborne Instrumentation for Astronomy V*, volume 9147 of *Society of Photo-Optical Instrumentation Engineers (SPIE) Conference Series*, page 91471D, July 2014. doi: 10.1117/12.2056431.

V. Parmentier and T. Guillot. A non-grey analytical model for irradiated atmospheres. I. Derivation. *Astronomy & Astrophysics*, 562:A133, Feb. 2014. doi: 10.1051/0004-6361/201322342.

V. Parmentier, A. P. Showman, and Y. Lian. 3D mixing in hot Jupiters atmospheres. I. Application to the day/night cold trap in HD 209458b. *Astronomy & Astrophysics*, 558:A91, Oct. 2013. doi: 10.1051/0004-6361/201321132.

B. Paxton, P. Marchant, J. Schwab, E. B. Bauer, L. Bildsten, M. Cantiello, L. Dessart, R. Farmer, H. Hu, N. Langer, R. H. D. Townsend, D. M. Townsley, and F. X. Timmes. Modules for Experiments in Stellar Astrophysics (MESA): Binaries, Pulsations, and Explosions. *Astrophysical Journal Supplement*, 220(1):15, Sept. 2015. doi: 10.1088/0067-0049/220/1/15.

S. Pelletier, B. Benneke, M. Ali-Dib, B. Prinoth, D. Kasper, A. Seifahrt, J. L. Bean, F. Debras, B. Klein, L. Bazinet, H. J. Hoeijmakers, A. Y. Kesseli, O. Lim, A. Carmona, L. Pino, N. Casasayas-Barris, T. Hood, and J. Stürmer. Vanadium oxide and a sharp onset of cold-trapping on a giant exoplanet. *Nature*, 619(7970):491–494, July 2023. doi: 10.1038/s41586-023-06134-0.

F. Pepe, M. Mayor, F. Galland, D. Naef, D. Queloz, N. C. Santos, S. Udry, and M. Burnet. The CORALIE survey for southern extra-solar planets VII. Two short-period Saturnian companions to <ASTROBJ>HD 108147</ASTROBJ> and <ASTROBJ>HD 168746</ASTROBJ>. *Astronomy & Astrophysics*, 388:632–638, June 2002. doi: 10.1051/0004-6361:20020433.

J. Pepper, R. W. Pogge, D. L. DePoy, J. L. Marshall, K. Z. Stanek, A. M. Stutz, S. Poindexter, R. Siverd, T. P. O'Brien, M. Trueblood, and P. Trueblood. The kilodegree extremely little telescope (kelt): A small robotic telescope for large-area synoptic surveys. *Publications of the Astronomical Society of the Pacific*, 119(858):923, aug 2007. doi: 10.1086/521836. URL `https://dx.doi.org/10.1086/521836`.

E. A. Petigura, G. W. Marcy, J. N. Winn, L. M. Weiss, B. J. Fulton, A. W. Howard, E. Sinukoff, H. Isaacson, T. D. Morton, and J. A. Johnson. The California-Kepler Survey. IV. Metal-rich Stars Host a Greater Diversity of Planets. *Astronomical Journal*, 155(2):89, Feb. 2018. doi: 10.3847/1538-3881/aaa54c.

L. Pino, D. Ehrenreich, A. Wyttenbach, V. Bourrier, V. Nascimbeni, K. Heng, S. Grimm, C. Lovis, M. Malik, F. Pepe, and G. Piotto. Combining low- to high-resolution transit spectroscopy of HD 189733b. Linking the troposphere and the thermosphere of a hot gas giant. *Astronomy & Astrophysics*, 612:A53, Apr. 2018. doi: 10.1051/0004-6361/201731244.

L. Pino, J.-M. Desert, L. Malavolta, and F. Borsa. Metals in the emission spectrum of Kelt-9b. In *AAS/Division for Extreme Solar Systems Abstracts*, volume 51 of *AAS/Division for Extreme Solar Systems Abstracts*, page 326.21, Aug. 2019.

D. Piskorz, B. Benneke, N. R. Crockett, A. C. Lockwood, G. A. Blake, T. S. Barman, C. F. Bender, J. S. Carr, and J. A. Johnson. Detection of water vapor in the thermal spectrum of the non-transiting hot jupiter upsilon andromedae b. *The Astronomical Journal*, 154(2):78, aug 2017. doi: 10.3847/1538-3881/aa7dd8. URL `https://doi.org/10.3847/1538-3881/aa7dd8`.

D. L. Pollacco, I. Skillen, A. Collier Cameron, D. J. Christian, C. Hellier, J. Irwin, T. A. Lister, R. A. Street, R. G. West, D. R. Anderson, W. I. Clarkson, H. Deeg, B. Enoch, A. Evans, A. Fitzsimmons, C. A. Haswell, S. Hodgkin, K. Horne, S. R. Kane, F. P. Keenan, P. F. L. Maxted, A. J. Norton, J. Osborne, N. R. Parley, R. S. I. Ryans, B. Smalley, P. J. Wheatley, and D. M. Wilson. The WASP Project and the SuperWASP Cameras. *Publications of the Astronomical Society of the Pacific*, 118(848):1407–1418, Oct. 2006. doi: 10.1086/508556.

J. B. Pollack, O. Hubickyj, P. Bodenheimer, J. J. Lissauer, M. Podolak, and Y. Greenzweig. Formation of the Giant Planets by Concurrent Accretion of Solids and Gas. *Icarus*, 124(1):62–85, Nov. 1996. doi: 10.1006/icar.1996.0190.

O. L. Polyansky, A. A. Kyuberis, N. F. Zobov, J. Tennyson, S. N. Yurchenko, and L. Lodi. ExoMol molecular line lists XXX: a complete high-accuracy line list for water. *Monthly Notices of the Royal*

Astronomical Society, 480(2):2597–2608, 08 2018. ISSN 0035-8711. doi: 10.1093/mnras/sty1877. URL `https://doi.org/10.1093/mnras/sty1877`.

R. G. Prinn and S. S. Barshay. Carbon Monoxide on Jupiter and Implications for Atmospheric Convection. *Science*, 198(4321):1031–1034, Dec. 1977. doi: 10.1126/science.198.4321.1031.

A. Quirrenbach, P. J. Amado, J. A. Caballero, R. Mundt, A. Reiners, I. Ribas, W. Seifert, M. Abril, J. Aceituno, F. J. Alonso-Floriano, M. Ammler-von Eiff, R. Antona Jiménez, H. Anwand-Heerwart, M. Azzaro, F. Bauer, D. Barrado, S. Becerril, V. J. S. Béjar, D. Benítez, Z. M. Berdiñas, M. C. Cárdenas, E. Casal, A. Claret, J. Colomé, M. Cortés-Contreras, S. Czesla, M. Doellinger, S. Dreizler, C. Feiz, M. Fernández, D. Galadí, M. C. Gálvez-Ortiz, A. García-Piquer, M. L. García-Vargas, R. Garrido, L. Gesa, V. Gómez Galera, E. González Álvarez, J. I. González Hernández, U. Grözinger, J. Guàrdia, E. W. Guenther, E. de Guindos, J. Gutiérrez-Soto, H. J. Hagen, A. P. Hatzes, P. H. Hauschildt, J. Helmling, T. Henning, D. Hermann, L. Hernández Castaño, E. Herrero, D. Hidalgo, G. Holgado, A. Huber, K. F. Huber, S. Jeffers, V. Joergens, E. de Juan, M. Kehr, R. Klein, M. Kürster, A. Lamert, S. Lalitha, W. Laun, U. Lemke, R. Lenzen, M. López del Fresno, B. López Martí, J. López-Santiago, U. Mall, H. Mandel, E. L. Martín, S. Martín-Ruiz, H. Martínez-Rodríguez, C. J. Marvin, R. J. Mathar, E. Mirabet, D. Montes, R. Morales Muñoz, A. Moya, V. Naranjo, A. Ofir, R. Oreiro, E. Pallé, J. Panduro, V. M. Passegger, A. Pérez-Calpena, D. Pérez Medialdea, M. Perger, M. Pluto, A. Ramón, R. Rebolo, P. Redondo, S. Reffert, S. Reinhardt, P. Rhode, H. W. Rix, F. Rodler, E. Rodríguez, C. Rodríguez-López, E. Rodríguez-Pérez, R. R. Rohloff, A. Rosich, E. Sánchez-Blanco, M. A. Sánchez Carrasco, J. Sanz-Forcada, L. F. Sarmiento, S. Schäfer, J. Schiller, C. Schmidt, J. H. M. M. Schmitt, E. Solano, O. Stahl, C. Storz, J. Stürmer, J. C. Suárez, R. G. Ulbrich, G. Veredas, K. Wagner, J. Winkler, M. R. Zapatero Osorio, M. Zechmeister, F. J. Abellán de Paco, G. Anglada-Escudé, C. del Burgo, A. Klutsch, J. L. Lizon, M. López-Morales, J. C. Morales, M. A. C. Perryman, S. M. Tulloch, and W. Xu. CARMENES instrument overview. In S. K. Ramsay, I. S. McLean, and H. Takami, editors, *Ground-based and Airborne Instrumentation for Astronomy V*, volume 9147 of *Society of Photo-Optical Instrumentation Engineers (SPIE) Conference Series*, page 91471F, July 2014. doi: 10.1117/12.2056453.

A. Quirrenbach, P. J. Amado, I. Ribas, A. Reiners, J. A. Caballero, W. Seifert, J. Aceituno, M. Azzaro, D. Baroch, D. Barrado, F. Bauer, S. Becerril, V. J. S. Bèjar, D. Benítez, M. Brinkmöller, C. Cardona Guillén, C. Cifuentes, J. Colomé, M. Cortés-Contreras, S. Czesla, S. Dreizler, K. Frölich, B. Fuhrmeister, D. Galadí-Enríquez, J. I. González Hernández, R. González Peinado, E. W. Guenther, E. de Guindos, H. J. Hagen, A. P. Hatzes, P. H. Hauschildt, J. Helmling, T. Henning, O. Herbort, L. Hernández Castaño, E. Herrero, D. Hintz, S. V. Jeffers, E. N. Johnson, E. de Juan, A. Kaminski, H. Klahr, M. Kürster, M. Lafarga, L. Sairam, M. Lampón, L. M. Lara, R. Launhardt, M. López del Fresno, M. López-Puertas, R. Luque, H. Mandel, E. G. Marfil, E. L. Martín, S. Martín-Ruiz, R. J. Mathar, D. Montes, J. C. Morales, E. Nagel, L. Nortmann, G. Nowak, E. Pallé, V. M. Passegger, A. Pavlov, S. Pedraz, D. Pérez-Medialdea, M. Perger, R. Rebolo, S. Reffert, E. Rodríguez, C. Rodríguez López, A. Rosich, S. Sabotta, S. Sadegi, M. Salz, A. Sánchez-López, J. Sanz-Forcada, P. Sarkis, S. Schäfer, J. Schiller, J. H. M. M. Schmitt, P. Schöfer, A. Schweitzer, D. Shulyak, E. Solano, O. Stahl, M. Tala Pinto, T. Trifonov, M. R. Zapatero Osorio, F. Yan, M. Zechmeister, F. J. Abellán, M. Abril, F. J. Alonso-Floriano, M. Ammler-von

Eiff, G. Anglada-Escudé, H. Anwand-Heerwart, B. Arroyo-Torres, Z. M. Berdiñas, G. Bergondy, M. Blümcke, C. del Burgo, J. Cano, J. Carro, M. C. Cárdenas, E. Casal, A. Claret, E. Díez-Alonso, M. Doellinger, R. Dorda, C. Feiz, M. Fernández, I. M. Ferro, G. Gaisné, I. Gallardo, M. C. Gálvez-Ortiz, A. García-Piquer, M. L. García-Vargas, R. Garrido, L. Gesa, V. Gómez Galera, E. González-Álvarez, L. González-Cuesta, S. Grohnert, U. Grözinger, J. Guàrdia, A. Guijarro, R. P. Hedrosa, D. Hermann, I. Hermelo, R. Hernández Arabí, F. Hernández Hernando, D. Hidalgo, G. Holgado, A. Huber, K. Huber, P. Huke, M. Kehr, M. Kim, R. Klein, J. Klüter, A. Klutsch, F. Labarga, N. Labiche, A. Lamert, W. Laun, F. J. Lázaro, U. Lemke, R. Lenzen, M. Llamas, J. L. Lizon, N. Lodieu, M. J. López González, M. López-Morales, J. F. López Salas, J. López-Santiago, H. Magán Madinabeitia, U. Mall, L. Mancini, J. A. Marín Molina, H. Martínez-Rodríguez, D. Maroto Fernández, C. J. Marvin, E. Mirabet, M. E. Moreno-Raya, A. Moya, R. Mundt, V. Naranjo, J. Panduro, J. Pascual, A. Pérez-Calpena, M. A. C. Perryman, M. Pluto, A. Ramón, P. Redondo, S. Reinhart, P. Rhode, H. W. Rix, F. Rodler, R. R. Rohloff, E. Sánchez-Blanco, M. A. Sánchez Carrasco, L. F. Sarmiento, C. Schmidt, C. Storz, J. B. P. Strachan, J. Stürmer, J. C. Suárez, H. M. Tabernero, L. Tal-Or, S. M. Tulloch, R. G. Ulbrich, G. Veredas, J. L. Vico Linares, M. Vidal-Dasilva, F. Vilardell, K. Wagner, J. Winkler, V. Wolthoff, W. Xu, and Z. Zhao. CARMENES: high-resolution spectra and precise radial velocities in the red and infrared. In C. J. Evans, L. Simard, and H. Takami, editors, *Ground-based and Airborne Instrumentation for Astronomy VII*, volume 10702 of *Society of Photo-Optical Instrumentation Engineers (SPIE) Conference Series*, page 107020W, July 2018. doi: 10.1117/12.2313689.

M. Rainer, A. Harutyunyan, I. Carleo, E. Oliva, S. Benatti, A. Bignamini, R. Claudi, E. Gonzalez-Alvarez, N. Sanna, A. Ghedina, G. Micela, E. Molinari, A. Tozzi, C. Baffa, A. Baruffolo, N. Buchschacher, M. Cecconi, R. Cosentino, G. Falcini, D. Fantinel, L. Fini, A. Galli, F. Ghinassi, E. Giani, C. Gonzalez, M. Gonzalez, R. Gratton, J. Guerra, M. H. Diaz, N. Hernandez, M. Iuzzolino, M. Lodi, L. Malavolta, J. Maldonado, L. Origlia, H. P. Ventura, A. Puglisi, C. Riverol, L. Riverol, J. S. Juan, S. Scuderi, U. Seeman, A. Sozzetti, and M. Sozzi. Introducing GOFIO: a DRS for the GIANO-B near-infrared spectrograph. In C. J. Evans, L. Simard, and H. Takami, editors, *Ground-based and Airborne Instrumentation for Astronomy VII*, volume 10702, page 1070266. International Society for Optics and Photonics, SPIE, 2018. doi: 10.1117/12.2312130. URL `https://doi.org/10.1117/12.2312130`.

I. Ramírez, J. Meléndez, J. Bean, M. Asplund, M. Bedell, T. Monroe, L. Casagrande, L. Schirbel, S. Dreizler, J. Teske, M. Tucci Maia, A. Alves-Brito, and P. Baumann. The Solar Twin Planet Search. I. Fundamental parameters of the stellar sample. *Astronomy & Astrophysics*, 572:A48, Dec. 2014. doi: 10.1051/0004-6361/201424244.

S. Ramkumar, N. P. Gibson, S. K. Nugroho, C. Maguire, and M. Fortune. High-resolution emission spectroscopy retrievals of MASCARA-1b with CRIRES+: strong detections of CO, H_2O, and Fe emission lines and a C/O consistent with solar. *Monthly Notices of the Royal Astronomical Society*, 525(2):2985–3005, Oct. 2023. doi: 10.1093/mnras/stad2476.

L. W. Ramsey. Fiber-Optic Instrumentation and the Hobby-Eberly Telescope. In S. Arribas, E. Mediavilla, and F. Watson, editors, *Fiber Optics in Astronomy III*, volume 152 of *Astronomical Society of the Pacific Conference Series*, page 235, Jan. 1998.

S. Redfield, M. Endl, W. D. Cochran, and L. Koesterke. Sodium Absorption from the Exoplanetary Atmosphere of HD 189733b Detected in the Optical Transmission Spectrum. *Astrophysical Journal Letters*, 673(1):L87, Jan. 2008. doi: 10.1086/527475.

G. R. Ricker, J. N. Winn, R. Vanderspek, D. W. Latham, G. Á. Bakos, J. L. Bean, Z. K. Berta-Thompson, T. M. Brown, L. Buchhave, N. R. Butler, R. P. Butler, W. J. Chaplin, D. Charbonneau, J. Christensen-Dalsgaard, M. Clampin, D. Deming, J. Doty, N. De Lee, C. Dressing, E. W. Dunham, M. Endl, F. Fressin, J. Ge, T. Henning, M. J. Holman, A. W. Howard, S. Ida, J. M. Jenkins, G. Jernigan, J. A. Johnson, L. Kaltenegger, N. Kawai, H. Kjeldsen, G. Laughlin, A. M. Levine, D. Lin, J. J. Lissauer, P. MacQueen, G. Marcy, P. R. McCullough, T. D. Morton, N. Narita, M. Paegert, E. Palle, F. Pepe, J. Pepper, A. Quirrenbach, S. A. Rinehart, D. Sasselov, B. Sato, S. Seager, A. Sozzetti, K. G. Stassun, P. Sullivan, A. Szentgyorgyi, G. Torres, S. Udry, and J. Villasenor. Transiting Exoplanet Survey Satellite (TESS). *Journal of Astronomical Telescopes, Instruments, and Systems*, 1:014003, Jan. 2015. doi: 10.1117/1.JATIS.1.1.014003.

F. Rodler, M. Lopez-Morales, and I. Ribas. Weighing the Non-transiting Hot Jupiter τ Boo b. *Astrophysical Journal Letters*, 753(1):L25, July 2012. doi: 10.1088/2041-8205/753/1/L25.

R. A. Rossiter. On the detection of an effect of rotation during eclipse in the velocity of the brigher component of beta Lyrae, and on the constancy of velocity of this system. *The Astrophysical Journal*, 60:15–21, July 1924. doi: 10.1086/142825.

L. Rothman, I. Gordon, R. Barber, H. Dothe, R. Gamache, A. Goldman, V. Perevalov, S. Tashkun, and J. Tennyson. Hitemp, the high-temperature molecular spectroscopic database. *Journal of Quantitative Spectroscopy and Radiative Transfer*, 111(15):2139–2150, 2010. ISSN 0022-4073. doi: https://doi.org/10.1016/j.jqsrt.2010.05.001. URL `https://www.sciencedirect.com/science/article/pii/S002240731000169X`. XVIth Symposium on High Resolution Molecular Spectroscopy (HighRus-2009).

J. F. Rowe, J. M. Matthews, S. Seager, R. Kuschnig, D. B. Guenther, A. F. J. Moffat, S. M. Rucinski, D. Sasselov, G. A. H. Walker, and W. W. Weiss. An Upper Limit on the Albedo of HD 209458b: Direct Imaging Photometry with the MOST Satellite. *Astrophysical Journal*, 646(2):1241–1251, Aug. 2006. doi: 10.1086/504252.

Z. Rustamkulov, D. K. Sing, S. Mukherjee, E. M. May, J. Kirk, E. Schlawin, M. R. Line, C. Piaulet, A. L. Carter, N. E. Batalha, J. M. Goyal, M. López-Morales, J. D. Lothringer, R. J. MacDonald, S. E. Moran, K. B. Stevenson, H. R. Wakeford, N. Espinoza, J. L. Bean, N. M. Batalha, B. Benneke, Z. K. Berta-Thompson, I. J. M. Crossfield, P. Gao, L. Kreidberg, D. K. Powell, P. E. Cubillos, N. P. Gibson, J. Leconte, K. Molaverdikhani, N. K. Nikolov, V. Parmentier, P. Roy, J. Taylor, J. D. Turner, P. J. Wheatley, K. Aggarwal, E. Ahrer, M. K. Alam, L. Alderson, N. H. Allen, A. Banerjee, S. Barat, D. Barrado, J. K. Barstow, T. J. Bell, J. Blecic, J. Brande, S. Casewell, Q. Changeat, K. L. Chubb, N. Crouzet, T. Daylan, L. Decin, J. Désert, T. Mikal-Evans, A. D. Feinstein, L. Flagg, J. J. Fortney, J. Harrington, K. Heng, Y. Hong, R. Hu, N. Iro, T. Kataria, E. M. R. Kempton, J. Krick, M. Lendl, J. Lillo-Box, A. Louca, J. Lustig-Yaeger, L. Mancini, M. Mansfield, N. J. Mayne, Y. Miguel, G. Morello, K. Ohno, E. Palle, D. J. M. Petit dit de la Roche, B. V. Rackham, M. Radica, L. Ramos-Rosado, S. Redfield, L. K. Rogers, E. L. Shkolnik,

J. Southworth, J. Teske, P. Tremblin, G. S. Tucker, O. Venot, W. C. Waalkes, L. Welbanks, X. Zhang, and S. Zieba. Early Release Science of the exoplanet WASP-39b with JWST NIRSpec PRISM. *Nature*, 614(7949):659–663, Feb. 2023. doi: 10.1038/s41586-022-05677-y.

M. Salz, S. Czesla, P. C. Schneider, E. Nagel, J. H. M. M. Schmitt, L. Nortmann, F. J. Alonso-Floriano, M. López-Puertas, M. Lampón, F. F. Bauer, I. A. G. Snellen, E. Pallé, J. A. Caballero, F. Yan, G. Chen, J. Sanz-Forcada, P. J. Amado, A. Quirrenbach, I. Ribas, A. Reiners, V. J. S. Béjar, N. Casasayas-Barris, M. Cortés-Contreras, S. Dreizler, E. W. Guenther, T. Henning, S. V. Jeffers, A. Kaminski, M. Kürster, M. Lafarga, L. M. Lara, K. Molaverdikhani, D. Montes, J. C. Morales, A. Sánchez-López, W. Seifert, M. R. Zapatero Osorio, and M. Zechmeister. Detection of He I λ10830 Å absorption on HD 189733 b with CARMENES high-resolution transmission spectroscopy. *Astronomy & Astrophysics*, 620:A97, Dec. 2018. doi: 10.1051/0004-6361/201833694.

A. Sánchez-López, F. J. Alonso-Floriano, M. López-Puertas, I. A. G. Snellen, B. Funke, E. Nagel, F. F. Bauer, P. J. Amado, J. A. Caballero, S. Czesla, L. Nortmann, E. Pallé, M. Salz, A. Reiners, I. Ribas, A. Quirrenbach, G. Anglada-Escudé, V. J. S. Béjar, N. Casasayas-Barris, D. Galadí-Enríquez, E. W. Guenther, T. Henning, A. Kaminski, M. Kürster, M. Lampón, L. M. Lara, D. Montes, J. C. Morales, M. Stangret, L. Tal-Or, J. Sanz-Forcada, J. H. M. M. Schmitt, M. R. Zapatero Osorio, and M. Zechmeister. Water vapor detection in the transmission spectra of HD 209458 b with the CARMENES NIR channel. *Astronomy & Astrophysics*, 630:A53, Oct. 2019. doi: 10.1051/0004-6361/201936084.

R. Sanchis-Ojeda and J. N. Winn. Starspots, Spin-Orbit Misalignment, and Active Latitudes in the HAT-P-11 Exoplanetary System. *The Astrophysical Journal*, 743(1):61, Dec. 2011. doi: 10.1088/0004-637X/743/1/61.

A. Santerne, A. S. Bonomo, G. Hébrard, M. Deleuil, C. Moutou, J. M. Almenara, F. Bouchy, and R. F. Díaz. SOPHIE velocimetry of Kepler transit candidates. IV. KOI-196b: a non-inflated hot Jupiter with a high albedo. *Astronomy & Astrophysics*, 536:A70, Dec. 2011. doi: 10.1051/0004-6361/201117807.

G. Scandariato, V. Nascimbeni, A. F. Lanza, I. Pagano, R. Zanmar Sanchez, and G. Leto. TOSC: an algorithm for the tomography of spotted transit chords. *Astronomy & Astrophysics*, 606:A134, Oct. 2017. doi: 10.1051/0004-6361/201730966.

G. Scandariato, V. Singh, D. Kitzmann, M. Lendl, A. Brandeker, G. Bruno, A. Bekkelien, W. Benz, P. Gutermann, P. F. L. Maxted, A. Bonfanti, S. Charnoz, M. Fridlund, K. Heng, S. Hoyer, I. Pagano, C. M. Persson, S. Salmon, V. Van Grootel, T. G. Wilson, J. Asquier, M. Bergomi, L. Gambicorti, J. Hasiba, Y. Alibert, R. Alonso, G. Anglada, T. Bárczy, D. Barrado y Navascues, S. C. C. Barros, W. Baumjohann, M. Beck, T. Beck, N. Billot, X. Bonfils, C. Broeg, J. Cabrera, A. Collier Cameron, S. Csizmadia, M. B. Davies, M. Deleuil, A. Deline, L. Delrez, O. Demangeon, B. O. Demory, A. Erikson, A. Fortier, L. Fossati, D. Gandolfi, M. Gillon, M. Güdel, K. G. Isaak, L. L. Kiss, J. Laskar, A. Lecavelier des Etangs, C. Lovis, D. Magrin, V. Nascimbeni, G. Olofsson, R. Ottensamer, E. Pallé, H. Parviainen, G. Peter, G. Piotto, D. Pollacco, D. Queloz, R. Ragazzoni, N. Rando, H. Rauer, I. Ribas, N. C. Santos, D. Ségransan, L. M. Serrano, A. E. Simon, A. M. S. Smith, S. G. Sousa, M. Steller, G. M. Szabó, N. Thomas, S. Udry, B. Ulmer, and N. Walton. Phase

curve and geometric albedo of WASP-43b measured with CHEOPS, TESS, and HST WFC3/UVIS. *Astronomy & Astrophysics*, 668:A17, Dec. 2022. doi: 10.1051/0004-6361/202243974.

E. Schlawin, S. Mukherjee, K. Ohno, T. J. Bell, T. G. Beatty, T. P. Greene, M. Line, R. C. Challener, V. Parmentier, J. J. Fortney, E. Rauscher, L. Wiser, L. Welbanks, M. Murphy, I. Edelman, N. Batalha, S. E. Moran, N. Mehta, and M. Rieke. Multiple Clues for Dayside Aerosols and Temperature Gradients in WASP-69 b from a Panchromatic JWST Emission Spectrum. *Astronomical Journal*, 168(3):104, Sept. 2024. doi: 10.3847/1538-3881/ad58e0.

A. D. Schneider and B. Bitsch. How drifting and evaporating pebbles shape giant planets. I. Heavy element content and atmospheric C/O. *Astronomy & Astrophysics*, 654:A71, Oct. 2021. doi: 10.1051/0004-6361/202039640.

H. Schwarz, C. Ginski, R. J. de Kok, I. A. G. Snellen, M. Brogi, and J. L. Birkby. The slow spin of the young substellar companion GQ Lupi b and its orbital configuration. *Astronomy & Astrophysics*, 593:A74, Sept. 2016. doi: 10.1051/0004-6361/201628908.

S. Seager and D. D. Sasselov. Theoretical Transmission Spectra during Extrasolar Giant Planet Transits. *Astrophysical Journal*, 537(2):916–921, July 2000. doi: 10.1086/309088.

S. Seager, W. Bains, and R. Hu. Biosignature Gases in H_2-dominated Atmospheres on Rocky Exoplanets. *Astrophysical Journal*, 777(2):95, Nov. 2013. doi: 10.1088/0004-637X/777/2/95.

D. Z. Seligman, L. A. Rogers, S. H. C. Cabot, J. W. Noonan, T. Kareta, K. E. Mandt, F. Ciesla, A. McKay, A. D. Feinstein, W. G. Levine, J. L. Bean, T. Nordlander, M. R. Krumholz, M. Mansfield, D. J. Hoover, and E. Van Clepper. The Volatile Carbon-to-oxygen Ratio as a Tracer for the Formation Locations of Interstellar Comets. *Planetary Science Journal*, 3(7):150, July 2022. doi: 10.3847/PSJ/ac75b5.

A. P. Showman and T. Guillot. Atmospheric circulation and tides of "51 Pegasus b-like" planets. *Astronomy & Astrophysics*, 385:166–180, Apr. 2002. doi: 10.1051/0004-6361:20020101.

A. P. Showman and L. M. Polvani. Equatorial Superrotation on Tidally Locked Exoplanets. *Astrophysical Journal*, 738(1):71, Sept. 2011. doi: 10.1088/0004-637X/738/1/71.

D. K. Sing. Observational Techniques With Transiting Exoplanetary Atmospheres. *arXiv e-prints*, art. arXiv:1804.07357, Apr. 2018. doi: 10.48550/arXiv.1804.07357.

D. K. Sing, J. J. Fortney, N. Nikolov, H. R. Wakeford, T. Kataria, T. M. Evans, S. Aigrain, G. E. Ballester, A. S. Burrows, D. Deming, J.-M. Désert, N. P. Gibson, G. W. Henry, C. M. Huitson, H. A. Knutson, A. Lecavelier Des Etangs, F. Pont, A. P. Showman, A. Vidal-Madjar, M. H. Williamson, and P. A. Wilson. A continuum from clear to cloudy hot-Jupiter exoplanets without primordial water depletion. *Nature*, 529(7584):59–62, Jan. 2016. doi: 10.1038/nature16068.

V. Singh, A. S. Bonomo, G. Scandariato, N. Cibrario, D. Barbato, L. Fossati, I. Pagano, and A. Sozzetti. Probing Kepler's hottest small planets via homogeneous search and analysis of optical secondary eclipses and phase variations. *Astronomy & Astrophysics*, 658:A132, Feb. 2022. doi: 10.1051/0004-6361/202039037.

I. Skillen, D. Pollacco, A. Collier Cameron, L. Hebb, E. Simpson, F. Bouchy, D. J. Christian, N. P. Gibson, G. Hébrard, Y. C. Joshi, B. Loeillet, B. Smalley, H. C. Stempels, R. A. Street, S. Udry, R. G. West, D. R. Anderson, S. C. C. Barros, B. Enoch, C. A. Haswell, C. Hellier, K. Horne, J. Irwin, F. P. Keenan, T. A. Lister, P. Maxted, M. Mayor, C. Moutou, A. J. Norton, N. Parley, D. Queloz, R. Ryans, I. Todd, P. J. Wheatley, and D. M. Wilson. The $0.5M_J$ transiting exoplanet WASP-13b. *Astronomy & Astrophysics*, 502(1):391–394, July 2009. doi: 10.1051/0004-6361/200912018.

A. Smette, H. Sana, S. Noll, H. Horst, W. Kausch, S. Kimeswenger, M. Barden, C. Szyszka, A. M. Jones, A. Gallenne, J. Vinther, P. Ballester, and J. Taylor. Molecfit: A general tool for telluric absorption correction. I. Method and application to ESO instruments. *Astronomy & Astrophysics*, 576:A77, Apr. 2015. doi: 10.1051/0004-6361/201423932.

P. Smith. ARDA: a 3D atmospheric modeling and retrieval code for high spectral resolution. In *American Astronomical Society Meeting Abstracts*, volume 241 of *American Astronomical Society Meeting Abstracts*, page 350.03, Jan. 2023.

C. Sneden, J. Bean, I. Ivans, S. Lucatello, and J. Sobeck. MOOG: LTE line analysis and spectrum synthesis. Astrophysics Source Code Library, record ascl:1202.009, Feb. 2012.

I. A. G. Snellen, R. J. de Kok, E. J. W. de Mooij, and S. Albrecht. The orbital motion, absolute mass and high-altitude winds of exoplanet HD209458b. *Nature*, 465(7301):1049–1051, June 2010. doi: 10.1038/nature09111.

I. A. G. Snellen, R. J. de Kok, R. le Poole, M. Brogi, and J. Birkby. FINDING EXTRATERRESTRIAL LIFE USING GROUND-BASED HIGH-DISPERSION SPECTROSCOPY. *The Astrophysical Journal*, 764(2):182, feb 2013. doi: 10.1088/0004-637x/764/2/182. URL `https://doi.org/10.1088/0004-637x/764/2/182`.

S. G. Sousa, N. C. Santos, V. Adibekyan, E. Delgado-Mena, and G. Israelian. ARES v2: new features and improved performance. *Astronomy & Astrophysics*, 577:A67, May 2015. doi: 10.1051/0004-6361/201425463.

S. G. Sousa, V. Adibekyan, N. C. Santos, A. Mortier, S. C. C. Barros, E. Delgado-Mena, O. Demangeon, G. Israelian, J. P. Faria, P. Figueira, B. Rojas-Ayala, M. Tsantaki, D. T. Andreasen, I. Brandão, A. C. S. Ferreira, M. Montalto, and A. Santerne. The metallicity-period-mass diagram of low-mass exoplanets. *Monthly Notices of the Royal Astronomical Society*, 485(3):3981–3990, May 2019. doi: 10.1093/mnras/stz664.

J. Southworth. Homogeneous studies of transiting extrasolar planets - IV. Thirty systems with space-based light curves. *Monthly Notices of the Royal Astronomical Society*, 417(3):2166–2196, Nov. 2011. doi: 10.1111/j.1365-2966.2011.19399.x.

J. Southworth. Homogeneous studies of transiting extrasolar planets - V. New results for 38 planets. *Monthly Notices of the Royal Astronomical Society*, 426(2):1291–1323, Oct. 2012. doi: 10.1111/j.1365-2966.2012.21756.x.

K. G. Stassun, K. A. Collins, and B. S. Gaudi. Accurate Empirical Radii and Masses of Planets and Their Host Stars with Gaia Parallaxes. *The Astronomical Journal*, 153(3):136, Mar. 2017. doi: 10.3847/1538-3881/aa5df3.

K. G. Stassun, R. J. Oelkers, M. Paegert, G. Torres, J. Pepper, N. De Lee, K. Collins, D. W. Latham, P. S. Muirhead, J. Chittidi, B. Rojas-Ayala, S. W. Fleming, M. E. Rose, P. Tenenbaum, E. B. Ting, S. R. Kane, T. Barclay, J. L. Bean, C. E. Brassuer, D. Charbonneau, J. Ge, J. J. Lissauer, A. W. Mann, B. McLean, S. Mullally, N. Narita, P. Plavchan, G. R. Ricker, D. Sasselov, S. Seager, S. Sharma, B. Shiao, A. Sozzetti, D. Stello, R. Vanderspek, G. Wallace, and J. N. Winn. The Revised TESS Input Catalog and Candidate Target List. *The Astronomical Journal*, 158(4):138, Oct. 2019. doi: 10.3847/1538-3881/ab3467.

K. B. Stevenson, J.-M. Désert, M. R. Line, J. L. Bean, J. J. Fortney, A. P. Showman, T. Kataria, L. Kreidberg, P. R. McCullough, G. W. Henry, D. Charbonneau, A. Burrows, S. Seager, N. Madhusudhan, M. H. Williamson, and D. Homeier. Thermal structure of an exoplanet atmosphere from phase-resolved emission spectroscopy. *Science*, 346(6211):838–841, Nov. 2014. doi: 10.1126/science.1256758.

J. M. Stone and D. Proga. Anisotropic Winds from Close-In Extrasolar Planets. *Astrophysical Journal*, 694(1):205–213, Mar. 2009. doi: 10.1088/0004-637X/694/1/205.

G. M. Szabó and L. L. Kiss. A Short-period Censor of Sub-Jupiter Mass Exoplanets with Low Density. *Astrophysical Journal Letters*, 727(2):L44, Feb. 2011. doi: 10.1088/2041-8205/727/2/L44.

G. Taffoni, U. Becciani, B. Garilli, G. Maggio, F. Pasian, G. Umana, R. Smareglia, and F. Vitello. CHIPP: INAF Pilot Project for HTC, HPC and HPDA. In R. Pizzo, E. R. Deul, J. D. Mol, J. de Plaa, and H. Verkouter, editors, *Astronomical Data Analysis Software and Systems XXIX*, volume 527 of *Astronomical Society of the Pacific Conference Series*, page 307, Jan. 2020.

O. Tamuz, T. Mazeh, and S. Zucker. Correcting systematic effects in a large set of photometric light curves. *Monthly Notices of the Royal Astronomical Society*, 356(4):1466–1470, Feb. 2005. doi: 10.1111/j.1365-2966.2004.08585.x.

C. J. F. Ter Braak. A Markov Chain Monte Carlo version of the genetic algorithm Differential Evolution: easy Bayesian computing for real parameter spaces. *Statistics and Computing*, 16(3): 239–249, Sept. 2006. doi: 10.1007/s11222-006-8769-1.

F. Tian. Atmospheric Escape from Solar System Terrestrial Planets and Exoplanets. *Annual Review of Earth and Planetary Sciences*, 43:459–476, May 2015. doi: 10.1146/annurev-earth-060313-054834.

G. Tinetti, A. Vidal-Madjar, M.-C. Liang, J.-P. Beaulieu, Y. Yung, S. Carey, R. J. Barber, J. Tennyson, I. Ribas, N. Allard, G. E. Ballester, D. K. Sing, and F. Selsis. Water vapour in the atmosphere of a transiting extrasolar planet. *Nature*, 448(7150):169–171, July 2007. doi: 10.1038/nature06002.

A. Tsiaras, I. P. Waldmann, T. Zingales, M. Rocchetto, G. Morello, M. Damiano, K. Karpouzas, G. Tinetti, L. K. McKemmish, J. Tennyson, and S. N. Yurchenko. A population study of gaseous exoplanets. *The Astronomical Journal*, 155(4):156, mar 2018. doi: 10.3847/1538-3881/aaaf75. URL `https://dx.doi.org/10.3847/1538-3881/aaaf75`.

J. A. Turner-Valle, J. Sullivan, J. E. Mentzell, and R. A. Woodruff. Wide Field Camera 3 instrument optical design for the Hubble Space Telescope. In J. C. Mather, editor, *Optical, Infrared, and Millimeter Space Telescopes*, volume 5487 of *Society of Photo-Optical Instrumentation Engineers (SPIE) Conference Series*, pages 317–329, Oct. 2004. doi: 10.1117/12.550893.

D. Turrini, E. Schisano, S. Fonte, S. Molinari, R. Politi, D. Fedele, O. Panić, M. Kama, Q. Changeat, and G. Tinetti. Tracing the Formation History of Giant Planets in Protoplanetary Disks with Carbon, Oxygen, Nitrogen, and Sulfur. *The Astrophysical Journal*, 909(1):40, Mar. 2021. doi: 10.3847/1538-4357/abd6e5.

A. Vidal-Madjar, A. Lecavelier des Etangs, J. M. Désert, G. E. Ballester, R. Ferlet, G. Hébrard, and M. Mayor. An extended upper atmosphere around the extrasolar planet HD209458b. *Nature*, 422 (6928):143–146, Mar. 2003. doi: 10.1038/nature01448.

H. R. Wakeford and P. A. Dalba. The exoplanet perspective on future ice giant exploration. *Philosophical Transactions of the Royal Society of London Series A*, 378(2187):20200054, Dec. 2020. doi: 10.1098/rsta.2020.0054.

H. R. Wakeford and D. K. Sing. Transmission spectral properties of clouds for hot Jupiter exoplanets. *Astronomy & Astrophysics*, 573:A122, Jan. 2015. doi: 10.1051/0004-6361/201424207.

H. R. Wakeford, D. K. Sing, D. Deming, N. P. Gibson, J. J. Fortney, A. S. Burrows, G. Ballester, N. Nikolov, S. Aigrain, G. Henry, H. Knutson, A. Lecavelier des Etangs, F. Pont, A. P. Showman, A. Vidal-Madjar, and K. Zahnle. HST hot Jupiter transmission spectral survey: detection of water in HAT-P-1b from WFC3 near-IR spatial scan observations. *Monthly Notices of the Royal Astronomical Society*, 435(4):3481–3493, Nov. 2013. doi: 10.1093/mnras/stt1536.

J. P. Wardenier, V. Parmentier, E. K. H. Lee, M. R. Line, and E. Gharib-Nezhad. Decomposing the iron cross-correlation signal of the ultra-hot Jupiter WASP-76b in transmission using 3D Monte Carlo radiative transfer. *Monthly Notices of the Royal Astronomical Society*, 506(1):1258–1283, Sept. 2021. doi: 10.1093/mnras/stab1797.

J. P. Wardenier, V. Parmentier, M. R. Line, and E. K. H. Lee. Modelling the effect of 3D temperature and chemistry on the cross-correlation signal of transiting ultra-hot Jupiters: a study of five chemical species on WASP-76b. *Monthly Notices of the Royal Astronomical Society*, 525(4): 4942–4961, Nov. 2023. doi: 10.1093/mnras/stad2586.

J. P. Wardenier, V. Parmentier, M. R. Line, M. Weiner Mansfield, X. Tan, S.-M. Tsai, J. L. Bean, J. L. Birkby, M. Brogi, J.-M. Désert, S. Gandhi, E. K. H. Lee, C. I. Levens, L. Pino, and P. C. B. Smith. Phase-resolving the Absorption Signatures of Water and Carbon Monoxide in the Atmosphere of the Ultra-hot Jupiter WASP-121b with GEMINI-S/IGRINS. *Publications of the Astronomical Society of the Pacific*, 136(8):084403, Aug. 2024. doi: 10.1088/1538-3873/ad5c9f.

A. J. Watson, T. M. Donahue, and J. C. G. Walker. The dynamics of a rapidly escaping atmosphere: Applications to the evolution of Earth and Venus. *Icarus*, 48(2):150–166, Nov. 1981. doi: 10.1016/0019-1035(81)90101-9.

M. Weiner Mansfield, M. R. Line, J. P. Wardenier, M. Brogi, J. L. Bean, H. Beltz, P. Smith, J. A. Zalesky, N. Batalha, E. M. R. Kempton, B. T. Montet, J. E. Owen, P. Plavchan, and E. Rauscher. The Metallicity and Carbon-to-oxygen Ratio of the Ultrahot Jupiter WASP-76b from Gemini-S/IGRINS. *Astronomical Journal*, 168(1):14, July 2024. doi: 10.3847/1538-3881/ad4a5f.

L. Welbanks, N. Madhusudhan, N. F. Allard, I. Hubeny, F. Spiegelman, and T. Leininger. Mass–metallicity trends in transiting exoplanets from atmospheric abundances of h2o, na, and k. *The Astrophysical Journal Letters*, 887(1):L20, dec 2019. doi: 10.3847/2041-8213/ab5a89. URL `https://dx.doi.org/10.3847/2041-8213/ab5a89`.

B. L. Welch. THE GENERALIZATION OF 'STUDENT'S' PROBLEM WHEN SEVERAL DIFFERENT POPULATION VARLANCES ARE INVOLVED. *Biometrika*, 34(1-2):28–35, 01 1947. ISSN 0006-3444. doi: 10.1093/biomet/34.1-2.28. URL `https://doi.org/10.1093/biomet/34.1-2.28`.

M. W. Werner, T. L. Roellig, F. J. Low, G. H. Rieke, M. Rieke, W. F. Hoffmann, E. Young, J. R. Houck, B. Brandl, G. G. Fazio, J. L. Hora, R. D. Gehrz, G. Helou, B. T. Soifer, J. Stauffer, J. Keene, P. Eisenhardt, D. Gallagher, T. N. Gautier, W. Irace, C. R. Lawrence, L. Simmons, J. E. Van Cleve, M. Jura, E. L. Wright, and D. P. Cruikshank. The Spitzer Space Telescope Mission. *Astrophysical Journal Supplement*, 154(1):1–9, Sept. 2004. doi: 10.1086/422992.

A. Wolszczan and D. A. Frail. A planetary system around the millisecond pulsar PSR1257 + 12. *Nature*, 355(6356):145–147, Jan. 1992. doi: 10.1038/355145a0.

A. Wyttenbach, D. Ehrenreich, C. Lovis, S. Udry, and F. Pepe. Spectrally resolved detection of sodium in the atmosphere of HD 189733b with the HARPS spectrograph. *Astronomy & Astrophysics*, 577:A62, May 2015. doi: 10.1051/0004-6361/201525729.

A. Wyttenbach, C. Lovis, D. Ehrenreich, V. Bourrier, L. Pino, R. Allart, N. Astudillo-Defru, H. M. Cegla, K. Heng, B. Lavie, C. Melo, F. Murgas, A. Santerne, D. Ségransan, S. Udry, and F. Pepe. Hot Exoplanet Atmospheres Resolved with Transit Spectroscopy (HEARTS). I. Detection of hot neutral sodium at high altitudes on WASP-49b. *Astronomy & Astrophysics*, 602:A36, June 2017. doi: 10.1051/0004-6361/201630063.

J. W. Xuan and M. C. Wyatt. Evidence for a high mutual inclination between the cold Jupiter and transiting super Earth orbiting π Men. *Monthly Notices of the Royal Astronomical Society*, 497 (2):2096–2118, Sept. 2020. doi: 10.1093/mnras/staa2033.

Q. Xue, J. L. Bean, M. Zhang, L. Welbanks, J. Lunine, and P. August. JWST Transmission Spectroscopy of HD 209458b: A Supersolar Metallicity, a Very Low C/O, and No Evidence of CH_4, HCN, or C_2H_2. *Astrophysical Journal Letters*, 963(1):L5, Mar. 2024. doi: 10.3847/2041-8213/ad2682.

S. W. Yee, E. A. Petigura, B. J. Fulton, H. A. Knutson, K. Batygin, G. Á. Bakos, J. D. Hartman, L. A. Hirsch, A. W. Howard, H. Isaacson, M. R. Kosiarek, E. Sinukoff, and L. M. Weiss. HAT-P-11: Discovery of a Second Planet and a Clue to Understanding Exoplanet Obliquities. *The Astronomical Journal*, 155(6):255, June 2018. doi: 10.3847/1538-3881/aabfec.

R. V. Yelle. Aeronomy of extra-solar giant planets at small orbital distances. *Icarus*, 170(1):167–179, July 2004. doi: 10.1016/j.icarus.2004.02.008.

S. N. Yurchenko, R. J. Barber, and J. Tennyson. A variationally computed line list for hot NH_3. *Monthly Notices of the Royal Astronomical Society*, 413(3):1828–1834, May 2011. doi: 10.1111/j.1365-2966.2011.18261.x.

K. Zahnle, M. S. Marley, and J. J. Fortney. Thermometric Soots on Warm Jupiters? *arXiv e-prints*, art. arXiv:0911.0728, Nov. 2009. doi: 10.48550/arXiv.0911.0728.

L. Zeng, S. B. Jacobsen, D. D. Sasselov, M. I. Petaev, A. Vanderburg, M. Lopez-Morales, J. Perez-Mercader, T. R. Mattsson, G. Li, M. Z. Heising, A. S. Bonomo, M. Damasso, T. A. Berger, H. Cao, A. Levi, and R. D. Wordsworth. Growth model interpretation of planet size distribution. *Proceedings of the National Academy of Science*, 116(20):9723–9728, May 2019. doi: 10.1073/pnas.1812905116.